Anderson-like localization in weakly interacting Bose-Einstein condensate: Localization-delocalization transitions and non-equilibrium dynamics

A Thesis Submitted
in partial fulfilment of the requirements
for the degree of
Doctor of Philosophy

by
Swarup Kanti Sarkar
Roll No. 196121031

under the supervision of
Dr. Pankaj Kumar Mishra

to the
DEPARTMENT OF PHYSICS
INDIAN INSTITUTE OF TECHNOLOGY Guwahati
October, 2025

Declaration

This is to certify that the work contained in this thesis entitled **"Anderson-like localization in weakly interacting Bose-Einstein condensate: Localization-delocalization transitions and non-equilibrium dynamics"** submitted by me to the Indian Institute of Technology, Guwahati, for the award of the degree of PhD, is a bonafide work carried out by me under the supervision of Dr. Pankaj Kumar Mishra and that this work has not been submitted elsewhere for a degree of diploma. I also wish to state that to the best of my knowledge and understanding nothing in this report amounts to plagiarism.

October 23, 2025

Swarup Kanti Sarkar
Department of Physics
Indian Institute of Technology
Guwahati

Certificate

It is certified that the work contained in this thesis entitled **"Anderson-like localization in weakly interacting Bose-Einstein condensate: Localization-delocalization transitions and non-equilibrium dynamics"** by **Swarup Kanti Sarkar**, has been carried out under my supervision, and this work has not been submitted elsewhere for a degree.

Pankaj Kumar Mishra

October 23, 2025

Dr. Pankaj Kumar Mishra
Associate Professor
Department of Physics
Indian Institute of Technology
Guwahati

Preface

Anderson localization (AL), originally proposed by P. W. Anderson in 1958, describes the suppression of quantum particle diffusion in disordered media due to interference effects. Initially formulated in the context of electron transport in disordered solids, since then the concept has become a cornerstone to understand the wave localization across a wide range of systems—from classical waves including light, microwaves, and sound to quantum matter waves in ultracold matter. In the realm of quantum matter waves, ultracold atomic Bose-Einstein condensates (BECs) have emerged as an ideal and highly controllable platform to study AL. The presence of coherence, tunable interactions, and the ability to engineer external potentials in BECs allow them for robust investigation of localization phenomena. Over the past two decades, the observation of AL in ultracold atomic BECs subjected to quasiperiodic optical lattices and random speckle potentials has led to a surge of theoretical and experimental research in the field.

A key theoretical framework underlying these studies is the Gross-Pitaevskii (GP) formalism that effectively captures the dynamics of weakly interacting condensates. The GP equation thus provides a versatile tool to explore the interplay between disorder, interactions, and spin-dependent couplings, enabling detailed analyses of ground-state properties and non-equilibrium dynamics associated with Anderson localization in BECs.

In this thesis, using the mean-field GP model, we have explored the effect of interparticle interactions, disorder, and spin-related couplings on the ground state and dynamics of the AL in BEC. In the following, we briefly outline the key findings of our work, which is divided into seven chapters.

Chapter 1 begins with a brief introduction to Anderson localization (AL) across various physical systems, including strongly correlated materials, photonic platforms, and quantum matter waves. To build a foundational understanding, we then present the basic physics of wave localization using simplified toy models. This is followed by an introduction to Bose-Einstein condensates (BECs), along with an overview of mean-field atomic interactions and the different types of disordered potentials employed to study localization in quantum matter waves. Subsequently, we describe the theoretical framework based on the mean-field Gross-Pitaevskii (GP) formalism, both for neutral atoms and for systems incorporating synthetic spin-orbit coupling. Following this we present an extensive literature review encompassing experimental, theoretical, and numerical studies with main focus on the roles of interatomic interactions, disorder, spin-orbit (SO) coupling, and Rabi coupling in dictating the ground state and dynamics of the localized state of the condensate. The chapter concludes by outlining the main motivation of the thesis for exploring different localization–delocalization phases of BECs.

In **Chapter 2**, we discuss the numerical schemes employed to solve the quasi-1D GP equations (GPEs). The chapter begins with an overview of the split-step Crank-Nicolson (CN) method, which is used to simulate the time evolution of SO-coupled binary condensates. This is followed by a description of the imaginary time propagation technique for obtaining ground states and the real-time propagation scheme for studying condensate dynamics. The chapter concludes with an example demonstrating the convergence of the ground-state of the GPEs.

In **Chapter 3**, we explore the ground state and out-of-equilibrium dynamics of quasi-one-dimensional scalar BECs confined in bichromatic and random disordered potentials. Increasing the repulsive interaction strength leads to a transition from localized to delocalized ground states. To investigate the dynamical behavior, we performed an interaction quench by suddenly switching off the nonlinearity from the value at which the ground state was prepared, and analyzed the resulting time evolution using observables such as the time correlator, power spectral density, and Lyapunov exponent. Regular (periodic or quasiperiodic) dynamics emerge in the localized regime when the quench is applied from a low interaction strength, while chaotic behavior arises in the delocalized phase under strong quenching. Notably, a quasiperiodic route to chaos was observed during the transition from regular to chaotic dynamics across the localization–delocalization crossover. Furthermore, the critical nonlinearity required to trigger chaotic dynamics decreases with decreasing disorder strength. We find similar nature of dynamical feature of the localization and delocalization state

for the condensate trapped in the random potential. This study demonstrates that quench-induced nonequilibrium dynamics offers a alternate approach to distinguish the localized and delocalized state of the condensate. The tool developed in the work show similar feature for the condensate trapped in quasiperiodic as well as random potentil.

In **Chapter 4**, we consider the spin-orbit (SO) coupled binary condensate to explore the role of interaction inhomogeneity in the localization-delocalization transition trapped in a weak quasiperiodic potential. When the inhomogeneity follows the quasiperiodic potential, the condensate exhibits transitions from localized to delocalized states as the interaction is tuned from attractive to repulsive values. Further, introducing a $\pi/2$ phase shift between the inhomogeneity and the potential leads to an interesting localization–delocalization–localization transition of the condensate. We have also explored the effects of SO and Rabi couplings on the localization-delocalization phases of the condensate. Additionally, a Gaussian variational approach is also employed to support our numerical findings. Finally, the stability of these localized-delocalized condensates are examined by probing velocity perturbations and trap quenching condensate dynamics.

After exploring different localization-delocalization phases in quasiperiodic potential, in **Chapter 5**, we extend the analysis of spin-orbit (SO) condensate trapped in a one-dimensional random potential. Here, we comprehensively study the combined effects of disorder, interactions, SO, and Rabi coupling on the localization-delocalization transition. Our studies reveal that the spin-dependent couplings create distinct localization regimes, resulting in various relations between localization and spin-related properties. First, we examine the localization in the linear condensate and find that the SO coupling can lead to a transition of the localized state from the "basin-like" to the "void" region of the potential—which differs from conventional Anderson localization. In the later part, we considered the different combinations of interactions with broken Manakov's symmetry, which leads to various spin-dependent localizations of the condensate. This involves spin population redistribution and spatial separation of spin components between the voids and basins of the potential. The interplay between SO coupling and nonlinear interactions amplifies these effects, leading to strong spin polarization and localization of one spin component by delocalizing the other component.

Following the previous chapters involving spin-symmetric quasiperiodic and random potentials, in **Chapter 6**, we focus on the localization and driven dynamics in a Rabi-coupled binary condensate subject to a spin-asymmetric quasiperiodic confine-

ment, where only one component is trapped while the other remains free. In that case, when the Rabi coupling increases above a critical value, it induces localization through population exchange between the components. With the inclusion of interactions, the localized condensate fragments across multiple potential minima, and the untrapped component follows the trapped one due to the role of Rabi coupling. Further, the condensate dynamics under the periodic driving of Rabi frequency exhibits various frequency-dependent delocalization patterns, including double (triple)-minima, tree-(parquet)-like, and frozen distributions with a correlated propagation of different spin populations are observed in the condensate density. Furthermore, the persistence of dynamical delocalization in the presence of interactions underscores the intrinsic resonance-driven nature of the phenomenon.

In **Chapter 7**, we present the summary and conclusion of the thesis, highlighting the various Anderson-like localization–delocalization phases and their associated non-equilibrium dynamics. Finally, this chapter concludes with a brief outline of the future scope of the work presented in the thesis.

We believe that this study addresses a gap in the current understanding of Anderson localization in ultracold matter and offers valuable insights for future research. We also hope that our findings will inspire experimental investigations involving synthetic spin-orbit and Rabi coupling, further advancing the field in the years to come.

Acknowledgements

"No matter how much time goes by or what unfolds in the present, some memories remain indelible–etched beyond the reach of forgetting. True appreciation is the highest form of prayer, for it acknowledges the presence of good wherever you shine the light of your thankful thoughts."

The journey of my Ph.D. has felt much like a train ride—where the experiences, lessons, memories, and above all, the people along the way have held as much meaning as the destination itself. As I stand at the end of this chapter of life, I wish to express my deepest gratitude to all those who traveled beside me, supported me, and made this journey unforgettable.

First, and foremost, I would like to express my sincere gratitude to my thesis supervisor, Dr. Pankaj Kumar Mishra, under whose guidance I began my academic journey from my Master's—a path that gradually evolved into this Ph.D. endeavour. Although I started as a novice in numerical programming, he never wavered in his faith in my potential or determination. His unwavering belief empowered me with the freedom to explore a range of diverse and exciting research directions. For that trust and enduring support, I remain profoundly grateful. I also deeply appreciate his constant encouragement and cooperation throughout this journey, both in academic matters and beyond. Working under his mentorship has been an enriching and inspiring experience, and I will always carry these memories with warmth and gratitude.

A special thanks to my Doctoral Committee members, Prof. Subhradip Ghosh, Dr. Kanhaiya Pandey, and Prof. Subhash Thota, for evaluating my work and giving inputs that helped me to finish this thesis. Also, I would like to thank the former Doctoral Committee members, Prof. Tapan Mishra and Prof. Anki Reddy Katha. Additionally, I deeply appreciate the support from the former HoDs Prof. Subhradip Ghosh, Prof. Perumal Alagarsamy, and current HoD Prof. Bosanta R. Boruah from the Physics Department at IIT Guwahati.

It is my pleasure to express my deep sense of gratitude to all of my collaborators for their invaluable expertise and contributions. First and foremost, I would like to thank Prof. Paulsamy Muruganandam (Bharathidasan University) for introducing me to the numerical techniques used in the analyzing the mean-field dynamics of the Bose-Einstein condensates. I am especially grateful for his guidance and support whenever I encountered difficulties with numerical implementations. I am also truly thankful to Dr. R. Ravishankar for providing essential numerical packages related to my work. His expertise in computational programming proved immensely helpful at various stages of my research. A heartfelt thanks goes to Prof. Tapan Mishra (NISER Bhubaneswar) for his fruitful collaboration on two of the initial works included in this thesis. Next, I owe a deep sense of appreciation to Prof. Evgeny Sherman (University of the Basque Country, Bilbao, Spain), who taught me how to grasp the fundamental Physics of very complex system from scratch. Also, I sincerely thank Dr. Shukhrat Mardonov (Ulugh Beg Astronomical Institute, Tashkent, Uzbekistan), for the fruitful collaboration for the later part of my thesis work.

Teachers hold a pivotal role in shaping not only student's future, but also their journey toward becoming a thoughtful and compassionate human being. In this spirit, I would like to express my heartfelt gratitude to all the teachers of the Department of Physics, IIT Guwahati, from whom I have had the privilege to learn beginning from my Master's days through the course work of my PhD. When it comes to my teachers, the list is indeed a long one, but I am especially grateful to Dr. Achinta K. Chatterjee and Dr. Uttam K. Sarkar of Malda College, whose inspiring teaching first initiated and further sustained my interest in Physics. Also, I am very much thankful to Apurba Sir and Rajkumar Sir for their enthusiastic and engaging approach to teaching physics.

I am thankful to my group members -Rony Da, Sonali, Sanu, Shawan, Joya, Sumit, Nalinikanta, Prembrata and Moumita di -for keeping very friendly environment in the group and fruitful discussions on different topics over tea.

I owe a special note of thanks to Rony da for being not only a supportive senior and collaborator, but also a good friend. Our wide range of conversations spanning from research to politics that I have with him enriched my understanding towards life in better sense.

During my stay at IIT Guwahati, I came across many seniors, juniors, and friends whose presence have made this journey pleasant and memorable. First, I would like to acknowledge my seniors–Rajesh da, Rakesh da, Anirban da, Sayan da, Arghya da, Pronoy da, Samit da, Partha da, Sanket da, Riajul da, Mandira di, and Surojit da– for their valuable suggestions and constant encouragement, which played a key role in helping me stay motivated throughout this journey. I truly thank all the juniors,

in particular, Avishek, Abhijeet, Amit, Himangsu, Niloy, Abhik, Sourav, Saswata and many more for their kind support. When it comes to friends, I would first like to acknowledge the M.Sc. 2017 batch of IIT Guwahati, along with all my fellow Ph.D. batchmates from July and December 2019, whose companionship has been an integral part of this journey. I am also thankful to my Siang Hostel friends, both past and present, who made hostel life truly memorable. The post-dinner walks and random conversations with Soumen, Subhrojyoti, Amit, Avishek, Samit da, and Rony da are the moments which I will cherish long after leaving the campus. I would like to extend my heartfelt thanks to my school friends from the VIVIANS 2014 batch, with special mention to Rishav, Pritam, and Dipayan for their enduring companionship since our school days. I also fondly remember the joy of the Saturday football matches and the wonderful friends that I played during my Ph.D. journey will always hold a special place in my heart. I am equally grateful to the central Gym facility at IIT Guwahati, which played a vital role in helping me maintain both physical and mental well-being throughout these years. The books I've read over the years have deeply shaped me, and my guitar has been a faithful companion in my quiet moments.

The thesis would not have been completed without our institute-level computational facilities, Param Ishan and Param Kamrupa, at IIT Guwahati. I especially acknowledge our departmental supercomputing facility, our group's cluster, where most of the simulations are performed. I am grateful to the Ministry of Health and Research Development (MHRD), India, for providing the financial support. I would also like to thank all the staff members of the Physics department for their kind cooperation and support throughout my stay at IIT Guwahati.

Above all, this Ph.D. journey would not have been possible without the unwavering support, encouragement, and blessings of my family members. Their unconditional love and countless sacrifices are beyond measure, and I know I can never fully repay them for everything they have done to help me reach this milestone. I am especially grateful to my Baba and Ma, whose constant support since my childhood has been the foundation of all my pursuits. A very special note of thanks goes to Miss Mousumi Biswas–a true mentor, philosopher, and teacher–whose steadfast presence has supported my family through both joyful and difficult times. Beyond academics, she has taught me some of life's most important lessons, and for that, I shall remain forever indebted to her. Lastly, I would like to thank Dr. Poly Karmakar for becoming a wonderful friend within a short time, and I sincerely hope that this bond continues to grow even stronger in the future.

To my family . . .

. . . and to every child whose dreams deserve to flourish in a world free from conflict . . .

Publications

1. Quench-induced chaotic dynamics of Anderson-localized interacting Bose-Einstein condensates in one dimension, **S. K. Sarkar**, T. Mishra, P. Muruganandam, and P.K. Mishra, Phys. Rev. A **107**, 053320 (2023).

2. Signature of localization-delocalization in collisional inhomogeneous spin-orbit coupled condensates **S. K. Sarkar**, R. Ravisankar, T. Mishra, P. Muruganandam, and P.K. Mishra, J. Phys. B: At., Mol. Opt. Phys. **58**, 065001 (2025).

3. Spin-dependent localization of spin-orbit and Rabi-coupled Bose-Einstein condensates in a random potential, **S. K. Sarkar**, Sh. Mardonov, E. Ya. Sherman, P. Muruganandam, P.K. Mishra, New Journal of Physics **27**, 023018 (2025).

4. Rabi-induced localization and resonant delocalization of a binary condensate in a spin-asymmetric quasiperiodic potential, **S. K. Sarkar**, Sh. Mardonov, E. Ya. Sherman, P.K. Mishra, Phys. Rev. A **112**, 043302 (2025).

Contents

Chapter 1

Introduction

In real materials, structural imperfections are ubiquitous in nature. These imperfections referred to as *disorder* disrupt the periodicity of a lattice, thereby affecting the transport properties of solids. In crystals, as electrons traverse in such a medium, they undergo scattering events that limit their mean-free path, which eventually reduces the electrical conductivity of solids. This raises some pertinent questions, like, what is the lower bound of electrical conductivity with the increase of disorder — will it simply suppress the electrical conductivity gradually, or will it lead to some fascinating phenomena along the way? These sorts of questions were addressed by Philip Anderson more than half a century ago using the seminal model of the electron dynamics in presence of the disorder. In 1958, through the seminal model Anderson demonstrated the complete suppression of electrons' diffusion leading to its localization in presence of the disorder that explains the metal-to-insulator transition in the presence of random disorder in certain solids. This phenomenon got popular with the name as *Anderson localization* (AL) [1, 2]. The AL model introduced a remarkable quantum mechanical description of the metal to insulator transition. In the early 1960s, Nevill Mott extended this model by incorporating the effect of a mobility edge, a critical energy separating extended and localized states of electrons [3, 4] which later led to the great advancement in understanding of the electronic structure of the magnetic and disordered system, in particular the electron transport in the amorphous semiconductors. For their pioneering work on the disordered systems, Anderson, his thesis advisor John van Vleck, and Mott were jointly awarded the 1977 Nobel Prize in Physics. Although Anderson's original paper hardly got noticed but later, understanding the fundamental significance of the work, he stated that,

"Very few believed [localization] at the time, and even fewer saw its importance; among those who failed to fully understand it at first was certainly its author. It has yet to receive adequate mathematical treatment, and one has to resort to the indignity of numerical simulations to settle even the simplest questions about it." —**Philip W. Anderson**, Nobel lecture, 1977

Even though Anderson's 1958 model laid the foundation for the localization of electrons, the theory faced many challenges to use it for generalized cases. For example, like any other phase transition, it strongly depends on the dimension of the medium. In 1959, Gertsenshtein and Vasil'ev theoretically showed that in one-dimensional systems, such as thin wires, all quantum states are localized for any nonzero disorder [5]. A similar conclusion was independently reached by Mott and Twose, who also received credit for this result. Demonstrating localization in higher dimensions proved to be more difficult. After 15 years, in 1973, Ragi Abou-Chacra and David Thouless solved the 2D localization problem by considering an artificial fractal model, where an electron makes an hopping in a Cayley tree [6]. This was followed in 1979 by the development of the scaling theory of localization by the so-called 'Gang of four'—Elihu Abrahams, Anderson, Donald Licciardello, and T. V. Ramakrishnan, which offered an unifying framework to understand the dimensionality in localization [7, 8]. However, this theory faced strong criticism from Mott, who argued that the mean free path l of a conducting electron can never be smaller than the lattice constant a, which implies a finite lower bound for conductivity. At the Fermi surface, the electron's de Broglie wavelength λ is approximately $2\pi a$, which aligns with an earlier but similar criterion proposed by Ioffe and Regel, who estimated $l \approx \lambda$, differing only by a factor of 2π. Ultimately, the Ioffe-Regel criterion prevailed, generalized as $2\pi l/\lambda \approx 1$ for complex media. Due to these theoretical intricacies, realizing AL in electronic condensed matter systems remained challenging. Although few notable experiments have investigated for localization of electrons [4, 9].

Apart from the condensed matter systems, the wave interference phenomena in AL led to a surge of interest in studying localization across various physical platforms where wave nature dominates. Soon after, experimental demonstrations of AL extended to classical wave systems, such as electromagnetic waves [10–14], microwaves [15–18], and acoustic waves [19] and quantum matter waves using ultracold atomic gases [20, 21]. In ultracold atoms, Bose-Einstein condensate (BEC) offers an ideal platform for studying the role of disorder and atomic interactions—a long-standing problem in localization physics, due to the dilute nature of quantum gases and precise controllability at the microscopic scale. The experimental realization of Anderson localization (AL) in BEC has significantly stimulated the scientific community over the last decade, also

prompting extensive theoretical and numerical investigations. The numerical modeling of dilute BECs has been performed using the mean-field Gross–Pitaevskii equation (GPE) with disorder introduced using two different types of disordered potentials, namely, quasiperiodic [20] and random speckle potential [21]. In recent years, substantial progress has been made on the complex interplay between disorder and interactions using this mean-field GPE model [22–24]. In addition to the investigation considering the stationary state of BECs, the condensate dynamics also has been explored by perturbing the stationary state using various techniques such as releasing the BECs from the confining trap [23, 25], giving momentum to the condensate [26], performing a sudden quench in coupling parameters [27, 28], or nonlinear interactions [29]. The interplay of interaction and disorder also leads to very intriguing non-equilibrium dynamics in BECs [30].

Nevertheless, in the study of localization in BECs, several important aspects remain unresolved — such as proper characterization of localization-delocalization, role of interaction, disorder strength and nature, and the influence of spin-orbit (SO) and Rabi coupling in dictating the localization of the condensate. Using the mean-field Gross-Pitaevskii (GP) framework, in this thesis, we aim to bridge this gap by conducting an extensive numerical simulation properly backed by analytical results for the scalar as well as complex spin-1/2 condensate coupled with the synthetic SO and Rabi couplings.

The outline of this chapter is as follows. First, we discuss the basics of Anderson localization (AL), followed by an extensive discussion on the state-of-art experiments on AL. As our main focus of the thesis is to characterize AL in BECs, we provide a brief introductory presentation of Bose-Einstein condensation. It is followed by the discussion of different atomic interactions and disordered potentials. Subsequently, we discuss briefly the remarkable experiments of AL using ultra-cold atomic BECs, which have motivated a plethora of numerical and theoretical studies using the GP framework. Further we present the mean-field GP equation for both scalar and spin-orbit (SO) coupled condensates. Finally the Chapter concludes with an extensive literature review of the AL in BECs, which is followed by the main motivation of our work and a brief layout of the subsequent chapters.

1.1 Anderson localization

Anderson localization describes the quantum transport of electrons in a disordered medium which involves the assumption that the electronic wave undergoes elastic scattering while encountering static point-like impurities. Intuitively one can understand it through multiple scattering phenomena. In what follows we will describe few of the toy model to understand this phenomenon. Let's consider an electron propagates in a disordered medium from point A to point B. While traversing, the electrons can choose different random paths for different realizations [see Fig. 1.1(a)]. In order to obtain the probability of the electron at B, one needs to sum and then square the amplitudes of all possible paths. The final probability contains two parts, namely, the first part is the classical, which is the sum of the probabilities of individual paths between A and B, finally leading to the classical Drude theory of diffusion. The second part originates from the quantum interference between different paths, which acquire a phase difference between two different trajectories. The disorder averaging can completely cancel the second term, and hence, finally, the classical diffusive term remains, describing the transport of free electrons. But in some cases, the interference term survives the disorder averaging. Let's assume an electron travels from A to B along some random path and then comes back to A in two possible paths as shown in Fig. 1.1(b). The two paths interfere constructively and the second interference term has a predominant effect over the classical diffusive contribution. The enhanced backscattering increases the return probability of the electron back to point A. This effect of reducing the conductance by coherent backscattering due to disorder is referred to as the *weak localization*, which has been realized in various experimental works [8, 31–34]. So far, we have only considered the contribution from a single loop reducing the metallic conductance of electrons, but in real systems many other contributions also take part in the transport which not only reduces the conductance but rather decimates transport of the electrons by trapping the them in fixed domain, this effect is defined as *strong localization* or *Anderson localization*. The original work done by Anderson [2] was based on the tight-binding model, where electron are assumed to be localized around the atomic sites and can make a hopping to the neighbouring sites. In presence of random disorder (e.g, impurities, irregularities) the electrons get localized in a particular regions as a results of multiple scattering from the random impurities sites. He showed it while for 1D and 2D even weak disorder strength can localize all the eigenstates of the electron wave functions, for 3D there exists a threshold strength of the disorder above which the states are localized. The density of the localized state exhibits the exponential decay in

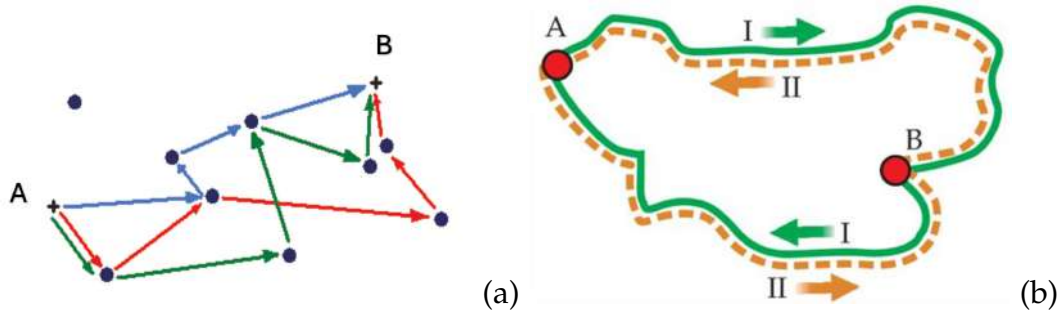

Figure 1.1: (a) An illustration of three different trajectories of a particle scattered from different impurities while traveling from point A to B, (b) loop trajectories of a particle between A and B where the trajectories I and II interfere constructively to enhance return probability. Figure is adapted from Ref. [35, 36]

space. In what follows we present a toy model to better explain the localization of the quantum matter wave in presence of random scattering in presence of impurities.

For simplicity we consider a one-dimensional model to show the localization which can be easily extended for higher dimensional cases [3]. Let's assume a quantum particle of energy E moves in a 1D periodic potential of length L, consisting of a series of equally spaced barriers with the same width b and height V_0 as depicted in Fig. 1.2 and potential is given by

$$V(x) = \begin{cases} 0 & \text{if} \quad x \in S_j \\ V_0 & \text{if} \quad x \in E_j, \end{cases} \tag{1.1}$$

where the domains are defined as:

$$\begin{aligned} S_j &= [ja, (j+1)a - b], \\ E_j &= [ja - b, ja]. \end{aligned} \tag{1.2}$$

The corresponding Schrödinger equation is given by

$$\begin{aligned} \frac{\partial^2\psi}{\partial x^2} + \frac{2m}{\hbar^2}E\psi = 0 \quad x \in S_j, \\ \frac{\partial^2\psi}{\partial x^2} + \frac{2m}{\hbar^2}(E - V_0)\psi = 0 \quad x \in E_j, \end{aligned} \tag{1.3}$$

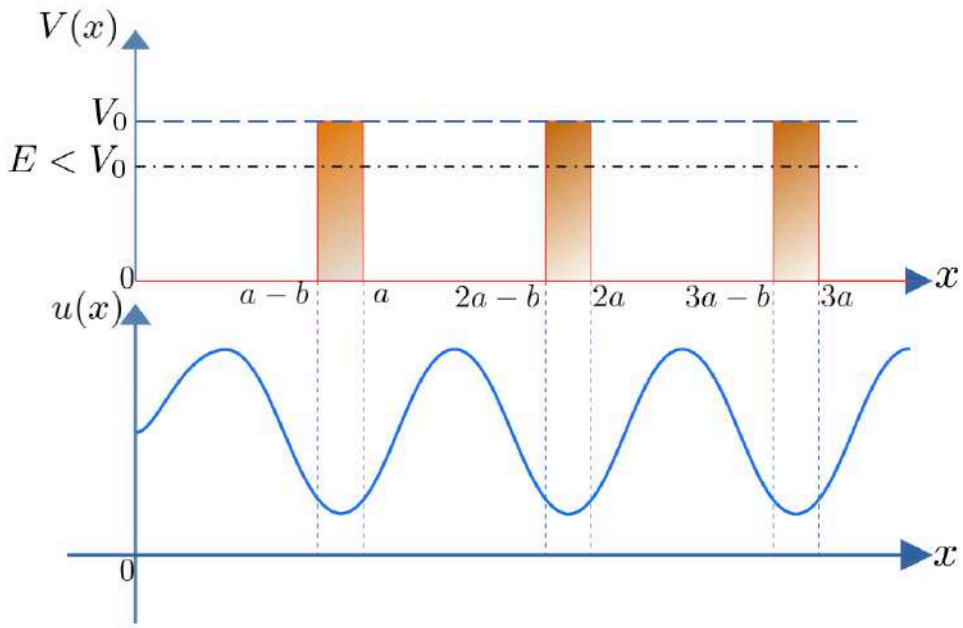

Figure 1.2: A qualitative representation of periodic potential $V(x)$ described in Eq. (1.1) and the periodic Bloch $u(x)$ wavefunction.

The Eq. (1.3) for $E < V_0$ yields

$$\psi(x) = \begin{cases} A_j e^{i\alpha x} + A'_j e^{-i\alpha x + \varphi_j} & \text{if} \quad x \in S_j \\ B_j e^{\beta x} + B'_j e^{-\beta x + \phi_j} & \text{if} \quad x \in E_j \end{cases} \tag{1.4}$$

with $\alpha = 2mE/\hbar^2$ and $\beta = 2m(V - E_0)/\hbar^2$. Due to the periodic nature of the potential, the solution of the Schrödinger equation asserts the wavefunction as a Bloch state, which can be written as :

$$\psi(x) = e^{ikx} u(x), \tag{1.5}$$

where $u(x)$ defines the periodic function with the same periodicity as the potential $V(x)$:

$$u(x + a) = u(x), \tag{1.6}$$

To obtain the right solution, one needs to impose the continuity and the differentiation

$\psi(x)$:

$$\begin{cases} \psi(a^+) = \psi(b^-), \\ \frac{\partial\psi(a^+)}{\partial t} = \frac{\partial\psi(b^-)}{\partial t}, \end{cases} \tag{1.7}$$

and the conditions of periodicity for $u(x)$:

$$\begin{cases} u(-b) = u(a-b), \\ \frac{\partial u(-b)}{\partial t} = \frac{\partial u(a-b)}{\partial t}, \end{cases} \tag{1.8}$$

Eq. (1.7), and Eq. (1.8) provide the conditions for k and E. The continuity gives us the shape of the eigenfunctions as $\psi(x) \equiv e^{ikx}u(x)$, with the periodic function $u(x)$. The shape of $u(x)$ is sinusoidal for the region $V(x) = 0$ region, whereas, for the $V(x) = V_0$ region, the contribution of two exponential functions joined together with the eigenfunction outside the barrier where $V(x) = 0$. The resultant extended periodic function is shown in the bottom panel of Fig. 1.2. In the case of a perfect periodic lattice system, the wavefunction is distributed uniformly all over the lattice sites.

However, the situation is quite different upon introduction of disorder by distributing the potential barriers of the same height at random positions instead of distributing equally. The distribution of the random potential barriers can be defined as [see Fig. 1.3]:

$$V_{\text{ran}}(x) = \begin{cases} 0 & x \in S_j, \\ V_0 & x \in E_j, \end{cases} \tag{1.9}$$

where the domains can be defined as :

$$\begin{aligned} S_j &\equiv [x_j + b, x_{j+1}], \\ E_j &\equiv [x_j, x_j + b], \end{aligned} \tag{1.10}$$

The position of each barrier x_j is a random variable, which follows the distribution as

$$P(x_j) = \begin{cases} C \neq 0 & \text{if} \quad b' < x_j - x_{j-1} < b'' \\ 0 & \text{if} \quad \text{otherwise} \end{cases} \tag{1.11}$$

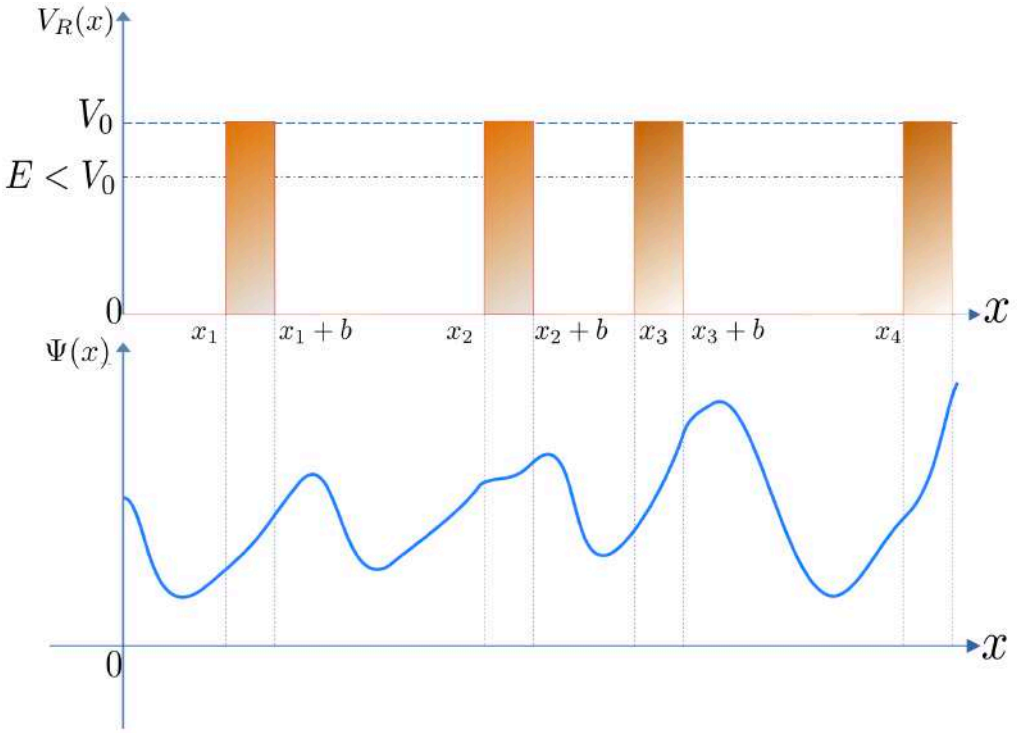

Figure 1.3: A qualitative representation of disordered potential $V_{\text{ran}}(x)$ described in Eq. (1.9) and the wavefunction $\psi(x)$ wavefunction.

where $b', b'' > b$. To probe strong disorder, the b' and b'' are kept very small. Here, the introduction of random disorder breaks the periodic symmetry of the wavefunction. In such cases, the exact solution of the Hamiltonian cannot be obtained analytically. Instead of that, we can find it by assuming a generic eigenstate $\psi(x)$ of the system by considering the energy $E < V_0$. In that case, the expression remains the same as in Eq. (1.4), and in a particular case of $A_j = A'_j$ can be considered as:

$$\psi(x) = \begin{cases} A_j \cos(\alpha x + \varphi_j) & \text{if } x \in S_j, \\ B_j e^{\beta x} + B'_j e^{-\beta x + \phi_j} & \text{if } x \in E_j, \end{cases} \tag{1.12}$$

By imposing the continuity and differentiation of $\psi(x)$ in $x = x_i$ we obtain

$$\begin{cases} 2A_{j-1} cos(\alpha x_j + \varphi_{j-1}) = B_j e^{\beta x_j} + B'_j e^{-\beta x_j + \phi_j}, \\ -2\alpha A_{j-1} sin(\alpha x_j + \varphi_{j-1}) = B_j \beta e^{\beta x_j} - B'_j \beta e^{-\beta x_j + \phi_j}, \end{cases} \tag{1.13}$$

By imposing the continuity and differentiation of $\psi(x)$ in $x = x_j + b$ we obtain

$$\begin{cases} 2A_j cos(\alpha(x_j + b) + \varphi_j) = B_j e^{\beta(x_j+b)} + B'_j e^{-\beta(x_j+b)+\phi_j}, \\ -2\alpha A_i sin(\alpha(x_j + b) + \varphi_j) = B_j \beta e^{\beta(x_j+b)} - B'_j \beta e^{-\beta(x_j+b)+\phi_j}. \end{cases} \tag{1.14}$$

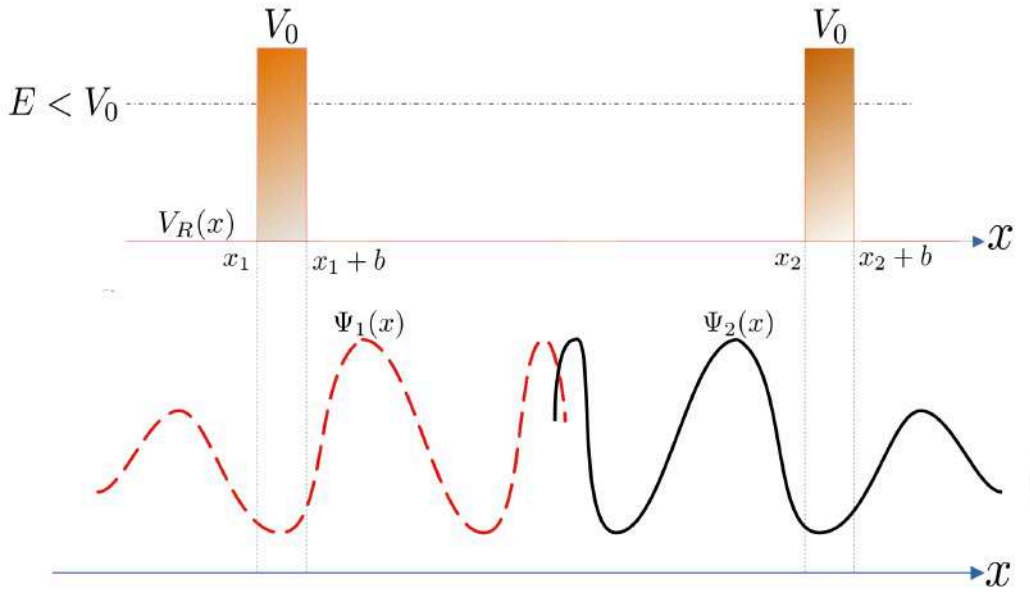

Figure 1.4: A pictorial representation of wavefunctions for a forbidden value of energy.

The shape of the eigenfunctions behaves sinusoidally outside the barriers, conquering different phases φ_j, which are randomly chosen due to the effect of the random positional distribution of the potential barriers. For strong disorder, the shape of wavefunction at $x \in S_j$ (at $V(x) = 0$ places) doesn't contribute to the global shape of the wavefunction. Hence, it is important to find the behavior at disorder positions $x \in E_j$. Due to the effect of the barriers, this is determined by the superposition of increasing and decreasing exponential functions. Both of them are important to satisfy the boundary conditions. If we assume $B_j = 0$, the two conditions from above equations become

$$\tan(\alpha x_j + \varphi_{j-1}) = \frac{\beta}{\alpha}. \tag{1.15}$$

Here, we consider case of $E \ll V_0$, which implies $\alpha \ll \beta$. For this case it is possible to solve the equation for particular φ_{j-1} values. It is important to consider both exponentially increasing and decreasing in the regions E_j. Here the coefficients B_j and B'_j are functions of φ_{j-1} which can be assumed as random variables. Increasing x from

zero, the main contributions of $\Psi(x)$ grow exponentially. The eigenfunction presented is no longer distributed uniformly over all the potential barriers, instead presenting an exponential nature in between the barriers [see Fig. 1.3].

In case of $E < V_0$, we derive the form of the wavefunction $|\psi(x)|^2$ in presence of disordered potential. To start with, consider the left edge of the random potential array in Fig. 1.3, i.e. $x = 0$, traversing towards right edge at $x = L$, the wavepacket passes through a lots of randomly placed potential barriers. To obtain the probability amplitude, we need to solve the Schrödinger equation by treating the wavefunctions differently inside or in-between the barriers. Solving for within one barrier gives that the $\psi(x)$ has contribution from both exponentially increasing and exponentially decreasing functions, but the increasing function dominates in compare to decreasing behaviour. Following that, in between two barriers, the shape of the $\psi(x)$ envelope is not much influenced in the limit of strong disorder. This signifies that a state $\psi(x)$ having energy less than the barrier height V_0 grows exponentially. For symmetry reasons, one can follow the same arguments but starting from $x = L$, and going to $x = 0$. Consequently, the $\psi(x)$ will be characterized through the exponential increasing function between $x = L$, and $x = 0$.

As a result, the wavefunction $\psi(x)$ grows exponentially both from left and right side; this paradox will overcome by introducing a localization center at x_0. The localization center is the point at which the probability density attains maximum amplitude: $|\psi(x_0)|^2 = \max[|\psi(x)|^2]$. Also, it is the same point where the two exponential joint analytically. This is not applicable for all energies, however, the set of energies satisfies this criterion forms the energy spectrum of the disordered potential. In Fig. 1.4, we show the wavefunction $\psi(x)$ does not belongs to that energy spectrum as it does not exist any localization center but the behavior of $\psi(x)$ inside a barrier qualitatively can be expressed as [3, 35]:

$$|\psi(x)|^2 \propto e^{-\frac{2|x-x_0|}{\ell}} + \vartheta(x), \tag{1.16}$$

where ℓ is the *localization length* and $\vartheta(x)$ depends on $\psi(x)$, which is locally influenced by the shape of the potential. The probability density exhibits exponential fall behavior from the localization center. Following that, Gogolin mathematically constructed the 1D correction to this exponentially decreasing function, which successively showed the existence of the Anderson transition state [37, 38].

Following the initial prediction of AL, the experimental observation of this intriguing disorder-induced phenomenon was challenging, primarily due to the significant

role of particle interactions. As a result, atomic crystals did not look upon as a suitable platform for realizing AL since thermally excited phonons and electron-electron interactions results a significant deviation from the prediction that of Anderson model [2]. The first observation on suppression of electron transport was made by Cutler and Mott in 1969 [4]. Subsequently, after the AL was conceptualized through the wave interference phenomenon, it has expanded to the field of optics [39]. In the quest for AL using wave interference phenomena, the first prediction of coherent backscattering [40] for its realization in experiment as *weak localization* was reported in the Ref. [41, 42] . Later, the *strong localization* was first observed with light and photonic lattices in different dielectric media [10, 11, 15, 17, 43, 44]. In case of light wave, unlike electrons, the photons do not interact with each other. As a result of this, the strong localization of photons in a random disordered medium resembles the actual Anderson model [10, 11]. In the early studies of the localization of light waves, the disordered medium was used as a random speckle to mimic the Anderson model. In the subsequent years, AL was realized for the quantum matter wave traopped in the quasiperiodic lattices which is generated by perturbing a periodic lattice potential in two-dimensional photonic lattices [12]. By measuring transverse diffusion (the perpendicular plane to the direction of propagation) of light it was demonstrated that transport of the photon changes from ballistic to diffusive for low disorder strength. Also, as the level of disorder increases, the transport gets fully suppressed, causing the localization of photons. Following that work, a similar kind of exponential localization phenomenon was reported using 1D photonic lattices [45].

Further AL has not only been confined to the field of optics, but it was also realized with the microwaves and acoustic waves. In the case of microwave localization, the disorder is introduced by perturbing a series of microwave resonators, which mimics the quasiperiodic lattice-like structure, causing the exponential localization of microwaves [15, 16, 18]. Additionally, in the case of acoustic waves, Weaver [19] performed an experiment using ultrasound waves where disorder was created by making several hundred scalloped slits in an aluminum plate. In this study, AL was characterized by analyzing the frequency spectrum of absorption energy. It was demonstrated that the lower frequencies get absorbed by the medium, while, the higher frequencies wave get transmitted through the diffusion .

Subsequently at later years, two experiments [21, 20] demonstrated localization of quantum matter waves corresponding to ultracold atomic Bose-Einstein condensates(BECs). With ultracold atoms, BECs offer an exceptional platform for studying AL not only due to the higher degree of control over disorder but also because of the un-

precedented tunability of atomic interaction strength, an aspect that researchers have not yet fully understood through other media. The first work demonstrated the exponential localization of a scalar BEC of ^{87}Rb atoms with negligible interactions released into a 1D magnetic waveguide containing controlled random disorder of speckle grains created by laser [21]. Subsequently, Roati *et al.* experimentally reported the localization of ^{39}K atomic condensate trapped in a one-dimensional quasi-periodic optical lattice with negligible atomic interactions [20].

As the localization of BECs constitutes a central theme of our thesis, in what follows we discuss these experimental observation of the localization in deatiled manner. First we provide a brief introduction of BECs which is followed by different kind of disordered potentials used in the experiment for the relaization of BECs in the lab experiment. Subsequently, we provide theoretical and numerical frameworks that have been used in our thesis.

1.2 Bose-Einstein condensation

Bose-Einstein condensate (BEC) is a quantum state of matter, formed when a dilute gas of Bosonic atoms cooled to extremely low temperatures, close to absolute zero. Under such conditions, a large fraction of atoms collapse to the ground state as the thermal de-Broglie wavelengths of atoms become comparable to interatomic spacing. The degenerate atoms behave collectively as a single macroscopic quantum entity.

The theoretical work for BEC was started back in 1924 when Satyendra Nath Bose derived Planck's distribution formula by considering the statistics of massless photons [46]. In the subsequent year, Albert Einstein extended Bose's work for massive particles utilizing the idea of de-Broglie's matter waves [47, 48]. They demonstrated that, unlike fermions, Bosons are not constrained by the Pauli exclusion principle and can occupy the same quantum state, leading to a phase transition due to the conservation of atom number, which leads to the formation of the Bose-Einstein condensate. Following their theoretical prediction, in 1938, Kapitza, Allen, and Misener experimentally realized the condensation-like phenomenon with liquid Helium cooled down below the lambda transition temperature [49, 50]. In that same year, London showed an intricate relation between BEC and condensation in liquid Helium [51]. Later, in 1941, Landau's work on superfluid Helium shed more light on the condensate theory [52]. Following that, building on the work by Penrose, Onsager around the 1950s showed the importance of phase coherence at the macroscopic level in order to real-

ize BEC [53, 54]. They also proposed a mathematical definition to attain a condensate applicable to interacting particles or ideal gases. In addition to that, their work demonstrated that a tiny fraction of atoms remained in the condensate at absolute zero temperature when superfluid He-II satisfied their criterion for BEC.

1.2.1 BEC for non-interacting ideal gases

The theoretical description of Bose-Einstein condensates (BECs) in a dilute gas of Bosons involves the quantum statistics of interacting Bosonic particles. However, in case of non-interacting ideal gases, a much simpler description of BEC can be derived utilizing statistical mechanics. This simplified model provides valuable insight into the phase transition and the critical temperature. Using that approach, to understand how the transition occurs from a thermal gas to BEC, assume N non-interacting Bosons occupy a large volume V. According to de-Broglie's hypothesis, the wavelength of each Bosons (λ_{dB}) follows a temperature dependency as $\lambda_{dB} = (2\pi\hbar^2/mk_BT)^{1/2}$, where m is the mass of a Bosonic particle, k_B is the Boltzman constant, and T represents the temperature. In case of thermal gas, λ_{dB} is much smaller than inter-particle spacing, whereas decreasing the temperature leads to an increase in the de-Broglie wavelength of the particles, and eventually the wave packets start to overlap with each other at a critical temperature. The critical temperature can be obtained using Bose-Einstein statistics. For high temperature limit, the particles can occupy all possible energy states of the system. Therefore, we can divide the populations of the lowest energy state and all other excited energy states as N_0 and N_{ex}, respectively which follows $N = N_0 + N_{\text{ex}}$. Now, when $T \gg T_c$, the maximum number of particles occupies the excited state of the system. Thus, the relation between the maximum excited state population with temperature is given by [55],

$$N_{\text{ex}}^{max} = 2.612V\left(\frac{mk_BT}{2\pi\hbar^2}\right)^{3/2}, \tag{1.17}$$

With lowering the temperature, particles from the excited state transfer to the minimum energy level, the critical temperature at which $N_{\text{ex}} = N$ is given by

$$T_c = \frac{2\pi\hbar^2}{mk_B}\left(\frac{N}{2.612V}\right)^{2/3}, \tag{1.18}$$

Below this critical temperature, the ground state population remains much higher

in comparison to the excited state population. The condensate population varies with system temperature as

$$\frac{N_0}{N} = 1 - \left(\frac{T}{T_c}\right)^{3/2}, \tag{1.19}$$

where N_0 is the ground state population. At $T \leq T_c$, the macroscopic occupation of the lowest energy level is the defining feature of BEC.

Another critical condition for the onset of BEC can be obtained from the condition for de-Broglie wavelength overlap. The criteria for overlapping of the de-Broglie wave packets at $T \leq T_c$ is given by,

$$n\lambda_{dB}^3 \leq 2.612, \tag{1.20}$$

where, $n = N/V$ define as number density. The formation of BEC occurs due to the dominance of the quantum effect due to the overlapping of de-Broglie wave packets.

1.2.2 BEC in laboratory experiments

In laboratory experiments, the pursuit of observing BECs began in the 1970s through compressing and cryogenic cooling of Hydrogen atoms. However, these early efforts faced many challenges, including difficulty in handling a large number of atoms ($\sim 10^3 - 10^4$) and atomic loss due to three-body recombination, which limits the achievable density in experiments. Later, in the 1980s, the discovery of the state-of-the-art technology in cooling and trapping of neutral alkali atoms marked a major breakthrough for advancing the field of ultracold atoms. Similarly, the development of these cooling techniques has been vital for experiments related to the observation of BECs. Although researchers first considered Hydrogen as the promising candidate for realizing BEC, after a meticulous competition between several research groups, the first observation of BEC was reported by the group of Cornell and Wiemann at JILA[1] in Boulder, Colorado, in 1995. The experiment was conducted by Anderson *et al.* [56] with 2×10^3 atoms in a gas of ^{87}Rb atoms at a critical temperature of 170 nK. Soon after that, the Ketterle group at MIT[2] reported BEC with ^{23}Na atoms [57]. Subsequently, BEC with ^{7}Li atoms has also been observed by the Hulet group at Rice University in Houston, Texas [58]. Finally, in 1998, the Kleppner group at MIT realized the condensate with atomic Hydrogen [59].

The figure 1.5 shows the velocity distribution of ^{87}Rb atoms after the time-of-flight

[1]Joint Institute for Laboratory Astrophysics
[2]Massachusetts Institute of Technology

experiment (releasing the condensate from trap under the gravitational field). The velocity distribution shows that at temperature below critical temperature ($T \sim 50$nK (right panel)) $T < T_c$, most of the atoms accumulate in the zero momentum state, which leads to the formation of a condensate of Rubidium atoms. In left panel, atoms are distributed randomly in momentum space with random velocities; hence, they act more like a thermal gas, and at the critical temperature ($T \sim 200$nK (middle panel)), particles start to accumulate at zero momentum state where the de-Broglie wavelength starts to overlap.

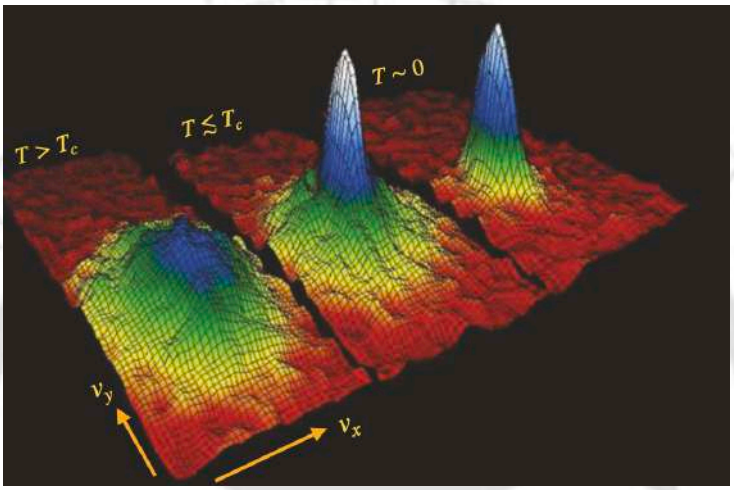

Figure 1.5: Velocity distribution of rubidium atoms after time-of-flight expansion of the cloud at different temperatures (from left:$T \sim 400$nK, middle: $T \sim 200$nK, right :$T \sim 50$nK) . On the left, for the temperature above critical temperature ($T > T_c$), atoms acquire larger momentum states; as a result, the atomic cloud exhibits a thermal Gaussian distribution. In the central figure, at $T \sim T_c$, the particle distribution shows that most of the atoms occupy the $k = 0$ state. At below critical temperature ($T < T_c$), the central peak shows that most number of atoms trapped at zero momentum state indicates a signature of BEC, surrounded by a cloud of thermal atoms with random velocities. The figure is adapted from the experiment at JILA, Boulder [56].

For these remarkable contributions to the field of ultracold atoms, the Nobel Prize in physics was awarded in 1997 to Steven Chu, Claude Cohen-Tannoudji, and William Phillips for the development of cooling and trapping techniques using lasers. Later in 2005, Eric Cornell, Carl Wiemann, and Wolfgang Ketterle were awarded the Nobel Prize for the first experimental observation of BEC in laboratory. Since then, the field has witnessed an unprecedented growth and opened the door for exploring several novel and intriguing phenomena, including topological defects such as quantum vortices [60, 61], quantum turbulence [62–64], supersolidity [65], Anderson localization [66], self-bound quantum droplets [67, 68]. The utilization of BEC for investigating various phenomena stems mainly from two key advantages, firstly, the precise tunability of atomic interactions through Feshbach resonance, and secondly, it can be trapped

in magnetic or optical potentials in a controlled manner. Experimentally, atomic interactions could be tuned from attractive to repulsive range using external magnetic or optical fields via the Feshbach resonance technique. Similarly, the external trapping potential can be engineered through optical dipole traps or optical lattices formed by the interference of laser beams.

For the study of Anderson Localization, precise control over interaction strength and disorder is very crucial. It also includes the reduction of atomic interaction to a negligible value and increasing disorder strength directly through the potential parameters. In continuation of our effort to provide a substantial background for our theoretical modeling, here we briefly discuss the methods and fundamental principles involved in tuning the interaction parameter in BECs in the following section.

1.2.3 Controlling atomic interaction through Feshbach resonance

In dilute Bose gases at ultracold temperature, the atomic interactions can be tuned with the help of scattering resonance phenomena. Particularly, the dominant interaction between two atoms can be described using a quantity called the s-wave scattering length a. The sign of a determines the type of interactions, such as positive and negative values of a define the repulsive and attractive interactions, respectively. The possibility of tuning atomic interaction through controlling s-wave scattering length can be accomplished with the magnetic or optical Feshbach resonance (FR) technique.

1.2.3.1 Magnetic Feshbach resonance

Feshbach resonance (FR), named after Herman Feshbach, was originally developed for studying nuclear reactions [69–71]. But eventually, it has become an important phenomenon in atomic physics to control atomic interaction by tuning scattering length in alkali atoms [72–74]. FR occurs in a scattering event when a pair of colliding atoms forms a molecular bound state with the application of a homogeneous magnetic field. The mechanism of forming a bound state is illustrated in Figure 1.6(a). Two atoms approach each other along their interaction potentials, denoted by V_0 and V_c, as open and closed channels respectively. The mixing between V_0 and V_c while forming a bound state modifies the effective interaction potential. Consequently, this modification of the scattering potential results in a variation of the scattering length a that is correlated with the position of the scattering potential. In experiments, this scattering length a can be tuned with an external magnetic field because of different magnetic moments associated with the open (V_0) and closed channel (V_c). The scattering length a depends

upon the magnetic field B as,

$$a = a_{\rm bg}\Big(1 - \frac{\Delta_B}{B - B_0}\Big), \tag{1.21}$$

where, $a_{\rm bg}$ is the off-resonant background scattering length, Δ_B is the width, B_0 represents magnetic field at position of resonance, and B is the external magnetic field. The specific parameters that determine the dependence of a on magnetic field changes for different atoms. For ^{39}K atoms, the a is shown as a function of B as shown in Fig. 1.6(b).

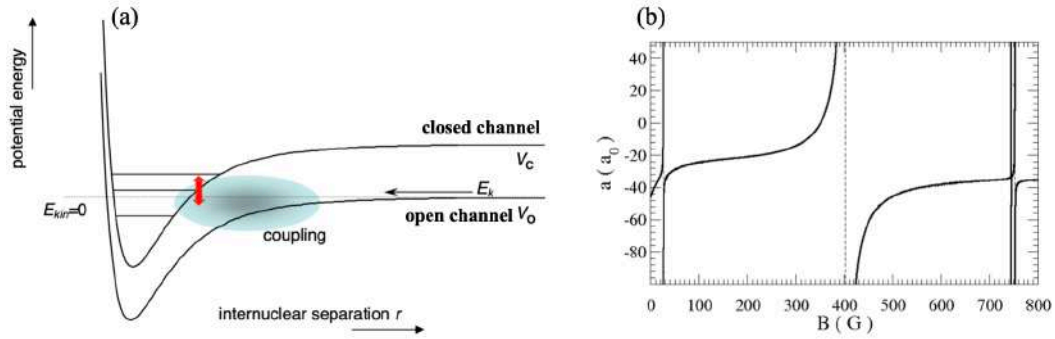

Figure 1.6: (a) Schematic diagram of the Feshbach resonance technique used in atomic collisions. The scattering state associated with the open channel V_0 is coupled to the closed channel V_c of another atom. The coupling between these channels modifies the scattering potential and scattering phases, which can be controlled using an external magnetic field. (b) variation of scattering length with external magnetic field for ^{39}K atomic collisions of hyperfine states. The resonance condition is depicted by the vertical dashed lines. Figure is taken from [75, 35].

After discussing the magnetic Feshbach resonance now we discuss about Optical Feshbach technique through which apart from other advantage even the interaction can be tuned in the inhomogeneous way.

1.2.3.2 Optical Feshbach resonance

Over the use of magnetic Feshbach resonance, optical control of scattering length offers an exceptional tool because of a few advantages, such as fast switching of scattering length or most importantly, creating inhomogeneity in atomic interaction that can affect only a certain part of the atomic cloud in a BEC. The reason is that lasers can switch very fast in comparison to magnetic fields and also generates spatially resolved intensity patterns. The theory of controlling scattering length using optical fields was first proposed by Fedichev *et al.* [76], and further extended by Bohn and Julienne [77]. Subsequently, it has been realized in experiments [78–81].

Optical Feshbach resonance (OFR) uses laser photons to form a bound state from

two colliding atoms. A qualitative description of OFR lies in the dressed state as depicted in Figure 1.7(a). This picture shows that the excited molecular potential V_e is shifted by the energy $\hbar\omega_1$ associated to a laser photon towards the ground state potential V_g. Experimentally, the coupling can be controlled using the intensity (I) and detuning (Δ_1) of laser light from photoassociation resonance. However, the process constitutes an inelastic collision between atoms; as a result of this, atoms can be lost while making a stimulated transition to an excited molecular state and that further results the subsequent spontaneous decay.

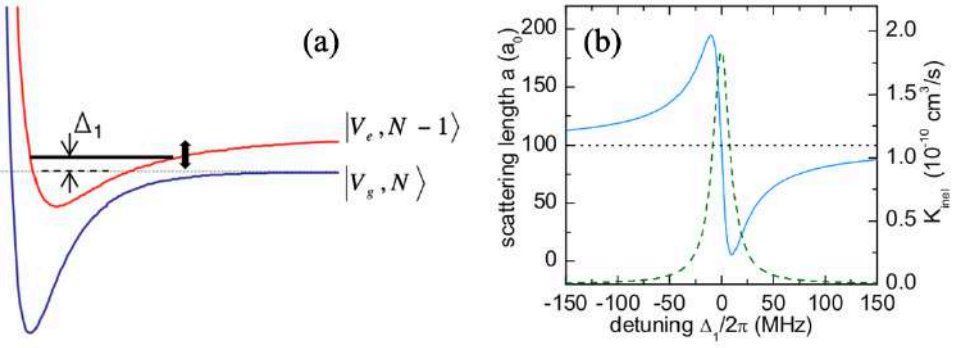

Figure 1.7: (a) Schematic diagram of optical coupling between collisional and molecular states. The excited potential $|V_e, N-1\rangle$ is separated from the ground state potential $|V_g, N\rangle$ by laser detuning Δ_1. Here, N is the number of photons in the light field. (b) Scattering length a (cyan solid line), and inelastic collision rate K_{inel} (green dashed line), which causes atomic loss as a function of laser detuning Δ_1 obtained for a condensate of ^{87}Rb atoms. This figure is adapted from Ref. [75, 79].

Bohn and Julienne [77] first proposed the analytical expression for the scattering length a and the inelastic atomic loss coefficient K_{inel} as a function of laser detuning Δ_1 . They assumed that the stimulated decay rate of excited molecular level is much smaller than spontaneous decay $\Gamma_{\text{stim}} \ll \gamma_1$ which turns out to be an appropriate criterion for experiments. As a result, the expression follows,

$$a = a_{\text{bg}} - \frac{1}{2k}\frac{\Gamma_{\text{stim}}\Delta_1}{\Delta_1^2 + (\gamma_1/2)^2}, \tag{1.22}$$

$$K_{\text{inel}} = \frac{2\pi\hbar}{m}\frac{1}{k}\frac{\Gamma_{\text{stim}}\gamma_1}{\Delta_1^2 + (\gamma_1/2)^2}, \tag{1.23}$$

with a_{bg} is the off-resonant background scattering length in case of no optical coupling, and k is the collisional wave vector. In case of experiment with ^{87}Rb atoms, Theis *et al.* [79] obtained the scattering length a and K_{inel} as a function of Δ_1 [see Fig. 1.7(b)] with parameters $\Gamma_{\text{stim}}/2\pi = 50\text{KHz}$, $\gamma_1/2\pi = 20\text{MHz}$, $k = 2.5 \times 10^5 \text{m}^{-1}$, and $a_{\text{bg}} = 100a_0$ where a_0 is the Bohr radius. However, it can be seen that besides the

laser detuning Δ_1, the scattering length a and K_{inel} implicitly depend upon the laser intensity I because $\Gamma_{\text{stim}} \propto I$. This depicts that the scattering length can be controlled by two parameters: laser detuning and intensity created by the lasers.

In the main chapters of the thesis we have considered the homogeneous as well as the inhomogeneous interactions which are primarily adapted using the magnetic and optical Feshbach resonance techniques, respectively.

1.2.4 Trapping of a BEC using optical dipole potentials

To study the Anderson localization (AL) in a BEC, one needs to use the optical potentials for confining a condensate. The optical potentials can be created by utilizing the dipole force of a laser and the atomic dipole moment. Utilizing the dipolar force, the manipulation of the intensity pattern originated due to the interference of two counter-propagating laser beams, leading to the formation of an optical lattice, which can be used to trap the ultracold atoms. In this section, we will discuss the fundamental concepts of optical potentials, including optical lattices and disordered potentials.

Dipolar force arises due to the dispersive interaction between the intensity gradient of the light field and the induced atomic dipole moment. Here, we derive an expression for the dipolar force using a semiclassical approach [82, 83], considering the atom as a simple oscillator and the incident light as a classical radiation field which induces the dipole moment :

$$\mathbf{E}(\mathbf{r},t) = \hat{\mathbf{e}}\tilde{E}(\mathbf{r})e^{-i\omega t} + \text{c.c.}, \quad \mathbf{p}(\mathbf{r},t) = \hat{\mathbf{e}}\tilde{p}(\mathbf{r})e^{-i\omega t} + \text{c.c.}, \tag{1.24}$$

where $\mathbf{p}$ is the induced dipole moment of an atom which oscillates with the same frequency ω as the driving field $\mathbf{E}$. Here $\hat{\mathbf{e}}$ is the unitary polarization vector.

The amplitude $\tilde{p}$ of the dipole moment is related to the field amplitude $\tilde{E}$ is given by

$$\tilde{p} = \alpha\tilde{E}, \tag{1.25}$$

where, α represents the complex polarizability depends on driving frequency ω. The interaction potential of the induced dipole moment is defined as

$$U_{\text{dip}} = -\frac{1}{2}\langle \mathbf{p}.\mathbf{E} \rangle = -\frac{1}{2\epsilon_0 c} Re(\alpha) I(r), \tag{1.26}$$

where $\langle . \rangle$ denote the time average over fast oscillating terms and $I(r)$ is the laser field intensity. The dipolar force is directly proportional to the real part of polarizability

and the intensity gradient of laser light. Conversely, the imaginary part of the polarizability is related to the loss of photons due to scattering with the incident field also termed as *scattering rate*. In case of far-off resonance regime, where the laser detuning is much larger in comparison to the radiative linewidth, the dipolar potential behaves conservatively by minimizing the scattering rate of atoms.

1.2.4.1 Periodic and quasiperiodic optical lattices

Next we discuss different varieties of the optical lattices, namely, the periodic and quasi-periodic optical lattices used in the experiment. The aforementioned dipole potentials can be used to create a periodic potential for atoms. In principle, it can be generated with the standing wave created due to the interference of two counter-propagating laser beams. This spatial modulation of laser interference pattern is called as *optical lattice*. The expression for the optical dipole potential can be derived starting from the electric field expression of two counter-propagating plane waves:

$$\mathbf{E}_1 = \hat{\mathbf{e}}\tilde{E}_1 \cos(kx + \omega t + \delta), \qquad \mathbf{E}_2 = \hat{\mathbf{e}}\tilde{E}_2 \cos(kx - \omega t - \delta), \tag{1.27}$$

where, $k = \omega/c$ is the light wavevector. The resultant intensity can be written as

$$I(x,t) = \epsilon_0 c \Big| \mathbf{E}_1(x,t) + \mathbf{E}_2(x,t) \Big|^2. \tag{1.28}$$

With the mediation over rapid oscillating terms, we obtain

$$I(x,t) = \frac{1}{2}\epsilon_0 c \Big[(\tilde{E}_1 - \tilde{E}_2)^2 + 4\tilde{E}_1\tilde{E}_2 \cos^2(kx) \Big], \tag{1.29}$$

In case of $\tilde{E}_1 = \tilde{E}_2 = \tilde{E}$, modifying Eq. (1.26), the interaction potential felt by the atom due to the standing wave is given by

$$U_{\text{dip}} \propto I_0 \cos^2(kx) = V_0 \cos^2(kx), \tag{1.30}$$

where, $I_0 = 2\epsilon_0 c E_0^2$, with E_0 is the amplitude of the electric field. The potential has the periodicity as $\pi/k = \lambda/2$, which depends on the wavelength of the laser light λ. Usually, the lattice depth $s = V_0/E_r$ is defined in terms of recoil energy $E_r = \hbar^2 k^2/2m$.

To incorporate the disorder into an optical lattice, one can form a quasi-periodic potential which can be created by superimposing the primary optical lattice with another secondary optical lattice of incommensurate wavelength. In that case, the quasi-

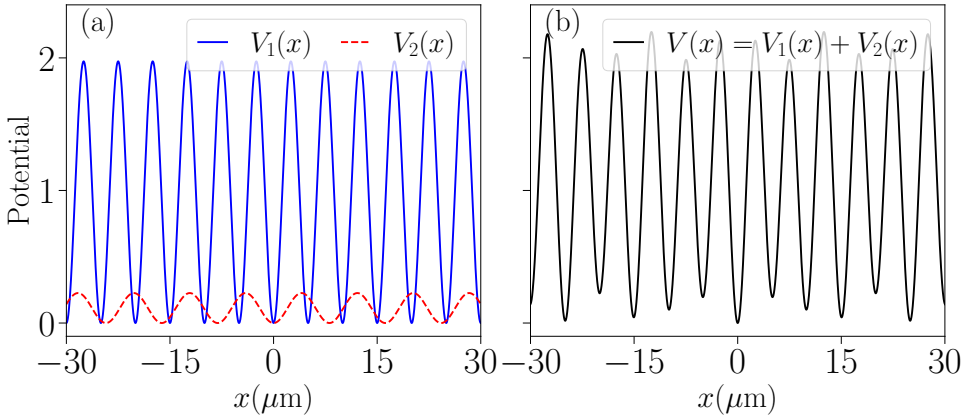

Figure 1.8: (a) Primary (V_1) and secondary optical lattice (V_2) as a function of x . (b) Representation of 1D quasi-periodic optical lattice ($V(x)$) created by superposition of the main (V_1) and secondary lattice (V_2) with wavelengths $\lambda_1 = 1032$nm, $s_1 = 10$ and $\lambda_1 = 862$nm, $s_2 = 0.3s_1$. The potential energy is expressed in the units of recoil energy $E = \hbar^2k^2/2m$. The parameters are the same as in Ref. [24].

periodic potential in 1D has the form as

$$V(x) = s_1E_1 \sin^2(k_1x) + s_2E_2 \sin^2(k_2x), \tag{1.31}$$

where, s_1 and s_2 are the strength of the primary and secondary optical lattices respectively and k_1 and k_2 denote the wave number of primary and secondary lattices respectively. This type of potential is commonly called as *bichromatic lattice* potential [see Fig. 1.8], characterized by a quasiperiodic modulation of the minimum energy of the primary lattice due to perturbations caused by the secondary lattice. If the amplitude of the secondary lattice is very large ($V_2 \sim V_1$), then it can shift the minima of the resultant lattice. However, while the deviation of the actual minima positions of the primary lattice can be estimated, we do not describe it in detail here. For further information, please refer to Ref. [35]. Usually, for quasiperiodic potential, the distance between two "impurities" is much smaller than other type of disordered potential, like, random speckles.

1.2.4.2 Random speckle potential

In addition to quasiperiodic potentials, another type of disordered potential is widely used to study AL is the *random speckle potential*. Laser speckles are generated when a coherent laser beam is scattered through a rough glass plate. The resulting reflected or transmitted light, when focused through a converging lens, produces a random distribution of light intensity that results the appearance of maxima and minima of different

amplitudes at different random positions, thereby creating the random speckle potential [see Fig. 1.9]. The basic principle of forming the speckle pattern is the random path created by each wave while scattering from the rough surface leading to a spatial modulation of the phase and amplitude of the resultant electric field. As the intensity is randomly distributed in space, its characterization can be done by evaluating the amplitude and finding the characteristic length scale of the potential. Using the standard deviation of the intensity, it is possible to calculate the standard deviation of the dipolar potential associated with the intensity distribution. Conversely, the disorder lengthscale can be obtained from the width of the self-correlation function C_I of the intensity distribution as

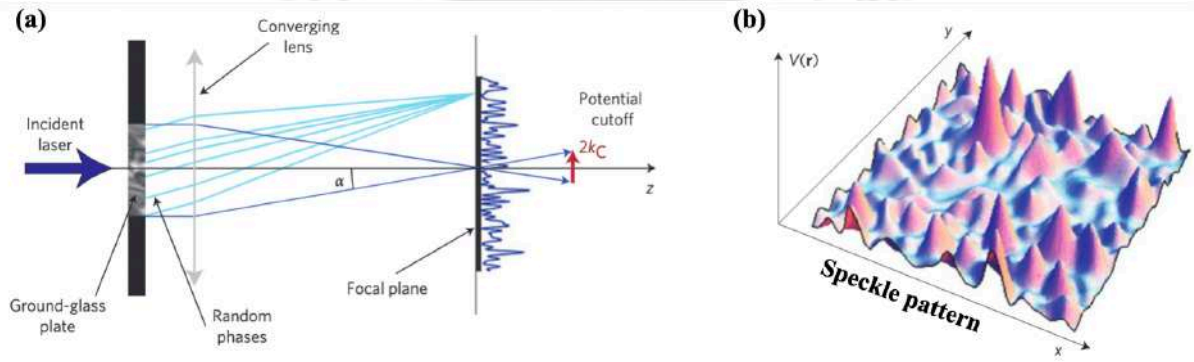

Figure 1.9: (a) Optical configuration to create random speckle potential. (b) A two-dimensional demonstration of random speckle potential. Image is taken from [84].

$$C_I(\delta\mathbf{r}) = \langle I(\mathbf{r})I(\mathbf{r}+\delta\mathbf{r})\rangle, \tag{1.32}$$

where, $\langle . \rangle$ denotes the statistical mean of the intensity and $I(\mathbf{r})$ is the intensity at point $\mathbf{r}$. The correlation width is defined as the smallest disorder grain size, which is also given as the diffraction limit by numerical aperture of the optical system and wavelength λ employed to create the speckle pattern as

$$\sigma_z \approx 1.22\lambda\frac{l}{D}, \tag{1.33}$$

where D is the beam diameter and l is the distance of the diffusive plate from the atoms. Consequently, the speckle grain size is inversely proportional to the dimension of the laser, setting the limit on the number of effective scatters.

Speckle disorder offers various advantages because of its applicability in ultracold atom experiments. Although the potential has a random distribution, the statistical properties are well-defined and can be tuned by tailoring the optical apparatus. How-

ever, the main difference between random and quasi-periodic potential is that in the case of 1D random speckle potential distributed unboundedly can localize the condensate with negligible disorder strength, whereas, for quasiperiodic potential, beyond a critical value of disorder strength, the extended state becomes localized.

1.2.4.3 Impurity model of disorder

In addition to laser speckle potentials, several other types of impurity disorder models have been proposed and implemented in theoretical and numerical studies to investigate localization. These models do not rely on dipolar interactions. Instead of this, disorder is introduced by randomly trapping atoms at selected sites of an optical lattice with less than full occupancy [85, 86]. The randomly distributed atoms then act as static scatterers. As a BECs or atomic cloud propagates through this disordered landscape, it encounters these randomly placed scatterers, leading to localization. In this scenario, the BEC experiences the impurity potential in the form of

$$V(r) = \sum_{i=1}^{N} \mathrm{U}(\mathbf{r} - \mathbf{r}_i), \tag{1.34}$$

with U is the potential created by a single scatterer, and $\mathbf{r}_i$ its random position. This model is useful for investigating disorder correlations as it determined by the shape of the potential $\mathrm{U}(\mathrm{r})$. For example, the delta-correlated impurities $U(\mathbf{r}) = \delta(\mathbf{r})$ defines the *white noise disorder*. Another commonly used model is Gaussian disorder, which is also employed to study Anderson-like localization in Bose-Einstein condensates (BECs). The Gaussian-correlated disorder potential is defined as [87]:

$$\mathrm{U}(\mathbf{r} - \mathbf{r}_i) = \exp\left(-\frac{(\mathbf{r} - \mathbf{r}_i)^2}{\zeta^2}\right), \tag{1.35}$$

where ζ is the width of each Gaussian spike. In this thesis, we employ this form of random Gaussian disorder [Eq. 1.35] apart from the bichromatic lattice to explore localization phenomena in one-dimensional BECs. Detailed discussions on the statistical properties and correlation function of this disordered potential are provided in the main chapters of this thesis.

1.2.5 Experimental evidence of Anderson localization in BECs

The motivation for implementing quasiperiodic and randomly disordered potentials in our thesis arises largely from two remarkable experimental discoveries of AL in non-interacting BECs: one is using a 1D quasiperiodic potential [20], and the other employing a 1D random speckle potential [21]. These discoveries provided the first direct evidence of the localization of quantum matter waves. Following that, AL also has been observed in three-dimensional speckle potentials [88, 89]. Additionally, these experimental breakthroughs have sparked extensive theoretical and numerical studies based on the mean-field Gross–Pitaevskii (GP) models, exploring the interplay between interactions and disorder, which strongly motivates further exploration in this thesis. Therefore, before delving into the theoretical framework, we briefly review the key experimental observations that underpin our study.

1.2.5.1 Localization of a condensate trapped in quasiperiodic potential

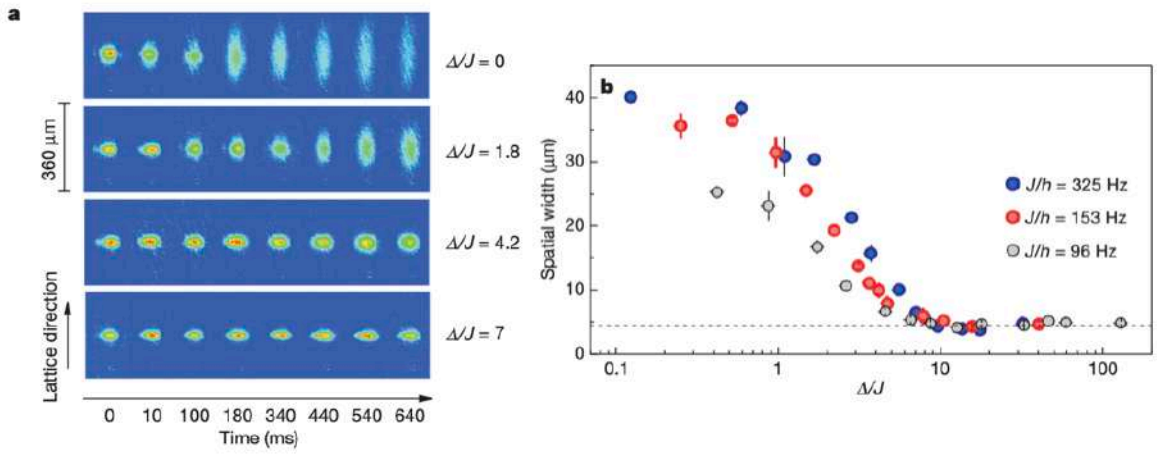

Figure 1.10: (a) Time-of-flight absorption images of a ^{39}K BEC demonstrate the effect of disorder on expansion dynamics. For $\Delta/J = 0$, the condensate undergoes ballistic expansion along the lattice direction. However, as the disorder strength increases to $\Delta/J = 4.2, 7$, the expansion is suppressed, and the condensate becomes localized near the center of the lattice for up to 640ms. Here, Δ/J denotes the ratio of disorder strength to tunneling energy. (b) Condensate width as a function of rescaled disorder strength Δ/J for three different values of J, at a fixed evolution time of 750 ms. The dashed line indicates the initial size of the condensate. The onset of localization appears in the same range of values of Δ/J for all three cases. Here, Δ/J represent the disorder to tunneling energy ratio. The figure is adapted from the Ref. [20].

In 2008, Roati *et al.*[20] reported the localization of a non-interacting BEC of ^{39}K atoms confined in 1D quasiperiodic potential. The quasiperiodic potential was created by superimposing two optical lattices with incommensurate wavelengths: $\lambda_1 =$

1032nm and $\lambda_2 = 832$nm. The strength of these optical lattices was controlled by tuning the lattice depths using Bragg diffraction measurements. The strengths of these lattices were tuned via Bragg diffraction measurements, allowing the lattice depths to vary within the ranges $V_1 = [0, 10E_1]$ and $V_2 = [0, 4E_2]$, where $E_i = h^2/(2m\lambda_i^2)$ are the respective recoil energies for the primary and secondary lattices. In the experiment, a condensate of ^{39}K atoms was first produced in an optical trap and then adiabatically loaded into the quasiperiodic potential over a timescale of a few hundred milliseconds to minimize excitations. The choice of ^{39}K is because of its broad resonance of scattering length and small negative background scattering length, which enabled precise control over interatomic interactions, from attractive to repulsive using Feshbach resonance. Their experimental realization of localization in the non-interacting regime also validated the theoretical predictions based on the Aubry–André model [90]:

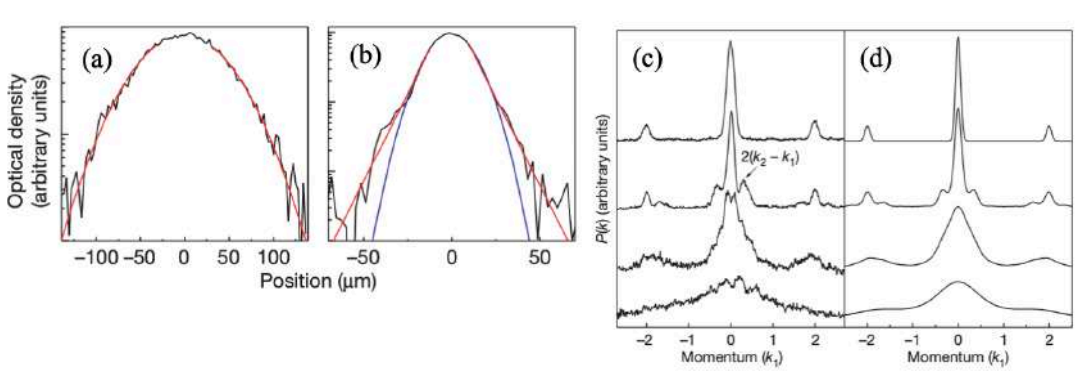

Figure 1.11: (a, b) Experimental optical density profiles (black) fitted with the function $f_\alpha(x)$ (red) for $\Delta/J = 1$ (a) and $\Delta/J = 15$ (b). For $\Delta/J = 1$, the fit demonstrates $\alpha = 2$, corresponding to a Gaussian profile, while for $\Delta/J = 15$, $\alpha \approx 1$, indicating exponential localization in logarithmic scale. (c, d) Experimental and theoretical momentum distributions for increasing Δ/J values (0, 1.1, 7.2, and 25 from top to bottom). Theoretical momentum distributions are derived from the Aubry–André eigenstates. At $\Delta = 0$, the interference pattern characterizes the periodic lattice potential, which eventually turns into a broadened distribution with additional peaks from lattice beating, reflecting the onset of exponential localization. Here, Δ/J represent the disorder to tunneling energy ratio .Figure adapted from Ref. [20].

Their observation is based on the diffusion dynamics of the time-of-flight experiment after releasing the magneto-optical trap. To keep the expansion of the condensate only along the lattice direction, they have also used a magnetic field gradient against gravity to let the condensate extend only in one dimension. Consequently, the absorption images of atomic densities after time-of-flight clearly demonstrate the complete suppression of the ballistic expansion for larger disorder strength Δ/J [third and fourth panel of Fig. 1.10(a)]. Here, the Δ/J represents the ratio of disorder strength to site-to-site tunneling energy related to the Aubry–André model of localization. In experiments, these two energy scales can be controlled independently by changing the

heights of the primary and secondary lattice potentials. For the incommensurate ratio of laser wavenumber, the AA model exhibits a sharp transition from extended to localized state at $\Delta/J = 2$. However, for the actual experimental parameters, the transition is shifted towards larger Δ/J values. To quantify the localization, they utilized the root mean square size of the condensate as a function of the rescaled disorder strength Δ/J for three different values of tunneling energy [see Fig. 1.10(b)]. Notably, in the case of localization for higher disorder strength, the spatial width remains in the same range as the initial width, irrespective of the tunneling energy.

Next, to validate the theoretical prediction of a transition from extended to localized eigenstates in the Aubry–André Hamiltonian, direct observation via atomic cloud expansion is hindered by imaging resolution limits. Instead of that, momentum distribution can be another possibility to demonstrate the exponential localization.

In Fig.1.11(a, b), the optical density profiles are shown for $\Delta/J = 1$ and $\Delta/J = 15$. The tails are fitted using the function $f_\alpha(x) = A \exp\left(-|(x - x_0)/l|^\alpha\right)$, where α is the fitting exponent. For $\Delta/J = 1$, the fit yields $\alpha = 2$, corresponding to a Gaussian profile. As the disorder strength increases to $\Delta/J = 15$, the exponent approaches $\alpha \approx 1$, indicating exponential localization of the condensate. Furthermore, the momentum distribution $P(k_1)$ calculated from the Aubry–André model [Fig.1.11(d)] closely matches the experimental results in Fig. 1.11(c), where localization is reflected by the broadening and flattening of the momentum distribution. These findings highlight the key experimental signatures of localization in a quasiperiodic potential. In the following we present the localization of the condensate in presence of the random potential.

1.2.5.2 Localization of a condensate in the presence of random speckle potential

In the same year, Billy *et al.*[21] performed an experiment with a condensate of ^{87}Rb atoms, released from a harmonic trap into a speckle disorder potential within an optical waveguide, where time-of-flight measurements revealed localization of the condensate. Their findings were supported by theoretical predictions from Sanchez-Palencia *et al.*[23], which demonstrated a transition from exponential to algebraic localization depending on the disorder strength.

However, a few important aspects of the experiment are worth highlighting. To generate a conservative speckle disorder, the optical field was highly detuned and operated at low intensity to minimize spontaneous photon scattering. The disorder was engineered to act effectively along a single direction (assumed to be z) by ensuring the correlation length σ_R was much larger than the atomic matter wave. Considering

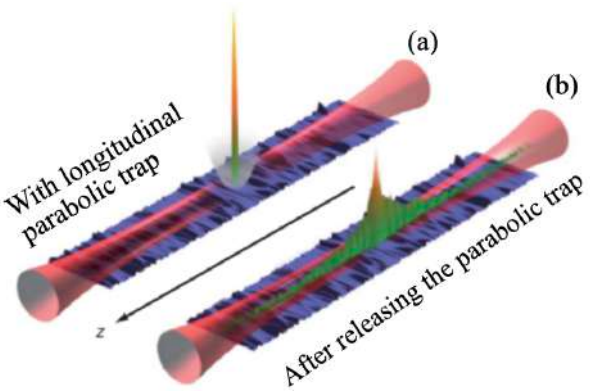

Figure 1.12: (a) A BEC of ^{87}Rb atoms is formed in a hybrid trap, combining a horizontal optical waveguide with strong transverse confinement and a weak longitudinal harmonic trap. (b) Upon switching off the longitudinal trap, the condensate begins to expand and subsequently localizes along the waveguide. Figure is adapted from Ref. [21].

this, the resulting correlation function along z is given by $V_R^2(\sin(z/\sigma_R)/(z/\sigma_R))^2$, with σ_R on the order of microns. The disorder strength was kept sufficiently weak so that the interaction energy primarily converted into kinetic energy in the condensate's tail

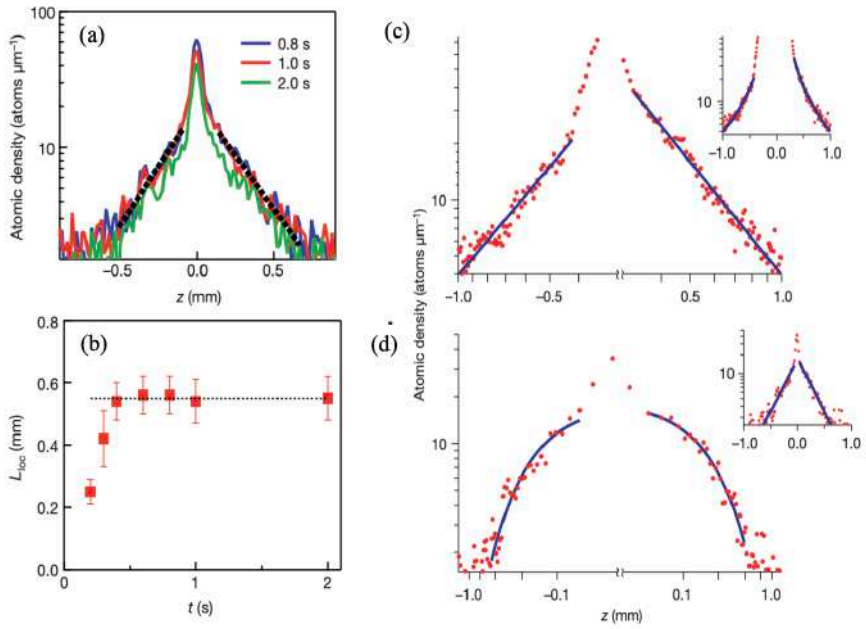

Figure 1.13: (a) Atomic density snapshots at various times are used to extract the localization length L_{loc} by fitting an exponential $\exp(-2|z|/L_{\mathrm{loc}})$ (dotted black line) to the density tails. (b) The time evolution of L_{loc} shows the suppression of the expansion of the BEC. (c) Log-log and semi-log (inset) plots of stationary density profiles distinguish between algebraic ($k_{\max}\sigma_R > 1$) and exponential ($k_{\max}\sigma_R < 1$) localization regimes. For $V_R/\mu_{\mathrm{in}} = 0.15$ and $k_{\max}\sigma_R = 1.16 \pm 0.14$, the power-law fit to the tails yields $\beta \approx 2$, indicating algebraic decay. (d) For $k_{\max}\sigma_R = 0.65$ at the same disorder strength, the density profile clearly exhibits exponential decay, as shown in the inset. Figure is taken from Ref. [21].

region.

The observation was based upon the time-of-flight absorption images [Fig.1.12(a,b)] after releasing the condensate into the disordered potential. Snapshots of the atomic density at different times [Fig.1.13(a)] reveal the suppression of the initial expansion and the exponential decay in the tails of the BEC, from which the localization length $L_{\rm loc}$ was extracted by fitting the form $\exp(-2|z|/L_{\rm loc})$. The evolution of $L_{\rm loc}$ with time [Fig.1.13(b)] shows clear suppression of expansion due to localization. Figures (c,d) further illustrate the distinction between algebraic and exponential localization, depending on the dimensionless parameter $k_{\rm max}\sigma_R$. For $k_{\rm max}\sigma_R > 1$, a power-law fit $1/|z|^{\beta}$ yields $\beta \approx 2$ [Fig.1.13(c)], indicating algebraic decay, while for $k_{\rm max}\sigma_R < 1$, the density exhibits clear exponential decay [Fig.1.13(d)], both measured at disorder strength $V_R/\mu_{\rm in} = 0.15$. Note that the algebraic decay of the atomic density with coefficient $\beta \approx 2$ was also predicted in a theoretical investigation by Sanchez-Palencia *et al.* [23], which complements the experimental results.

Subsequent to these experiments in 1D, several other experiments have also been conducted to realize the AL in the case of 2D [91] and 3D [89, 88, 92] employing random speckle disordered potentials. Motivated by these experiments, several theoretical and numerical studies have investigated the interplay between disorder and interactions in weakly interacting BECs using a mean-field approach. In the mean-field limit, the mathematical model describing the BEC is a nonlinear Schrödinger-like Gross-Pitaevskii equation (GPE), which will be described in the following section.

1.3 Theoretical Framework for Weakly Interacting BECs: The Gross-Pitaevskii Equation

A system of N weakly interacting bosons can be described by a second quantized Hamiltonian with a Bosonic field operator $\widehat{\Psi}(\mathbf{r},t)$, where $\mathbf{r} \equiv (x,y,z)^T$ and t represents the time. For convenience, we denote $\widehat{\Psi}(\mathbf{r},t) = \widehat{\Psi}(\mathbf{r})$ and consider a limiting condition where all bosons are condensed into the same single-particle state. Then the second quantized Hamiltonian for all particles of weakly interacting by binary collisions and confined in an external trap is given by [93–96]:

$$\widehat{H} = \int d\mathbf{r}\widehat{\Psi}^{\dagger}(\mathbf{r}) \left(-\frac{\hbar^2}{2m}\nabla^2 + V_{\rm ext}(\mathbf{r}) \right) \widehat{\Psi}(\mathbf{r}) + \frac{1}{2}\iint d\mathbf{r}d\mathbf{r}'\widehat{\Psi}^{\dagger}(\mathbf{r})\widehat{\Psi}^{\dagger}(\mathbf{r}')V_{\rm int}\left(\mathbf{r}-\mathbf{r}'\right)\widehat{\Psi}(\mathbf{r}')\widehat{\Psi}(\mathbf{r}), \tag{1.36}$$

where $\hat{\Psi}(\mathbf{r})^{\dagger}$ and $\hat{\Psi}(\mathbf{r})$ are the creation and annihilation field operators to create and annihilate particles at position $\mathbf{r}$, respectively. Here, the first term $-\frac{\hbar^2}{2m}\nabla^2$ is the momentum operator responsible for the kinetic energy of the particles, $V_{\text{ext}}(\mathbf{r})$ is the external trapping potential through which the disorder can be introduced and $V_{int}(r-r')$ is the two body interacting potential. The creation and annihilation operators satisfy the crucial Bose commutation relations as [93, 96] :

$$\left[\hat{\Psi}(\mathbf{r}),\hat{\Psi}(\mathbf{r}')\right]=\left[\hat{\Psi}^{\dagger}(\mathbf{r}),\hat{\Psi}^{\dagger}(\mathbf{r}')\right]=0, \qquad \left[\hat{\Psi}(\mathbf{r}),\hat{\Psi}^{\dagger}(\mathbf{r}')\right]=\delta(\mathbf{r}-\mathbf{r}'), \tag{1.37}$$

where $\delta(\mathbf{r})$ is the Dirac delta function. In case of dilute alkali gases at ultracold temperatures, the atomic interactions are dominated by low-energy two-body s-wave collisions. As a result, the elastic and hard-sphere collisions can be approximated by the pseudo potential [97]:

$$V_{\text{int}}(\mathbf{r}-\mathbf{r}')=\tilde{U}_0\delta(\mathbf{r}-\mathbf{r}'), \tag{1.38}$$

where $\tilde{U}_0 = 4\pi\hbar^2 a_0/m$, with a_0 being the s-wave scattering length, which remains positive for repulsive interaction and negative for attractive interaction. Substituting Eq. (1.38) into Eq. (1.36) and integrating over all $\mathbf{r}$-space leads to

$$\hat{H}=\int d\mathbf{r}\hat{\Psi}^{\dagger}(\mathbf{r})\left(-\frac{\hbar^2}{2m}\nabla^2+V_{\text{ext}}(\mathbf{r})\right)\hat{\Psi}(\mathbf{r})+\frac{\tilde{U}_0}{2}\int d\mathbf{r}\hat{\Psi}^{\dagger}(\mathbf{r})\hat{\Psi}^{\dagger}(\mathbf{r})\hat{\Psi}(\mathbf{r})\hat{\Psi}(\mathbf{r}). \tag{1.39}$$

By applying the Heisenberg equation of motion $i\hbar\partial_t\hat{\Psi}(r,t)=\left[\hat{\Psi}(r,t),\hat{H}\right]$ and commutation relations [Eq. (1.37)], we obtain the following equations with field operators:

$$\mathrm{i}\hbar\frac{\partial}{\partial t}\hat{\Psi}(\mathbf{r},t)=\left[-\frac{\hbar^2}{2m}\nabla^2+V_{\text{ext}}(\mathbf{r})+\int d\mathbf{r}\hat{\Psi}^{\dagger}(\mathbf{r},t)V_{\text{int}}\left(\mathbf{r}-\mathbf{r}'\right)\hat{\Psi}(\mathbf{r}',t)\right]\hat{\Psi}(\mathbf{r},t). \tag{1.40}$$

Due to the macroscopic occupation of the single-particle state at the mean-field limit, the Bosonic field operator $\hat{\Psi}(\mathbf{r},t)$ can be composed of a mean-field wave function $\psi(\mathrm{r},t)$ and it's fluctuation counterpart $\delta(\mathbf{r},t)$ as:

$$\hat{\Psi}(\mathbf{r})=\sqrt{N}\psi(\mathbf{r})+\delta\hat{\Psi}(\mathbf{r}), \tag{1.41}$$

with N is the total number of atoms in the condensate, and the fluctuation operator satisfies $\langle\delta\hat{\Psi}(\mathbf{r},t)\rangle\equiv 0$. The macroscopic wave function $\psi(\mathbf{r},t)$ can be written as the expectation value of $\hat{\Psi}$, i.e. $\psi(\mathbf{r})=\langle\hat{\Psi}(\mathbf{r})\rangle/\sqrt{N}$. Inserting (1.41) into (1.40), and considering the leading order in ψ and neglecting the terms related to δ, we obtain the

time-dependent Gross-Pitaevskii equation (GPE) as [93, 96]:

$$i\hbar\frac{\partial\psi(\mathbf{r},t)}{\partial t} = \left[-\frac{\hbar^2}{2m}\nabla^2 + V_{\text{ext}}(\mathbf{r}) + g|\psi(\mathbf{r},t)|^2\right]\psi(\mathbf{r},t), \tag{1.42}$$

where $g = 4\pi\hbar^2 N a_0/m$ represents the two-body interaction coefficient.

In this approximation, dropping the fluctuation term neglects the thermal and quantum depletion of the condensate. As a result, the GPE (Eq. 1.42) is only valid for the condensate at absolute zero temperatures. The normalization condition of the wave function $\psi(\mathbf{r},t)$ is defined as:

$$\int_{\mathbb{R}^3}|\psi(\mathbf{r},t)|^2 d^3\mathbf{r} = 1. \tag{1.43}$$

To find the stationary state solution of Eq. (1.42), one can substitute the $\psi(\mathbf{r},t) = \phi(\mathbf{r})\exp(-i\mu t/\hbar)$, with μ being the chemical potential of the condensate and ϕ is the ground state of the condensate. Consequently, utilizing the normalization criterion (1.43), we obtain the chemical potential and energy as,

$$\mu = \int d^3\mathbf{r}\left[|\nabla\psi(\mathbf{r})|^2 + V_{\text{ext}}|\psi(\mathbf{r})|^2 + g|\psi(\mathbf{r})|^4\right], \tag{1.44}$$

$$E = \int d^3\mathbf{r}\left[|\nabla\psi(\mathbf{r})|^2 + V_{\text{ext}}|\psi(\mathbf{r})|^2 + \frac{g}{2}|\psi(\mathbf{r})|^4\right], \tag{1.45}$$

where the first term represents the kinetic energy, the second is the external potential energy, and the third term represents the interaction energy of the condensate. The additional factor of $1/2$ in the third term of E (1.45) arises from avoiding double counting of pairwise interactions among N indistinguishable bosons.

In our numerical simulations, we non-dimensionalize the GPE (1.42) with respect to harmonic trap configuration used in most of the experiments, i.e. $V(\mathbf{r}) = \frac{1}{2}(\omega_x^2x^2 + \omega_y^2y^2 + \omega_z^2z^2)$, with ω_x, ω_y, and ω_z being the trapping frequencies along x, y, and z directions, respectively. In this approach, the dimensionless quantities can be defined as [98–100]

$$\tilde{t} = \omega_{\text{min}}t, \quad \tilde{x} = \frac{x}{a_{\text{ho}}}, \quad \tilde{\psi} = a_{\text{ho}}^{3/2}\psi, \tag{1.46}$$

to non-dimensionalize the GPE (1.42), where $\omega_{\text{min}} = \min\{\omega_x, \omega_y, \omega_z\}$ has the unit of t^{-1}, and $a_{\text{ho}} = \sqrt{\hbar/m\omega_{\text{min}}}$ is the harmonic oscillator length scale. By rescaling with

Eq. (1.46), the dimensionless form of the GPE becomes:

$$\mathrm{i}\frac{\partial\tilde{\psi}(\tilde{\mathbf{r}},t)}{\partial\tilde{t}} = \left[-\frac{1}{2}\nabla^2 + V_{\mathrm{ext}}(\tilde{\mathbf{r}}) + g|\psi(\tilde{\mathbf{r}},t)|^2\right]\psi(\tilde{\mathbf{r}},t). \tag{1.47}$$

For simplicity, we henceforth denote $\tilde{\psi}(\tilde{\mathbf{r}}) \equiv \psi(\mathbf{r})$.

1.3.0.1 Dimension Reduction of the Gross–Pitaevskii Equation: From 3D to 1D

Experimental studies on Bose–Einstein condensates have demonstrated that strong confinement in one or two spatial directions can effectively reduce the dimensionality of the GPE (1.47). This reduction is achieved by separating the dynamics along the tightly confined dimensions[101–104]. Since our work involves a cigar-shaped, quasi-one-dimensional BEC, we focus on the dimensional reduction of the GPE from three to one dimension in the following.

Consider a cigar-shaped condensate where the transverse directions are tightly confined in comparison to the longitudinal direction, i.e. $\omega_y \gg \omega_x, \quad \omega_z \gg \omega_x$ and therefore anisotropy follows $\gamma_y = \omega_y/\omega_x \gg 1, \quad \gamma_z = \omega_z/\omega_x \gg 1$. Further, the 3D GPE can be reduced to 1D GPE by considering $V(x,y,z) = V_{\parallel}(x) + \frac{1}{2}(\gamma_y^2 y^2 + \gamma_z^2 z^2)$, where $V_{\parallel}(x)$ is the external trap along longitudinal direction. Due to the effect of the strong transverse confinement, the condensate dynamics along these directions are frozen. Consequently, the wavefunction can be represented as,

$$\Psi(x,y,z,t) = \psi(x)\frac{(\gamma_y\gamma_z)^{1/4}}{\sqrt{\pi}}\exp\Big(-\frac{\gamma_y y^2 + \gamma_z z^2}{2}\Big). \tag{1.48}$$

After integrating out the transverse space variables,(y,z), we obtain the 1D GPE for a cigar-shaped quasi-1D BEC as,

$$\mathrm{i}\frac{\partial\psi(x,t)}{\partial t} = \left[-\frac{1}{2}\frac{\partial^2}{\partial x^2} + V_{\mathrm{ext}}(x) + \beta|\psi(x,t)|^2\right]\psi(x,t), \tag{1.49}$$

where $\beta = g\frac{\sqrt{\gamma_y\gamma_z}}{2\pi}$, and the potential V_{ext} is either bichromatic (1.31) or random disordered potential (1.34).

1.3.1 Spin-orbit coupled binary Bose-Einstein condensates

Since the realization of Bose–Einstein condensation (BEC) in neutral atoms [56, 57], they have become a fertile ground for exploring light–matter interactions that mani-

fest in the generation of synthetic gauge fields. The concept of gauge fields arises from the behaviour of charged particles in the presence of external electromagnetic fields. In contrast, these fields are engineered in controlled experimental platforms—such as ultracold atomic systems—to mimic the behavior of charged particles in the absence of actual electromagnetic fields. Utilizing these, several proposals have been made to couple the condensate's atomic momentum with the spin degrees of freedom associated with the hyperfine states of neutral atoms. These ideas are based on spatially dependent couplings between different hyperfine states, induced by the geometric configuration of laser fields.

Following the proposals, the first experimental realization of a synthetic spin–orbit (SO) coupled BEC was achieved in 2011 by the NIST[1] group [105], by coupling two hyperfine states using coupled Raman lasers with ^{87}Rb condensate. In their technique, they have generated one-dimensional SO coupling with a combination of equal Rashba [106] and Dresselhaus [107] types of SO interaction. Subsequently, similar techniques also have been utilized to induce SO coupling in Fermi gases [108], spin-1 BECs [109], etc. As our thesis involves the study of SO coupling in localization, we briefly discuss the synthetic SO-coupled BECs starting from a fundamental description of SO coupling and gauge field, which is followed by a brief experimental demonstration of the generation of pseudo spin-1/2 BEC [105].

1.3.1.1 Spin-orbit coupling of an atom

Spin-orbit (SO) coupling in an atom is a purely quantum mechanical phenomenon that arises when an electron's spin degrees of freedom couple with its orbital angular momentum. This interaction plays a central role in various condensed matter phenomena, such as spintronics, topological insulators, and the spin-Hall effect. SO coupling can be understood simply by considering a negatively charged electron moving with velocity $\mathbf{v}$ in an electric field $\mathbf{E}$. The motion of the charged particle around the nucleus of the atom induces an effective magnetic field $\mathbf{B}_{\text{eff}}$ due to the relativistic Lorentz transformation of the electric field in electron's rest frame. The effective magnetic field relies on the special theory of relativity, where the electric field from one inertial frame can be seen as the magnetic field in another frame of reference. Consequently, the effective magnetic field experienced by the electron spin is given by:

$$\mathbf{B_{eff}} = -\frac{\mathbf{v} \times \mathbf{E}}{c^2}, \tag{1.50}$$

[1]National Institute of Standards and Technology

where c is the velocity of light in vacuum. As a result, the coupling of the magnetic field with the spin angular momentum of an electron is defined as the Zeeman interaction, which leads to the generation of the SO-coupled Hamiltonian of the form:

$$H_{SO} = -\mu_s \cdot \mathbf{B_{eff}} \equiv -\frac{g_s \mu_B \mathbf{E_0}}{2mc^2}(\mathbf{k} \times \sigma) \cdot \hat{z}, \tag{1.51}$$

with, electric field as $\mathbf{E} = E_0\hat{z}$. The Hamiltonian can be modified in terms of

$$H_{SO} = -\alpha_{SO}(\mathbf{k} \times \sigma) \cdot \hat{z}, \tag{1.52}$$

where, $\alpha_{SO} = \frac{g_s \mu_B \mathbf{E_0}}{2mc^2}$ with μ_B as the Bohr's magneton, while g_s denotes the gyromagnetic ratio of the electron and $\sigma = \{\sigma_x, \sigma_y, \sigma_z\}$ are the Pauli spin matrices. The different momentum vectors with Pauli spin matrices define the combinations for Rashba, Dresselhaus, or their summation in 2D materials.

1.3.1.2 Different types of spin-orbit couplings

The SO interaction can be distinguished depending on the asymmetry between the orbital angular momentum and electron spin. In SO coupling, the orbital angular momentum of the electron gets affected due to the effective magnetic field. The motion of the charged electron in an electric field possesses the Lorentz force ($\mathbf{F} = -e\mathbf{p} \times \mathbf{B}/m$), which eventually generates Zeeman energy. The Rashba coupling in SO interaction originates due to the lack of inversion symmetry in a 2D material. On the other hand, the linear Dresselhaus [107] SO coupling originated from the breakdown of the bulk inversion symmetry of different zinc-blende III-V semiconductor materials. The Hamiltonian corresponding to the Dresselhaus type SO coupling is proportional to $\propto -\hat{\sigma}_x k_y - \hat{\sigma}_y k_x$.

Therefore, a general Hamiltonian for linear SO coupling in 2D spin-1/2 systems can be written as,

$$H = \frac{\hbar \mathbf{k}^2}{2m}\hat{1} + \frac{\Omega}{2}\sigma_z - \lambda_R(k_y\sigma_x - k_x\sigma_y) - \lambda_D(-k_y\sigma_x - k_x\sigma_y), \tag{1.53}$$

where the first term is for the kinetic part, the second term is for Rabi coupling, which originated from the intensity of Raman lasers, the third and fourth terms correspond to the Rashba and Dresselhaus SO interaction strengths, with λ_R and λ_D being their SO coupling strengths. In case of equal Rashba and Dresselhaus coupling strength ($\lambda_R = \lambda_D = \lambda$), the effective SO coupling term is $2\lambda k_x \hat{\sigma}_y$.

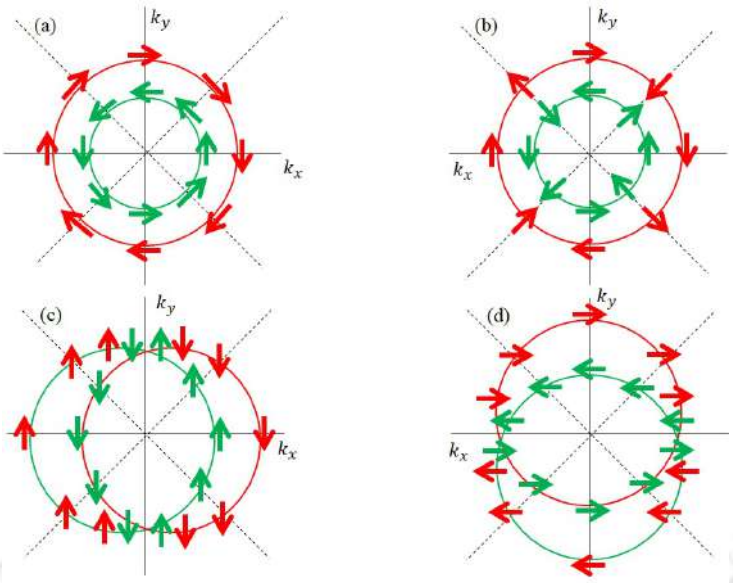

Figure 1.14: Spin orientations in (k_x, k_y) plane associated to different SO coupling. (a) 2D Rashba SO coupling $\lambda_R(k_y\sigma_x - k_x\sigma_y)$ with broken mirror symmetry. (b) 2D Dresselhaus SO coupling $\lambda_D(-k_y\sigma_x - k_x\sigma_y)$ having bulk inversion asymmetry. (c) and (d) depict 1D SO coupling as a consequence of the equal combination of Rashba and Dresselhaus SO coupling strength ($\lambda_R = \lambda_D = \lambda$) corresponding to $-2\lambda k_x\hat{\sigma}_y$ and $2\lambda k_y\sigma_x$ respectively. Here, the arrows are used to show the spin orientation: red for the up-spin and green for the down-spin. Figure is adapted from Ref. [110].

Both Rashba and Dresselhaus SO coupling lock spin to the linear momentum and split the spin sub-bands in energy. Such band splitting is also observed in the experiments of the NIST group in the case of pseudospin-1/2 condensates [105].

In Fig. 1.14, we illustrate the Rashba and Dresselhaus configuration in 2D spin-1/2 systems. The red and green color arrows are associated with spin-up and spin-down components. The Rashba SO coupling [see figure 1.14(a)] results in the momentum-dependent spin splitting, where the spin orientation depends on the momentum direction. The spin configuration associated with Dresselhaus coupling λ_D shows the bulk inversion asymmetry [Fig. 1.14(b)]. With the linear combination of the Dresselhaus and Rashba coupling, one can obtain the spin configuration corresponding to the one-dimensional SO coupling [see Fig. 1.14(c) and (d)].

1.3.1.3 Theory of gauge field

In quantum mechanical description, if a charged particle with charge q and mass m undergoes an electromagnetic field, the Hamiltonian of the system can be written in

terms of a scalar ϕ and a vector potential $\mathbf{A}$ as,

$$H = \frac{1}{2m}(\mathbf{P} - \frac{q\mathbf{A}}{c})^2 + q\phi, \tag{1.54}$$

where c is the velocity of light in vacuum. Then, the resultant electric and magnetic fields can be defined as

$$\mathbf{E} = -\nabla\phi - \frac{\partial \mathbf{A}}{\partial t}, \qquad \mathbf{B} = -\nabla\mathbf{A}. \tag{1.55}$$

The information of the gauge potential $\mathbf{A}$ can give rise to the electric and magnetic field for a charged particle. However, the gauge potential $\mathbf{A}$ being a vector it constitutes with three-directional components as $\mathbf{A} = (A_x, A_y, A_z)$. Now, depending upon its commutation relationships, the vector potential can be characterized into two different parts: Abelian, $[A_i, A_j] = 0$, and non-Abelian $[A_i, A_j] \neq 0$ vector potential, where $i, j = x, y, z$.

Usually, in experiments, the Abelian gauge field is used to generate the synthetic magnetic fields. In principle, the method used to generate synthetic magnetic fields for neutral atoms was developed from a fundamental concept of quantum mechanics, i.e., the Berry phase. With this approach, producing the synthetic magnetic field has various advantages, like tuning parameters while studying the quantum Hall effect. In contrast to that, synthetic SO coupling arises from the non-Abelian gauge field in the case of Bosonic systems. In addition to this, the realization of synthetic SO coupling also sets the stage for topological insulators.

1.3.1.4 Synthetic one-dimensional spin-orbit coupled Bose-Einstein condensates

In solid-state materials, the intrinsic SO coupling manifests various exotic phenomena such as spin-Hall effect [111], spintronic devices [112], topological insulators [113, 114] and quantum simulations [115, 116]. In the case of fermions, the SO coupling arises from the coupling between the spin of the fermions and orbital angular momentum. Unlike fermions, in ultracold Bosonic gases, realizing SO coupling is quite challenging because the neutral atoms do not possess any interaction between spin and momentum. However, researchers from the NIST group in 2011 [105] engineered a synthetic SO coupled BEC by creating a one-dimensional SO coupling with the superposition of equal Rashba and Dresselhaus strengths by dressing two atomic hyperfine states with a pair of lasers. The achievement of synthetic SO coupling in ultracold Bosons is the first experiment where researchers have achieved the SO coupling using bosonic

atoms. In their experiment, the SO coupling strength can be controlled by tuning the laser geometry, which can give rise to a quantum phase transition from spin-mixed to spin-separated phase.

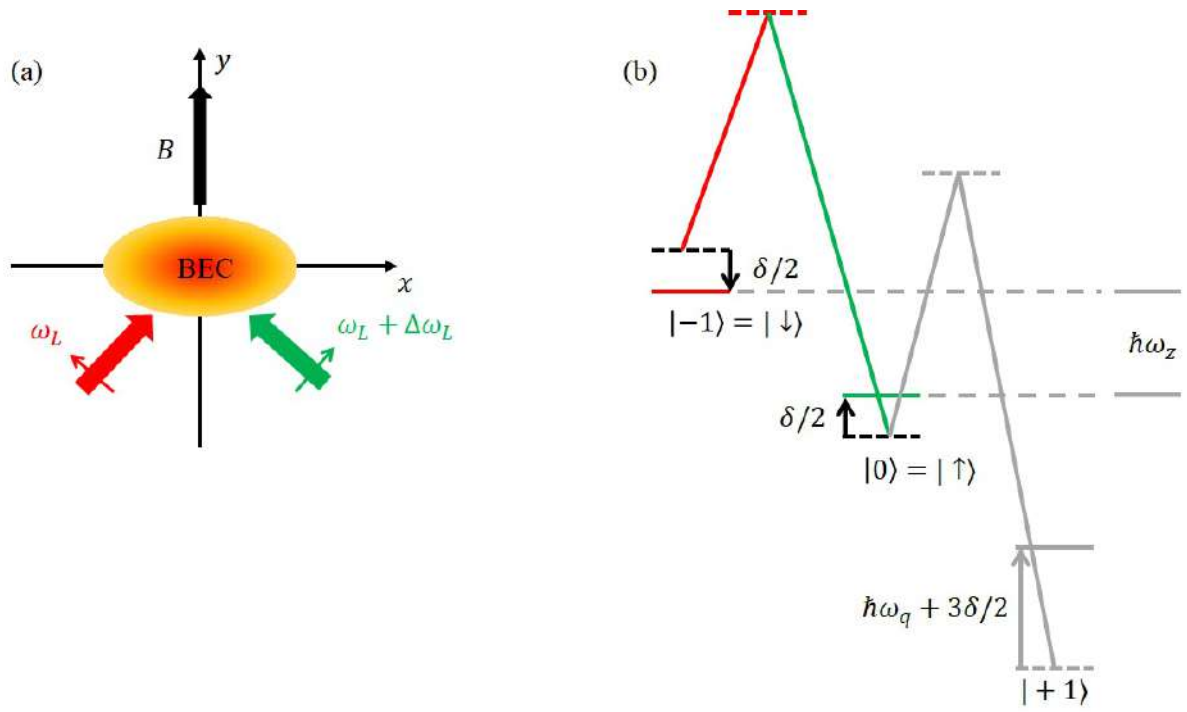

Figure 1.15: (a) Schematic diagram of the experimental setup [105] for the realization of synthetic SO coupling when BEC cloud is subjected to a strong magnetic field along z direction and two Raman Laser beams. (b) Level diagram of $F = 1$ ground state manifold, which gets Zeeman splitting with a strong bias magnetic field. Two Raman lasers couple the hyperfine states $|\uparrow\rangle = |F = 1, m_F = 0\rangle$ and $|\downarrow\rangle = |F = 1, m_F = -1\rangle$, differing in energy by $\hbar\omega_z$. The other hyperfine state $|F = 1, m_F = +1\rangle$ is decoupled by utilizing the quadratic Zeeman effect.

In Fig. 1.15, we show the schematic diagram of the experiment. In their experiment, they considered ^{87}Rb atoms with $F = 1$ ground state manifold, produced in an optical dipole trap with frequencies $(f_x, f_y, f_z) = (50, 50, 140)$Hz. A bias magnetic field $B\hat{y}$ is applied to break the degeneracy of $F = 1$ manifold due to Zeeman shifts into $|F = 1, m_F = +1\rangle$, $|F = 1, m_F = -1\rangle$, and $|F = 1, m_F = 0\rangle$. These three hyperfine levels of the rubidium atoms can be used as different components of a condensate [see Fig. 1.15(b)]. These hyperfine states are coupled by introducing a pair of Raman lasers. Two Raman lasers with a wavelength of $\lambda = 804.1nm$ are positioned perpendicular to each other, propagating along the directions $y + x$ and $y - x$, with frequencies ω_L and $\omega_L + \Delta\omega_L$, respectively. However, the bias magnetic field induces a Zeeman shift $\hbar\omega_Z \approx 4.81$MHz between the states $|F = 1, m_F = 0\rangle$, and $|F = 1, m_F = -1\rangle$, and this shift is equal to the frequency difference $\Delta\omega_L$ between the two lasers. In contrast, the

state $|F = 1, m = 1\rangle$ is decoupled from the rest of the system due to the large quadratic Zeeman shift $\hbar\omega_q + 3\delta/2$. By neglecting this state, the system can be reduced to an effective spin-1/2 system, with the two remaining states represented as pseudo-spin-up $|\uparrow\rangle = |m_F = 0\rangle$ and pseudo-spin-down $|\downarrow\rangle = |m_F = -1\rangle$. These two states are coupled with a Raman frequency $\hbar\Omega$, which can be controlled by the intensity of the laser.

The Hamiltonian for the SO-coupled BEC is given by

$$H = \frac{\hbar^2 k_x^2}{2m} + \frac{\hbar^2 k_L}{m} k_x \sigma_z + \frac{\hbar\Omega}{2}\sigma_x, \tag{1.56}$$

where, $k_L = \dfrac{\sqrt{2}\pi}{\lambda_L}$ with λ_L as the wavelength of the Raman lasers, m is the mass of the ^{87} Rb atoms, $(\sigma_x, \sigma_y, \sigma_z)$ are the Pauli matrices spin component, and Ω is the Rabi coupling strength between the two dressed states.

The corresponding dimensionless SO coupled GPE for the spin-up ($\psi_\uparrow$) and spin-down ($\psi_\downarrow$) states are given by

$$\begin{aligned}
\mathrm{i}\partial_t \psi_\uparrow(x,t) &= \left[-\frac{1}{2}\partial_x^2 + V_{\text{ext}} - \mathrm{i}k_L\partial_x + g_{\uparrow\uparrow}|\psi_\uparrow(x,t)|^2 + g_{\uparrow\downarrow}|\psi_\downarrow(x,t)|^2\right]\psi_\uparrow(x,t) + \Omega\psi_\downarrow(x,t),\\
\mathrm{i}\partial_t \psi_\downarrow(x,t) &= \left[-\frac{1}{2}\partial_x^2 + V_{\text{ext}} + \mathrm{i}k_L\partial_x + g_{\downarrow\downarrow}|\psi_\downarrow(x,t)|^2 + g_{\uparrow\downarrow}|\psi_\uparrow(x,t)|^2\right]\psi_\downarrow(x,t) + \Omega\psi_\uparrow(x,t),
\end{aligned} \tag{1.57}$$

where, V_{ext} is the external trapping potential, which we use one-dimensional quasiperiodic (1.31) and random disordered potential (1.34) in our work. Here, $g_{\uparrow\uparrow}, g_{\downarrow\downarrow}$ and $g_{\uparrow\downarrow}, g_{\downarrow\uparrow}$ represents the intra- and inter-species interactions, respectively.

The realization of synthetic SO coupling in BECs significantly motivated both theoretical and numerical studies onset of localization. In the following, we present a comprehensive review of the literature on Anderson localization (AL) in BECs, highlighting existing gaps that our work aims to address.

1.4 Theoretical advancements on localization in BECs using the mean-field GP Model

Since the theoretical proposal by Anderson [2], Anderson localization (AL) has inspired extensive research across a range of physical systems, including electromagnetic

waves [10–14], acoustic waves [19], condensed matter systems [4, 7, 8], and very recent surface gravity waves of water [117]. These realizations highlight the universality of AL, spanning from microscopic to macroscopic scales. Across these studies, a central focus has been to understand the role of disorder and interactions onset of localization. In that context, the observation of AL in ultracold atomic gases using BECs has opened up new avenues for exploration [20, 21]. For a comprehensive discussion of these experiments, please refer to the section 1.2.5. Following these experiments, researchers have understood the potential of ultracold systems due to their unprecedented controllability of the interaction and potential parameters for investigating localization. These experimental works also inspired various numerical and theoretical studies incorporating the mean-field Gross–Pitaevskii (GP) equation, helping to elucidate the roles of disorder and interactions, a question that remained open for several decades.

The mean field GP model has been extensively employed to investigate AL in BECs, particularly in presence of quasiperiodic and random speckle potentials. This model was utilized not only in studying the ground-state properties of the condensate but also in exploring nonequilibrium dynamics under the influence of disorder and mean-field atomic interactions. As a result, the literature on localization in BEC is both extensive and compelling. In this section, we provide a concise overview of the relevant literature, highlighting the key features and recent advancements. We then outline the primary motivation and objectives of our thesis, with a focus on various localization–delocalization phases and the associated condensate dynamics. Overall, this thesis aims to address several questions concerning the interplay of disorder, interactions, and coupling strengths—such as spin-orbit (SO) and Rabi coupling—which may offer valuable insights for applications in quantum simulation and emerging quantum technologies.

The first major theoretical breakthrough using the Gross–Pitaevskii (GP) model came in 2007, when Sánchez-Palencia *et al.*[23] proposed that an initially confined, weakly interacting one-dimensional BEC, expanding in the presence of a weak speckle disorder exhibits AL. They also identified two distinct regimes of localization: exponential and algebraic, depending on the relation between the condensate's healing length and the correlation length of the disordered potential, and later extended this concept to the localization of Bogolyubov quasiparticles in interacting condensates[118]. Around the same time, Shapiro [119] demonstrated that the expansion dynamics of a two-dimensional interacting condensate trapped in random speckle disorder can be controlled using a single parameter related to the chemical potential and the time scale of 2D-GP equation. The theoretical predictions of exponential and algebraic localiza-

tion were experimentally validated by Billy et al. [21], marking a crucial milestone in the field.

Subsequent numerical studies further enriched the landscape of localization. For instance, Adhikari and Salasnich[22] numerically explored the localization of a quasi-1D BEC trapped in a quasiperiodic potential and further explored the role of repulsive interactions towards the destruction of exponential localization. Building on this, Cheng and Adhikari [120, 121] employed the time-dependent GP equation to study binary cigar-shaped condensates and revealed the spatial symmetry breaking between the components induced by the asymmetry between inter- and intra-species interactions. Furthermore, the study of a similar kind of investigation performed for binary pancake-shaped quasi-2D BEC [122]. Interestingly, in 2D BEC, no symmetry breaking was observed between the components, unlike in quasi-1D, due to the enhanced effect of disorder. In a subsequent work, the asymmetry between quasiperiodic potentials along different axial directions results in the localization of a vortex in a 2D or 3D condensate [123]. Apart from these studies, in a very recent work, Santos and Cardoso [124] used a slightly different approach to create asymmetry in a binary condensate with one component subjected to a quasiperiodic trap and the other remaining free in space. With this setting, they have reported an induced kind of localization within the trapless component by tuning a Rabi-like coupling parameter that couples the two components.

Parallel to these developments with quasiperiodic disorder, random speckle disorder also drew significant interest, particularly after Clément *et al.* [125, 87] reported the subduing of transport and disorder-induced trapping of quasi-1D and 3D interacting BECs. Within the GP framework, Cheng and Adhikari [126] further demonstrated Anderson-like localization of weakly interacting cigar-shaped BECs in a random disordered potential and its fragmentation under strong repulsion. Xi *et al.* [127] extended this idea to a quasi-1D binary condensate trapped in a similar random environment and found that the emergence of phase separation between components crucially depends on the interplay between disorder and interaction strength—a phenomenon that is usually absent in regular harmonic traps.

Despite the comprehensive studies on scalar and binary BECs having substantially advanced the understanding of localization, the recent experimental realization of synthetic SO-coupled BECs [105] has added a compelling new dimension to this field. The interplay between Rabi coupling, SO interaction, and spin-dependent nonlinearities introduces a complex and rich framework, making these systems particularly intriguing for further exploration. Nevertheless, only a handful of numerical studies have

examined localization in SO-coupled BECs subjected to quasiperiodic [24, 128, 129] and random [130] disorder. Typically, disorder potentials play a crucial role in localizing a condensate. Conversely, in spinor BECs, a similar localization effect can be achieved solely through the SO and Rabi couplings, even without modifying the disorder strength. Interestingly, the couplings drive a phase transition from a plane-wave to a density-modulated stripe phase for regular harmonic traps, which significantly changes in the presence of disorder. This distinctive tunability has motivated growing interest in using spinor BECs to probe disorder-induced phenomena.

Beyond these coupling effects, different types of atomic interactions also play a significant role in steering the system between localized and delocalized phases. For example, Muruganandam *et al.*[131] investigated the localization of a dipolar BEC in a weak quasiperiodic potential, highlighting how long-range dipolar interactions influence localization within the 3D GP framework. Another fascinating avenue involves spatially inhomogeneous interactions, inspired by the optical Feshbach resonance technique, which was discussed in Section 1.2.3.2. Unlike homogeneous repulsive interactions, which tend to delocalize the condensate, spatial inhomogeneity can mimic the optical dipole potentials (including quasi-periodic optical lattices, random disordered potentials), which enables both localization and delocalization depending on the interactions [132, 133].

In addition to examining the behavior of the stationary ground state, condensate dynamics also captured significant attention due to the nonlinear behavior of GP models. To explore the condensate dynamics, various mechanisms have been utilized to perturb the ground state of the system like, releasing the BECs from the confining trap [23, 25], giving momentum to the condensate [26], performing a quenching in coupling parameters [27, 28] or interaction parameters [29] and also by time dependent driving [134, 135] act as a perturbation to the ground state of a condensate. However, from the experimental perspective, releasing a condensate from a trap under the influence of gravity is a very common technique which is known as *time-of-flight* technique to study the time evolution of the condensate. Utilizing this method, several experiments have demonstrated the effect of random disordered potential towards suppressing the expansion of a condensate [125, 136–138]. In contrast to that, Doggen and Kinnunen in their theoretical investigation reported the transition from a localized state to a delocalized state by quenching the nonlinearity from a finite value to zero — which demonstrates the sensitivity of localized states to the non-adiabatic changes of interactions [139]. During the localization to delocalization phase transition, a wealth of novel phases have also been explored, including superfluid, Bose glass phases, etc. On a sim-

ilar line, Damski *et al.* [140] theoretically showed the dynamical phase transition from a superfluid to a Bose glass phase for interacting BECs trapped in a 2D speckle potential. In case of non-equilibrium dynamics, the competition between interaction and disorder also induced chaotic dynamics through perturbing the condensate by different means [141–145]. For instance, Brezinova et al. [30] numerically demonstrated that an expanding BEC can exhibit chaotic dynamics while transferring from a harmonic to either periodic or aperiodic (including quasiperiodic or random disordered trap) while the disorder strength is raised above the threshold value. Based on the chaotic dynamics, distinguishing the localized and delocalized condensates remains challenging. The non-equilibrium dynamics related to localized and delocalized phases of a condensate to characterize them is one of the questions that we are going to address in this thesis. Apart from the perturbation dynamics of the condensates, several works have reported the complex dynamics of the SO and Rabi coupled condensate trapped in a random disordered potential [146–148]. In contrast, time dependent driving in BECs also facilitates many fascinating effects like momentum space Anderson localization driven by quantum kicked rotor [149–152], time periodic driving of Rabi field act as a 'switch' to mimic one component into the other by exchanging their populations in a binary configuration of BECs [153, 135] etc. Additionally, in the high frequency limit, the time-periodic Rabi field is also utilized to tune the SO coupling in experiments [134, 154].

With recent advancements in the localization of BECs, various aspects of Anderson localization (AL) have become clearer, particularly the role of interactions and disorder—long-standing challenges in the field—as well as the related condensate dynamics influenced by disorder. Since disorder is ubiquitous in physical systems, the study of disorder and AL continues to evolve in diverse directions. For example, recent investigations have explored AL in macroscopic systems like surface gravity waves [117], whereas at the microscopic level, localization of binary mixtures under beyond mean-field quantum and thermal corrections was studied [155]. However, several important questions remain less explored, such as distinguishing localization from delocalization through the study of non-equilibrium condensate dynamics. We believe that distinguishing the localization-delocalization phases using the dynamical approach provides a valuable tool for experiments, especially with speckle potentials, where characterizing delocalized phases is difficult from localized phases. In contrast to the dynamical studies, SO-coupled BECs have not been studied in a comprehensive manner with different interactions and coupling parameters, regardless of quasiperiodic or random disorder. As a result, this thesis comprises a series of works focused

on understanding different localization-delocalization phase transition and their associated non-equilibrium dynamics in scalar as well as SO-coupled BECs.

1.5 Outline of the thesis

The outline of the following chapters is as follows :

In **Chapter 2**, we present the numerical scheme used to solve the GP equations for both scalar and SO coupled BECs. We begin by outlining the split-step Crank-Nicolson (CN) method, applied to solve the time-dependent SO coupled binary GPEs. This is followed by a discussion of the imaginary-time propagation and real-time propagation methods to obtain ground states and associated condensate dynamics. Further, we extend the discussion to the quasi-1D scalar GP equation. Finally, the chapter ends with an example demonstrating the convergence of the ground state.

In **Chapter 3**, as a part of the first problem, we have analyzed the effect of interaction on ground state and dynamics of a scalar BEC trapped in a one-dimensional quasiperiodic and random disordered potential. First, we have explored the role of increasing interaction on the ground state localized under both types of potential. After obtaining the ground state, we perform an interaction quench– suddenly switching off the interaction strength to zero from its initial value to investigate the out-of-equilibrium dynamics and have established that the time correlation of the wave function exhibits periodic nature for the interaction at which condensate exhibits localization and chaotic nature at the interaction for which condensate is delocalized. This quench-induced evolution reveals a transition from regular to chaotic dynamics as the quenching interaction strength increases. Finally, we have concluded the chapter by comparing the results from both quasiperiodic and random disordered potentials.

In **Chapter 4**, as the second problem, we analyze the rentrant nature of the localization of the SO and Rabi coupled pseudospin-1/2 binary BEC confined in a quasiperiodic potential in presence of the inhomogenous interaction. The combined effect of interaction and spin-dependent couplings results in a very intriguing localization-delocalization phase transition of the condensate. We have further employed the Gaussian variational approach to complement our numerical findings. Finally, we show the manifestation of the localization-delocalization dynamical transition of the condensate as the dynamics is generated through the velocity perturbations and trap quenching techniques.

In **Chapter 5**, we extend our analysis to explore various localization–delocalization transition by considering the confinement of the spinor BEC a random disordered po-

tential. Here we present a comprehensive study of how disorder, spin-orbit (SO) coupling, and Rabi coupling influence the ground-state properties. Our results reveal distinct spin-dependent Anderson-like localization phases arising from the interplay of disorder and SO coupling. Additionally, we investigate the impact of interactions with broken Manakov symmetry on these spin-dependent phases, highlighting their role in shaping the condensate's spatial and spin structure.

Following the analysis of spin-symmetric spinor condensates under quasiperiodic and random potentials in the previous two chapters, **Chapter 6** presents the final problem of this thesis, where we investigate the ground state and dynamics of a spin-asymmetric Rabi-coupled condensate where we report the presence of Rabi-coupling induced localization and dynamically induced delocalization of the condensate. The asymmetry is introduced by trapping only one component under a quasiperiodic potential, while keeping the other component free. We analyze how Rabi coupling induces localization by facilitating population exchange between components, both in non-interacting and interacting regimes. Additionally, we study the condensate dynamics under periodic modulation of the Rabi frequency, revealing distinct frequency-dependent delocalization patterns that persist even in the presence of interactions.

In **Chapter 7**, we discuss the summary and conclusion of our thesis work based on different Anderson-like localization-delocalization phases and non-equilibrium dynamics of BECs. Finally, the chapter ends with a discussion of the possible future scope of this thesis work.

Chapter 2

Numerical simulation method to solve the mean-field dynamical equation of Anderson localization

In this chapter, we outline the numerical scheme employed to solve the quasi-1D scalar and SO-coupled GP equations. Due to the nonlinear nature of the GP equation, various numerical techniques have been developed to obtain converged ground states and the dynamics of BECs. In our thesis work, we mainly adopt the split-step Crank-Nicolson (CN) algorithm for numerical simulations. The structure of the chapter is as follows. We begin with a detailed description of the split-step Crank-Nicolson method used to solve the time-dependent GPE for both scalar and SO coupled BECs. We then discuss the imaginary and real-time propagation schemes employed to obtain the ground state and study the dynamics of the condensate. Finally, we present an example to show the convergence of the ground state of the condensate.

2.1 Split-step Crank-Nicolson scheme

Crank-Nicolson (CN) method serves as a robust implicit scheme, known for its unconditional stability even for solving nonlinear equations. It offers significant advantages due to its split-step technique, where the derivative terms (kinetic and SO coupling) and the non-derivative terms (potential, nonlinearity, and Rabi coupling) are handled separately, enhancing both stability and accuracy. Additionally, time-splitting further improves the method's efficiency in treating nonlinear contributions [156]. To keep this chapter self-contained, we first present the split-step technique applied to SO-coupled

GPEs, followed by a brief illustration of the same for scalar BECs. We then outline the imaginary and real-time propagation schemes used to compute the ground state and the condensate dynamics, respectively.

The time-dependent SO and Rabi coupled GPEs with external potential V_{ext} in the dimensionless form (Eq. (1.57) from Chapter 1) is given by the following set of equations:

$$\mathrm{i}\partial_t\psi_\uparrow(x,t) = \left[-\frac{1}{2}\partial_x^2 - \mathrm{i}k_L\partial_x + V_{\text{ext}} + g_{\uparrow\uparrow}|\psi_\uparrow(x,t)|^2 + g_{\uparrow\downarrow}|\psi_\downarrow(x,t)|^2\right]\psi_\uparrow(x,t) + \Omega\psi_\downarrow(x,t), \tag{2.1a}$$

$$\mathrm{i}\partial_t\psi_\downarrow(x,t) = \left[-\frac{1}{2}\partial_x^2 + \mathrm{i}k_L\partial_x + V_{\text{ext}} + g_{\downarrow\downarrow}|\psi_\downarrow(x,t)|^2 + g_{\uparrow\downarrow}|\psi_\uparrow(x,t)|^2\right]\psi_\downarrow(x,t) + \Omega\psi_\uparrow(x,t). \tag{2.1b}$$

To solve the above set of equations using the split-step Crank–Nicolson (CN) scheme, the equations are decomposed into two parts: the derivative and non-derivative components. The derivative part includes the kinetic energy term (first term) and the spin-orbit (SO) coupling term (second term), while the remaining terms—such as the external potential, nonlinear interaction terms, and Rabi coupling—are treated as the non-derivative part. The solution procedure begins with the numerical integration of the non-derivative part, using an initial guess for the stationary condensate wavefunctions $\psi_{\uparrow(\downarrow)}$. In our case, a Gaussian profile is used as the initial ansatz, although other functional forms, such as a Thomas–Fermi profile, may also be employed. This initial input is then evolved under the non-derivative part, producing an intermediate solution that incorporates the effects of the potential, nonlinear interactions, and Rabi coupling. This intermediate solution is subsequently used as an input for the integration of the derivative part. For this step, we apply a centered difference scheme in space with a discretization step Δx, and employ a semi-implicit time-splitting approach to ensure improved numerical stability and accuracy [157–159, 156]. The time evolution continues until a converged ground state is reached. Convergence is typically assessed through the stability of physical observables such as normalization, chemical potential, and the condensate wavefunction profile over successive iterations.

To facilitate convergence to the ground state, we employ the imaginary time propagation method, a commonly used technique that will be discussed later in this section. An additional advantage of the semi-implicit CN scheme is its preservation of normalization throughout the evolution, reflecting the conservation of atom number in a

condensate. Furthermore, the time-splitting error is of order Δt^2, leading to improved accuracy and faster convergence [156]. For clarity, the algorithm is summarized in the following flowchart, followed by a step-by-step description of the CN method implementation.

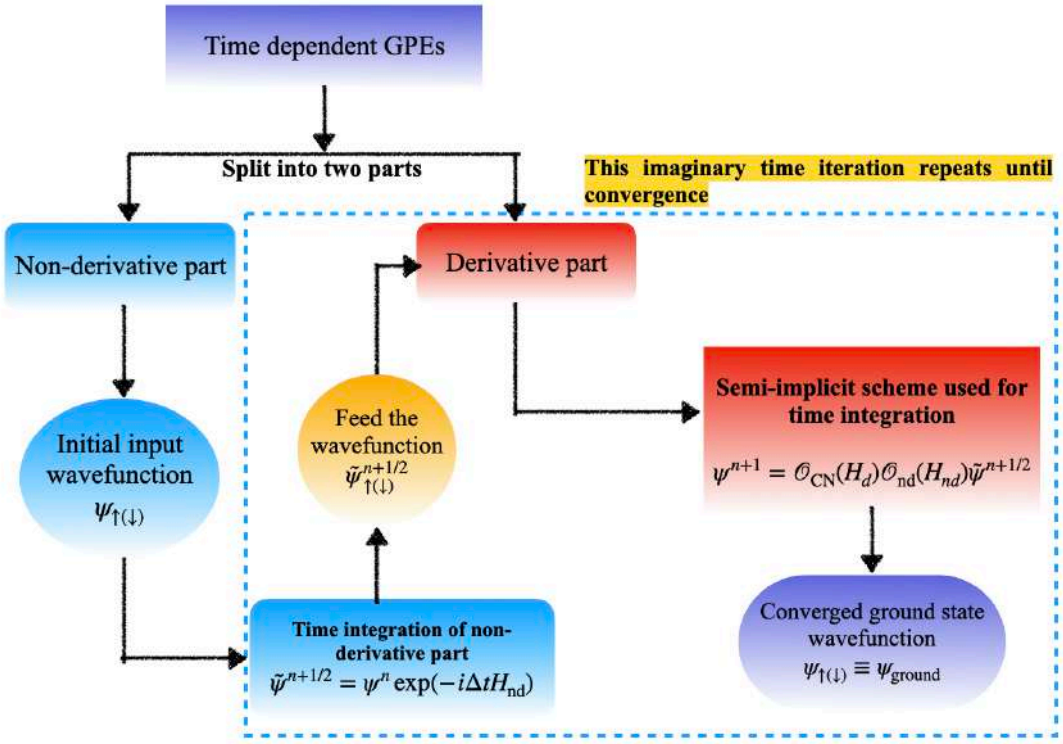

Figure 2.1: Illustration of the split step CN method to solve time dependent GPEs using imaginary time propagation method.

Using the Crank–Nicolson scheme, the equations in (2.1) are splitted into two components: a derivative part and a non-derivative part, as follows:

$$\mathrm{i}\frac{\partial \Psi}{\partial t} = \left[H_{\mathrm{d}} + H_{\mathrm{nd}}\right]\Psi, \tag{2.2}$$

where, H_{d} and H_{nd} represent the derivative and non-derivative part of the Hamiltonian operator, respectively and $\Psi \equiv \left(\psi_{\uparrow}, \psi_{\downarrow}\right)^T$ with T is the transposition.

As a result of this non-derivative and derivative parts of Eq. (2.1a)) can be written

in the more explicit form, respectively, as given below:

$$\mathrm{i}\frac{\partial \psi_\uparrow}{\partial t} = \left[V_{\text{ext}} + g_{\uparrow\uparrow}|\psi_\uparrow|^2 + g_{\uparrow\downarrow}|\psi_\downarrow|^2\right]\psi_\uparrow + \Omega\psi_\downarrow \equiv H_{\uparrow,A1}\psi_\uparrow + H_{\uparrow,A2}\psi_\downarrow, \tag{2.3a}$$

$$\mathrm{i}\frac{\partial \psi_\uparrow}{\partial t} = -\frac{1}{2}\frac{\partial^2 \psi_\uparrow}{\partial x^2} - \mathrm{i}k_L\frac{\partial \psi_\uparrow}{\partial x} \equiv H_{\uparrow,B}\psi_\uparrow, \tag{2.3b}$$

with the Hamiltonian $H_{\uparrow,A1}, H_{\uparrow,A2}, H_{\uparrow,B}$ is given by,

$$H_{\uparrow,A1} = \left[V_{\text{ext}} + g_{\uparrow\uparrow}|\psi_\uparrow|^2 + g_{\uparrow\downarrow}|\psi_\downarrow|^2\right], \qquad H_{\uparrow,A2} = \Omega \tag{2.4a}$$

$$H_{\uparrow,B} = -\frac{1}{2}\frac{\partial^2}{\partial x^2} - \mathrm{i}k_L\frac{\partial}{\partial x}. \tag{2.4b}$$

Similarly, Eq. (2.1b) can be expressed in the derivative and non-derivative form of the Hamiltonian, respectively, as given below:

$$\mathrm{i}\frac{\partial \psi_\downarrow}{\partial t} = \left[V_{\text{ext}} + g_{\downarrow\downarrow}|\psi_\downarrow|^2 + g_{\downarrow\uparrow}|\psi_\uparrow|^2\right]\psi_\downarrow + \Omega\psi_\uparrow \equiv H_{\downarrow,A1}\psi_\downarrow + H_{\downarrow,A2}\psi_\uparrow, \tag{2.5a}$$

$$\mathrm{i}\frac{\partial \psi_\downarrow}{\partial t} = -\frac{1}{2}\frac{\partial^2 \psi_\downarrow}{\partial x^2} - \mathrm{i}k_L\frac{\partial \psi_\downarrow}{\partial x} \equiv H_{\downarrow,B}\psi_\downarrow, \tag{2.5b}$$

with the Hamiltonian $H_{\downarrow,A1}, H_{\downarrow,A2}, H_{\downarrow,B}$ is given by,

$$H_{\downarrow,A1} = \left[V_{\text{ext}} + g_{\downarrow\downarrow}|\psi_\downarrow|^2 + g_{\downarrow\uparrow}|\psi_\uparrow|^2\right], \qquad H_{\downarrow,A2} = \Omega \tag{2.6a}$$

$$H_{\downarrow,B} = -\frac{1}{2}\frac{\partial^2}{\partial x^2} - \mathrm{i}k_L\frac{\partial}{\partial x}. \tag{2.6b}$$

To perform the time evolution of the wavefunction, we begin by discretizing the total time interval into N_t time steps, with time step Δt. Starting from the initial time t_0, the wavefunction is first evolved by numerically integrating the non-derivative part of the Hamiltonian, yielding an intermediate solution at time $t_0 + \Delta t$. This intermediate wavefunction then serves as the initial condition for integrating the derivative part of the Hamiltonian, resulting in the final wavefunction at $t_0 + \Delta t$. After detailing the CN scheme employed for this time evolution, we proceed to describe the real-time and imaginary-time propagation methods used to investigate the dynamics and obtain the ground state of the condensate, respectively.

2.1.1 Real-time propagation

In real-time propagation, we first solve Eq.(2.3a) and (2.5a) by choosing an initial Gaussian wavefunction as $\psi_\uparrow(x,t_0) = \psi_\downarrow(x,t_0) = \exp(-x^2/2)/\sqrt{\pi}$, at a time t_0 to obtain the intermediate solution at $t = t_0 + \Delta t$. However, initially we consider the out-of-phase initial condition among the trial wavepacket: $\psi_\uparrow(x,t) = -\psi_\downarrow(x,t)$. Then the intermediate solution is used as initial value to solve Eq. (2.3b), and (2.5b) yielding the final solution at $t = t_0 + \Delta t$ as $\psi_\uparrow(x, t_0 + \Delta t)$, and $\psi_\downarrow(x, t_0 + \Delta t)$, respectively. This process is repeated up to the desired time with time step Δt.

Assume at time $t_n = n\Delta t$ the condensate wavefunctions $(\psi_\uparrow^n,\ \psi_\downarrow^n)$ advanced with a time step Δt by integrating the non-derivative part of Hamiltonian (Eq. 2.4b, and 2.6a) to generate the intermediate solution $(\psi_\uparrow^{n+1/2},\ \psi_\downarrow^{n+1/2})$. Therefore, the advancement in the wave function is carried out for small Δt without discretizing the wavefunction in space as given by

$$\mathrm{i}\frac{\partial}{\partial t}\Psi^n = \mathcal{O}_{nd}(\mathbf{M})\Psi^n, \tag{2.7}$$

with

$$\mathbf{M} = \begin{pmatrix} H_{\uparrow,A1} & H_{\uparrow,A2} \\ H_{\downarrow,A2} & H_{\downarrow,A1} \end{pmatrix}, \tag{2.8}$$

where $\Psi = (\psi_\uparrow,\ \psi_\downarrow)^T$, $\mathcal{O}_{nd}(\mathbf{M})$ is the time-evolution operation with the matrix $\mathbf{M}$. The matrix elements are given in Eq. (2.4) and Eq. (2.6). Here, the subscript *'nd'* stands for the *non-derivative* part of the operator.

As the matrix $\mathbf{M}$ contains the *diagonal* and *off-diagonal* terms, therefore, we treat them separately to solve the equation (2.7). Hence, the matrix can be written as,

$$\mathbf{M} = \begin{pmatrix} H_{\uparrow,A1} & 0 \\ 0 & H_{\downarrow,A1} \end{pmatrix} + \begin{pmatrix} 0 & H_{\uparrow,A2} \\ H_{\downarrow,A2} & 0 \end{pmatrix} \equiv \mathbf{M}_{\mathrm{diag}} + \mathbf{M}_{\mathrm{off-diag}} \tag{2.9}$$

Here, the diagonal matrix M_{diag} can be handled with the usual time propagation method like first order ODEs [104, 98, 99, 156, 160],

$$\mathrm{i}\frac{\partial}{\partial t}\Psi^{n+1/2} = (\mathbf{M}_{\mathrm{diag}})\Psi^n, \tag{2.10}$$

$$\begin{pmatrix} \psi_{\uparrow}^{n+1/2} \\ \psi_{\downarrow}^{n+1/2} \end{pmatrix} = \begin{pmatrix} \exp\left(-\mathrm{i}\Delta t H_{\uparrow,A1}\right) & 0 \\ 0 & \exp\left(-\mathrm{i}\Delta t H_{\downarrow,A1}\right) \end{pmatrix} \begin{pmatrix} \psi_{\uparrow}^{n} \\ \psi_{\downarrow}^{n} \end{pmatrix}. \tag{2.11}$$

To diagonalize the off-diagonal matrix $\mathbf{M}_{\mathrm{off-diag}}$ terms, one needs to do an *unitary transformation* in order to transform the off-diagonal matrix into a diagonal matrix [160, 161]. However, to do so, we choose an unitary operator as,

$$\Lambda = \begin{pmatrix} 1/2 & 1/2 \\ 1/2 & -1/2 \end{pmatrix}, \qquad \Lambda^{-1} = \begin{pmatrix} 1 & 1 \\ 1 & -1 \end{pmatrix}. \tag{2.12}$$

Next, using the Λ and Λ^{-1} matrices, our original off-diagonal matrix can be written as $\mathbf{M}_{\mathrm{off-diag}} = \Lambda P \Lambda^{-1}$, where the matrix P can be defined as a diagonal matrix in terms of Ω,

$$P = \begin{pmatrix} \Omega & 0 \\ 0 & -\Omega \end{pmatrix}. \tag{2.13}$$

Following this transformation, the Eq.(2.7) can be written for the $\mathbf{M}_{\mathrm{off-diag}}$ matrix as,

$$\mathrm{i}\frac{\partial}{\partial t}\Psi^{n+1/2} = (\mathbf{M}_{\mathrm{off-diag}})\Psi^{n}, \tag{2.14}$$

$$\mathrm{i}\frac{\partial}{\partial t}\Psi^{n+1/2} = (\Lambda P \Lambda^{-1})\Psi^{n}. \tag{2.15}$$

Therefore, after performing the matrix operations on Ψ^n explicitly. Finally, the form of the transformed wavefunctions can be written as,

$$\begin{pmatrix} \psi_{\uparrow}^{n+1/2} \\ \psi_{\downarrow}^{n+1/2} \end{pmatrix} = \begin{pmatrix} \cos(\Omega\Delta t) & -\mathrm{i}\sin(\Omega\Delta t) \\ -\mathrm{i}\sin(\Omega\Delta t) & \cos(\Omega\Delta t) \end{pmatrix} \begin{pmatrix} \psi_{\uparrow}^{n} \\ \psi_{\downarrow}^{n} \end{pmatrix}. \tag{2.16}$$

Consequently, the series of operations using (2.11) and (2.16) will result in propagating the wavefunctions $(\psi_{\uparrow}^{n},\ \psi_{\downarrow}^{n})$ over a time step $t_n + \Delta t$, including the nonlinearity, external potential and Rabi-coupling. However, there are other techniques to incorporate the off-diagonal Rabi and diagonal terms, which can be found in Ref. [162]

Next, we use the semi-implicit Crank-Nicolson method for the time propagation of

the derivative operators $H_{j,B}$ Eq. (2.4b) and Eq. (2.6b), with $j = \{\uparrow, \downarrow\}$

$$\frac{\psi_j^{n+1} - \psi_j^{n+1/2}}{-\mathrm{i}\Delta t} = \frac{1}{2} H_{j,B} \left(\psi_j^{n+1} + \psi_j^{n+1/2}\right). \tag{2.17}$$

The formal solution to (2.17) is

$$\psi_j^{n+1} = \mathcal{O}_{CN}(H_{j,B})\psi_j^{n+1} \equiv \frac{1 - \mathrm{i}\Delta t H_{j,B}/2}{1 + \mathrm{i}\Delta t H_{j,B}/2} \psi_j^{n+1/2}, \tag{2.18}$$

which combine with equation (2.7) provides

$$\Psi^{n+1} = \mathcal{O}_{CN}(H_{j,B})\mathcal{O}_{nd}(\mathbf{M})\Psi^n, \tag{2.19}$$

where $j = \uparrow, \downarrow$, $\mathcal{O}_{CN}$ represents the time-evolution operation with $H_{j,B}$ and suffix 'CN' indicates the Crank-Nicolson algorithm. Operation $\mathcal{O}_{CN}$ is used to propagate the intermediate solution $\psi_j^{n+1/2}$ by the time step Δt to generate the solution ψ_j^{n+1} at the next time step $t_{n+1} = (n+1)\Delta t$.

The numerical integration of the derivative parts (2.3b) and (2.5b) are performed with semi-implicit Crank-Nicolson scheme [157, 163]. Using the semi-implicit CN scheme, the equations (2.3b) and (2.5b) can be mapped onto N_x one-dimensional spatial grids along x. The discretization of those equations along the spatial grid point x is as follows [157–160, 156]:

$$\begin{aligned}\frac{\mathrm{i}\left(\psi_{\uparrow,k}^{n+1} - \psi_{\uparrow,k}^{n+1/2}\right)}{\Delta t} =& \frac{-1}{4h_x^2}\left[\left(\psi_{\uparrow,k+1}^{n+1} - 2\psi_{\uparrow,k}^{n+1} + \psi_{\uparrow,k-1}^{n+1}\right) + \left(\psi_{\uparrow,k+1}^{n+1/2} - 2\psi_{\uparrow,k}^{n+1/2} + \psi_{\uparrow,k-1}^{n+1/2}\right)\right] \\ & - \frac{\mathrm{i}k_L}{4h_x}\left[\left(\psi_{\uparrow,k+1}^{n+1} - \psi_{\uparrow,k-1}^{n+1}\right) + \left(\psi_{\uparrow,k+1}^{n+1/2} - \psi_{\uparrow,k-1}^{n+1/2}\right)\right], \end{aligned} \tag{2.20}$$

$$\begin{aligned}\frac{\mathrm{i}\left(\psi_{\downarrow,k}^{n+1} - \psi_{\downarrow,k}^{n+1/2}\right)}{\Delta t} =& \frac{-1}{4h_x^2}\left[\left(\psi_{\downarrow,k+1}^{n+1} - 2\psi_{\downarrow,k}^{n+1} + \psi_{\downarrow,k-1}^{n+1}\right) + \left(\psi_{\downarrow,k+1}^{n+1/2} - 2\psi_{\downarrow,k}^{n+1/2} + \psi_{\downarrow,k-1}^{n+1/2}\right)\right] \\ & + \frac{\mathrm{i}k_L}{4h_x}\left[\left(\psi_{\downarrow,k+1}^{n+1} - \psi_{\downarrow,k-1}^{n+1}\right) + \left(\psi_{\downarrow,k+1}^{n+1/2} - \psi_{\downarrow,k-1}^{n+1/2}\right)\right], \end{aligned} \tag{2.21}$$

and rewrite as

$$\psi_{\uparrow,k}^{n+1} - \psi_{\uparrow,k}^{n+1/2} = \frac{i\Delta t}{4h_x^2}\left[\left(\psi_{\uparrow,k+1}^{n+1} - 2\psi_{\uparrow,k}^{n+1} + \psi_{\uparrow,k-1}^{n+1}\right) + \left(\psi_{\uparrow,k+1}^{n+1/2} - 2\psi_{\uparrow,k}^{n+1/2} + \psi_{\uparrow,k-1}^{n+1/2}\right)\right] - \frac{k_L\Delta t}{4h_x}\left[\left(\psi_{\uparrow,k+1}^{n+1} - \psi_{\uparrow,k-1}^{n+1}\right) + \left(\psi_{\uparrow,k+1}^{n+1/2} - \psi_{\uparrow,k-1}^{n+1/2}\right)\right], \tag{2.22}$$

$$\psi_{\downarrow,k}^{n+1} - \psi_{\downarrow,k}^{n+1/2} = \frac{i\Delta t}{4h_x^2}\left[\left(\psi_{\downarrow,k+1}^{n+1} - 2\psi_{\downarrow,k}^{n+1} + \psi_{\downarrow,k-1}^{n+1}\right) + \left(\psi_{\downarrow,k+1}^{n+1/2} - 2\psi_{\downarrow,k}^{n+1/2} + \psi_{\downarrow,k-1}^{n+1/2}\right)\right] + \frac{k_L\Delta t}{4h_x}\left[\left(\psi_{\downarrow,k+1}^{n+1} - \psi_{\downarrow,k-1}^{n+1}\right) + \left(\psi_{\downarrow,k+1}^{n+1/2} - \psi_{\downarrow,k-1}^{n+1/2}\right)\right], \tag{2.23}$$

where $\psi_{\uparrow,k}^{n} \equiv \psi_{\uparrow}(x_k, t_n)$ and $\psi_{\downarrow,k}^{n} \equiv \psi_{\downarrow}(x_k, t_n)$ represent the up and down components of the condensate, respectively, at spatial point x_k and at time t_n. For the discretization along x, we choose $x_k = -N_x h_x/2 + kh_x$, $k = 0, 1, 2, \ldots, N_x$ where N_x is the total number of grids in the x-direction and h_x is the spatial step. The above equations are essentially a set of algebraic equations of $\psi_{\uparrow,k+1}^{n+1}$, $\psi_{\uparrow,k}^{n+1}$, $\psi_{\uparrow,k-1}^{n+1}$, $\psi_{\downarrow,k+1}^{n+1}$, $\psi_{\downarrow,k}^{n+1}$ and $\psi_{\downarrow,k-1}^{n+1}$ at time t_{n+1}, which are solved using the closed boundary conditions. After rearranging the algebraic equations originating from [Eq.(2.22)- (2.23)] can written explicitly in a tri-diagonal matrix form [156, 160, 161],

$$A_k^- \psi_{\uparrow,k-1}^{n+1} + A_k^0 \psi_{\uparrow,k}^{n+1} + A_k^+ \psi_{\uparrow,k+1}^{n+1} = b_k, \tag{2.24a}$$

$$D_k^- \psi_{\downarrow,k-1}^{n+1} + D_k^0 \psi_{\downarrow,k}^{n+1} + D_k^+ \psi_{\downarrow,k+1}^{n+1} = d_k, \tag{2.24b}$$

where $A_k^0 = D_k^0 = 1 + i\Delta t/(2h_x^2)$, $A_k^+ = D_i^- = k_L\Delta t/(4h_x) - i\Delta t/(4h_x^2)$, and $A_k^- = D_k^+ = -k_L\Delta t/(4h_x) - i\Delta t/(4h_x^2)$ and

$$b_k = \frac{i\Delta t}{4h_x^2}\left(\psi_{\uparrow,k+1}^{n+1/2} - 2\psi_{\uparrow,k}^{n+1/2} + \psi_{\uparrow,k-1}^{n+1/2}\right) - \frac{k_L\Delta t}{4h_x}\left(\psi_{\uparrow,k+1}^{n+1/2} - \psi_{\uparrow,k-1}^{n+1/2}\right) + \psi_{\uparrow,k}^{n+1/2}, \tag{2.25a}$$

$$d_k = \frac{i\Delta t}{4h_x^2}\left(\psi_{\downarrow,k+1}^{n+1/2} - 2\psi_{\downarrow,k}^{n+1/2} + \psi_{\downarrow,k-1}^{n+1/2}\right) + \frac{k_L\Delta t}{4h_x}\left(\psi_{\downarrow,k+1}^{n+1/2} - \psi_{\downarrow,k-1}^{n+1/2}\right) + \psi_{\downarrow,k}^{n+1/2}. \tag{2.25b}$$

All quantities in b_k and d_k are referred to the time step $t_{n+1/2}$, which are known from the evolution using the non-derivative part of the Hamiltonian. The unknowns in Eq. (2.23) are the quantities like $\psi_{\uparrow,k\pm1}^{n+1}$, $\psi_{\uparrow,k}^{n+1}$, $\psi_{\downarrow,k\pm1}^{n+1}$ and $\psi_{\downarrow,k}^{n+1}$ at time step t_{n+1} which can be obtained by term using the forward recursion relation given by

$$\psi_{j,k+1}^{n+1} = \alpha_{j,k}\psi_{j,k}^{n+1} + \beta_{j,k}, \tag{2.26}$$

where, $j \equiv \{\uparrow, \downarrow\}$, and $\alpha_{j,k}$, $\beta_{j,k}$ are the coefficients that needs to be calculated. Substituting equation (2.26) in the equation (2.23) yields the solution given by,

$$\psi_{\uparrow,k}^{n+1} = \gamma_{\uparrow,k}(A_k^- \psi_{\uparrow,k-1}^{n+1} + A_k^+ \beta_{\uparrow,k} - b_k), \tag{2.27a}$$
$$\psi_{\downarrow,k}^{n+1} = \gamma_{\downarrow,k}(D_k^- \psi_{\downarrow,k-1}^{n+1} + D_k^+ \beta_{\downarrow,k} - d_k), \tag{2.27b}$$

with

$$\gamma_{\uparrow,k-1} = -1/(A_k^0 + A_k^+ \alpha_{\uparrow,k}), \tag{2.28a}$$
$$\gamma_{\downarrow,k-1} = -1/(D_k^0 + D_k^+ \alpha_{\downarrow,k}), \tag{2.28b}$$

$$\alpha_{\uparrow,k-1} = \gamma_{\uparrow,k} A_k^-, \qquad \beta_{\uparrow,k-1} = \gamma_{\uparrow,k}(A_k^+ \beta_{\uparrow,k} - b_k) \tag{2.29a}$$
$$\alpha_{\downarrow,k-1} = \gamma_{\downarrow,k} A_k^-, \qquad \beta_{\downarrow,k-1} = \gamma_{\downarrow,k}(D_k^+ \beta_{\downarrow,k} - d_k). \tag{2.29b}$$

By applying the recursion relations (2.27), (2.28), and (2.29), we compute the coefficients $\alpha_{j,k}$ and $\beta_{j,k}$, where the index k runs from $N_x - 2$ down to 0. The initial values are set as $\alpha_{N_x-1} = 0$ and $\beta_{j,N_x-1} = \psi_{j,N_x}^{n+1}$. Once the coefficients $\alpha_{j,k}$, $\beta_{j,k}$, and $\gamma_{j,k}$ are obtained, the solution is constructed using the relation (2.26) across the spatial domain, progressing from 0 to $N_x - 1$, while enforcing closed boundary conditions [156]. In particular, the wavefunction at the first spatial grid point is known from the boundary condition: $\psi_0^{n+1} = 0$, and it also vanishes at the final lattice point.

For direct real-time propagation, the initial wavefunction at $t = 0$ is typically selected as the analytically known ground state of the harmonic potential in the absence of interactions, i.e., with $g_{\uparrow\uparrow(\downarrow\downarrow)} = g_{\uparrow\downarrow(\downarrow\uparrow)} = 0$. As time evolves, the interaction strength is gradually increased at a very slow (adiabatic) rate until the desired nonlinearity is reached. Alternatively, for more complex potential landscapes or to achieve faster convergence, it is often advantageous to first obtain the ground state via imaginary-time propagation. The resulting converged wavefunction can then be used as the initial condition for real-time propagation to study the system's dynamical behavior.

In our work, to investigate the dynamical behavior of the condensate, we implement interaction quenching in a scalar Bose–Einstein condensate (BEC) after obtaining the interacting ground state. Furthermore, to examine the stability of both localized and delocalized condensate states, a velocity perturbation is introduced by imparting equal and opposite velocities to the spin-up and spin-down components of the con-

densate.

2.1.2 Imaginary-time propagation

The imaginary-time propagation method is employed to obtain a converged ground-state solution of the Gross–Pitaevskii equations (GPEs). In this approach, the real time t in the GPE is replaced with an imaginary time by the transformation $t \to -\mathrm{i}t$, and $\Delta t \to -\mathrm{i}\Delta t$. This substitution modifies the wavefunctions from $\psi_j(x,t) = \psi_{j,0}(x)\exp(-\mathrm{i}E_0 t)$ to $\psi_{j,0}(x)\exp(-E_0 t)$, resulting in exponential damping that drives the system towards the lowest-energy state [156]. This technique effectively filters out excited states, making it particularly suitable for identifying the ground state when the solution is unknown. For instance, in the presence of a disordered potential, the shape and position of the Bose–Einstein condensate (BEC) ground state are typically unknown. In such cases, imaginary-time propagation proves to be a powerful and reliable tool for accurately determining the ground state.

By changing the time into imaginary-time ($t \to -\mathrm{i}t$), the dynamical equations Eq. (2.7), (2.10), (2.11), and (2.16) can be modified as follows,

$$-\frac{\partial}{\partial t}\Psi^n = \mathcal{O}_{nd}(\mathbf{M})\Psi^n, \tag{2.30}$$

$$-\frac{\partial}{\partial t}\Psi^{n+1/2} = (\mathbf{M}_{\mathrm{diag}})\Psi^n, \tag{2.31}$$

$$\begin{pmatrix}\psi_\uparrow^{n+1/2}\\ \psi_\downarrow^{n+1/2}\end{pmatrix} = \begin{pmatrix}\exp\left(-\Delta t H_{\uparrow,A1}\right) & 0\\ 0 & \exp\left(-\Delta t H_{\downarrow,A1}\right)\end{pmatrix}\begin{pmatrix}\psi_\uparrow^{n}\\ \psi_\downarrow^{n}\end{pmatrix}, \tag{2.32}$$

and

$$\begin{pmatrix}\psi_\uparrow^{n+1/2}\\ \psi_\downarrow^{n+1/2}\end{pmatrix} = \begin{pmatrix}\cos(-\mathrm{i}\Omega\Delta t) & -\mathrm{i}\sin(-\mathrm{i}\Omega\Delta t)\\ -\mathrm{i}\sin(-\mathrm{i}\Omega\Delta t) & \cos(-\mathrm{i}\Omega\Delta t)\end{pmatrix}\begin{pmatrix}\psi_\uparrow^{n}\\ \psi_\downarrow^{n}\end{pmatrix}. \tag{2.33}$$

Subsequently, the equations (2.3b) and (2.5b) can be discretized similarly to real-

time propagation.

$$-\frac{\partial \psi_\uparrow}{\partial t} = -\frac{1}{2}\frac{\partial^2 \psi_\uparrow}{\partial x^2} - \mathrm{i}k_L \frac{\partial \psi_\uparrow}{\partial x} \equiv H_{\uparrow,B}\psi_\uparrow, \tag{2.34}$$

$$-\frac{\partial \psi_\downarrow}{\partial t} = -\frac{1}{2}\frac{\partial^2 \psi_\downarrow}{\partial x^2} + \mathrm{i}k_L \frac{\partial \psi_\downarrow}{\partial x} \equiv H_{\downarrow,B}\psi_\downarrow. \tag{2.35}$$

After obtaining the ground state of the condensate, the converged wavefunction can be utilized to investigate the non-equilibrium dynamics through real-time propagation. During imaginary-time propagation, the energy of the system decreases exponentially, which in turn causes the total number of atoms to decay over time iterations. To prevent this loss of the total number of atoms, one needs to normalize the condensate wavefunctions at each iteration while doing imaginary-time propagation. The normalization condition is given by

$$\int_{-L}^{L} |\psi_\uparrow(x)|^2 + |\psi_\downarrow(x)|^2 dx = N, \tag{2.36}$$

where the spatial domain is discretized over the system size $x \in [-L, L]$, with $L = (N_x/2)h_x$. In our work, we choose the total number of atoms to be normalized at $N = 1$.

2.1.2.1 Extension of semi-implicit CN method for scalar GP equation

As our study involves the localization of quasi-1D scaler BEC, we extend very briefly of the aforementioned Crank-Nicolson method for 1D scaler GP equation. Therefore, the scaler GP dynamical equation (Eq. (1.49) from chapter 1) can be defined as,

$$\mathrm{i}\frac{\partial \psi(x,t)}{\partial t} = \left[-\frac{1}{2}\frac{\partial^2}{\partial x^2} + V_{\mathrm{ext}}(x) + g|\psi(x,t)|^2\right]\psi(x,t) \tag{2.37}$$

Here, the *non-derivative* and *derivative* part contains $H_{\mathrm{nd}} = V_{\mathrm{ext}}(x) + g|\psi(x,t)|^2$, and $H_{\mathrm{d}} = -\frac{1}{2}\frac{\partial^2}{\partial x^2}$, respectively. Next, the non-derivative part can be numerically integrated using

$$\psi^{n+1/2} = \exp(-\mathrm{i}H_{\mathrm{nd}}\Delta t)\psi^n, \tag{2.38}$$

and the derivative part can be written as,

$$\frac{\psi^{n+1}-\psi^{n+1/2}}{-\mathrm{i}\Delta t}=\frac{1}{2}H_{\mathrm{d}}\left(\psi^{n+1}+\psi^{n+1/2}\right), \tag{2.39}$$

where the terms can be written explicitly as,

$$\frac{\mathrm{i}\left(\psi_k^{n+1}-\psi_k^{n+1/2}\right)}{\Delta t}=\frac{-1}{4h_x^2}\left[\left(\psi_{k+1}^{n+1}-2\psi_k^{n+1}+\psi_{k-1}^{n+1}\right)+\left(\psi_{k+1}^{n+1/2}-2\psi_k^{n+1/2}+\psi_{k-1}^{n+1/2}\right)\right]. \tag{2.40}$$

The CN coefficients can be calculated using a similar recursion relation (2.27) as the SO coupled GPEs. Finally, the time-propagated wavefunction can be written as,

$$\psi^{n+1}=\mathcal{O}_{CN}(H_{\mathrm{d}})\mathcal{O}_{nd}(H_{\mathrm{nd}})\psi^{n}. \tag{2.41}$$

For the imaginary-time propagation, we use a similar transformation as $t\rightarrow -\mathrm{i}t$, and $\Delta t\rightarrow -\mathrm{i}\Delta t$ with the normalization condition,

$$\int_{-L}^{L}|\psi(x)|^2dx=1. \tag{2.42}$$

2.1.3 Convergence of ground state

dx	dt	μ	x_{rms}
0.1	0.01	−1.526689	0.50996
0.08	0.005	−1.526689	0.50814
0.06	0.001	−1.522443	0.50669
0.05	0.0005	−1.522294	0.50647
0.025	0.0001	−1.522296	0.50623
0.01	0.0001	−1.522299	0.50619

Table 2.1: Demonstration of convergence of simulation runs for different dx and dt for localized phase of a condensate. The imaginary-time scheme has been used to obtain the SO-coupled localized condensate with parameters $\Omega=1.0, k_L=1$. Here, we have used the external potential as a 1D-quasiperiodic potential of the form, $V_{\mathrm{ext}}(x)=-V_1\cos(k_1x)-V_2\cos(k_2x)$, where $V_1=1.0, V_2=0.5, k_1=2.0, k_2=\sqrt{5}+1$. The chemical potential (μ) and rms size of condensate (x_{rms}) show convergence upto four decimal places upon decreasing the $dx\lesssim 0.05$.

To demonstrate the effectiveness of the split-step Crank–Nicolson (CN) method employing both imaginary- and real-time propagation for determining the ground state and dynamics of the condensate, in this section we present an example focused on

the convergence of the ground state. This example explores how different spatial and temporal step sizes affect the results. Convergence is evaluated primarily through the chemical potential μ and the root-mean-square (rms) size x_{rms} of the condensate

First, we consider the localized SO and Rabi coupled condensate confined in a quasiperiodic potential of the form, $V_{\text{ext}}(x) = -V_1\cos(k_1 x) - V_2\cos(k_2 x)$, where $V_1 = 1.0, V_2 = 0.5, k_1 = 2.0, k_2 = \sqrt{5}+1$ and other parameters $\Omega = 1.0, k_L = 1.0$. We choose a Gaussian profile with an antisymmetric initial condition as $\psi_\uparrow(x) = -\psi_\downarrow$ to obtain the ground state. By using the imaginary-time propagation scheme, we use different values of spatial (dx) and time steps (dt) as described in Table 2.1 to test the convergence of the ground state. Here, the values of dx and dt have been followed the Courant-Friedrichs-Lewy (CFL) condition ($dt/dx^2 \lesssim 1$).

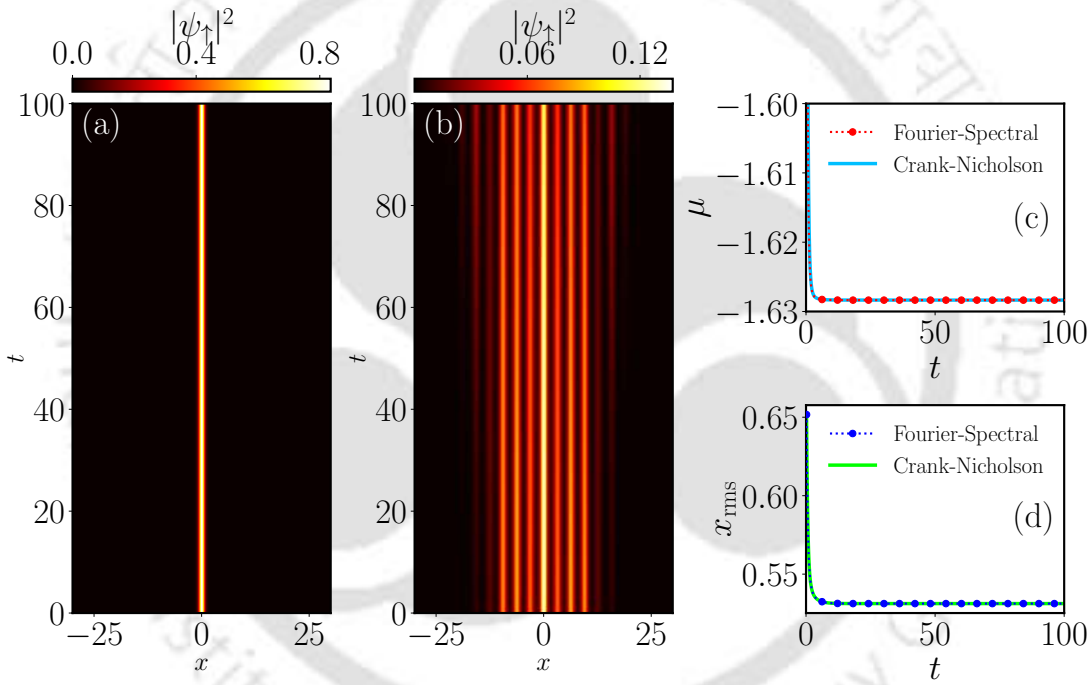

Figure 2.2: Spatio-temporal evolution of (a) localized and (b) delocalized condensate at $k_L = 1.0, \Omega = 1$, and $k_L = 0.6, \Omega = 1$, respectively. The temporal evolution of (c) chemical potential (μ) and (d) rms size (x_{rms}) of the localized condensate. The temporal evolution shows the convergence of the localized ground state.

We find that for $dx \lesssim 0.05$, the chemical potential μ and the root-mean-square (rms) size (x_{rms}) of the condensate remain unchanged. Following this convergence, for most of our simulation runs presented in the paper, we choose the spatial step ($dx = 0.025$) and time step ($dt = 0.0001$) for the Imaginary as well as real-time propagation.

In Fig. 2.2, we present the spatio-temporal evolution of the condensate density for both localized (Fig. 2.2(a)) and delocalized states (Fig. 2.2(b)). Additionally, we also

compare the time evolution of the μ, and x_{rms} showing the convergence with time. Also, we compare our results with *split-step Fourier spectral method* [161]. The corresponding spatio-temporal evolution of the localized condensate density (in (a)) shows stability with time. Similarly, the delocalized condensate also remains stable with time.

2.2 Summary and Conclusion

In this chapter, we have discussed the numerical technique employed to solve the dimensionless one-dimensional SO- and Rabi-coupled GPEs, as well as the scalar GPE. A brief overview of the split-step Crank–Nicolson (CN) method has been provided, outlining the steps involved in obtaining the ground state via imaginary-time propagation and studying the dynamics through real-time propagation. Additionally, we have presented an example showcasing the grid independence and convergence of ground states across different phases of the condensate confined in a quasiperiodic trap.

Chapter 3

Quench induced chaotic dynamics of Anderson localized interacting Bose-Einstein condensates

In this chapter, we present the effect of interactions on ground-state localization and corresponding dynamics of scalar BECs confined in one-dimensional quasiperiodic and random disordered potentials. The increase in atomic interaction leads to delocalization of the exponentially localized condensate, as the interaction increases beyond a threshold value. We inspect the localized and delocalized states by perturbing the system via quenching the interaction strength instantaneously to zero and studying the dynamics of the condensate, which we further corroborate using the out-of-time-order correlator. The temporal behaviour of the time correlator displays regular dynamics for the localized state, while it shows temporal chaos for the delocalized state. We confirm this dynamical behaviour by analyzing the power spectral density of the time correlator. We further identify that the condensate admits a quasiperiodic route to chaotic dynamics for both potentials. Through this, we establish the strong connection between the spatially delocalized state of the condensate and its temporal chaos.

The Chapter is organized as follows. First we present a very brief introduction including the motivation of the work presented in this Chapter. Further, we provide the details of different quantities like time correlator function, Lyapunov exponent, etc., which are especially used to characterize the dynamical behaviour of the localized and delocalized states. Following this, we present a detailed numerical simulation results based on the mean-field Gross-Pitaevskii model. The work presented in the Chapter is published in Physical Review A [164].

3.1 Introduction

The introduction related to Anderson Localization (AL) in Bose-Einstein condensates (BECs) has been extensively discussed in Chapter 1. However, to make this chapter self-contained, in this section, we provide a brief overview that emphasizes the role of mean-field interactions on localized condensates and associated dynamics of the condensates. After realizing the AL in ultracold atomic BECs in quasiperiodic [165], and random [21] disordered potentials, this topic has motivated various theoretical and numerical works to understand the effect of atomic interactions and disorder in presence of quasiperiodic [22, 166, 120, 167–170, 128, 171] and random speckle potential [172, 126, 173, 174, 130]. Overall, it has been reported that the interaction leads to the destruction of the exponential localization of a condensate, whereas the disorder tries to localize it. In this context, the experimental work in Ref. [175] showed the destruction of localization due to the effect of interactions in BECs. Few other works also examined the subdiffusive nature of the delocalized state [176, 25, 175]. Subsequently, in 3D disordered potential, Cherroret *et al.* [177] demonstrated that even weak interactions among particles can disrupt the transition from the subdiffusive regime to the transport inhibited regime, which is known as the Anderson transition.

On the other hand, considerable attention has been paid to understanding the out-of-equilibrium dynamics of matter waves. Several studies have been conducted associated with the dynamics of a BEC released from an external trap in different scenarios. For instance, Doggen and Kinnunen reported the transition from the localized to the delocalized state by quenching the nonlinearity from a finite value to zero [139]. Efforts have also been made to understand the dynamics of the localized BEC trapped in disordered optical lattices. In this context, several wealth of novel scenarios has been explored for both interacting and non-interacting condensates trapped in disordered potentials. Like, Damski *et al.* [140] reported the dynamical phase transition from a superfluid to Bose-glass for interacting condensates trapped under a 2D speckle potential. Sánchez-Palencia *et al.*[23] showed the existence of AL in the case of an expanding condensate in the presence of a random speckle potential. Their study further revealed two different regimes of localization: exponential and algebraic, depending on the relation between the condensate's healing length and the correlation length of the disordered potential. Subsequently, they have extended it for quasiparticles for interacting condensates[118]. At that same time, Shapiro [119] analyzed the similar expansion dynamics of a two-dimensional interacting condensate trapped in random speckle disorder. He showed the advantage of controlling the dynamics using the

chemical potential and time scale of the GP equation.

The dynamical evolution of Bose-Einstein condensates (BECs) also unveiled a strong connection between chaos and the interplay of interactions and disorder in the system [30, 141–143]. Brezinova *et al.* [30] demonstrated that, in time-of-flight experiments, the expansion dynamics of a BEC exposed to periodic or aperiodic potentials (such as quasiperiodic, random disorder) can exhibit chaotic behaviour once the disorder strength exceeds a critical threshold. In this work, we also aim to demonstrate a similar chaotic nature of the condensate by suddenly quenching the nonlinearity of the condensate to zero. The out-of-equilibrium dynamics is primarily generated in such systems by releasing the BECs from the trap [23, 175], by performing a partial quenching [27] of interactions [29]. However, in the case of random potential where the localization state contains more complex phases, like the Bose-glass phase, the Lifshitz phase, etc., distinguishing the localized to delocalized phase transition is more challenging, and to the best of our knowledge, it has not been done comprehensively.

In this work, we use a slightly different protocol to analyze the localized and delocalized states of the BEC in the presence of the quasiperiodic and random potential. After obtaining the interacting ground state, we apply the complete cessation of the nonlinear interactions. This process initiates the temporal dynamics of the condensate, which has been systematically captured by examining different entities: the time correlator function, power spectral density, and the Lyapunov exponent. By using the time correlator function, we observe that the localized state exhibits periodic or quasiperiodic oscillations with time, while the delocalized state exhibits chaotic dynamics. Therefore, by studying the dynamics of the correlation function of condensate, we provide a robust tool to characterize the localized and delocalized states using a dynamical approach.

The Chapter is organized as follows: In Sec. 3.2, we formulate the mean-field model with a quasi-1D scalar GP equation and numerical simulation details. It is followed by a brief description of different physical observables of interest in Sec. 3.3 to capture the condensate dynamics and to characterize different phases of the condensate. In Sec. 3.4, we present the numerical results on delocalization of the localized condensate for both quasiperiodic and random disordered potentials. In both cases, we first analyze the effect of interactions on the ground state, which is followed by the quenching dynamics of the condensate. Finally, we conclude our work in Sec. 3.5.

3.2 Mean-field Gross-Pitaevskii model for scalar BEC

We consider the condensates confined in strong transverse confinement, which can be modeled using the non-dimensional 1D GPEs as [22]:

$$\mathrm{i}\frac{\partial\psi(x,t)}{\partial t} = \left[-\frac{1}{2}\frac{\partial^2}{\partial x^2} + V(x) + g\,|\psi(x,t)|^2\right]\psi(x,t), \tag{3.1}$$

where, $V(x)$ is the trapping potential, $g = 2a_sN/a_\perp^2$ with a_s being the s-wave scattering length is the nonlinearity, N being the total number of atoms in the condensate and $a_\perp$ is the length scale corresponding to the transverse harmonic confinement [126]. We have chosen the transverse harmonic length $a_\perp = \sqrt{\hbar/(m\omega_\perp)}$ as the characteristic length scale with $\omega_\perp$ being the transverse trap frequency, $\omega_\perp^{-1}$ as the characteristic timescale, and $\hbar\omega_\perp$ as the characteristic energy scale of the condensate, where m is the mass of an atom, to obtain the non-dimensionalized Eq. (5.2). The wave function is re-scaled as $\psi(x,t) = a_\perp^{1/2}\tilde{\psi}(x,t)$, where $\tilde{\psi}(x,t)$ is the non-dimensionalized wave function. For brevity, we have omitted the tilde sign over the non-dimensionalized wave function.

In this study, we have separately considered the trapping potential $V(x)$ as a quasiperiodic and random disordered potential to analyze the characteristics and dynamics of the localization of the condensates. In experiments, the quasiperiodic potential can be realized as a superposition of two counter-propagating laser beams of slightly different wavelengths, which takes the form as [20]

$$V(x) = \frac{4\pi^2 s_1}{\lambda_1^2}\cos^2\left(\frac{2\pi}{\lambda_1}x\right) + \frac{4\pi^2 s_2}{\lambda_2^2}\cos^2\left(\frac{2\pi}{\lambda_2}x\right), \tag{3.2}$$

where s_1 and s_2 denote the amplitude of the primary and secondary lattice, respectively. Following the experimental consideration of the primary and secondary optical lattice wavelengths as $\lambda_1 = 1032\,\mathrm{nm}$ and $\lambda_2 = 862\,\mathrm{nm}$ respectively, we take the ratio of the non-dimensional wave length (in terms of $a_\perp \approx 1\mu\mathrm{m}$) as $\hat{\lambda}_2/\hat{\lambda}_1 \approx 0.86$ for all our simulation runs [22].

To understand the resemblance of this localization and associated dynamical behaviour with the ones in the presence of random potential, we have considered the random disordered potential consisting of N_s identical spikes randomly distributed

along the x-axis [178, 84] with a form

$$V(x) = V_0 \sum_{j=1}^{N_s} h(x - x_j), \tag{3.3}$$

where V_0 is the strength of the spike, $h(x - x_j)$ is the potential of the spike at position x_j. The spike potential is considered to have the form of a Gaussian in space with width σ as [178]

$$h(x) = \frac{1}{\sigma\sqrt{\pi}} \exp\left(-\frac{x^2}{\sigma^2}\right). \tag{3.4}$$

The auto-correlation of $V(x)$ is denoted as,

$$C(d) = \langle V(x)V(x+d)\rangle - \langle V(x)\rangle^2, \tag{3.5}$$

where $\langle V(x)\rangle$ is the mean of the potential defined as,

$$\langle V(x)\rangle \equiv \frac{1}{2L}\int_{-L}^{L} V(x)dx = \frac{V_0}{D}, \tag{3.6}$$

with D as the average spacing between the spikes. Here, the correlation length and correlation energy can be estimated by giving a fit to $C(d)$ (Eq. 3.5) with a Gaussian function of the form

$$C(d) \approx V_R^2 \exp\left(-d^2/\sigma_R^2\right), \tag{3.7}$$

where amplitude V_R represents correlation energy and σ_R represents the correlation length. To generate the potential we select $N_s = 300$, $L = 30$, and width $\sigma = 0.1$. In this case, the value of correlation energy is $V_R = 4.3974$ and $\sigma_R(\approx \sqrt{2}\sigma) = 0.1340$.

3.3 Approach to characterize the dynamics of the localized state

In this section, we provide the details of the theoretical approach that we have used to characterize the dynamics of the localized state.

3.3.1 Time correlation function and Power spectral density

For our analysis, we use the time correlation function to characterize the dynamics of the different states. Once we obtain the ground state, we investigate the dynamics of the condensate by a sudden quenching of the nonlinearity of the condensate. The time correlator function is defined in terms of the absolute value of the overlap function as

$$c(t) = |\langle \psi(x,0)| \, |\psi(x,t)\rangle| \,, \tag{3.8}$$

where $\psi(x,0)$ represents the ground state obtained using imaginary time propagation with respect to repulsive interaction parameters. For convenience, we treat this wave function at reference time $t = 0$. After obtaining the ground state $\psi(x,0)$ we quench the nonlinearity to zero in the next time step (dt) and evolve the state using the GPE (Eq. 5.2) and obtain the evolved wave function at time t as $\psi(x,t)$ with zero nonlinearity. Here $< . >$ denotes the average over the entire space. The $c(t)$ can be expressed in a more explicit manner as,

$$c(t) = \left| \int |\psi(x,0)|^2 \exp(-i\phi(x,t)) dx \right| \tag{3.9}$$

where $\phi(x,t)$ is the phase picked up by the ground state wave function $\psi(x,0)$ upon time evolution. The time correlator function can be viewed as the integration of the phase acquired by the quenched state over the whole spatial points at time t. There are several laboratory experiments that suggest a direct measurement of the phase acquired by the condensate using the atom interferometry [179–181]. Once the phase difference ϕ acquired by the quenched condensate is determined, the $c(t)$ can be calculated using Eq. 3.9.

In general, the value of transverse frequency is $\omega_\perp = 2\pi \times 70$ Hz in a typical experiment [21]. Using this frequency strength, if we convert the real time corresponding to one time step of our simulation which is $dt = 5 \times 10^{-4}$, we find that it comes out to be $dt \sim 1.13\mu s$. Therefore, the instantaneous quenching timescale in our simulation is of the order of $1.13\mu s$. However, in the laboratory experiments, the quench in the nonlinear interaction is achievable through the Feshbach resonance within a typical time of about 100 μs [182, 183]. We have verified our results by increasing the quenching timescale to 100 μs considered in the experiment; however, we could not find any significant change in the results presented in this Chapter.

To get a deeper understanding of the dynamics and, in particular, the chaotic dynamics of the delocalized state, we analyze the power spectral density (PSD) of the

$c(t)$, which is given by [184, 185],

$$\text{PSD} = \frac{1}{2\pi\mathcal{N}}|\hat{c}(\omega)|^2, \tag{3.10}$$

where $\hat{c}(\omega)$ is the discrete Fourier transform of the time correlator, $c(t)$ evaluated at $t = m\,dt$ ($m = 0, 1, \ldots, \mathcal{N}$, and $\mathcal{N}$ is the length of the discrete time series).

3.3.2 Lyapunov exponent

In our studies, we aim to establish a possible connection between delocalization and chaos, which we execute by computing the maximal Lyapunov exponent. In dynamical systems, Lyapunov exponents are defined as the mean rate of divergence of two nearby trajectories with time. In phase space, the rate of divergence of separation between two trajectories, with an infinitesimal initial separation $\delta\mathbf{X}_0$, can be computed as [30],

$$|\delta\mathbf{X}(t)| \approx e^{\lambda t}|\delta\mathbf{X}_0| \tag{3.11}$$

$$\lambda_{\max} = \lim_{t\to\infty}\frac{1}{t}\ln\frac{|\delta\mathbf{X}(t)|}{|\delta\mathbf{X}_0|} \tag{3.12}$$

If the exponent is positive ($\lambda_{max} > 0$), neighbouring trajectories diverge exponentially, which is a signature of the chaotic behaviour in the system.

In general, for the known sets of dynamical equations, the exponents can be easily computed by using the phase space trajectory of the variables. However, computation of the exponents directly from the time series is not so straightforward. The reconstruction of phase space from the time series data is mainly executed using the time delay τ [186] and the embedding dimension D [187]. We use the Average mutual information (AMI) method to estimate the τ from the time series of the time correlator function data, while the False nearest neighbour (FNN) method has been used to compute the D [188]. The details of AMI and FNN have been illustrated in the following. For our analysis, the usual time series of the correlator function $c(t)$ is represented in the phase space using τ and D. Further, we select a reference point on the phase space trajectory, which is used to measure its separation from the nearest neighbour point on the phase space. First, we store the information of initial separation in L_i, and as time progresses, the separation between the trajectories is computed until its value exceeds a threshold

ϵ. Typically, we consider the $\epsilon \sim \mathcal{O}(10^{-2})$. Thereafter, the Wolf algorithm [189] is used to evaluate the Lyapunov exponents, which have three control parameters, namely, D, τ, and the threshold value of length ϵ. The Lyapunov exponent is computed using,

$$\lambda_{\max} = \frac{1}{N\Delta t} \sum_{i=1}^{M-1} \log_2 \frac{L_i^{'}}{L_i} \tag{3.13}$$

where, N is the total number of reference points usually depends upon the number of data points present in the time series, Δt is the time step associated to the time correlator, L_i is the initial separation and $L_i^{'}$ corresponds to the final separation measured for i^{th} a segment of the phase space trajectory, M is the number of times the ratio of final to initial separation has been calculated to complete the reference trajectory. The reference trajectory can be defined as the line from where the calculation of L_i has started by searching for the nearest neighbour point from the reference point. As time progresses, the reference point also changes on the reference trajectory to calculate the next $L_i^{'}$. For our analysis, we consider the embedded dimension $D = 3$, time step Δt as 0.0005 for quasiperiodic potential and 0.001 for random disordered potential.

3.3.2.1 Selection criteria for the embedding dimension and delay time of time series of the correlation function

To get the embedding dimension and delay time, the first step involves reconstructing the phase space from the time series data. Let us assume we have a set of N discrete data points in the time series of the correlation function, given as $c_1, c_2, c_3, c_4, \ldots, c_N$. By considering the delay time τ and an embedding dimension D, we obtain the D-dimensional delay coordinate as $Y(\tilde{t}) = (c(\tilde{t}), c(\tilde{t}+\tau), \ldots, c(\tilde{t}+(D-1)\tau))$. Note that both $\tilde{t} \in [1, N]$ and $\tau \in [1, N]$ are integers used to index the time series data of $c(t)$; it can be mapped to the real time by multiplying the factor dt. Usually, the choice of τ is such that the values of $c(\tilde{t})$ and $c(\tilde{t}+\tau)$ are sufficiently independent to be a useful component of the time correlator vector $c(\tilde{t})$, but it should not be so independent that it has no connection at all. To choose the optimum value of τ, we calculate the average mutual information $I(\tau)$ of the variable $c(\tilde{t})$ and $c(\tilde{t}+\tau)$ for various values of τ given as [190].

$$I(\tau) = \sum_i \sum_j P_{i,j}(\tau) log_2 \frac{P_{i,j}(\tau)}{P_i P_j}. \tag{3.14}$$

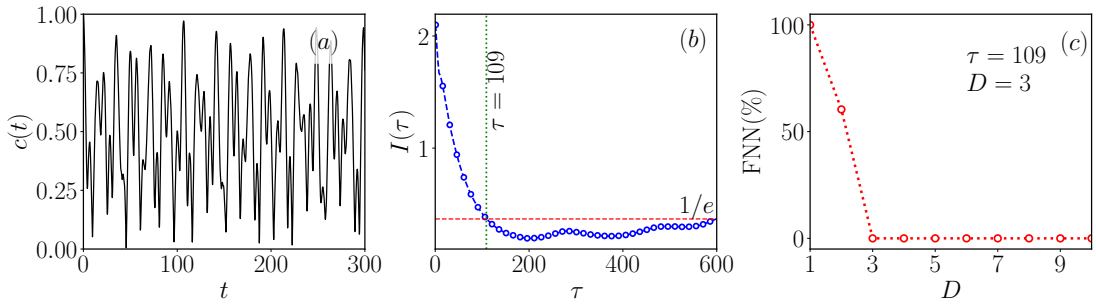

Figure 3.1: (a) Plot showing the temporal variation of the time correlator function $c(t)$ at $g = 9.0$ and $s_2/s_1 = 1.0$ (b) Variation of the average mutual information (AMI) with the time delay τ of $c(\tilde{t})$. Here, the value of the optimum time delay $\tau = 109$ is estimated using the $1/e$ fall of the AMI function. The red dotted line is drawn at $1/e$ as a guide for estimating the optimum value. (c) Variation of false nearest neighbours (FNN) with the embedding dimension D. Here, the optimum embedding dimension $D = 3$, at which point the FNN falls to first zero. Here, the time series $c(t)$ has dimension of time, average mutual information (AMI) and false nearest neighbour (FNN) is dimensionless quantity.

Here, P_i represents the probability that $c(\tilde{t})$ falls inside the i^{th} bin of the histogram constructed from the data points of c, and $P_{i,j}$ is the joint probability that $c(\tilde{t})$ and $c(\tilde{t}+\tau)$ should respectively come under the i^{th} and j^{th} bins of the histogram. Following this, the optimum τ is calculated by examining the value of τ at which $I(\tau)$ either achieves its first minimum [190] or drops below the value of $1/e$ [191]. Whichever criterion gives the minimum τ is chosen. This value of τ represents the delay time at which $c(\tilde{t}+\tau)$ contributes the maximum information to our knowledge of $c(\tilde{t})$. The next step is to determine the embedding dimension D, which can be estimated using the method of false nearest neighbours (FNN). In this process, we consider the data points that are neighbours to each other in the original one-dimensional time series of $c(\tilde{t})$. Then, we check the separation between these neighbours when the time series is embedded into a higher-dimensional space. If the embedding process significantly changes the distance between the neighbouring points, they are referred to as false neighbours, indicating the need to increase D. Therefore, the entire scheme is based on gradually increasing the embedding dimension D for the optimum τ, and for each value of D, computing the percentage of false neighbours with respect to the true neighbours. Only the value of D for which the number of FNN drops to 0 or subsequent increments in D leave the FNN unchanged is considered the optimum embedding dimension. Let's denote the i^{th} nearest neighbour of the coordinate vector $y(t)$ as $y^i(t)$. The separation between them can be represented in the D-dimensional phase space as

$$R_D^2(t,\tau) = \sum_{j=0}^{D-1} \left[c(\tilde{t}+\tau) - c^{(i)}(\tilde{t}+\tau)\right]^2. \tag{3.15}$$

Following the discussion mentioned above, as we go from a D-dimensional phase space to a $D+1$ dimensional phase space using time-delayed embedding, the separation between the i^{th} neighbours of a new vector $y(t)$ can be written as

$$R_{D+1}^2(\tilde{t},\tau) = R_D^2(\tilde{t},\tau) + \left[c(\tilde{t}+D\tau) - c^{(i)}(\tilde{t}+D\tau)\right]^2. \tag{3.16}$$

In Fig. 3.1, we demonstrate the calculation of τ and D using the chaotic time series of the time correlator obtained after the quenching of the ground state prepared for $g = 9.0$ and $s_2/s_1 = 1.0$, with other parameters being the same as those in Fig. 3.2. Following the method discussed above, we obtain the optimum τ and D as 109 and 3, respectively, for this case.

3.4 Results

Here, we provide detailed numerical results of ground states and their associated dynamics. For our present analysis, we consider the quasiperiodic potential (Eq. 6.3) and random disordered potential (Eq. 4.4) to investigate the dynamics of the Bose gas following a quench of the initial ground state (localized or delocalized). While the imaginary-time split-step Crank-Nicolson integration scheme is used for ground state preparation, post-quench dynamics is evolved using the real-time split-step Crank-Nicolson integration schemes [156, 192]. In imaginary time propagation, we have considered $dx = 0.025$ and $dt = 0.0005$ for the simulation of the condensate trapped in quasiperiodic potential, and for random disordered potential, we choose $dx = 0.04$ and $dt = 0.001$. For all simulations, we have used closed boundary conditions with $\psi_{boundary} = 0$. Also, we have performed the grid independence test by decreasing spatial resolution to $dx = 0.007$ and confirmed that all the results presented in the Chapter remain unchanged. The ground state for different nonlinearities has been obtained using an imaginary time propagation scheme in which the Gaussian wave packet centered at $x = 0$ has been chosen as an initial condition.

In the following, we first present our analysis of the condensate trapped in a quasiperiodic optical lattice, and then we will focus on the case of the random lattice.

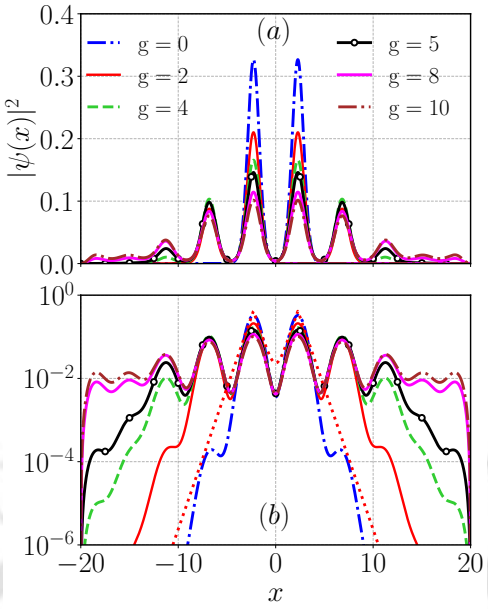

Figure 3.2: Variation of density with different nonlinearity for $\lambda_1 = 10$, $\lambda_2/\lambda_1 = 0.86$, $s_1 = 3$, and $s_2/s_1 = 1.0$ in the (a) linear and (b) semilog scale. The wave function gets localized near $x = 0$ for $g = 0$. As we increase the nonlinearity, it results in the spread of the wave function. In the localized states ($g = 0, 2, 4$), the condensate density exhibits an exponential tail. For $g \gtrsim 5$, the condensate gets spanned in the whole box, exhibiting a delocalized nature. In (b), the dotted red line represents the double exponential fit to the condensate ground state for $g = 0$.

3.4.1 Delocalization in presence of quasiperiodic optical lattice

In this subsection, we first explored the effect of nonlinearity on the localized state of condensates trapped in the bichromatic optical lattice potential. It is followed by an analysis of the dynamical characteristics of the condensates once we switch off the nonlinear interactions after having the ground state of the condensate. As mentioned before, in this case, we vary λ_1 while keeping the ratio $\lambda_2/\lambda_1 \simeq 0.86$ fixed in Eq. (6.3). This assumption has been made by following the experimental work of Roati *et al.* [20] where the value of transverse harmonic oscillator length is taken as $a_\perp \approx 1\,\mu$m, which yields $\lambda_1 \simeq 1.0$ and $\lambda_2 \simeq 0.86$. In our simulations, we consider the space step as 0.025, while we fix the time step as 0.0005 [22] and use the Gaussian wave packets centered around zero as an initial condition for all our simulations.

There are two ways through which the delocalization of the condensate trapped in the optical lattice potential can occur. One is to increase the nonlinear repulsive interaction, and the other is to decrease the disorder strength upon tuning the ratio of the laser amplitude s_2/s_1 [22, 30]. We begin by analyzing the effect of nonlinearity on the localized condensates. The ground states for different localized states for weak nonlinear interaction have already been analyzed by Adhikari and Salasnich [22]. As

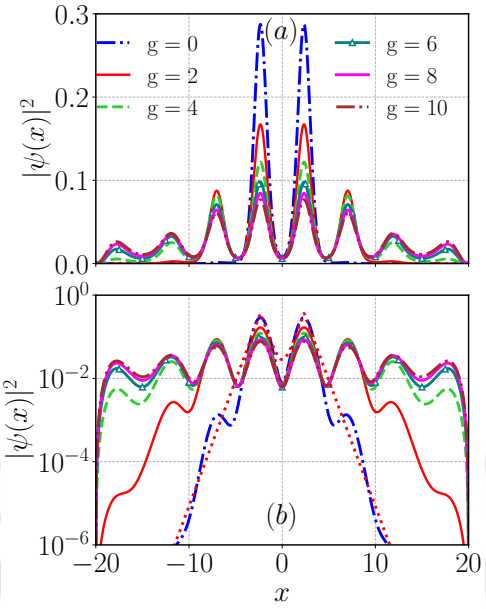

Figure 3.3: (a) Spatial profile of the condensate density for different nonlinearities at $s_2/s_1 = 0.5$. The other parameters are the same as those in Fig. 3.2. The condensate exhibits a localized nature for noninteracting cases ($g = 0$), which further shows delocalization upon increasing the nonlinearity ($g \gtrsim 4$). (b) Density variation in semilog scale for different nonlinearities. The dotted red line represents the double exponential fit to the condensate ground state for $g = 0$. The exponential fall of the condensate density around its center characterizes the localization behaviour. The density exhibits delocalized states with increasing nonlinearities.

we are interested in the analysis of the dynamics of these states, to make the manuscript self-contained, in the following, we briefly present the nature of different ground states for various nonlinearities.

In Fig. 3.2(a), we show the spatial distribution of the ground state density for different nonlinear interactions with $s_1 = 3.0$, $s_2/s_1 = 1.0$, and $\lambda_1 = 10$. It is easy to see that for the non-interacting case ($g = 0$), the condensate gets localized between $-5 \lesssim x \lesssim 5$ with the maximum density around $x \sim \pm 2$. As we increase the nonlinearity to $g = 2$, we notice a decrease in the density around the central region ($x \sim 0$), resulting in the appearance of peaks at larger values of x. However, the condensate appears to be confined between $-10 \lesssim x \lesssim 10$. Further, an increase in the nonlinearity to $g = 4$ results in an expansion of the localized condensate in the space. As the nonlinearity exceeds a threshold value ($g \gtrsim 5$), the matter wave localization gets destroyed, which is quite noticeable from the nature of the condensate that appears to get spanned in the whole box as shown for $g = 8$ (pink line) and $g = 10$ (brown line) in Fig. 3.2 (a). These features are more noticeable from the behaviour of the tail of the density profile that displays exponential fall in the localized state, a feature which is absent for the delocalized state [cf. Fig. 3.2(b)]. For comparison, we also undertake a similar analysis of the

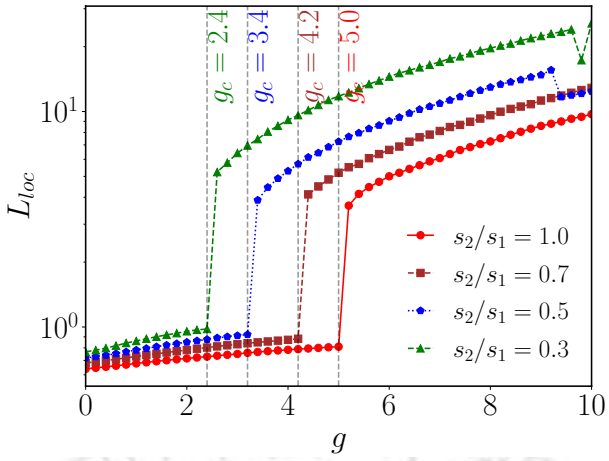

Figure 3.4: Variation of localization length (L_{loc}) with the nonlinearity for different s_2/s_1. The L_{loc} is calculated using the $1/e$ fall of the fitted curve $ae^{-|x-x_0|/L_{loc}} + ae^{-|x+x_0|/L_{loc}}$ with x_0 is point of maximum density in space. Here $x_0 = \pm 2.275$. L_{loc} starts increasing beyond g_c. The g_c increases upon increase upon an increase in s_2/s_1. The other parameters are the same as those in Fig. 3.2.

localization by lowering the strength of the quasiperiodic optical lattice to $s_2/s_1 = 0.5$. In Fig. 3.3, the spatial profile of the ground state of the matter wave density for different nonlinearities has been illustrated. We find that in this case also, the matter wave remains localized for low nonlinearity as expected. As we increase the nonlinearity, the condensate gets delocalized at a smaller g ($\gtrsim 4$) as compared to those for higher disorder strength ($s_2/s_1 = 1.0$), which happens at $g \gtrsim 5$.

To quantify this transition, we compute the localization length by fitting the localized states with the function $y = ae^{-|x-x_0|/L_{loc}} + ae^{-|x+x_0|/L_{loc}}$, where, L_{loc} is the localization length, a is the parameter and x_0 is the localization center. The variation of L_{loc} with respect to g is plotted in Fig. 3.4 for different values of s_2/s_1. We find that when the condensate is in the localized state, the L_{loc} varies linearly with g. However, a discontinuous jump occurs in L_{loc} for certain values of g, beyond which the delocalization happens in the density profile. The threshold value of the nonlinearity at which the delocalization occurs decreases when we decrease the disorder strength s_2/s_1.

To shed light on the transition of the condensate from the localized to the delocalized state, it is pertinent to include the relevant physical cause. To achieve this, we computed the energies of different components, such as the kinetic energy $E_k = \frac{1}{2}\int dx|\nabla\psi|^2$, potential energy $E_{pot} = \int V(x)|\psi|^2 dx$, and interaction energy $E_{int} = \frac{1}{2}\int g|\psi|^4 dx$, where ψ is the ground state wave function obtained by using imaginary time propagation of Eq. 5.2 with finite g. In Fig. 3.5, we present the variation of different energies, E_k (■), E_{int} (●), and E_{pot} (⬢), for different s_2/s_1. We observe that while E_{pot} and E_{int} increase, E_k decreases with an increase in g. Interestingly, we find that below

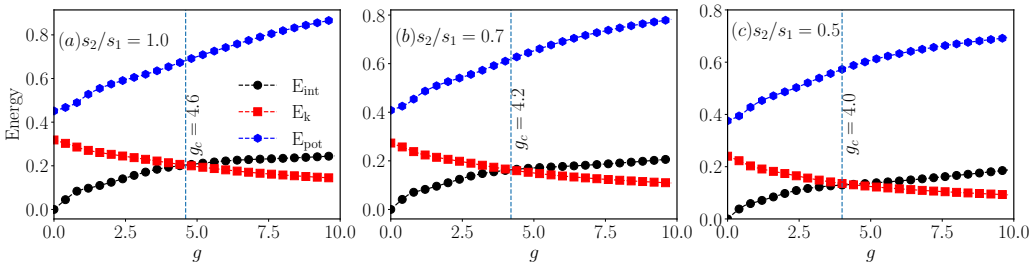

Figure 3.5: Variation of interaction E_{int}, kinetic E_k and potential E_{pot} energies with nonlinear interaction for different disorder strength: (a) $s_2/s_1 = 1.0$, (b) $s_2/s_1 = 0.7$, and (c)$s_2/s_1 = 0.5$. All the other parameters are the same as Fig. 3.2. In the localized regime, E_k dominates over E_{int}; however, in the delocalized regime, E_{int} dominates over E_k. The threshold nonlinear interaction (g_c) for different s_2/s_1 values are consistent with those obtained from the localization length. The vertical lines are drawn to guide the eyes for g_c.

the threshold value of the critical nonlinear strength (g_c), E_k dominates over E_{int}, while we observe the opposite trend above the critical g_c. This trend holds for all values of s_2/s_1 considered.

In the following, we will analyze the characteristics of these states using their dynamical evolution.

3.4.1.1 Quench dynamics of the localized and delocalized states

To study the detailed dynamics of the localized and delocalized condensate, we consider the ground states obtained for different nonlinearities and perform the time evolution by applying an instantaneous quench of the nonlinear interaction to zero. This protocol introduces the dynamics in the condensates, which have been captured by evolving the GPEs using the real-time scheme [156].

To probe the spatio-temporal evolution after quenching of the condensate prepared at different values of g, in Fig. 3.6, we plot the spatio-temporal evolution of the density of the condensates after sudden cessation of g. For $g = 0$, the localized condensate propagates with time without any distortion as can be seen from Fig. 3.6(a). However, the localized condensate at $g = 4$ develops oscillatory behaviour, as depicted in Fig. 3.6(b). The oscillatory behaviour becomes more and more irregular for higher values of nonlinearity [cf. Fig. 3.6(c-d)]. Interestingly, we find that the condensate, which was in the delocalized state, exhibits chaotic oscillation with time, as depicted in Fig. 3.6(d) (for $g = 10$).

Note that the absence of any spatial change in the condensate after the quench may be attributed that the condensate is trapped tightly near the minima of the external potential, and it remains so with zero nonlinear interaction as time progresses. Also, the

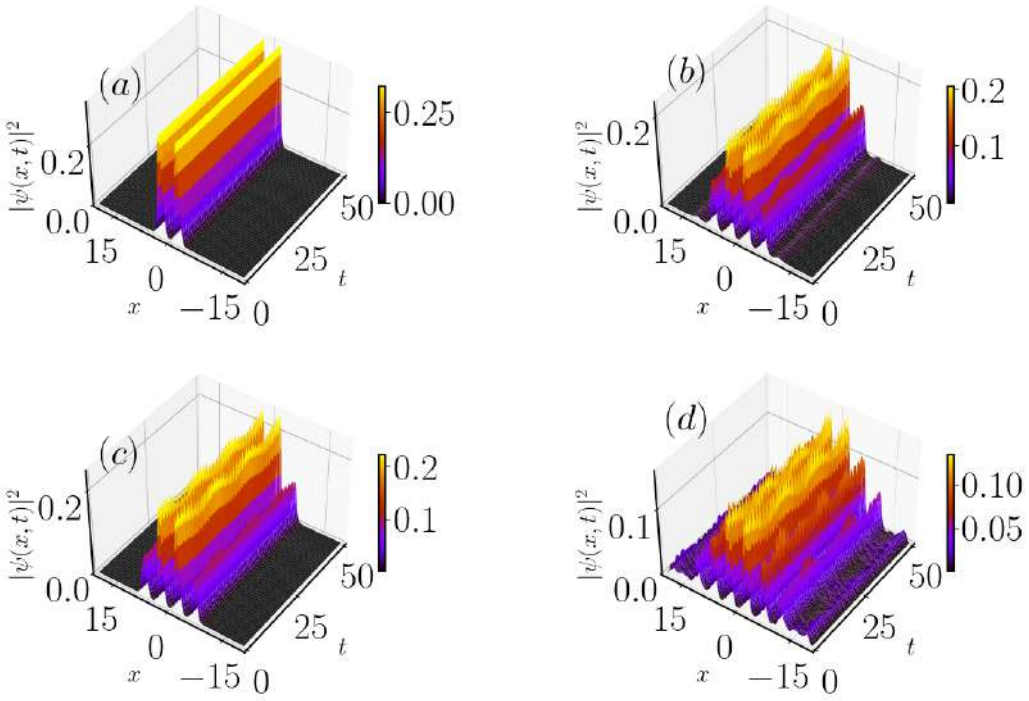

Figure 3.6: Pseudo color representation of the spatio-temporal evolution of the condensate after quenching the nonlinearity to zero as the ground state was prepared for different g: (a) $g = 0$, (b) $g = 4$, (c) $g = 5$, and (d) $g = 10$. Other parameters are the same as in Fig. 3.2.

dispersion due to the kinetic part is quite low because the trapped energy dominates over other energies for all the values of s_2/s_1 (see Fig. 3.5). The role of the random potential here is to contribute to the spatial phase with a random value in the condensate with time, which also reflects in the temporal behaviour of the time correlator function, which we shall discuss later.

We investigate the dynamics of localized matter wave density by computing the time correlator $c(t)$ (Eq. (3.8)) and analyzing its temporal evolution. For this, we consider the ground state obtained for a particular g as $\psi(0)$ and condensate wave function at a time t after quenching of the nonlinearity to zero as $\psi(t)$. In Fig. 3.7, we show the temporal evolution of $c(t)$ for the ground state prepared at different values of g. Figures 3.7(a)-(f) depict the evolution of $c(t)$ for $g = 1$, 2, 3, 4, 5, and 10, respectively. For the localized state prepared at $g = 1$, $c(t)$ exhibits periodic oscillations of amplitude very close to unity. The localized state with $g = 2$ shows similar oscillatory behaviour as shown in Fig. 3.7(b). For $g = 3$, the $c(t)$ displays some modulated oscillation indicating the presence of more than one frequency. However, for $g = 5$ and $g = 10$, which correspond to delocalized condensate, the $c(t)$ exhibits aperiodic or chaotic temporal features. This indicates that quenching of nonlinearity generates periodic, quasiperi-

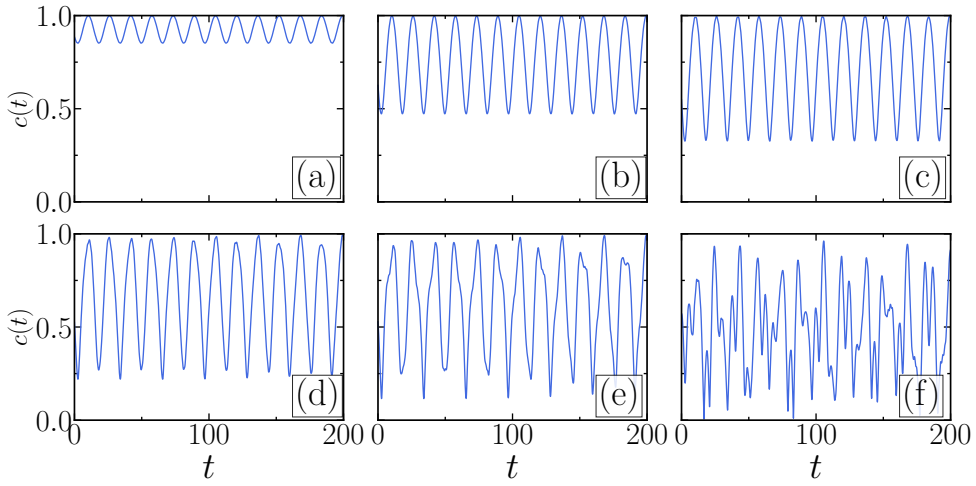

Figure 3.7: Temporal variation of the time correlation function, $c(t)$ at $s_2/s_1 = 1.0$, $s_1 = 3$ and $\lambda_1 = 10.0$ for different nonlinearities (a) $g = 1$, (b) $g = 2$, (c) $g = 3$, (d) $g = 4$, (e) $g = 5$, and (f) $g = 10$. In the localized state ($g \lesssim 5$), $c(t)$ exhibits periodic or quasiperiodic behaviour, which becomes chaotic in the delocalized state. The time period corresponding to periodic oscillation is $T \approx 15.426$ (i.e., $\omega \approx 0.407$).

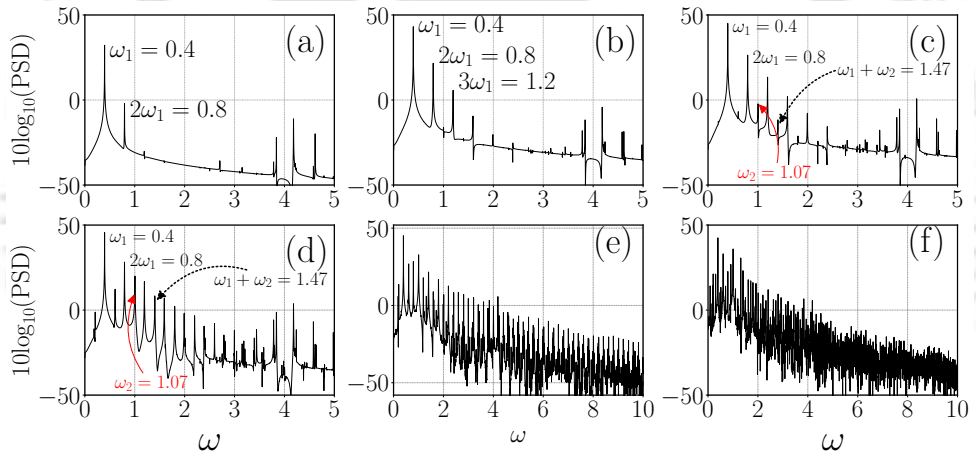

Figure 3.8: PSD of time correlation function (Fig. 3.3) for different nonlinearities, (a) $g = 1$ (periodic), (b) $g = 2$ (periodic), (c) $g = 3$ (quasiperiodic), (d) $g = 4$ (quasiperiodic), (e) $g = 5$ (chaotic), and (f) $g = 10$ (chaotic). Other parameters are the same as in Fig. 3.3. An increase in the nonlinearity leads to the generation of two incommensurate frequencies $\omega_1 = 0.40$ and $\omega_2 = 1.07$ at $g \sim 3$. Finally, a large number of frequencies get generated, a signature of chaotic behaviour at higher nonlinearity ($g \gtrsim 5$).

odic, and chaotic type dynamics depending upon whether the corresponding ground state is localized or delocalized.

To further investigate the nature of the different frequencies present in the dynamics and route to chaotic behaviour of the delocalized state, we compute the PSD of the time correlator, using the formula defined in Eq. (3.10), corresponding to the periodic, quasiperiodic and chaotic states as discussed above. Figure 3.8 depicts the PSD of $c(t)$ corresponding to the periodic, quasiperiodic, and chaotic states. We see that the peri-

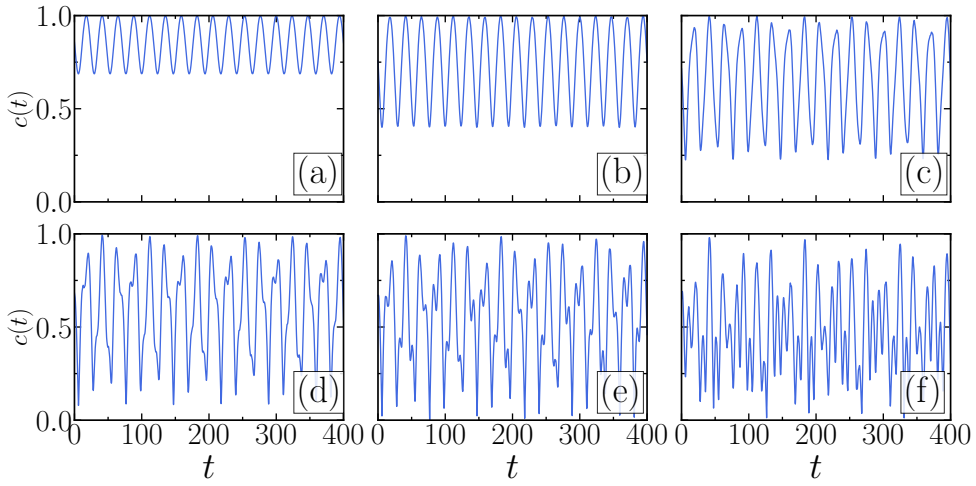

Figure 3.9: Temporal evolution of the time correlator function at $s_2/s_1 = 0.5$, $s_1 = 3$, $\lambda_1 = 10.0$ for different nonlinearities: (a) $g = 1$, (b) $g = 2$, (c) $g = 3$, (d) $g = 4$, (e) $g = 5$, and (f) $g = 10$. The temporal behaviour of the localization and delocalization has similar qualitative features to those for $s_2/s_1 = 1.0$, and the only difference is reflected in the decrease in the nonlinearity at which the correlation shows the chaotic behaviour. The time period for the periodic oscillation is $T \approx 23.691$ ($\omega \approx 0.265$).

odic behaviour of the dynamical state for $g = 1$ involves the fundamental frequency $\omega_1 = 0.40$ together with the presence of its higher harmonics [see Fig. 3.8(a)]. We observe similar behaviour in the dynamics of the localized state at $g = 2$ as depicted in Fig. 3.8(b). The PSD of $c(t)$ for $g = 3$ shows peaks at the frequencies at $\omega_1 = 0.40$ and $\omega_2 = 1.07$, respectively [see Fig. 3.8(c)]. The irrational ratio of the two frequencies indicates the quasiperiodic nature of $c(t)$ for $g = 3$. Further, for $g = 4$ [Fig. 3.8(d)], apart from the frequencies ω_1 and ω_2, other higher frequencies around ω_1 and ω_2 as well as sub-harmonics, like, $\omega_2 + \omega_1$, $\omega_2 + 2\omega_1$, etc. start appearing. We notice more frequencies start getting populated around ω_1 and ω_2 for the dynamics of condensate that show delocalized state for higher nonlinearity (for $g \gtrsim 4$) as depicted in Figs. 3.8(e)-(f). The exponential fall behaviour of frequencies in the dynamics of the delocalized state confirms the fully developed temporal chaos [193, 194]. The inverse of the rate of decay ($\tilde{\mu}$) of the PSD with the frequency of the chaotic state is of the order of ~ 1.4 in the high frequency range. In general, $\tilde{\mu}$ is related with Lyapunov exponent [193]. We find that the dynamics of the localized state exhibit periodic oscillations for weak nonlinear interaction, which transform into quasiperiodic for stronger nonlinear interaction. The value of g at which the condensate exhibits a delocalized nature has a chaotic time correlator. With this, we find a systematic generation of the frequencies that finally leads to the chaotic dynamics of the delocalized state, which suggests a quasiperiodic route to chaos. We find the presence of the same quasiperiodic route to chaos for the lower disorder strengths (s_2/s_1), which we discuss below.

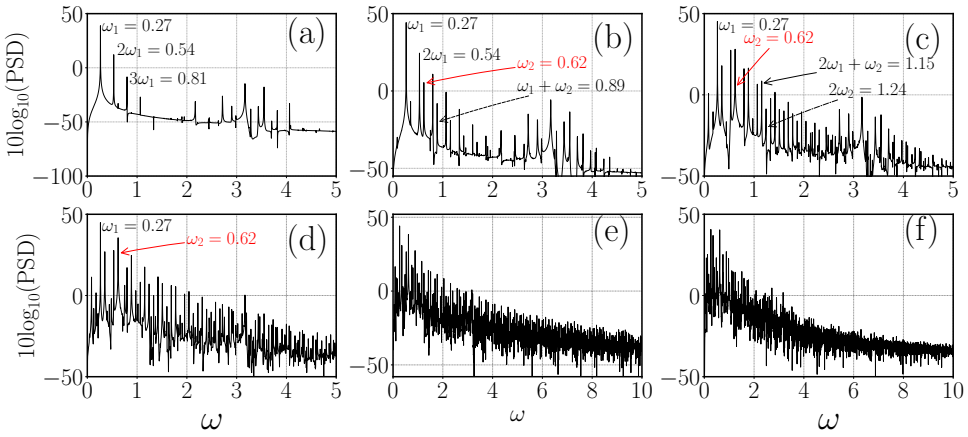

Figure 3.10: PSD of time correlator function shown in Fig. 3.9 at different nonlinearities: (a) $g = 1$, (b) $g = 2$, (c) $g = 3$, (d) $g = 4$, (e) $g = 5$, and (f) $g = 10$. Other parameters are the same as in Fig. 3.8. The system undergoes a transition from the localized ($g = 1, 2, 3$) to the delocalized state ($g = 4, 5, 10$) with the appearance of frequencies around quasiperiodic frequencies (ω_1 and ω_2) in the PSD of the time correlation function upon increasing the nonlinearity.

Next, we move our focus to investigating the nature of the dynamics of the condensate for a lower disorder strength ($s_2/s_1 = 0.5$). In Fig. 3.9 we plot $c(t)$ for different values of g. Here, the amplitude of $c(t)$ appears to be slightly higher compared to those obtained for $s_2/s_1 = 1$ (Fig. 3.7) after quenching the nonlinearity ($g = 1 \to 0$). Similar to the higher disorder strength, in case of $s_2/s_1 = 0.5$ the $c(t)$ shows periodic (Fig. 3.9(a-b)), quasiperiodic (Fig. 3.9(c-d)) and chaotic oscillation (Fig. 3.9(e-f)) as the nonlinearity is quenched, respectively, from $g = \{1, 2\}$, $g = \{3, 4\}$, and $g = \{5, 10\}$ to zero. One noticeable effect of disorder strength (s_2/s_1) is observed in terms of the magnitude of the fundamental (ω_1) and quasiperiodic frequencies (ω_1 and ω_2), which show a decreasing trend upon the decrease in s_2/s_1. In Fig. 3.10, we illustrate the PSD of the time correlator presented in Fig. 3.9. Figure 3.10(a) shows the presence of fundamental frequency $\omega_1 = 0.27$ along with its higher harmonics $2\omega_1 = 0.54$, $3\omega_1 = 0.81$ in the dynamics of the localized state when the nonlinearity is instantaneously quenched as $g = 1 \to 0$. In the case of quench dynamics of the high nonlinearity state, for example, $g = 2$, we find other eigenfrequencies such as $\omega_2 = 0.62$, apart from the fundamental frequency at $\omega_1 = 0.27$, which indicates the quasiperiodic nature of $c(t)$. At higher nonlinearity $g \gtrsim 4$, more frequencies around ω_1 and ω_2 start getting populated (see Fig. 3.10(d)-(f)). The appearance of other frequencies in the case of the delocalized state ($g = 4 \to 0$) exhibits exponential decay behaviour, indicating the presence of chaotic dynamics. We find that for $s_2/s_1 = 0.5$, the chaotic dynamics appear for the state when $g \gtrsim 4$, which is less than those for $s_2/s_1 = 1$. However, it is interesting to note that for both the disorder strengths ($s_2/s_1 = 0.5, 1$), *quasiperiodic route to chaos*

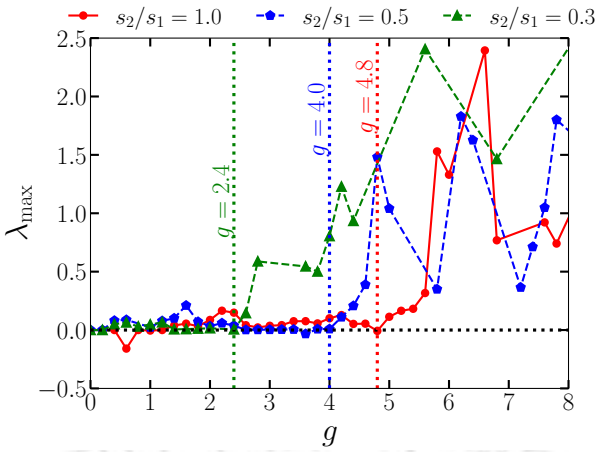

Figure 3.11: Variation of the Lyapunov exponent (λ_{max}) against nonlinearity for different disordered strengths: $s_2/s_1 = 1$ (dash-dotted line with solid-red circles), $s_2/s_1 = 0.5$ (dashed line with solid-blue pentagons) and $s_2/s_1 = 0.3$ (dashed line with solid green triangles). For localized state $\lambda_{max} \lesssim 0$, while for delocalized state $\lambda_{max} > 0$, indicating the chaotic dynamics. The threshold g_c above which $\lambda_{max} > 0$ (a characteristic for the delocalized state) decreases upon the decrease in s_2/s_1. Vertical dotted lines are drawn to guide the eyes for different g_c.

has been observed in the dynamics when the condensate makes a transition from the localized to the delocalized state.

To further quantify the chaotic nature of the dynamics in more systematic manner, we compute the maximal Lyapunov exponent (λ_{max}) as given in Eq. (3.12) corresponding to the dynamics of the condensate using the time series of the time correlator function $c(t)$. In Fig. 3.11, we show the variation of the λ_{max} with the interaction strength for different values of s_2/s_1. The increase of λ_{max} towards a positive value indicates the chaotic nature of the time correlator function. We find that the Lyapunov exponent fluctuates about zero until $g \sim 4.8$ for $s_2/s_1 = 1$. When $g \gtrsim 4.8$, we witness a systematic increase in the Lyapunov exponent, and it remains positive ($\lambda_{max} > 0$), indicating the chaotic nature of the time correlator functions for that range of g. Therefore, the above analysis provides the value of the critical nonlinearity, beyond which the condensate has a delocalized state and thus the corresponding dynamics is chaotic. Lowering the disorder strength results decrease in the value of the critical nonlinearity (g_c) beyond which λ_{max} becomes positive. Further, for $s_2/s_1 = 0.5$, the critical nonlinearity beyond which the condensate has chaotic dynamics is $g_c \sim 4$, while for $s_2/s_1 = 0.3$ it is $g_c \sim 2.4$. Note that the value of g_c calculated through this analysis provides accurate nonlinearity at which the condensate is delocalized in space and has dynamically chaotic behaviour, which may be important feedback for the experiments. At this juncture, it is worth mentioning that Březinová *et al.* [30] observed a similar kind of chaotic behaviour in the dynamics of the delocalized state when the condensate was subject to

weak periodic or aperiodic (quasiperiodic and random disordered potential) trap.

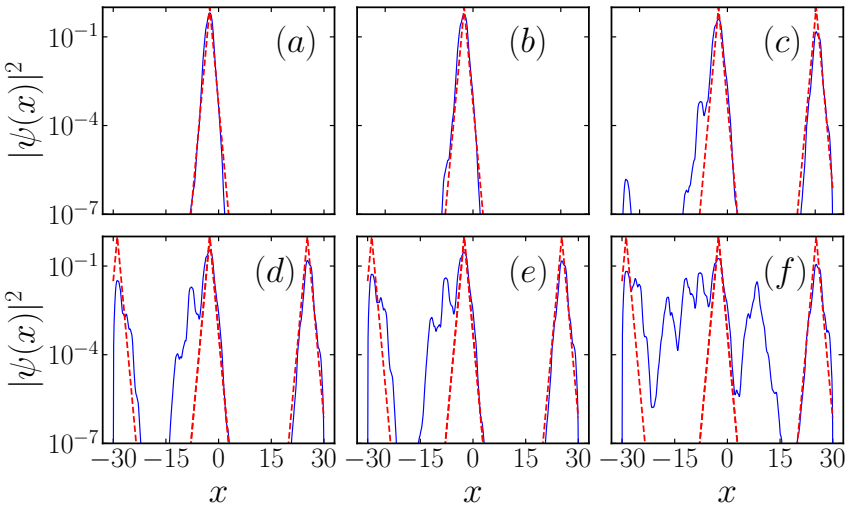

Figure 3.12: Variation of density (in semilog scale) at $V_0 = 1.0$ for different nonlinearities: (a) $g = 0$, (b) $g = 1$, (c) $g = 3$, (d) $g = 4$, (e) $g = 5$, and (f) $g = 10$. The dotted red line is the exponential function drawn near the localized region to guide the eyes to show the deviation of the matter wave from the localized nature.

So far, we have analyzed the dynamics of the condensates in the presence of the quasiperiodic potential and found that while the localized state exhibits either periodic or quasiperiodic dynamics, delocalized states show chaotic dynamics upon quenching the nonlinearity to zero. Also, the route to chaos upon increasing the nonlinear interaction appears to be quasiperiodic in nature. Several studies indicate the similarity in the condensate dynamics for the condensate trapped in the quasiperiodic potential and in the random-speckle potential [30]. To shed more light on this interesting feature, in the following subsection, we present the spatial and temporal behaviour of condensate in the presence of the random disordered potential.

3.4.2 Delocalization in presence of random disordered potential

In this subsection, we discuss the effect of the non-linearity on the localized condensate trapped in the random disordered potential. The details to generate the random potential are given in Sec. 3.2. First, we discuss the ground states of the condensate trapped in the random disordered potential at different nonlinearities for a single disorder realization. It is followed by the dynamics of the condensate in a similar line of analysis performed for the condensate trapped in a quasiperiodic potential, where we have used the quenching of nonlinear interaction from finite to zero to generate the dynamics. Finally, we characterize the dynamics using the PSD and largest Lyapunov

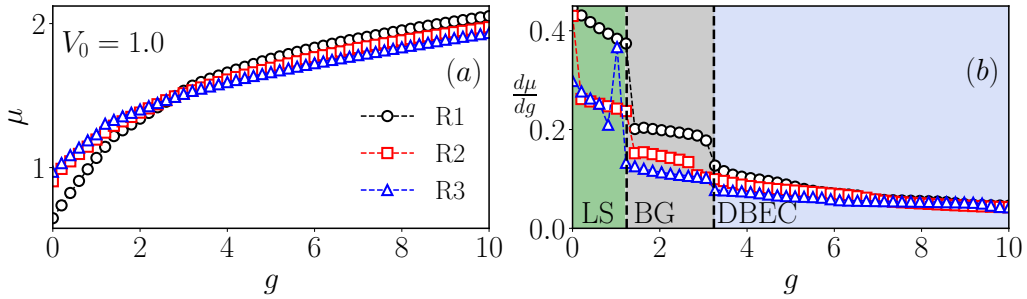

Figure 3.13: Plots showing the different states of the condensate trapped in the random disordered Gaussian potential of strength $V_0 = 1.0$ based on the nature of μ in different ranges of g. The other parameters are the same as Fig. 3.12. (a) Variation of chemical potential μ with g for three different random realizations: R_1 (black circle), R_2 (red square), and R_3 (blue triangle) (b) Variation of $d\mu/dg$ with g distinguishing different regimes for the condensate: Localized state (LS) for lower g with higher $d\mu/dg \sim 0.2 - 0.4$, Bose glass (BG) state at intermediate g with $d\mu/dg \sim 0.12 - 0.2$, and delocalized BEC (DBEC) state at higher g with $d\mu/dg \sim 0.05 - 0.12$. The vertical dotted lines are drawn to guide the eyes to distinguish different localized states of the condensate.

exponent analysis of the time correlator function.

Apart from the localized and delocalized states as those observed for quasiperiodic potential, we also witness the presence of the Bose glass phase for the condensate trapped in the random disordered potential [195–198]. Lugan *et al.* theoretically demonstrated that the condensate undergoes a transition from Lifshitz glass to a delocalized state upon the increase of the nonlinear interaction [199]. In Fig. 3.12, we plot the density profile (blue line) in a semi-log scale for different values of g. Here, the red dashed lines are the exponential curve near the localized region drawn to display an estimate of the exponential fall of the density in space. For the non-interacting condensate, i.e., $g = 0$, the density profile shows the exponential fall, which is quite evident from the excellent matching of the density profile with the drawn exponential curve [see Fig. 3.12(a)], complementing the localized nature of the condensate. The spatial profile of the condensate for $g = 1$ also shows exponential fall as depicted in Fig. 3.12(b). However, as discussed earlier, due to the random nature of the potential, we witness the presence of another region of the localized condensate, apart from what is present near $x \sim 0$, on increasing g further. For instance, at $g = 3$, one part of the condensate gets localized near $x = 0$, while another part gets localized near $x \sim 25$. The condensate near both regions appears to fall exponentially, which is quite clear from the fitting of the spatial profile of the condensate with the exponential curve (red dotted line). Note that such a kind of bifurcations of the condensate into multiple localized states has been in general termed as fragmented BECs [126, 124] or Bose glass [196–198]. However, a further increase in g ($\gtrsim 5$) results in the deviation of the tail of the localized condensate from the exponential nature, as apparent from

Fig. 3.12(d)-(f), also termed as the delocalized state.

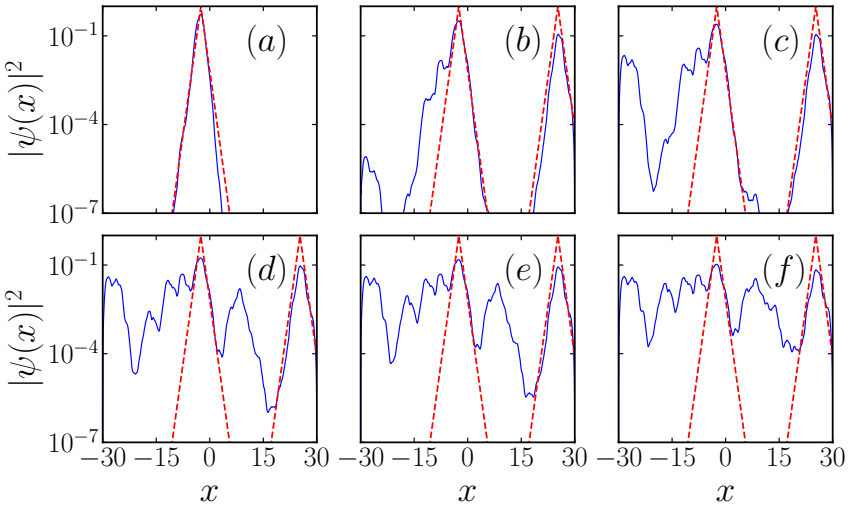

Figure 3.14: Variation of density (in semilog scale) trapped in random potential at $V_0 = 0.5$ with different nonlinearities: (a) $g = 0$, (b) $g = 2$, (c) $g = 3$, (d) $g = 5$, (e) $g = 6$, and (f) $g = 10$. The dotted red line is the exponential function drawn near the localized region to guide the eyes to show the deviation of the matter wave from the localized nature.

Next, we will characterize the different ground state phases of the condensate trapped in the random potential, namely, localized state (LS) for weak interaction, Bose glass (BG) for intermediate interaction, and delocalized Bose-Einstein condensate (DBEC) for high nonlinear interaction. We will do so using the chemical potential μ defined as

$$\mu = \int dx \left[\frac{1}{2}|\nabla\psi|^2 + V(x)|\psi|^2 + g|\psi|^4\right], \tag{3.17}$$

where ψ corresponds to the ground state wave function. In Fig. 3.13(a), we plot the μ as a function of g for three different random realizations (R_1, R_2, and R_3).

For all realizations, μ shows a sharp increase with g. The rate of increase of μ with g keeps decreasing with the increase in g. In order to quantify the distinct nature of the variation of μ, we compute $d\mu/dg$ for different g. As the compressibility of the condensate is $\kappa \propto (d\mu/dn)^{-1}$, where n is the condensate and a function of g, the inverse of $d\mu/dg$ can also be attributed to the compressibility of the gas. In Fig.3.13(b), we display the $d\mu/dg$ for different g for all the realizations (R_1, R_2, and R_3) presented in Fig. 3.13(a). In the LS, $d\mu/dg \sim 0.2 - 0.4$ has the largest value, the intermediate value of $d\mu/dg \sim 0.12 - 0.2$ represents the BG state, while the lowest $d\mu/dg \sim 0.05 - 0.12$ represents the DBEC state. Overall, we find that the compressibility is higher for the DBEC phase, intermediate for the BG, and smallest for the LS, which is in accordance with the typical behaviour of localized and delocalized gases. The trend observed for

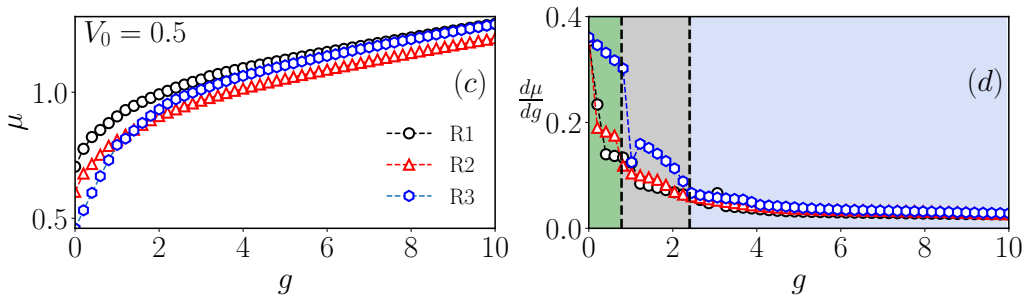

Figure 3.15: Plots showing the different states of the condensate trapped in the random Gaussian potential of strength $V_0 = 0.5$ based on the nature of μ in different ranges of g. The other parameters are the same as Fig. 3.14. (a) Variation of chemical potential μ with nonlinear interaction g for three different random realizations: R_1 (black circle), R_2 (red square), and R_3 (blue triangle) (b) Variation of $d\mu/dg$ with g distinguishing different regimes for the condensate: Localized state (LS) for lower g with higher $d\mu/dg \sim 0.12 - 0.36$, Bose glass (BG) state at intermediate g with $d\mu/dg \sim 0.06 - 0.12$, and delocalized BEC (DBEC) state at higher g with $d\mu/dg \sim 0.04 - 0.06$. The vertical dotted lines are drawn to guide the eyes to distinguish different localized states of the condensate.

μ in different regimes of the condensate trapped in the random potential is consistent with earlier studies [196–198].

In Fig. 3.14, we show the density profile in the semi-log scale for $V_0 = 0.5$ of the random disordered potential. For this parameter, we find that for the lower nonlinearity ($g \lesssim 3$), the condensate is localized, and we observe a delocalized state for higher nonlinearities. However, all the phases, like LS, BG, and DBEC, are of similar nature as those for $V_0 = 1$ [see Fig. 3.12]. It is straightforward to see that decreasing the potential strength decreases the critical nonlinearity above which the condensate gets delocalized, which is around $g_c \sim 3$ for $V_0 = 0.5$ compared to $g \sim 5$ that for $V_0 = 1$. To further identify the different regions of the condensate upon increasing the nonlinearity, In Fig. 3.15 we show the variation of μ as well $d\mu/dg$ with g for $V_0 = 0.5$ in the panel (a) and (b) respectively. For this case, we also obtain the presence of different regimes based on the values of $d\mu/dg$ as those observed for $V_0 = 1.0$. Note that although the μ is lower for $V_0 = 0.5$ than those for $V_0 = 1$, the value of $d\mu/dg$ for different regimes of localization appears to be the same.

In the following, we present the dynamics of the different states observed for the condensate trapped in the random disordered potential.

3.4.2.1 Quench dynamics of the condensates trapped in random potential

In Fig. 3.16, we depict the spatio-temporal evolution of the condensate density after quenching the nonlinearity to zero from different initial values of g. For $g = 0$ [cf. Fig. 3.16(a)], the localized condensate propagates with time without any distortion.

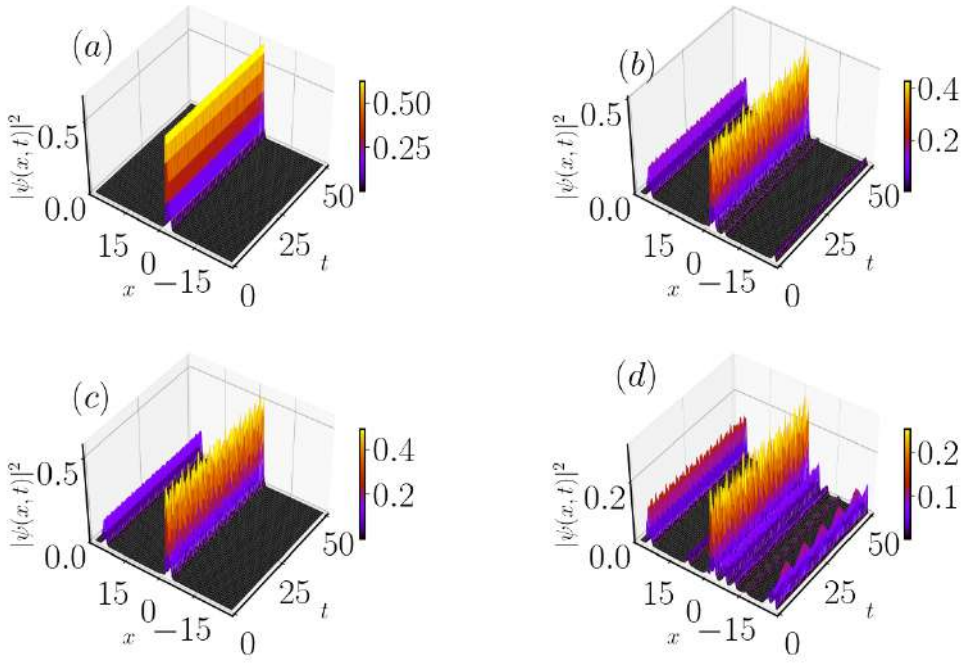

Figure 3.16: Spatiotemporal evolution of the condensate at different nonlinearities (a)$g = 0$, (b) $g = 4$, (c) $g = 5$, and (d) $g = 10$ trapped under the Gaussian random-disordered potential for $V_0 = 1.0$. The condensate remains localized near $x = -2.51$ for low non-linearity $g = 1$. An increase in the nonlinearity results in the delocalized condensate along with more fluctuations in the density, especially near $x = 0$.

The condensate develops fluctuation with time upon the increase in the value of g [see Fig. 3.16(b)-(d]), especially near the region $x = 0$. The temporal oscillation becomes more irregular for higher nonlinearity, and the corresponding dynamics display chaos, a dynamical feature similar to that obtained for the condensate trapped in the quasiperiodic potential. Note that as discussed for the situation of no expansion along the x-direction for the condensate trapped in quasiperiodic potential, once the dynamics appear due to quenching in the non-linearity, we find a similar scenario for the condensate dynamics trapped with a random potential. In this case, we also observed that the potential energy dominates over the kinetic energy and thus does not allow the condensate to diffuse around the minima of the potential well.

We characterize the condensate dynamics by analyzing the temporal evolution of $c(t)$ for different values of g, which are plotted in Fig. 3.17. Figure 3.17(a) illustrates the periodic temporal evolution of $c(t)$ with a period $T \approx 1.309$ for the localized state upon quenching the nonlinearity from $g = 1.6 \to 0$. Figure 3.17(b) shows the evolution of $c(t)$ for the localized state when the g is quenched as $g = 2 \to 0$. The corresponding dynamics show the quasiperiodic oscillation with the presence of two frequencies, which becomes more pronounced for $g = 3$ as depicted in Fig. 3.17(c). As we analyze the quench dynamics for the state at higher nonlinearity ($g \gtrsim 5$) for which the

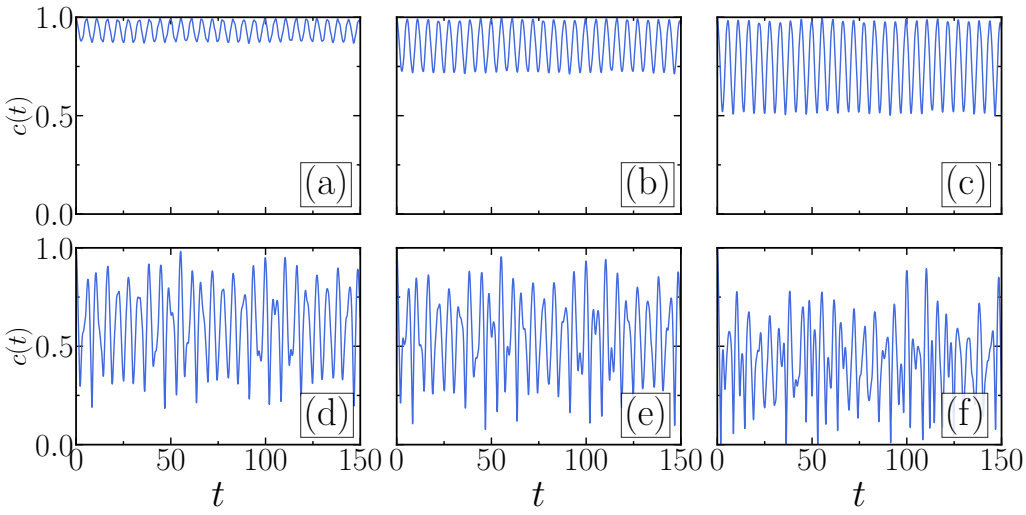

Figure 3.17: Temporal evolution of the time correlation function for quenching from (a) $g = 1.6$, (b) $g = 2$, (c) $g = 3$, (d) $g = 5$, (e) $g = 6$, and (f) $g = 10$ to $g = 0$. The other parameters are the same as in Fig. 3.12. In the localized state($g \lesssim 5$), the correlation function exhibits a periodic or quasiperiodic behaviour, which becomes chaotic at higher g. Here, the disorder strength $V_0 = 1.0$.

ground state exhibits a delocalized nature, we find that the corresponding $c(t)$ exhibits aperiodic or chaotic oscillation [see Figs. 3.17(d)-(f)]. These dynamical behaviours for different states will become clear as we investigate the PSD of the time correlation, which we discuss below.

In Fig. 3.18, we plot the PSD of the time correlation function presented in Fig. 3.17. The PSD for the localized state quenched from $g = 1.6 \rightarrow 0$ is illustrated in Fig. 3.18(a). It shows the presence of fundamental frequencies at $\omega_1 = 1.13$ along with its higher harmonics like $2\omega_1 = 2.26$, confirming the dynamics to be periodic. However, a quenching from $g = 2 \rightarrow 0$ generates another frequency at $\omega_2 = 4.09$ along with ω_1, as shown in Fig. 3.18(b), indicating the quasiperiodic nature of the dynamics of the condensate. The dynamics of the localized states with higher nonlinearity ($g = 3$) exhibit the generation of more frequencies around the two frequencies ω_1 and ω_2, as illustrated in 3.18(c-d). However, for $g \gtrsim 5$, more frequencies start appearing near ω_1 and ω_2 in the PSD. The condensate has a delocalized ground state for $g \gtrsim 5$, shows the presence of a wide range of frequencies in the dynamics, and the corresponding PSD shows the exponential variation with the angular frequency; a typical signature of the chaotic dynamics. The PSD plots for $g = 6$ [Fig. 3.18 (e)] and $g = 10$ [Fig. 3.18 (f)] indeed show the exponential distribution with the frequencies. Interestingly, similar to the case of quasiperiodic potential, we find that the delocalized state exhibits a chaotic state when the condensate is trapped in random disordered potential. The quasiperiodic route to the chaos that exists in the dynamics is similar to those obtained with the

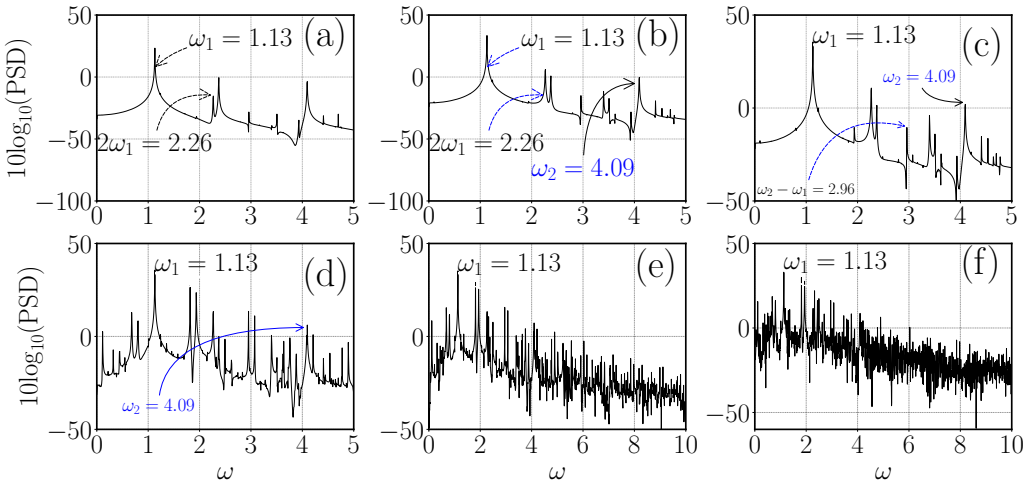

Figure 3.18: PSD of time correlation function (as shown in Fig. 3.17) for the situation when the nonlinearity is quenched from (a) $g = 1.6$, (b) $g = 2$, (c) $g = 3$, (d) $g = 5$, (e) $g = 6$, and (f) $g = 10$ to $g = 0$ for $V_0 = 1.0$. Increasing the nonlinearity generates two incommensurate frequencies $\omega_1 = 1.13$, and $\omega_2 = 4.09$ at $g \sim 2$. Finally, the region near these frequencies starts getting populated, leading to the chaotic behaviour at higher nonlinearity ($g \gtrsim 5$).

condensate trapped in the quasiperiodic potential.

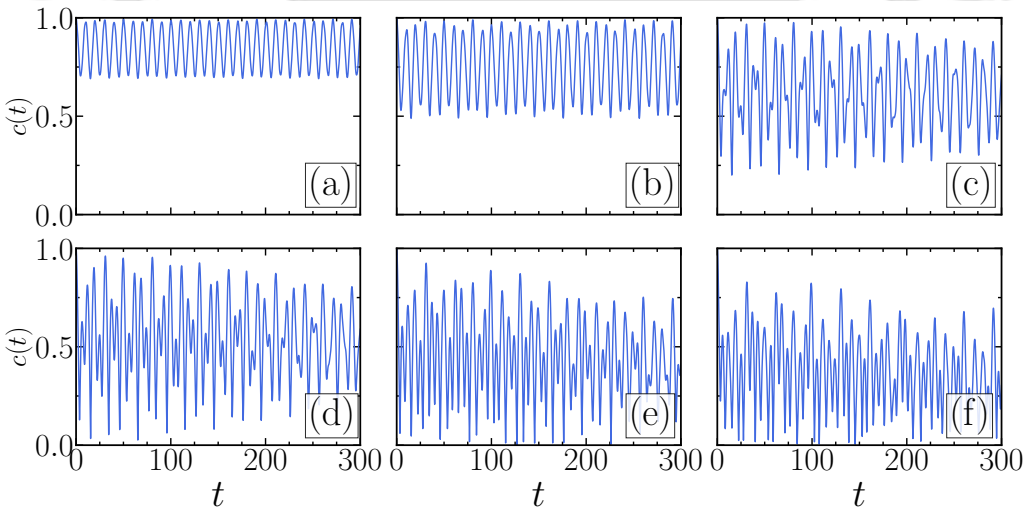

Figure 3.19: Variation of time correlation function with time at $V_0 = 0.5$ after quenching of steady state from (a) $g = 1.4$, (b) $g = 1.6$, (c) $g = 3$, (d) $g = 4$, (e) $g = 6$, and (f) $g = 10$. The other parameters are the same as in Fig. 3.14. In the localized state ($g \lesssim 4$), the correlation function exhibits either periodic ($g = 1.4$) or quasiperiodic ($g = 1.6, 2, 3$), which becomes chaotic after quenching the system from higher nonlinearity.

As we decrease the strength of the random disordered potential, the critical value of the nonlinearity at which the chaotic behaviour appears in the time correlator decreases. Fig. 3.19 depicts $c(t)$ at different nonlinearities for the disorder strength $V_0 = 0.5$ of the random disordered potential. In this case, the nature of $c(t)$ is periodic for

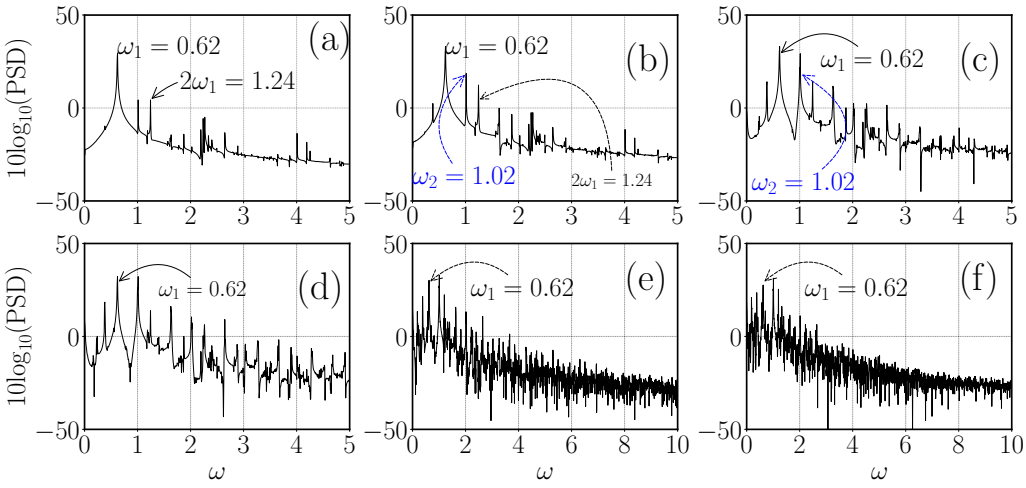

Figure 3.20: The PSD of time correlation function (as shown in Fig. 3.19) at $V_0 = 0.5$ after quenching at different nonlinearities, (a) $g = 1.4$, (b) $g = 2$, (c) $g = 3$, (d) $g = 4$, (e) $g = 6$, and (f) $g = 10$ to $g = 0$. Increasing the nonlinearity generates two incommensurate frequencies $\omega_1 = 0.62$, $\omega_2 = 1.02$ at $g \sim 2$. Here, frequencies get populated near ω_1 and ω_2 when we quench the system from low nonlinearity rather than $V_0 = 1.0$.

$g = 1.4$, quasiperiodic for $g = 2, 3$, and chaotic for $g = 4$ and $6, 10$. As we analyze the corresponding PSD, we find the presence of fundamental frequency at $\omega_1 = 0.62$ (as shown in Fig. 3.20(a)), which is lower than those for $V_0 = 1$, which is $\omega_1 = 1.13$. An increase in $g = 2$ leads to the generation of another frequency $\omega_2 = 1.02$, which is incommensurate with the fundamental frequency (ω_1), indicating the quasiperiodic nature of the dynamics [see Fig. 3.20(b)]. Further, an increase in the nonlinear interaction to $g = 3$ [Fig. 3.20(c)], and $g = 4$ [Fig. 3.20(d)] generates other frequencies, whose origin can be understood as a combination of ω_1 and ω_2. However, for $g = 6$ and $g = 10$, the PSD exhibits exponential distribution with the frequencies indicating the fully chaotic state. Interestingly, the route to chaos for $V_0 = 0.5$ remains a quasiperiodic route, similar to what we obtained for $V_0 = 1$.

After associating the delocalized state with the chaotic dynamics, we now focus on complementing the studies by computing the maximal Lyapunov exponent (λ_{max}) of the time series $c(t)$. In Fig. 3.21, we plot the variation of λ_{max} averaged over five different random realizations with g for different sets of V_0. For a given V_0, λ_{max} remains negative or close to zero for the localized state, while it becomes positive for the delocalized state. For instance, for $V_0 = 1$, the $\lambda_{max} \sim 0$ for $g \lesssim 3.8$. However, beyond this nonlinearity, λ_{max} becomes positive and remains above zero for a higher value of g. The threshold value of the nonlinearity for $V_0 = 1$ indicates the delocalized feature of the condensate. Decreasing the potential strength to $V_0 = 0.5$ decreases the threshold nonlinearity to $g_c \sim 2.4$. Further, decrease to $V_0 = 0.3$ make the $g_c \sim 2.0$.

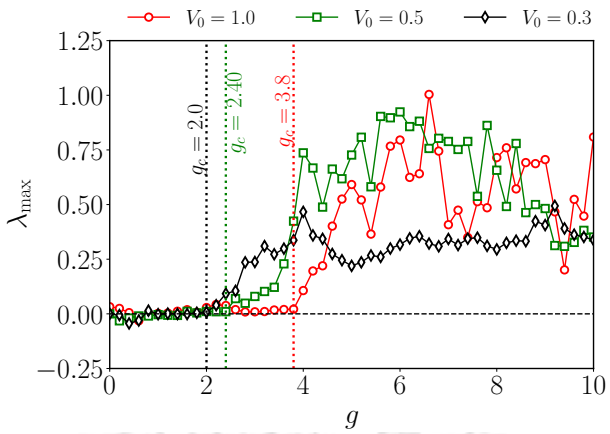

Figure 3.21: Plot showing the maximal Lyapunov exponent (λ_{max}) averaged over five different random realizations, plotted against nonlinearity for different strengths of the random potential: $V_0 = 1$ (red), $V_0 = 0.5$ (green), and $V_0 = 0.3$ (black). The localized state has $\lambda_{max} \lesssim 0$, while the delocalized states have $\lambda_{max} > 0$, indicating chaotic dynamics. The threshold g_c above which $\lambda_{max} > 0$, a characteristic of the delocalized state, decreases as V_0 decreases. Vertical dotted lines are included to guide the eyes for different g_c values. The g_c value is evaluated by taking the average over five realizations.

Next, in Fig. 3.22, we present a comparative analysis of the g_c at which the dynamics of the condensate begin to exhibit a positive Lyapunov exponent for both the quasiperiodic optical lattice (blue circles) and the random disordered potential (red diamonds). We observe that the critical value g_c increases for both potentials as the disorder strength increases. Although the g_c appears to be of the same order for both disorder potentials at low disorder strengths, for higher disorder strengths, g_c is higher for the quasiperiodic potentials than for the random disordered potentials.

3.5 Summary and Conclusion

In this chapter, we have studied the effect of atomic interaction on the ground state and the associated dynamics of Bose-Einstein condensates in a one-dimensional bichromatic optical lattice and random disordered potentials. We identified that increasing the nonlinearity strength leads to the delocalization of the condensates. Further, we have analyzed the condensate dynamics by quenching the nonlinearities to zero from the value at which the ground state was prepared.

The dynamics were captured through the time correlation function. For small interaction quenching, it demonstrates regular dynamics of the condensate, while it becomes chaotic at large nonlinearities where delocalization occurs. We also identified a quasiperiodic route to chaos for both bichromatic and random disordered potentials. For a random disordered potential, the regular and chaotic dynamics of the time cor-

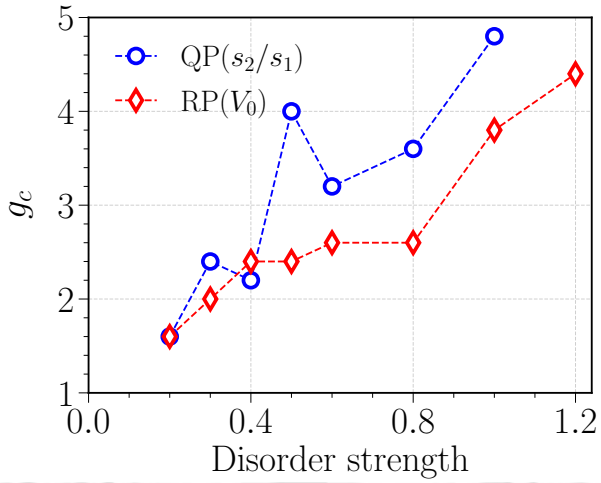

Figure 3.22: Plot showing the variation of the critical non-linearity strength (g_c) with the disorder strength ratio s_2/s_1 for the quasiperiodic (QP) lattice and the potential strength V_0 for the random potential (RP). The data points for the random potential are the averaged data over five different disorder realizations.

relator function clearly distinguished the localized and delocalized regions of the condensate. The power spectral density displays a broadband spectrum, and the maximal Lyapunov exponent is positive when it exhibits chaotic dynamics. The power spectral density and largest Lyapunov exponent confirm the presence of chaotic dynamics. Further, we have found that the critical nonlinearity for delocalization decreases by decreasing the ratio of amplitudes of the secondary to primary laser for quasiperiodic potential or the strength of the random disordered potential. The critical nonlinearity above which the dynamics became chaotic between quasiperiodic and random disordered potential is comparable for low disordered strength, whereas as the disorder strength increases, the critical nonlinearity for quasiperiodic is comparatively higher compared to random disordered potential.

Our studies upon quenching the nonlinear interaction provide a tool to characterize the localized and delocalized states by describing the regular and chaotic dynamics of the condensate, respectively. Also, we have shown that this dynamical approach for characterization of localized-delocalized states can be applicable to any kind of disordered potential.

Chapter 4

Signature of localization-delocalization transitions in interacting spin-orbit coupled binary condensate

In the previous chapter, we examined localized and delocalized phases in a BEC, showing that interaction quenching can induce chaotic dynamics linked to spatial delocalization. We also found that increasing disorder leads to localization, while strong interactions trigger the delocalization of the condesate. In this chapter, we study spin-orbit coupled binary BECs with inhomogeneous interactions in a one-dimensional quasiperiodic potential. We demonstrate a reentrant localization–delocalization transition, controlled by tuning either the interaction from attractive to repulsive or the spin-orbit coupling strength. Numerical results, supported by a Gaussian variational model, reveal that localization can be controlled without altering the quasiperiodic potential, but rather by modulating interaction inhomogeneity. This Chapter is based on our work published in Journal of Physics B [200].

4.1 Introduction

The introduction related to Anderson Localization in SO coupled binary BECs has been quite extensively presented in Chapter 1. However, to make the Chapter self-contained here we provide a very brief overview of the series works that highlight the role of interaction and SO coupling in dictating the localization-delocalization transition of the condensate in presence of interaction.

Anserson Localization (AL) has attracted a great deal of attention in condensed

matter [2, 4, 7–9]. Following this such localization transitions have been observed other systems such as electromagnetic waves [10–14], microwaves [15–18], acoustic waves [19], quantum matter waves [36, 1], and in the non-interacting [21] and in the interacting Bose-Einstein condensates(BECs) [20].

Among the various platforms in recent years the localization in other complex system, binary BECs [201, 202, 122], SO coupled spinor BECs, etc. [105, 24, 128, 203, 124, 204] have become untenable source of platform to explore the rich Physics of localization-delocalization transitions. Theoretically, it has been demonstrated that the SO coupling influences the appearance of localization, whereas the Rabi coupling slightly promotes the delocalization [129]. Akin to SO coupling, interactions among atoms play a vital role in dictating the localization-delocalization phenomena in the condensate. For instance, several numerical studies show that the increase of repulsive interaction induces the localization to delocalization transitions for the condensate trapped in the disordered potential [23, 22, 123, 126, 120, 132]. Subsequent studies have reported the symmetry breaking of a localized binary condensate in the presence of inter-species and intra-species atomic interactions [120, 121]. Santos and Cardoso demonstrated that even with only one component subjected to the quasiperiodic potential, the interspecies interaction induces the localization in the other component [124].

Apart from the standard delocalization-localization transition, a new class of localization transition known as the reentrant localization transition in quasiperiodic lattices has attracted a great deal of attention in recent years. While in the conventional localization transition, the states after the localization transition remain localized with an increase in the disorder in the system, in the case of reentrant localization, the localized system delocalizes again before getting localized for the second time as a function of the quasiperiodic potential strength [205, 206]. This kind of behavior can also be described as localization-delocalization transition. Such intriguing reentrant localization has been studied extensively in recent years [207], including in non-Hermitian lattices [208], leading to their experimental observations [209–212]. In that context, few theoretical studies have been reported about intermediate critical phases where extended and localized states co-exist in the presence of spin-orbit interaction and quasiperiodic disordered potential in strongly correlated system [213–215]. In the continuum systems, however, this kind of localization-delocalization-localization behavior has not been analyzed with the same rigour as those in the strongly correlated system. Although a recent study has revealed the localization-delocalization transition upon variation of SO coupling in a *non-interacting* condensate trapped in a disordered

quasiperiodic potential [128]. However, a complete understanding of the reentrant localization for weakly *interacting* BECs is lacking.

In this Chapter, we present an extensive numerical study that explores the impact of inhomogeneous interactions in the localization of SO coupled BECs subjected to a quasiperiodic optical lattice potential. We consider the spatial dependent interactions induced by the external optical fields to have the same form as the quasiperiodic potential with the parameters depending on the intensity of the lasers [216, 217]. This setting leads to the localization of the condensate with the variation of interaction strength. However, by implementing an additional phase shift $\pi/2$ between the inhomogeneous interaction and trapping potential, we obtain the signature of localization-delocalization transition, where we find an intermediate delocalized phase sandwiched between two localized phases with the variation of the strength of the inhomogeneity of the nonlinearity. Furthermore, we complement this behavior in the localization through the Gaussian variational approach. At last, we obtain the signatures of such localization properties from the dynamical behavior of the condensate.

The Chapter is organized as follows. Section 4.2 introduces a mean-field theoretical model of SO coupled BEC with GPE framework trapped in a quasiperiodic potential and inhomogeneous interaction. Next, Section 4.3 presents the numerical and variational results, including the effect of inhomogeneous interactions and SO coupling parameters. In Section 4.3.5, the stability dynamics of localized and delocalized states are explored under velocity perturbations and quenching trap strength. Finally, in Section 4.4, we summarize this chapter.

4.2 Governing dynamical Mean-field equation and simulation details

We consider a pseudo spin-1/2 quasi-1D condensate with strong transverse confinement, modeled using the coupled Gross-Pitaevskii equations (GPEs) as [218–220]:

$$\mathrm{i}\frac{\partial\psi_\uparrow}{\partial t} = \left[-\frac{1}{2}\frac{\partial^2}{\partial x^2} + \left(g_{\uparrow\uparrow}|\psi_\uparrow|^2 + g_{\uparrow\downarrow}|\psi_\downarrow|^2\right) + V(x)\right]\psi_\uparrow - \mathrm{i}k_L\frac{\partial\psi_\uparrow}{\partial x} + \Omega\psi_\downarrow, \tag{4.1a}$$

$$\mathrm{i}\frac{\partial\psi_\downarrow}{\partial t} = \left[-\frac{1}{2}\frac{\partial^2}{\partial x^2} + \left(g_{\downarrow\downarrow}|\psi_\downarrow|^2 + g_{\downarrow\uparrow}|\psi_\uparrow|^2\right) + V(x)\right]\psi_\downarrow + \mathrm{i}k_L\frac{\partial\psi_\downarrow}{\partial x} + \Omega\psi_\uparrow, \tag{4.1b}$$

where $\psi_\uparrow$ and $\psi_\downarrow$ represent the wavefunctions for pseudo spin-up and spin-down components, respectively. Here, $g_{\uparrow\uparrow}$ and $g_{\downarrow\downarrow}$ are the intra-species nonlinearities for spin-up and spin-down components, and $g_{\uparrow\downarrow}$ represents the interspecies interaction strength. k_L is the SO coupling strength and Ω is the Rabi coupling strength. $V(x)$ represents the trapping potential. For our studies, we consider $g_{\uparrow\uparrow} = g_{\downarrow\downarrow} = g$. The wave functions follow the normalization condition as

$$\int_{-\infty}^{\infty} \left(|\psi_\uparrow|^2 + |\psi_\downarrow|^2 \right) dx = 2. \tag{4.2}$$

To obtain the non-dimensionalized Eq. (5.1), we consider the transverse harmonic oscillator length $a_\perp = \sqrt{\hbar/(m\omega_\perp)}$ as a characteristic length scale with $\omega_\perp$ as the transverse harmonic trapping frequency, ω^{-1} as the timescale and $\hbar\omega_\perp$ as the characteristic energy scale. The interaction parameters can be defined in terms of $g = 2Na_{\uparrow\uparrow}/a_\perp$, and $g_{\uparrow\downarrow} = 2Na_{\uparrow\downarrow}/a_\perp$, where $a_{\uparrow\uparrow}$ and $a_{\uparrow\downarrow}$ represent the intra-component and inter-component scattering lengths, respectively. The SO coupling is re-scaled as $k_L \equiv k_L' a_\perp$ and Rabi coupling as $\Omega \equiv \Omega'/(2\omega_\perp)$. The wavefunction is rescaled as $\psi_{\uparrow,\downarrow}(x,t) \equiv \psi'_{\uparrow,\downarrow}(x,t)\sqrt{a_\perp}$. Here, variables with prime represent the dimensional quantities.

To analyze the characteristics and dynamics of the localization of the condensate, we consider a quasiperiodic trapping potential $V(x)$ of the form [128],

$$V(x) = -V_1 \cos(k_1 x) - V_2 \cos(k_2 x), \tag{4.3}$$

where V_1 and V_2 are the primary and secondary optical lattice amplitudes, respectively. For all calculations, we consider the primary and secondary lattice strengths as $V_1 = 1$ and $V_2 = 0.1$, respectively, with the angular wavenumber ratio as the golden ratio, i.e., $k_2/k_1 = (\sqrt{5}+1)/2$. With this angular wave number, the wavelength of the laser beams will have the values as $\lambda_1 \approx 3.1415 a_\perp$ and $\lambda_2 \approx 1.9416 a_\perp$, respectively, where $a_\perp$ denotes the characteristic length scale approximately equal to 1.17μm. Note that in the experiment of Roati *et al.* [20], the ratio k_2/k_1 is 1.1971.

To make the parameters considered in numerical simulations experimentally feasible, we consider the two hyperfine states of ^{87}Rb atom as pseudo spin-up state $|\uparrow\rangle \equiv |F = 1, m_F = 0\rangle$, and pseudo spin-down state $|\downarrow\rangle \equiv |F = 1, m_F = -1\rangle$. Following the experiment of Lin *et al.* [105], we consider $N \sim 1.8 \times 10^5$ number of atoms in a harmonic trap strongly confined along the perpendicular direction with frequency $\omega_\perp \approx 2\pi \times 83.66$ Hz, and along the axial direction the trapping frequency is chosen to be $\omega_x \approx 2\pi \times 7.07$ Hz. In the experiment, the wavelength of the Raman lasers, $\lambda_L =$

804.1nm, and its geometry provide a tool for tuning the SO-coupling strength (k_L). The SO coupling strength k_L can be tuned within the range $k'_L = [0.1 - 4]a_\perp$ using a pair of Raman lasers. On the other hand, the intensity of the Raman lasers is attributed to the variation of Rabi coupling frequency Ω, where, in experiments, it can be adjusted within the interval $\Omega' = 2\pi \times [105.13 - 669.28]$Hz, which is associated to the dimensionless Rabi-coupling frequency $\Omega = [0.1 - 4]$. Furthermore, the interaction coefficients can be tuned by varying the number of atoms in a condensate.

One of the main focuses of the present work is to show the role of inhomogeneity in the interaction, describing the localization and delocalization of the condensate. For that, here we provide a generalized expression for the spatial dependence of the atomic scattering length depending upon the intensity $I(x)$ and detuning parameter of the laser beam. In general, the spatial dependence of the scattering length can be expressed as [76, 79, 216, 133],

$$a(x) = a^0 + \frac{\alpha I(x)}{\gamma_s + \beta I(x)}, \tag{4.4a}$$

$$a_{\uparrow\downarrow}(x) = a^0_{\uparrow\downarrow} + \frac{\alpha I(x)}{\gamma_s + \beta I(x)} \tag{4.4b}$$

Here, a^0 and $a^0_{\uparrow\downarrow}$ denote the intra- and interspecies s-wave scattering lengths when the optical fields are absent. α and β are the constants depending upon the laser detuning [79]. γ_s is the spontaneous decay rate between two atomic levels. In the experiment, the laser detuning is considered to be larger than the spontaneous decay rate, which minimizes the decay of the atomic state, which in turn helps to realize the optical Feshbach resonance. Here, $I(x)$ is the intensity of the laser beam generated due to the stimulated transition between two atomic states [77, 80, 81]. Note that the above formula is approximated from Eq. 1.22 from Chapter 1 for large detuning of the laser.

Theis *et al.* [79] experimentally demonstrated that the scattering length of ^{87}Rb condensate can be measured upon variation of laser detuning utilizing the optical Feshbach resonance technique. They estimated that the scattering length a is within the range $10a_0$ to $190a_0$, considering the background scattering length value of ^{87}Rb as $a^0 = 100a_0$, resulting in the variation of the scattering length in the range $-90a_0$ to $+90a_0$. One can tune the interaction from attractive to repulsive regions with the above technique. Recently, Carli *et al.* [221] experimentally demonstrated the dynamical evolution of BECs in a collisionally inhomogeneous environment. They observed various dynamical phases of expanding condensates in a quasi-1D geometry, including the formation, decay, and cascading of soliton-like phases. Their investigation of interaction

inhomogeneity opens new avenues for exploring various phenomena in BECs.

The spatial dependence of the scattering length $a(x)$ can be achieved using the space dependence intensity, $I(x)$ of the laser beam as described in Eq. (4.4a) and (4.4b). Without loss of generality, it is reasonable to consider the nonlinearity proportional to the optical lattice potential $V(x)$, as it is created using the laser field intensity [216, 222, 132]. In this work, we assume $a_{\uparrow\uparrow}(x) = a_{\downarrow\uparrow}(x) = a(x)$. With this consideration, $g_{\uparrow\uparrow}(x)$, $g_{\downarrow\downarrow}(x)$ and $g_{\uparrow\downarrow}(x)$ can be written as,

$$g_{\uparrow\uparrow}(x) = \epsilon_0 + \epsilon V(x), \tag{4.5a}$$

$$g_{\downarrow\downarrow}(x) = g_{\uparrow\uparrow}(x), \tag{4.5b}$$

$$g_{\uparrow\downarrow}(x) = \eta_0 + \eta V(x). \tag{4.5c}$$

Here, ϵ_0 and η_0 are the homogeneous interactions associated with the background scattering length. Similarly, ϵ and η denote the inhomogeneity interaction strength. Using the optical Feshbach resonance as the inhomogeneous interaction could be tuned independently compared to the homogeneous counterpart [79]. Therefore, for our analysis, we consider the homogeneous interaction as $\epsilon_0 = \eta_0 = 0$ to focus totally on the effect of the inhomogeneous part of the interaction on localization-delocalization [133, 123].

We also consider a scenario where the trapping potential (4.3) and spatially dependent nonlinear interactions (4.5a)-(4.5c) have a phase difference θ_1, θ_2. With this, the nonlinear interactions take the form:

$$g_{\uparrow\uparrow}(x) = -\epsilon \sum_{l=1}^{2} V_l \cos\left(k_l x - \theta_1\right), \tag{4.6a}$$

$$g_{\uparrow\downarrow}(x) = -\eta \sum_{l=1}^{2} V_l \cos\left(k_l x + \theta_2\right). \tag{4.6b}$$

Here, V_l denotes the optical lattice amplitude, identical to V_1 and V_2 as described in Eq. 4.3. Similarly, k_l represents the angular wavenumber corresponding to the wavelength of the laser beam. Both V_l and k_l are kept the same as the quasiperiodic potential (Eq. 4.3). In our case, we consider two scenarios: (i) $\theta_1 = \theta_2 = \theta = 0$, and (i) $\theta_1 = \theta_2 = \theta = \pi/2$. For the first case, the spatial inhomogeneity is the same as the quasiperiodic potential with $\theta = 0$. In contrast, the $\theta = \pi/2$ introduces a phase shift between interaction inhomogeneity and quasiperiodic potential. To further generalize our analysis, we also explore cases with unequal phase shifts, i.e., $\theta_1 \neq \theta_2$, between the

interaction and the quasiperiodic potential as discussed in 4.3.3.2.

The dynamical equations [Eqs. (4.1a) and (4.1b)] are solved using the split-step Crank-Nicholson method [156, 223, 224] with the box size as $[-102.4 : 102.4]$, space step $\Delta x = 0.025$ and time step $\Delta t = 10^{-4}$. For all simulations, we consider the Gaussian wavefunction centered at zero as an initial state for both components and also assume the antisymmetric condition $\psi_\uparrow(x) = -\psi_\downarrow(-x)$ between the components as it represents the ground state of the Hamiltonian with lowest energy [123, 225]. While solving the dynamical equations, we employ an imaginary-time scheme to obtain the ground state and a real-time propagation scheme to investigate the condensate dynamics.

4.3 Results

In this section, we present the effect of the inhomogeneous interaction and the Rabi and SO coupling on the spatial profile of the ground state obtained using the imaginary time propagation. First, we focus on analyzing the impact of the inhomogeneity on the localization of the ground state. Following this, we investigate the effect of phase shift between the interaction and potential in bringing the interesting interplay between the localized and delocalized states that finally leads to the manifestation of the localization-delocalization features of the localization with a change in the interaction inhomogeneity. We complement our numerical observation by employing the Gaussian variational approach. Finally, we present a detailed analysis of the dynamics of the localized and delocalized states induced by several means, namely, by giving small velocity perturbations and quenching of the potential.

4.3.1 Effect of interaction inhomogeneity on the Localization-delocalization transition of the condensate

In a recent work, Li *et al.* [128] demonstrated that the condensate remains localized for a higher ratio of secondary to the primary optical lattice strength (V_2/V_1) for the entire range of SO and Rabi coupling parameters. However, for small $V_2/V_1(\sim 0.1)$, the condensate exhibits a delocalized nature, which undergoes a transition to the localized state upon either increasing the Rabi coupling for a fixed SO coupling or increasing the SO coupling for a fixed Rabi coupling.

While in the former case, the condensate remains delocalized with a small value of SO coupling strength, whereas, for moderate SO coupling strength, the condensate

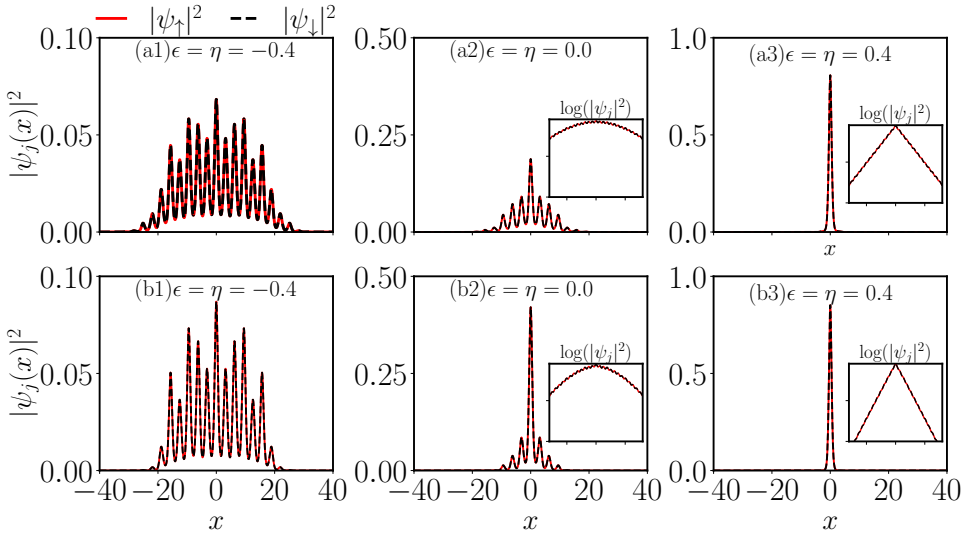

Figure 4.1: Density profile of $|\psi_\uparrow|^2$ (red line) and $|\psi_\downarrow|^2$ (dashed black line) components for different inhomogeneity parameter $\epsilon = \eta = -0.4$ (a1,b1), $\epsilon = \eta = 0$ (a2,b2), and $\epsilon = \eta = 0.4$ (a3,b3) at $k_L = 0$, $\Omega = 0.0$ (upper panel) and $k_L = 0.6, \Omega = 1$ (lower panel). Insets in [(a2, a3, b2, b3)] show the spatial variation of density profile in semilog scale that explicitly displays the exponential tail of the localized condensate in (a3) and (b3).

remains localized at high Rabi coupling. In the latter case, it shows the localization-delocalization behavior with the change in the SO coupling for small Rabi coupling. In this work, we aim to explore the effect of interaction inhomogeneity alongside the SO and Rabi coupling parameters on the state of the condensate, which is initially delocalized when no inhomogeneity or coupling parameters are included. In the following, we will examine how these factors, namely, inhomogeneity and the coupling parameters overall, affect the condensate's localization by fixing the lattice strength ratio as $V_2/V_1 = 0.1$.

In Fig. 4.1, we show the spatial profile of the density for different sets of spatial inhomogeneity parameters by considering the coupling parameters as $\Omega = 0$, $k_L = 0$ (left column) and $\Omega = 1$, $k_L = 0.6$ (right column). In the absence of the SO and Rabi coupling, the condensate density profile exhibits a delocalized nature for zero ($\epsilon = \eta = 0$) and attractive inhomogeneity ($\epsilon = \eta = -0.4$) as depicted in the Figs. 4.1(a2) and (a1), respectively. The condensate starts showing a tendency to localization for the repulsive inhomogeneous interaction, quite evident with the exponential tail as shown in the inset of Fig. 4.1(a3). As we consider the SO and the Rabi coupling to a finite value, we find that the spatial spread of the condensate becomes narrower compared to those with the coupling parameters for the attractive and zero inhomogeneity parameters, which is quite evident from the Fig. 4.1(b1) and (b2), respectively. Here, it is interesting

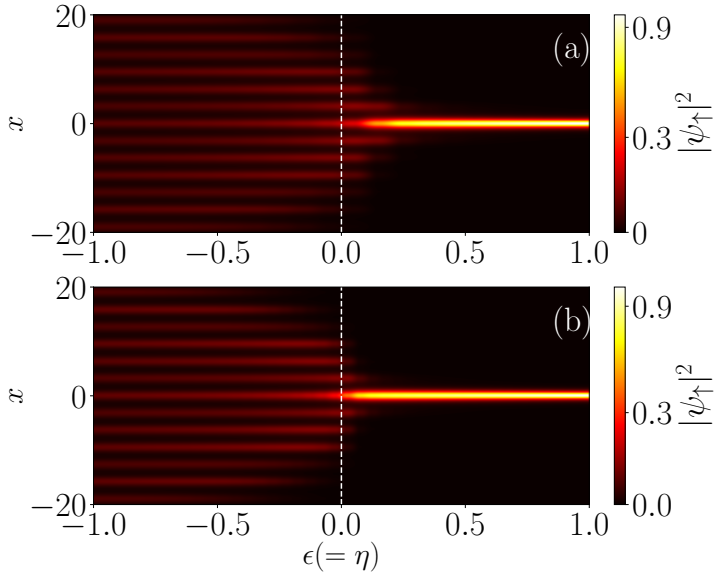

Figure 4.2: Pseudo color representation of the spatial variation of ground state density of the spin-up component ($|\psi_\uparrow|^2$) with the inhomogeneity parameter $\epsilon = \eta$ for (a) $k_L = 0$, $\Omega = 0$ and (b) $k_L = 0.6$, $\Omega = 1.0$. For the zero coupling parameter, the condensate exhibits a delocalized state for $\epsilon = \eta \lesssim 0.2$ and a localized state for $\epsilon = \eta > 0.2$. However, for finite coupling parameter ($\Omega = 1$, $k_L = 0.6$) the localization state is realized for $\epsilon = \eta \gtrsim 0$. Here, the white dashed line is drawn at $\epsilon = \eta = 0$ to compare the effect of k_L and Ω.

to note that even for repulsive inhomogeneity, the condensate exhibits the localization [Fig. 4.1(b3)] contrary to the situation when inhomogeneity is absent. Note that, in the absence of inhomogeneity, even a small repulsive nonlinear interaction destroys the localization of the condensate [164].

To investigate the effect of inhomogeneity in a more systematic way in Fig. 4.2, we show the pseudocolour density profile of the condensate with a continuous variation of the inhomogeneity parameter for zero [Fig. 4.2(a)] and finite couplings, $\Omega = 1$ and $k_L = 0.6$ [Fig. 4.2(b)]. For this case, we find that the condensate remains delocalized for the entire range of the attractive interaction inhomogeneity as well as for small repulsive interaction inhomogeneity. However, we witness localization for larger repulsive inhomogeneity interactions. The overall features indicate that for zero coupling parameters ($\Omega = k_L = 0$), the density gets localized for $\epsilon(= \eta) \gtrsim 0.2$. However, with $k_L = 0.6$ and $\Omega = 1$, the condensate display localization even without interaction inhomogeneity ($\epsilon(= \eta) \gtrsim 0$). This particular feature suggests an interplay between interaction inhomogeneity and the coupling parameters towards the localization of the condensate. On the one hand, while the attractive inhomogeneity tends to delocalize the condensate, the coupling parameters try to restore the localization. To shed more light on this aspect, in the following, we will present a systematic analysis of the role

of these competing factors on delocalization, which will be connected further to bring the localization-delocalization behavior of the condensate in a similar line observed in the many-body system [205].

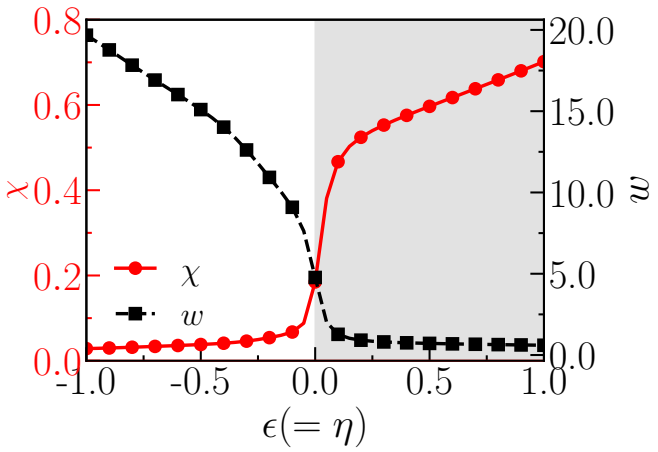

Figure 4.3: The IPR χ (red circle marked solid line) and the width w (black square marked dashed line) of the condensate as a function of inhomogeneity parameter $\epsilon(=\eta)$ for $k_L = 0.6$ and $\Omega = 1.0$. The increase in χ is accompanied by a decrease in the width of the condensate, which starts beyond the critical inhomogeneity parameter $\epsilon(=\eta) \geq 0.1$, indicating a transition from the delocalized to localized state. The localized range is shown with the grey-shaded area. Here, the left and right vertical axis shows the variation of χ and w, respectively.

The extent of localization and delocalization of the condensate has been characterized using two quantities, namely, the inverse participation ratio (IPR) χ and the width (w) of the condensate, which are defined as [128, 205],

$$\chi_j = \frac{1}{N_j^2}\int |\psi_j|^4 dx, \tag{4.7a}$$

$$w_j^2 = 2\int (x - x_m)^2 |\psi_j|^2 dx, \tag{4.7b}$$

where $N_j = \int_{-\infty}^{\infty} |\psi_j(x)|^2 dx$ represents the population of the j^{th} component of the condensate with $j \in \{\uparrow, \downarrow\}$ and x_m is the center of mass of the condensate. Since we choose equal number of atoms in each component, the condensate density remains same in both components, and hence, the IPR and width can be considered as $\chi_\uparrow = \chi_\downarrow \equiv \chi$ and $w_1 = w_2 \equiv w$, respectively. Consequently, we show the results pertaining solely to the spin-up components. Please note that in general the state of the condensate is categorized broadly in localized state (for $\chi \gtrsim 0.5$) and delocalized state (for $\chi \lesssim 0.5$) [128]. However, here, based on the real space profile of the condensate, which appears to span over a very localized region, we have introduced the three states of the condensate localization. We set the criteria that the condensate can be characterized as in the

localized state if $\chi \geq 0.5$. Otherwise, for the lower IPR ($0.3 \lesssim \chi \lesssim 0.5$), the condensate is in the intermediate localized state and the delocalized state for ($\chi \lesssim 0.3$).

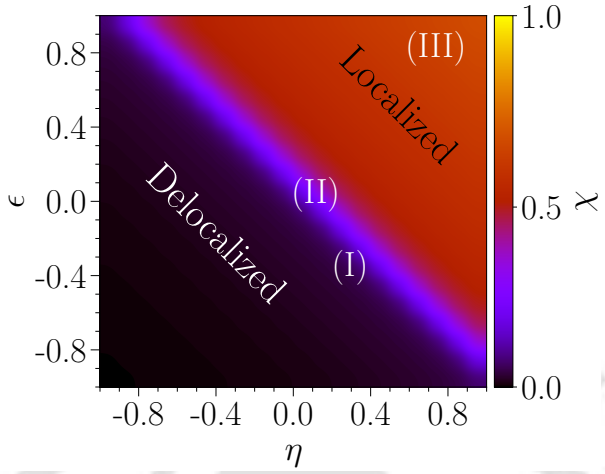

Figure 4.4: Pseudo color representation of the IPR (χ) in the $\epsilon - \eta$ plane for $k_L = 0.6$ and $\Omega = 1.0$. For $\chi \gtrsim 0.5$, the condensate is characterized in the localized state, while with $\chi < 0.5$, it is termed as delocalized. Three distinct regions, I, II, and III, represent the delocalized, intermediate localized, and localized states.

In Fig. 4.3, we illustrate the variation of the IPR (in the left vertical axis) and width (in the right vertical axis) of the condensate with respect to the change in the interaction inhomogeneity, considering the equal inter- and intra-interaction ($\epsilon = \eta$). In accordance with the above discussion, we find that the χ remains close to zero for attractive interaction inhomogeneity ($\epsilon = \eta < 0$), indicating the delocalized state of the condensate and increases to $\chi \sim 0.5$ as soon as inhomogeneity gets tuned towards the repulsive region ($\epsilon = \eta \gtrsim 0$). This trend further continues by increasing the interaction inhomogeneity. Overall, we find that the slightly repulsive nature of the interaction inhomogeneity is good enough to localize the condensate. This feature of χ in characterizing the localization of the condensate is very well complemented by the variation of the width (w) of the condensate, as shown using the black dashed squared line in Fig. 4.3. The width remains high ($w \gtrsim 5$) until ($\epsilon = \eta < 0$), for which the condensate remains delocalized. In the case of the localized condensate for repulsive interactions, the condensate width becomes nearly equal to one. To understand the effect of the interaction inhomogeneity on the localization of the condensate, we perform an extensive simulation for different ranges of interaction inhomogeneity ($|\epsilon| = |\eta| < 1$) by keeping the SO and Rabi coupling fixed at $k_L = 0.6$ and $\Omega = 1$. In Fig. 4.4, we present the pseudo color of IPR χ in the $\epsilon - \eta$ plane. Here, we have used the criteria, $\chi \gtrsim 0.5$, to designate the state of the condensate as a localized state. When both intraspecies (ϵ) and interspecies (η) are positive, the condensate remains in the localized state with

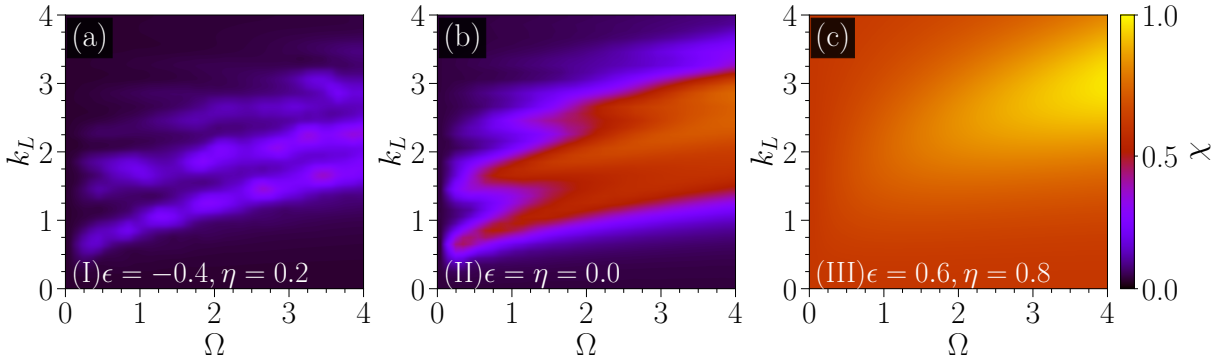

Figure 4.5: Pseudo color representation of the IPR χ in $k_L - \Omega$ plane in three distinct regions of the inhomogeneity parameters as indicated in the Fig. 4.4: (a) for $\epsilon = -0.4$, and $\eta = 0.2$ in the region I, (b) for $\epsilon = \eta = 0.0$ in region II, and (c) for $\epsilon = 0.6, \eta = 0.8$ in region III. Regions I and III remain in the delocalized and localized states for all ranges of Ω and k_L. Region II exhibits the localization-delocalization transition upon tuning the SO and Rabi coupling.

$\chi \gtrsim 0.6$. However, if both interactions are attractive, the IPR remains in the range $0.03 \leq \chi \leq 0.1$, indicating the delocalized state of the condensate.

Next, we present the effect of SO (k_L) and Rabi (Ω) couplings on the localization and delocalization of the condensate with spatial-dependent interactions. For this analysis, we select three sets of parameters ϵ, and η of Fig. 4.4. These parameters are associated with three different regions: region I with $\epsilon = -0.4, \eta = 0.2$, region II with $\epsilon = \eta = 0.0$, and region III with $\epsilon = 0.6$, $\eta = 0.8$, as marked in Fig. 4.4.

In Fig. 4.5(a) we show the phase diagram in $k_L - \Omega$ plane for $\epsilon = -0.4$, and $\eta = 0.2$. We notice that the IPR χ remains within the range $0 \lesssim \chi \lesssim 0.4$ for all ranges k_L and Ω, revealing that the condensate still associates with the delocalized state. Fig. 4.5(b) illustrates the χ in the $\Omega - k_L$ plane for the region II ($\epsilon = \eta = 0$) located at the phase boundary between the delocalized and localized phases in the $\epsilon - \eta$ plane (see Fig. 4.4). Furthermore, for this case, χ lies within the range $0.1 \lesssim \chi \lesssim 0.75$, implying a transition from delocalized to the localized state of the condensate. We further find the localization-delocalization transition as SO coupling is increased in the range $0 \leq k_L \leq 4$ while keeping Ω fixed at a low value ($\Omega \sim 1$). Similar localization-delocalization phase transition has also been reported earlier by Li *et al.* [128] by tuning the k_L for non-interacting condensate. After the comprehensive picture of the condensate phase in $\Omega - k_L$ plane for the non-interacting case, next, we consider repulsive inhomogeneous interactions with $\epsilon = 0.6$, $\eta = 0.8$ marked as region III in Fig. 4.4. For this case, the χ value lies within $0.60 \lesssim \chi \lesssim 1.0$, suggesting a complete localization of the condensate as shown in Fig. 4.5(c). Interestingly, we find that the condensate becomes strongly localized ($\chi \sim 1$) for high SO and Rabi coupling parameters, even

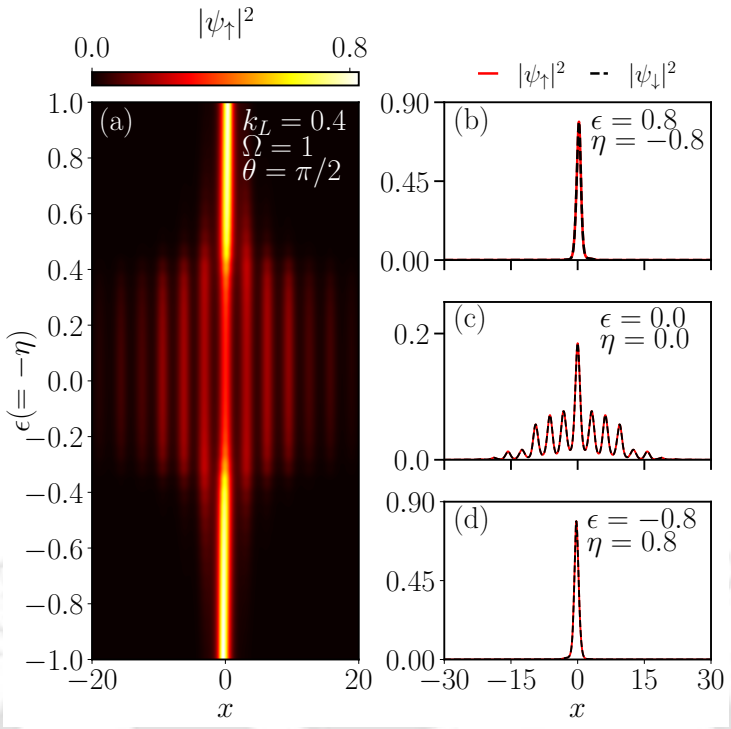

Figure 4.6: Effect of inhomogeneity on the density profile of the condensate for $\pi/2$ phase difference between the nonlinearity and potential with $k_L = 0.4$ and $\Omega = 1.0$. (a) Pseudo color representation of density spatial profile with respect to the inhomogeneous interaction parameter $\epsilon(=-\eta)$. (b)-(d) spatial density profile for $\epsilon(=-\eta) = 0.8$ (localized), $\epsilon(=-\eta) = 0$ (delocalized), and (d)$\epsilon(=-\eta) = -0.8$ (localized). The condensate undergoes localization-delocalization-localization phases upon increasing the strength of the inhomogeneity from the attractive to repulsive region.

when the interactions in the condensate are repulsive, in contrast to the homogeneous interaction where the repulsive interaction weakens the localization [164]. In the latter part of the Chapter, we will relate the enhancement of the localization, which occurs with an increase in the repulsive interactions in the presence of spatial inhomogeneity, to the growing nature of the depth of the effective potential of the condensate, as derived using the variational approach.

4.3.2 Localization-delocalization transition in presence of collisional inhomogeneities

In the previous section, we investigated the effect of spatially inhomogeneous interaction for the case when the spatial inhomogeneity in the nonlinear interaction is similar to that of the quasiperiodic potential. Next, we consider the situation when there happens to be $\pi/2$ phase difference between the trapping potential and inhomogeneous interactions as given in Eqs. (4.6a) and (4.6b).

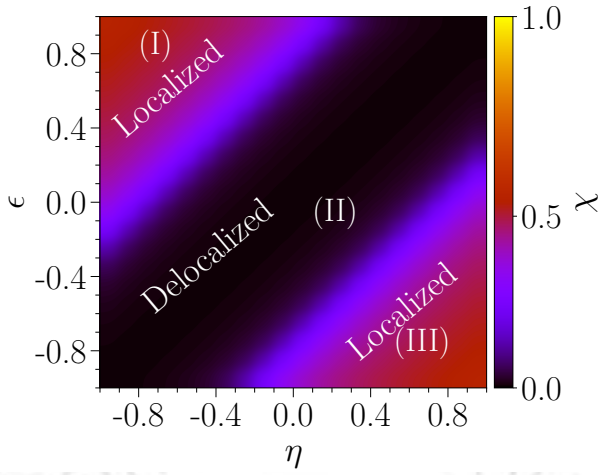

Figure 4.7: Pseudo color representation of the IPR χ in the $\epsilon - \eta$ plane showing localization-delocalization-localization feature of the condensate for $\pi/2$ phase between the inhomogeneity and potential. The parameters are $k_L = 0.4$, $\theta = \pi/2$, and $\Omega = 1.0$. Localized ($\chi \gtrsim 0.5$), intermediate localized ($0.3 < \chi \lesssim 0.5$) and delocalized ($\chi \lesssim 0.3$) have been observed. I, II, and III denote the three distinct regimes in the inhomogeneous parameters space chosen to investigate the effect of Ω and k_L on the localization and delocalization.

In Fig. 4.6(a), we present the variation of the condensate density with the inhomogeneous interaction strength ϵ and η by assuming $\epsilon = -\eta$. We find that the condensate exhibits localization for $-0.4 \gtrsim \epsilon(= -\eta) \gtrsim -1.0$, $0.4 \lesssim \epsilon(= -\eta) \lesssim 1.0$ while, it displays delocalized nature $-0.4 \lesssim \epsilon(= -\eta) \lesssim 0.4$ as the coupling parameters are fixed to $k_L = 0.4$ and $\Omega = 1$. In Figs. 4.6(b)-(d), we show the density profile for three sets of parameters $\epsilon = -\eta = 0.8$, $\epsilon = -\eta = 0$, and $\epsilon = -\eta = 0.8$, respectively. In the case of Fig. 4.6(b), the condensate is localized at $x_0 \approx 0.3$, whereas in Fig.4.6(d), the condensate is localized at $x_0 \approx -0.3$. The shifting of the center of mass of the condensate is explained further using the effective potential using the variational approach in Sec. 4.3.3. In contrast, Fig. 4.6(c) illustrates a completely delocalized phase of the condensate in the absence of inhomogeneity.

Next, to get a comprehensive picture of the localized and delocalized phases due to the effect of the inhomogeneities, we show the pseudo-color representation of χ in the $\epsilon - \eta$ plane for $\Omega = 1$ and $k_L = 0.4$ in Fig. 4.7. We noted that the delocalized region, where χ remains near zero, is sandwiched between two localized regions with $\chi \gtrsim 0.5$. This particular feature of the localization-delocalization transition with interaction inhomogeneities closely resembles the reentrant localization feature in previous studies using the Aubrë-Andre models [205]. Note that as we consider $\theta_1 = \theta_2 = \pi/2$, the symmetry of the Hamiltonian remains intact, and so the localization-delocalization-localization appears to be symmetric with respect to $\epsilon \to -\epsilon, \eta \to -\eta$. However,

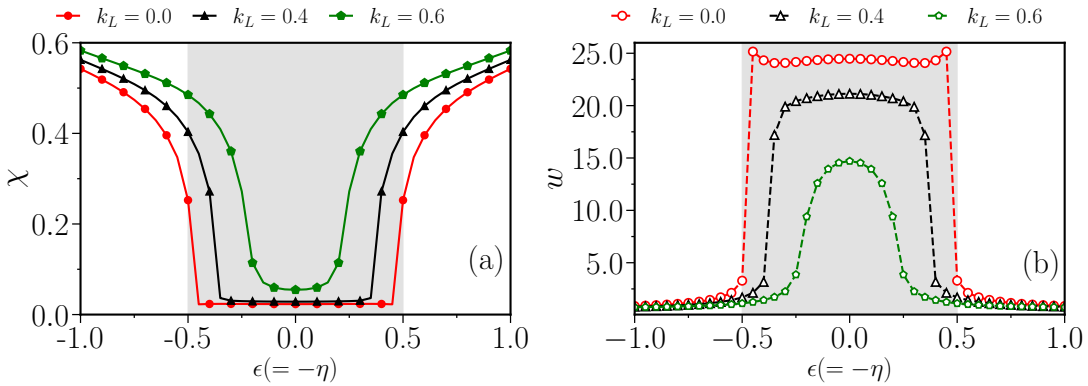

Figure 4.8: Variation of (a) IPR (χ) and (b) width (w) of the condensate as a function of the interaction inhomogeneity parameter $\epsilon = -\eta$ for $k_L = 0$ (red circles), $k_L = 0.4$ (black triangle), and $k_L = 0.6$ (green pentagons) by fixing $\Omega = 1$. Increasing k_L reduces the range of inhomogeneity parameters in which delocalization is observed.

this symmetry breaks as we destroy the symmetry of the Hamiltonian by considering $\theta_1 \neq \theta_2$. In the following, we provide one example for $\theta_1 \neq \theta_2$ to show the asymmetric nature of the transition.

Further, we analyze the effect of spin-orbit coupling parameters on the localization-delocalization. In Fig. 4.8(a), we show the variation of IPR χ with the interaction inhomogeneity $\epsilon(= -\eta)$ at three different values of $k_L = 0.0, 0.4$ and 0.6. Conversely, Fig. 4.8(b) illustrates the condensate width w for the same values of k_L. In figure (a), for the case of $k_L = 0.4$, one can notice that the IPR increases between $0.4 \leq \chi \leq 0.6$ in between $\epsilon(= -\eta) \lesssim -0.5$ and $\epsilon(= -\eta) \gtrsim 0.5$, resembling the localized regions. On the other hand, the χ value remains almost constant ($\chi \sim 0$) in between $-0.5 \lesssim \epsilon(= -\eta) \lesssim 0.5$ depicting the delocalized region. Conversely, the condensate width w complements the IPR χ by showing $w \lesssim 1$ in the localized regions, and in the delocalized region the width becomes $w \gg 1$. Another notable fact is that with the increment of k_L from zero, the minimum value of χ in the delocalized region and the maximum value in the localized region increase. For instance, in the delocalized region, the χ value remains in the order of $\sim \mathcal{O}(10^{-2})$, whereas the localized region is featured with a larger χ value greater than > 0.5. Also, one may notice that the delocalized region (grey shaded region) shrinks as the k_L value increases with the variation of $\epsilon(= -\eta)$. On the other hand, the condensate width w (dashed line with open markers) nicely complements the IPR behaviour by showing a larger value of $w \gtrsim 10.0$ in delocalized regions and a smaller value $w \lesssim 1.0$ in localized regions.

Next, in Fig. 4.9(a,b), we show the pseudocolor density profile representation as a function of $(\epsilon = -\eta)$ for the cases $\theta_1 = \theta_2 = \pi/2$ and $\theta_1 = \pi/2, \theta_2 = \pi/3$, respectively. At one hand for $\theta_1 = \theta_2 = \pi/2$ the localization-delocalization transition takes place for

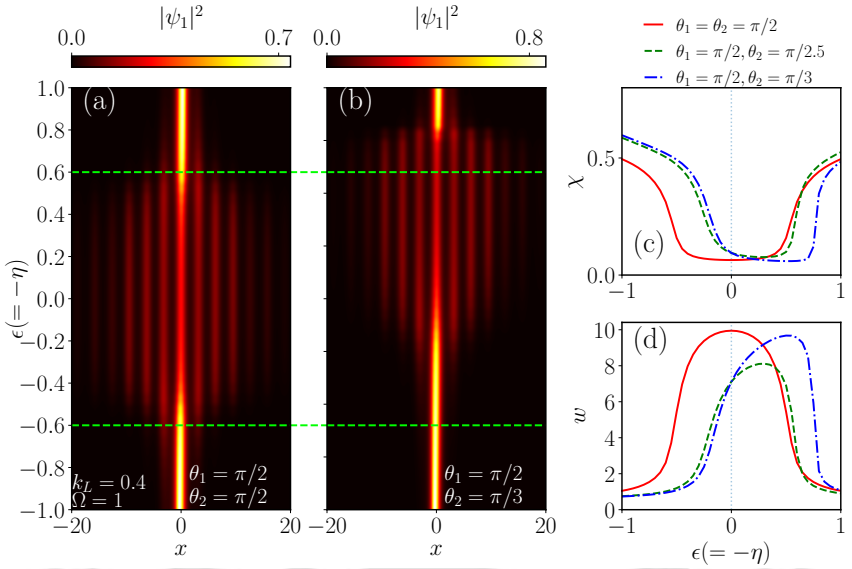

Figure 4.9: Pseudocolor representation of the spatial variation of the ground state density of the spin-up component ($|\psi_1|^2$) with the inhomogeneity parameter $\epsilon(=-\eta)$ for (a) $\theta_1 = \theta_2 = \pi/2$, and (b) $\theta_1 = \pi/2$, $\theta_2 = \pi/3$. Upon choosing $\theta_1 = \theta_2$ results in the symmetric localized and delocalized regions about $\epsilon = -\epsilon$ while $\theta_1 \neq \theta_2$ leads to break that symmetry about $\epsilon = -\epsilon$ as shown in (b). Variation of (c) form-factor χ, and (d) width w of the condensate as a function of interaction inhomogeneity $\epsilon = (-\eta)$. Upon inclusion of unequal θ_1, and θ_2 in interaction inhomogeneity leads to break the symmetry about $\epsilon = -\epsilon$. The coupling parameters are considered at $k_L = 0.4$, $\Omega = 1.0$. The green dashed line is drawn to compare the symmetric delocalized region in Figure (b) with (a).

$\epsilon \to -\epsilon, \eta \to -\eta$, but for $\theta_1 = \pi/2$, $\theta_2 = \pi/3$ the transition is not symmetrical about $(\epsilon \to -\epsilon, \eta \to -\eta)$ [see Fig. 4.9(b)]. To make our claim more concrete in Figs. 4.9(c,d), we plot the form-factor χ and the width w of the condensate, for various combination of the phase factor in the interaction inhomogeneity, such as (a) $\theta_1 = \theta_2 = \pi/2$, (b) $\theta_1 = \pi/2$, $\theta_2 = \pi/2.5$, as (c) $\theta_1 = \pi/2$, $\theta_2 = \pi/3$. It is evident that upon choosing $\theta_1 \neq \theta_2$, the symmetry in the appearance of localization-delocalization transition with respect to the change in the sign of the interaction of the inhomogeneity parameter ceases to exist. Therefore, the symmetrical behavior of localization-delocalization transition can be broken by choosing different phase shift between the interaction inhomogeneity and the quasiperiodic potential.

In order to get a more comprehensive picture, we construct the phase diagram in $k_L - \Omega$ plane by keeping ϵ and η fixed at different regions, i.e., (I), (II), and (III) as shown in Fig. 4.7. The phase diagram in Fig. 4.10(a) corresponds to the localized region at (I) ($\epsilon = -\eta = 0.8$) where the χ value lies within the range $0.49 \lesssim \chi \lesssim 0.88$, clearly demonstrating the localized feature of the condensate. On the other hand, when we decrease the interaction parameters towards delocalized region such as region (II) ($\epsilon = -\eta = -0.1$), the associated IPR in Fig. 4.10(b) exhibits similar localization-

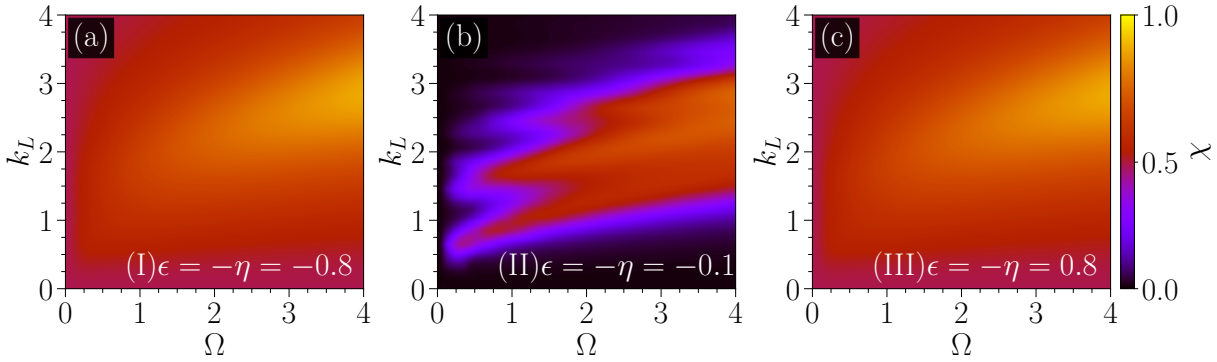

Figure 4.10: Pseudo color representation of the IPR in the $\Omega - k_L$ plane in three distinct regions (I, II, and III) of interaction inhomogeneity parameter space as shown in the Fig. 4.7: (a) $\epsilon = -\eta = 0.8$, region I, (b)$\epsilon = -\eta = -0.1$, region II, and (c) $\epsilon = -\eta = -0.8$, region III. Both regions I and III exhibit the localization for all ranges of Ω and k_L, while region II displays a localization-delocalization transition by varying k_L for Ω close to 1.

delocalization phenomenon as shown previously in Fig. 4.5(b). Next, Fig. 4.10(c) corresponds to the region (III) ($\epsilon = -\eta = -0.8$), which shows the localized condensate for all the range of coupling parameters.

So far, our investigations have mainly focused on numerical analysis through which we have characterized various localized and delocalized regions with variations in interactions as well as the coupling strength of the system. To understand localization-delocalization transitions, either by tuning the coupling parameters or changing the interaction strengths, we adopt the Gaussian variational approach in the following.

4.3.3 Role of inhomogeneity in the localization-delocalization transition

In this section, using the variation approach, we present a plausible explanation for the observation of localization-delocalization obtained using the numerical simulation, as presented in Sec. 4.3.2. In what follows, we discuss the analytical model using the variational approach to disentangle the role of different localizing and delocalizing factors in spatially inhomogeneous SO-coupled BECs.

4.3.3.1 Variational analysis

Using the time-dependent variational approach [24], the Lagrangian density of Eqs. (4.1a) and (4.1b) can be written as,

$$\mathcal{L} = \sum_{j=1}^{2} \left\{ \frac{i}{2}\left(\psi_j^*\dot{\psi}_j - \psi_j\dot{\psi}_j^*\right) - (-1)^j \frac{i}{2}k_L\left[\psi_j^*\psi_j' - \psi_j(\psi_j^*)'\right] - \frac{1}{2}|\psi_j'|^2 - \frac{1}{2}g(x)|\psi_j|^4 \right.$$
$$\left. - V(x)|\psi_j|^2 \right\} - g_{12}(x)|\psi_1|^2|\psi_2|^2 - \Omega\left(\psi_1^*\psi_2 + \psi_1\psi_2^*\right). \tag{4.8}$$

Here, we slightly changed the notation as $j \in \{\uparrow,\downarrow\} \equiv \{1,2\}$ in variational approximation only for convenience. Otherwise, it remain $\{\uparrow,\downarrow\}$. In the equation, the asterisk denotes the complex conjugate, the prime represents the derivative (d/dx), and the overdot denotes the time derivative (d/dt). Here, the notation $j = 1$ and 2 refers to the spin-up and spin-down components, respectively.

To obtain the corresponding dynamical equations, we use the Gaussian Ansatz with time-dependent variational parameters N_j, w_j, β_j, x_{0_j}, and ϕ_j of the form:

$$\psi_j(x,t) = \frac{1}{\pi^{1/4}}\sqrt{\frac{N_j}{w_j}}\exp\left[-\frac{(x-x_{0_j})^2}{2w_j^2}\right] \times \exp\left[(-1)^j i\beta_j(x-x_{0_j}) + i\phi_j\right], \tag{4.9}$$

where N_j is the number of atoms, w_j represents the width of the condensate centered at x_{0_j}, β_j and ϕ_j are respectively the chirp and phase of the condensate with a Gaussian profile. At this stage, it will be worthwhile to point out that the variational Ansatz is more appropriate to comprehend the characteristics of the localized region of the condensate, not the behavior of the delocalized regions. To complement the delocalized state using the variational analysis, one needs to consider the superposition of more than one Gaussian wavefunction that will contain a large number of variational parameters and will come with added complexities. The effective Lagrangian with the Gaussian Ansatz can be obtained by substituting Eq. (4.9) into Eq. (4.8) and integrating over space variable with the potential Eq. (4.3) and the nonlinearity Eq. (4.6). The detailed calculation for the dynamical equation of motion using the Lagrangian given

as,

$$L = \sum_{j=1}^{2} \Bigg[N_j(-1)^j \beta_j \dot{x}_{0_j} - N_j \dot{\phi}_j + N_j \beta_j k_L - \frac{N_j}{2}\left(\frac{1}{2w_j^2} + \beta_j^2\right) - \frac{N_j}{2^{3/2}\sqrt{\pi} w_j} \Bigg[\epsilon_0 - \epsilon \sum_{l=1}^{2} V_l \cos\left(k_l x_{0_j}\right) \exp\left(-\frac{k_l^2 w_j^2}{8}\right) \Bigg] + N_j \sum_{l=1}^{2} V_l \cos\left(k_l x_{0_j}\right) \exp\left(-\frac{k_l^2 w_j^2}{4}\right) \Bigg] - \frac{N_1 N_2}{\sqrt{\pi}\sqrt{w_1^2 + w_2^2}} \exp\left(-\frac{(x_{01} - x_{02})^2}{w_1^2 + w_2^2}\right) \times \Bigg[\eta_0 - \eta \sum_{l=1}^{2} V_l \cos\left(\frac{k_l \left(w_1^2 x_{0_2} + w_2^2 x_{0_1}\right)}{w_1^2 + w_2^2}\right) \times \exp\left(-\frac{k_l^2 w_1^2 w_2^2}{4\left(w_1^2 + w_2^2\right)}\right) \Bigg] - 2\sqrt{N_1 N_2} L_\Omega, \tag{4.10a}$$

where

$$L_\Omega = \Omega \sqrt{\frac{2w_1 w_2}{(w_1^2 + w_2^2)}} \cos\left[\frac{\left(\beta_1 w_1^2 - \beta_2 w_2^2\right)\left(x_{0_1} - x_{0_2}\right) - \phi\left(w_1^2 + w_2^2\right)}{w_1^2 + w_2^2}\right] \times \exp\left(-\frac{(x_{0_1} - x_{0_2})^2 + (\beta_1 + \beta_2)^2 w_1^2 w_2^2}{2(w_1^2 + w_2^2)}\right), \tag{4.10b}$$

with $\phi = \phi_2 - \phi_1$, and $\rho = x_{0_1} - x_{0_2}$ The Euler-Lagrangian equation associated with variational parameters α_j is given by

$$\frac{\partial L}{\partial \alpha_j} - \frac{d}{dt}\frac{\partial L}{\partial \dot{\alpha}_j} = 0, \tag{4.11a}$$

where α_j corresponds to the variational parameters N_j, β_j, ϕ_j, x_{0_j}, and w_j.

Therefore, the Euler equation of motion associated to x_{0_j} is given by

$$\dot{x}_{0_j} = (-1)^{1-j}\left[-k_L + \beta_j + \sqrt{\frac{N_{3-j}}{N_j}}\,\frac{\partial L_\Omega}{\partial \beta_j}\right]. \tag{4.11b}$$

Further, the equation of motion associated with N_j can be written as:

$$\dot{N}_j = (-1)^j 2\Omega\sqrt{N_1 N_2}\sqrt{\frac{2w_1 w_2}{w_1^2 + w_2^2}} \sin\left[\frac{\left(\beta_1 w_1^2 - \beta_2 w_2^2\right)\left(x_{0_1} - x_{0_2}\right)}{\left(w_1^2 + w_2^2\right)} - \phi\right], \times \exp\left[-\frac{\left(x_{0_1} - x_{0_2}\right)^2 + \left(\beta_1 + \beta_2\right)^2 w_1^2 w_2^2}{2\left(w_1^2 + w_2^2\right)}\right]. \tag{4.11c}$$

The Euler equation of motion corresponding to ϕ_j is given by

$$\dot{\phi}_j = -\frac{1}{4w_j^2} + \frac{\beta_j^2}{2} - \frac{N_j}{\sqrt{2\pi}w_j}\left[\epsilon_0 - \epsilon\sum_{l=1}^{2} V_l \cos\left(k_l x_{0j}\right)\exp\left(-\frac{k_l^2 w_j^2}{8}\right)\right]$$
$$-\frac{N_{3-j}}{\sqrt{\pi\left(w_1^2+w_2^2\right)}}\exp\left(-\frac{\left(x_{0_1}-x_{0_2}\right)^2}{w_1^2+w_2^2}\right)\left[\eta_0 - \eta\sum_{l=1}^{2} V_l\cos\left(k_l\frac{w_1^2x_{0_2}+w_2^2x_{0_1}}{w_1^2+w_2^2}\right)\right.$$
$$\left.\exp\left(-\frac{k_l^2w_1^2w_2^2}{4(w_1^2+w_2^2)}\right)\right] - \sqrt{\frac{N_{3-j}}{N_j}}L_\Omega + \beta_j\sqrt{\frac{N_{3-j}}{N_j}}\frac{\partial L_\Omega}{\partial\beta_j}$$
$$+\sum_{l=1}^{2} V_l\cos\left(k_l x_{0_j}\right)\exp\left(-\frac{k_l^2w_j^2}{4}\right). \tag{4.11d}$$

The equation of motion associated to β_j is given by,

$$\dot{\beta}_j = \frac{N_j\epsilon}{(-1)^{3-j}2\sqrt{2\pi}w_j}\sum_{l=1}^{2}\left(V_l k_l\right)\sin\left(k_l x_{0_j}\right)\exp\left(-\frac{k_l^2w_j^2}{8}\right) + \frac{1}{(-1)^{3-j}}\sum_{l=1}^{2}\left(V_l k_l\right)\sin\left(k_l x_{0j}\right)$$
$$\exp\left(-\frac{k_l^2w_j^2}{4}\right) - \frac{2\eta_0 N_{3-j}\left(x_{0_1}-x_{0_2}\right)}{\sqrt{\pi}\left(w_1^2+w_2^2\right)^{3/2}}\exp\left(-\frac{\left(x_{0_1}-x_{0_2}\right)^2}{w_1^2+w_2^2}\right)$$
$$-\frac{\eta N_{3-j}(-1)^{j-3}}{\sqrt{\pi}\left(w_1^2+w_2^2\right)^{3/2}}\exp\left(-\frac{\left(x_{0_1}-x_0\right)^2}{w_1^2+w_2^2}\right)\sum_{l=1}^{2}V_l\left[\left(-k_l w_{3-j}^2\right)\sin\left(k_l\frac{w_1^2x_{0_2}+w_2^2x_{0_1}}{w_1^2+w_2^2}\right)\right.$$
$$\left.+(-1)^j 2\left(x_{0_1}-x_{0_2}\right)\cos\left(k_l\frac{w_1^2x_{0_2}+w_2^2x_{0_1}}{w_1^2+w_2^2}\right)\right]\times\exp\left(-\frac{k_l^2w_1^2w_2^2}{4\left(w_1^2+w_2^2\right)}\right)\sqrt{\frac{N_{3-j}}{N_j}}(-1)^{j-3}\frac{\partial L_\Omega}{\partial x_{0_j}}$$
$$-\frac{\dot{N}_j}{N_j}\beta_j. \tag{4.11e}$$

Finally, the Euler equation of motion with respect to w_j is given by,

$$\begin{aligned}
&\frac{N_j}{2w_j^3}+\frac{N_j^2}{2\sqrt{2\pi}w_j^2}\left[\epsilon_0-\frac{\epsilon}{4}\sum_{l=1}^{2}V_l\left(k_l^2w_j^2+4\right)\exp\left(-\frac{k_l^2w_j^2}{8}\right)\cos\left(k_lx_{0j}\right)\right]\\
&-\frac{N_jw_j}{2}\sum_{l=1}^{2}\left(V_lk_l^2\right)\cos\left(k_lx_{0_j}\right)\exp\left(-\frac{k_l^2w_j^2}{4}\right)+\frac{N_1N_2\eta_0w_j}{\sqrt{\pi}\left(w_1^2+w_2^2\right)^{5/2}}\left(w_1^2+w_2^2-2\left(x_{0_1}-x_{0_2}\right)^2\right)\\
&\times\exp\left(-\frac{\left(x_{0_1}-x_{0_2}\right)^2}{w_1^2+w_2^2}\right)-\frac{\eta N_1N_2w_j}{2\sqrt{\pi}\left(w_1^2+w_2^2\right)^{5/2}}\exp\left(-\frac{\left(x_{0_1}-x_{0_2}\right)^2}{w_1^2+w_2^2}\right)\\
&\times\sum_{l=1}^{2}V_l\Bigg[\left(-4\left(x_{0_1}-x_{0_2}\right)^2+2w_1^2+2w_2^2+k_l^2\omega_{3-j}^4\right)\cos\left(k_l\frac{w_1^2x_{0_2}+w_2^2x_{0_1}}{w_1^2+w_2^2}\right)\\
&+(-1)^j4k_l\left(x_{0_1}-x_{0_2}\right)\omega_{3-j}^2\sin\left(k_l\frac{w_1^2x_{0_2}+w_2^2x_{0_1}}{w_1^2+w_2^2}\right)\Bigg]\exp\left(-\frac{k_l^2w_1^2w_2^2}{4\left(w_1^2+w_2^2\right)}\right)\\
&-\sqrt{N_jN_{3-j}}\frac{\partial L_\Omega}{\partial w_j}=0.
\end{aligned}\tag{4.11f}$$

Note that the equation of motion corresponding to w_j does not contain the time derivative of the condensate width w_j like other equations (4.11d)-(4.11e). Due to this reason, the variational approach does not seem to fit to analyze the dynamics of the width of the condensate. However, the condensate width obtained from the variational approach demonstrates good agreement in the localized region, as indicated by the shaded area in Fig. 4.12. In contrast, the condensate in the delocalized region exhibits a spatially modulated stripe pattern (see Fig. 4.1(a1)), which cannot be captured by the Gaussian variational approach. First, we focus on analyzing the stationary state upon solving the coupled equations (Eq. (4.1a) and Eq. (4.1b)) considering equal atoms in both components (i.e., $N_1 = N_2$). In order to obtain the stationary conditions, we need to make the time derivative of Eq. (4.11b)–Eq. (4.11e) equal to zero. As a result, we obtain $\beta_1 = \beta_2 = \beta$, $w_1 = w_2 = w$, and $x_{0_1} = -x_{0_2} = x_0$ as the initial condition. Using these initial conditions, the equations of motion associated with x_0, w, and β have the form,

$$k_L-\beta-\sqrt{\frac{N_{3-j}}{N_j}}\ \frac{\partial L_\Omega}{\partial\beta_j}=0,\tag{4.12a}$$

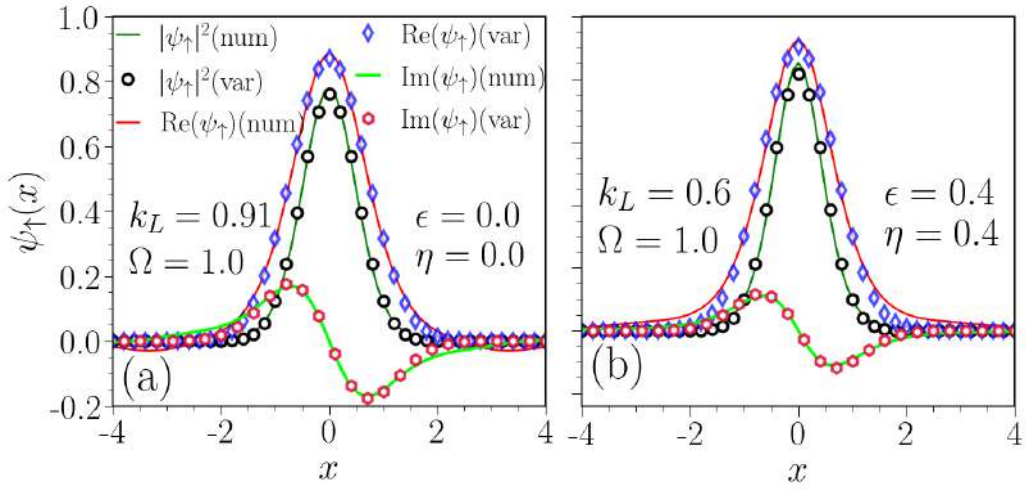

Figure 4.11: Ground state density profile obtained using numerical (with lines) and variational scheme (with markers) for (a) $k_L = 0.91$, $\epsilon(= \eta) = 0$, and (b) $k_L = 0.6$, $\epsilon(= \eta) = 0.4$. The real and imaginary parts of the spin-up condensate wavefunction obtained from the numerical simulation and variational approach agree well.

$$\frac{1}{2w^3} + \frac{1}{2\sqrt{2\pi}w^2}\left[\epsilon_0 - \frac{\epsilon}{4}\sum_{l=1}^{2} V_l\left(k_l^2w^2+4\right)\exp\left(-\frac{k_l^2w^2}{8}\right)\cos\left(k_lx_0\right)\right]$$
$$-\frac{w}{2}\sum_{l=1}^{2}\left(V_lk_l^2\right)\cos\left(k_lx_0\right)\exp\left(-\frac{k_l^2w^2}{4}\right) + \frac{\eta_0}{2\sqrt{2\pi}w^4}\left(w^2-4x_0^2\right)\exp\left(-\frac{2x_0^2}{w^2}\right)$$
$$-\frac{\eta}{2\sqrt{2\pi}w^4}\sum_{l=1}^{2} V_l\left(-4x_0^2+w^2+\frac{k_l^2w^4}{4}\right)\exp\left(-\frac{k_l^2w^2}{8}\right) + 2\Omega\left(\beta^2w+\frac{x_0^2}{w^3}\right)$$
$$\times\exp\left(-\frac{x_0^2+\beta^2w^4}{w^2}\right) = 0, \tag{4.12b}$$

$$\frac{(-1)^{j-1}N_j\epsilon}{2\sqrt{2\pi}w}\sum_{l=1}^{2}\left(V_lk_l\right)\sin\left(k_lx_0\right)\exp\left(-\frac{k_l^2w^2}{8}\right) + \sum_{l=1}^{2}\left(V_lk_l\right)\sin\left(k_lx_0\right)\exp\left(-\frac{k_l^2w^2}{4}\right)$$
$$-\frac{\sqrt{2}\eta_0N_{3-j}x_0}{\sqrt{\pi}w^3}\exp\left(-\frac{2x_0^2}{w^2}\right) - \frac{(-1)^{2j-1}\eta N_{3-j}}{2^{3/2}\sqrt{\pi}w^3}\exp\left(-\frac{2x_0^2}{w^2}\right)\sum_{l=1}^{2}(-1)^j4V_lx_0\exp\left(-\frac{k_l^2w^2}{8}\right)$$
$$+\sqrt{\frac{N_{3-j}}{N_j}}(-1)^{j-1}\frac{\partial L_\Omega}{\partial x_{0_j}} = 0. \tag{4.12c}$$

In Fig. 4.11 we show a comparison between the density profile of the spin-up component obtained using GPEs (with solid line) and that using the variational approach [Eq. (4.12a)–(4.12c)] shown with open markers considering $k_L = 0.91$, $\epsilon = \eta = 0$, and $\Omega = 1.0$ [see Fig. 4.11(a)], and $\epsilon = \eta = 0.4$, $k_L = 0.6$ and $\Omega = 1.0$ [see Fig. 4.11(b)]. At

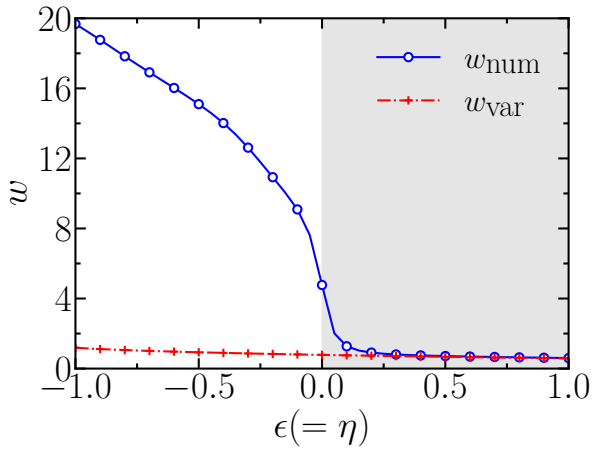

Figure 4.12: Comparison of numerical (w_{num}) and variational condensate width (w_{var}) as a function of interaction inhomogeneity as $\epsilon(=\eta)$ at $k_L = 0.6$, and $\Omega = 1$. (w_{num}) (circle marked solid-blue line) obtained using the numerical integration of Eq. (4.1a) and Eq. (4.1b), and (w_{var}) (red-dash dotted line) obtained using the solution of Eq. (4.12a)–(4.12c) with proper initial conditions. In the localized region $(\epsilon(=\eta) > 0)$, the w_{num} shows good agreement with the variational method while, in the delocalized region $(\epsilon(=\eta) < 0)$, the variational method fails to accurately match the numerical condensate width.

stationary state, $|\psi_\uparrow|^2 = |\psi_\downarrow|^2$, $\text{Im}\,\psi_\uparrow = \text{Im}\,\psi_\downarrow$, and $\text{Re}\,\psi_\uparrow = -\text{Re}\,\psi_\downarrow$. Noting this, hereafter, we consider the spin-up component for the discussion. The density profile calculated using the numerical GPEs and variational approach agrees well in the localized state. For the non-interacting case ($\epsilon = \eta = 0$), the variational approach (Eq. (4.12b)) reveals that the kinetic energy (first term) is responsible for the delocalization. However, the Rabi-coupling and the optical lattice potential contribute to localization of the condensate, which is in line with the observations made earlier (refer to the discussion in Sec. 4.3.1). Further, to highlight the effect of inhomogeneities on the localization in Fig. 4.11(b), we illustrate the density profile for $\epsilon = \eta = 0.4$, $k_L = 0.6$, and $\Omega = 1.0$. The density profile obtained using the variational approach agrees well with those obtained using GPEs with slightly higher amplitude than those for non-interacting cases, indicating a stronger localization with repulsive nonlinearity.

Note that, the equation of motion corresponding to w_j [see Eq.(4.11f)] does not contain the time derivative of the condensate width w_j as like the other equations (4.11d)-(4.11e). Due to this reason, the variational approach does not seem to fit to analyze the dynamics of the width of the condensate. However, the condensate width obtained from the variational approach demonstrates good agreement in the localized region, as indicated by the shaded area in Fig. 4.12. In contrast, the condensate in the delocalized region exhibits a spatially modulated stripe pattern (see Fig. 4.1(a1)), which cannot be captured by the Gaussian variational approach.

In Fig. 4.13 we show the variation of total energy (E_{total}) with interaction inhomo-

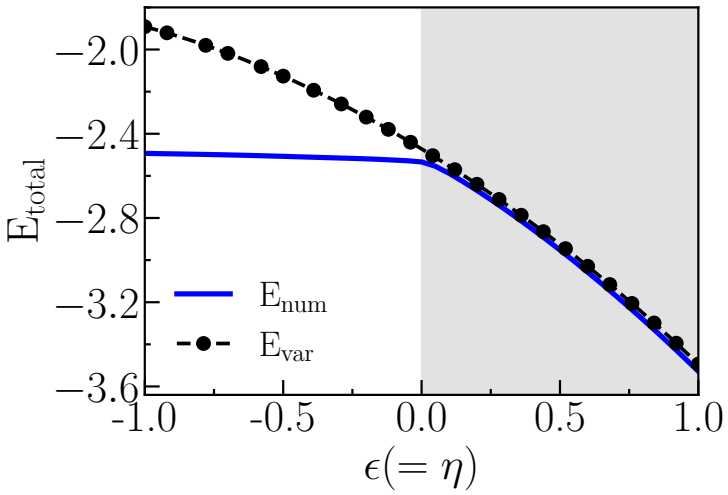

Figure 4.13: Variation of the ground state energy as a function of the inhomogeneity parameter ($\epsilon = \eta$). E_{num} (solid-blue line) and E_{var} (dashed line with dots) represent the total energy obtained from numerical simulation and analytical variational approach, respectively. Here $k_L = 0.6$ and $\Omega = 1$. There is good agreement between the numerical and variational energy in the localized region ($\epsilon = n > 0$) where energy increases towards more negative values, indicating the formation of stronger localization with an increase in the inhomogeneity. In the delocalized region, $E_{\text{num}} \sim -2.5$ for negative inhomogeneity parameter.

geneity as ($\epsilon = \eta$). For attractive interaction ($\epsilon = \eta \leq 0$), the total energy calculated using numerics remains constant at $E_{\text{num}} = -2.5$. On the other hand, for repulsive interactions ($\epsilon(= \eta) \geq 0$), the E_{num} decreases monotonically upon increasing interaction strength, indicating that the localized condensate minimizes the energy. For negative inhomogeneous interaction, the total energy E_{var} calculated using the variational approach fails to agree with those obtained using the numerical simulation. The discrepancy between the variational and numerical simulation results for the delocalized region can be attributed to the assumption of a Gaussian-like Ansatz for the wave function in the variational analysis. One needs to consider the superposition of a large number of Gaussian states to emulate the behaviour of a delocalized state, which will make the variational calculation quite complex.

The localization appears to arise from the interplay between interactions and the quasiperiodic optical lattice in a collisionally inhomogeneous environment. To account for this, we consider a phase difference of $\theta = \pi/2$ between the interaction and the potential, as given in Eqs. (4.6a) and (4.6b), respectively, which we further substitute into the Lagrangian [Eq. (4.8)]. Using the Euler-Lagrange formalism, we calculate the equations of motion with respect to the variational parameters. The details of the Lagrangian are provided in the following.

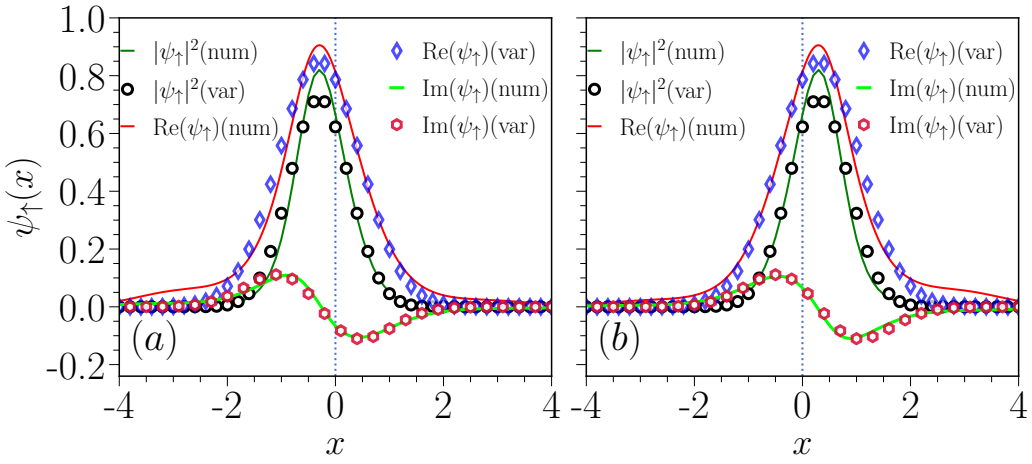

Figure 4.14: Comparison of the condensate density profile obtained numerically (solid line) and using the variational approach (open markers) for different inhomogeneity parameters when the phase difference between the nonlinear inhomogeneity and potential is $\pi/2$. (a) For $\epsilon = -\eta = -0.8$, and (b) For $\epsilon = -\eta = 0.8$. The other parameters are $k_L = 0.6, \theta_j = \pi/2$, and $\Omega = 1.0$. Incorporating the phase shift $\pi/2$ between the potential and inhomogeneity results in the condensate localizing at an off-center position at (a) $x = -0.3$ and (b) $x = 0.3$. The real (Re) and imaginary (Im) parts of the condensate wavefunction show good agreement between the wave function profile obtained from numerical simulation and that from using the variational approach.

4.3.3.2 Lagrangian and effective potential for the phase shift $\pi/2$ between optical lattice potential and nonlinearity

The Lagrangian and the equation for effective potential for the case of $\theta_1 = \theta_2 = \theta = \pi/2$ between optical lattice and interaction inhomogeneity. Here, $j \in \{1,2\} \equiv \{\uparrow,\downarrow\}$ represents the spin-up and spin-down components, respectively.

$$
\begin{aligned}
L =& \sum_{j=1}^{2}\Bigg[N_j(-1)^j\beta_j\dot{x}_{0_j} - N_j\dot{\phi}_j + N_j\beta_j k_L - \frac{N_j}{2}\left(\frac{1}{2w_j^2}+\beta_j^2\right) - \frac{N_j}{2^{3/2}\sqrt{\pi}w_j}\Bigg[\epsilon_0 \\
&- \epsilon\sum_{l=1}^{2}V_l\sin\left(k_l x_{0_j}\right)\exp\left(-\frac{k_l^2 w_j^2}{8}\right)\Bigg] + N_j\sum_{l=1}^{2}V_l\cos\left(k_l x_{0_j}\right)\exp\left(-\frac{k_l^2 w_j^2}{4}\right)\Bigg] \\
&- \frac{N_1N_2}{\sqrt{\pi}\sqrt{w_1^2+w_2^2}}\exp\left(-\frac{(x_{01}-x_{02})^2}{w_1^2+w_2^2}\right)\Bigg[\eta_0 + \eta\sum_{l=1}^{2}V_l\sin\left(\frac{k_l\left(w_1^2x_{0_2}+w_2^2x_{0_1}\right)}{w_1^2+w_2^2}\right) \\
&\times\exp\left(-\frac{k_l^2w_1^2w_2^2}{4\left(w_1^2+w_2^2\right)}\right)\Bigg] - 2\sqrt{N_1N_2}L_\Omega,
\end{aligned}
\tag{4.13}
$$

where, L_Ω is same as Eq. (4.10b). Next, in Fig. 4.14(a) and Fig. 4.14(b), we show a comparison between the density profiles obtained from the numerical simulation

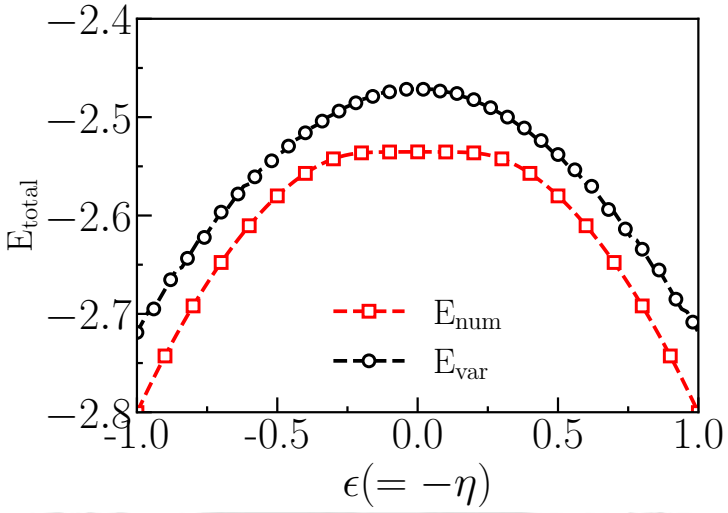

Figure 4.15: Variation of numerical (E_{num}) and variational (E_{var}) total energy with inhomogeneity $\epsilon(=-\eta)$ with $k_L = 0.6$, and $\Omega = 1.0$. Tuning the inhomogeneity leads to a monotonic decrease in the total energy in the localized regions, that is $-1 \lesssim \epsilon(=-\eta) \lesssim -0.3$ or $0.3 \lesssim \epsilon(=-\eta) \lesssim 1.0$ whereas, in the delocalized region $-0.3 \lesssim |\epsilon(=-\eta)| \lesssim 0.3$, the total energy remains almost constant at $E_{\text{num}} \sim -2.56$. In both cases, energy follow a symmetric nature in either side of delocalization regions.

(solid lines) and that from the variational approach (marked with open markers) for $\epsilon = -0.8$, $\eta = 0.8$ and $\epsilon = 0.8$, $\eta = -0.8$, respectively. For both the combination of the strength of the inhomogeneity, the condensate gets localized off-center. For instance, in Fig. 4.14(a), the condensate gets localized at $x \approx -0.3$, while, in Fig. 4.14(b), the localization happens at $x \approx 0.3$. To unravel the reason for this particular nature of localization of the condensate at the off-center position in space, we analyze the nature of the effective potential as depicted in Fig. 4.17(a). We find that increasing the strength of interaction results in shifting the minima of the effective potential V^{eff} either left or right, which depends solely on the nature of the interaction inhomogeneity. The left shift happens for the attractive ($\epsilon = -\eta = -1.0$) while the right shift happens for the repulsive intraspecies ($\epsilon = -\eta = 1.0$) interactions. The detailed discussion is provided in the following section 4.3.4.

To get more insight into the probable cause for the localization and delocalization transition, in Fig. 4.15, we show a variation of the total energy as a function of the interaction inhomogeneity obtained from the numerical simulation and using the variational approach. The energy shows a monotonically decreasing trend with the interaction inhomogeneity strength for $0.3 \lesssim |\epsilon(=-\eta)| \lesssim 1$. However, for $0 \lesssim |\epsilon(=-\eta)| \lesssim 0.3$ the energy assumes the constant value around $E_{\text{num}} \approx -2.56$. Variational energy E_{var} qualitatively follows a similar trend as that of E_{num} in both localized and delocalized regions. The decreasing trend explains the formation of more localized bound

state, whereas, the constant plateau at comparatively higher energy ($E_{\text{num}} \approx -2.56$) forms more weakly bound states relative to the other case.

4.3.4 Effective Potential for localization-delocalization of the condensate

To understand the role of inhomogeneity in the localization of the condensate, we resort to derive the dynamical equation of the condensate moving under the influence of effective potential mainly generated due to the spatial inhomogeneity [120, 132].

The effective potential V_j^{eff} can be derived from the Eq. (4.11b) and Eq. (4.11e), which has the form of:

$$\frac{\partial^2 x_{0_j}}{\partial t^2} = -\dot{\beta}_j = -\frac{\partial V_j^{\text{eff}}}{\partial x_{0_j}}, \tag{4.14a}$$

$$\begin{aligned} V_j^{\text{eff}} = &-\frac{\epsilon}{2^{3/2}\sqrt{\pi} w_j} \sum_{l=1}^{2} V_l \cos\left(k_l x_{0_j}\right) \exp\left(-\frac{k_l^2 w_j^2}{8}\right) - \sum_{l=1}^{2} V_l \cos\left(k_l x_{0_j}\right) \exp\left(-\frac{k_l^2 w_j^2}{4}\right) \\ &+ \frac{(-1)^{3-j}\eta_0}{\sqrt{\pi}\left(w_1^2 + w_2^2\right)^{1/2}} \exp\left(-\frac{\left(x_{0_1} - x_{0_2}\right)^2}{w_1^2 + w_2^2}\right) - \frac{\eta}{\sqrt{\pi}\sqrt{w_1^2 + w_2^2}} \exp\left(-\frac{\left(x_{01} - x_{02}\right)^2}{w_1^2 + w_2^2}\right) \\ &\times \sum_{l=1}^{2} V_l \cos\left(\frac{k_l\left(w_1^2 x_{0_2} + w_2^2 x_{0_1}\right)}{w_1^2 + w_2^2}\right) \times \exp\left(-\frac{k_l^2 w_1^2 w_2^2}{4\left(w_1^2 + w_2^2\right)}\right) + L_\Omega. \end{aligned} \tag{4.14b}$$

The effective potential obtained in Eq. (4.14b) is mainly composed of five different terms. The first term involving interactions ϵ contributes towards localization in the case of repulsive interactions. The second term, containing the quasiperiodic optical lattice potential, is responsible for the localization of the condensate. The third term contains η_0, which determines the state of localization or delocalization depending upon the component and the sign of η_0. The last term containing the Rabi-coupling [See Eq.(4.14b)] contributes towards either localization or delocalization for the in-phase or out-of-phase state of the condensate, respectively. For our calculation, we choose $\phi = \pi$ between the two components in all cases, which implies that the role of Rabi coupling towards localization. Further, the condensate width w_j, and chirp β_j appearing in the effective potential can be estimated by solving Eqs. (4.12a–4.12c). After substituting the w_j, and β_j, we compute the $V_j^{\text{eff}}(x_0)$ for various spatial inhomogeneity and coupling parameters, which has been depicted in Fig. 4.16.

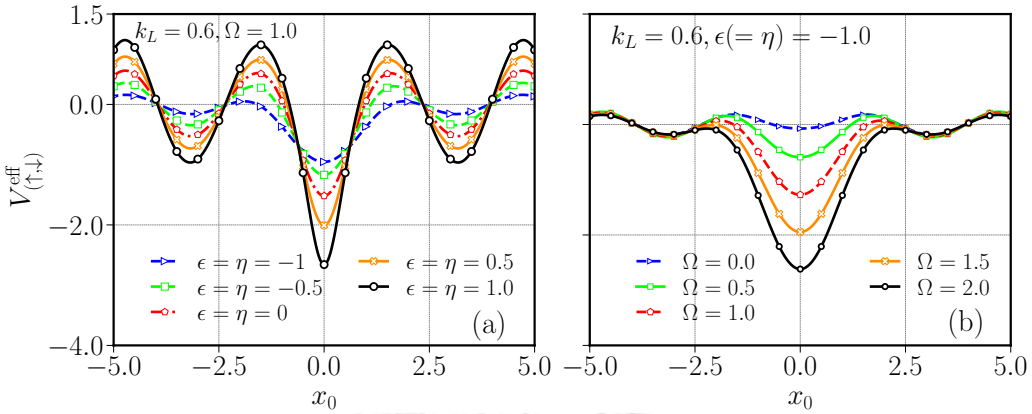

Figure 4.16: Effective potential ($V^{\text{eff}}_{(1,2)}$) profile for the condensate obtained using variational approach [Eq. 4.14b]: (a) for different inhomogeneous interaction parameter keeping $\Omega = 1$ and $k_L = 0.6$ and (b) for different Ω keeping $k_L = 0.6$ and inhomogeneity interaction as $\epsilon(= \eta) = -1.0$. The depth of the effective potential at the central point ($x_0 \sim 0$) increases upon increasing the repulsive interaction compared to those for $\epsilon = \eta = 0$, indicating the localization of the condensate for repulsive interaction inhomogeneity. However, the trend is opposite for an increase in the attractive interaction, implying the delocalization for them. Upon an increase of Ω in (b), the central depth increases, suggesting the localization of condensate for this increment.

In Fig. 4.16(a), we show the profile of V_{eff} corresponding to the spin-up component upon varying the inhomogeneous interactions while keeping the intra- and inter-component interaction same for $k_L = 0.6$ and $\Omega = 1$. We find that the effective potential attains a global minimum at $x_0 = 0$, and the depth of the global minimum increases upon an increase in the spatial repulsive inhomogeneous interaction. For instance, at $\epsilon = \eta = 1$ (open circled black solid line), a larger depth of effective potential ($V_{\text{eff}} \sim 2.5$) indicates that the condensate gets more localized as the repulsive interaction increased. However, for attractive interaction(ϵ or $\eta < 0$), the depth of minima at $x_0 \sim 0$ becomes of the order of other minima of the effective potential, indicating the delocalized state of the condensate. This observation aligns with the earlier numerical results obtained with the one-component BECs [132]. Additionally, this result closely matches the observed transition from localized to delocalized states when interaction parameters are varied from positive to negative (see Fig. 4.3).

In a similar line as discussed above, to understand the role of Rabi coupling in attaining the localization, we show the effective potential in Fig. 4.16(b) as Ω is increased for the condensate with $\epsilon = \eta = -1$ and $k_L = 0.6$. For $\Omega = 0$, the minima of the effective potential at $x_0 = 0$ are of the same width as the minima at other x_0, indicating the delocalized state of the condensate. As the Rabi-coupling increased from zero, the depth of the effective potential at $x_0 = 0$ increases and becomes significantly higher compared to the minima at other x_0 for $\Omega \gtrsim 0.5$. This variation of the effec-

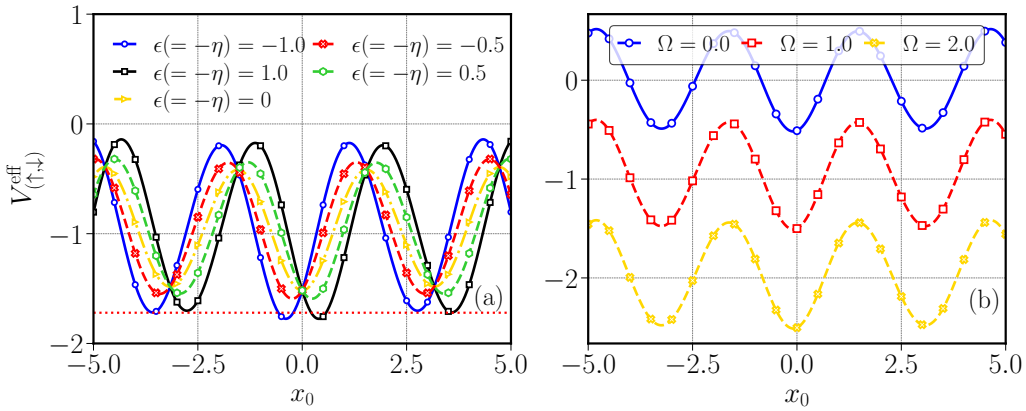

Figure 4.17: (a) Variation of effective potential ($V^{\text{eff}}_{(1,2)}$) as obtained in Eq. 4.15 of spin-components with x_0 for different inhomogeneous interaction parameters $\epsilon(=-\eta)$ when the phase difference between the spatial inhomogeneity and potential considered is $\pi/2$. For $\epsilon=\eta=0$, the potential is peaked at $x_0=0$, which is the delocalized state. However, for $|\epsilon(-\eta)|=0.5$ and 1, the central minima depth increases compared to those for zero inhomogeneity, indicating the localization state. (b) Variation of effective potential with x_0 for different Ω with $k_L=0.6$, $\epsilon=\eta=0$. As the value of Ω increases, the depth of the central potential also increases, implying that the Rabi coupling contributes towards the localization of the condensate.

tive potential with increasing Ω indicates that the role of Rabi coupling is to localize the condensate in the presence of inhomogeneous interaction, where it was initially delocalized, in line with the numerical observation made in Sec . 4.3.1.

Next, we turn our focus on analyzing the role of spatial inhomogeneity in the localization-delocalization that arises when the inhomogeneous nonlinear interaction carries the $\pi/2$ phase difference in spatial dependence, as those for the trapping quasiperiodic potential as described in Sec. 4.3.2. The form of the effective potential V_{eff} can be written as,

$$V_j^{\text{eff}} = -\frac{\epsilon}{2^{3/2}\sqrt{\pi}w_j}\sum_{l=1}^{2}V_l\sin\left(k_l x_{0_j}\right)\exp\left(-\frac{k_l^2w_j^2}{8}\right)-\sum_{l=1}^{2}V_l\cos\left(k_l x_{0_j}\right)\exp\left(-\frac{k_l^2w_j^2}{4}\right)$$
$$-\frac{\eta_0}{\sqrt{\pi}\left(w_1^2+w_2^2\right)^{1/2}}\exp\left(-\frac{\left(x_{0_1}-x_{0_2}\right)^2}{w_1^2+w_2^2}\right)+\frac{\eta}{\sqrt{\pi}\sqrt{w_1^2+w_2^2}}\exp\left(-\frac{\left(x_{01}-x_{02}\right)^2}{w_1^2+w_2^2}\right)$$
$$\sum_{l=1}^{2}V_l\sin\left(\frac{k_l\left(w_1^2x_{0_2}+w_2^2x_{0_1}\right)}{w_1^2+w_2^2}\right)\exp\left(-\frac{k_l^2w_1^2w_2^2}{4\left(w_1^2+w_2^2\right)}\right)+L_\Omega. \tag{4.15}$$

Interestingly, the spatial variation of the effective potential in Fig. 4.17(a) vividly illustrates the shifting of the minima with the increment of nonlinear interactions $\epsilon(=-\eta)$ as a result of the captivating interplay between the potential and spatial dependence of the interaction. For instance, as we move from $\epsilon=\eta=0$, the local min-

ima at $x_0 = 0$ shifts either in the direction of positive or negative x_0, as depicted for $\epsilon = -\eta = 0.2$ (green dashed line) or $\epsilon = -\eta = -0.2$ (purple dashed line), respectively. Notably, the displacement of the minima occurs symmetrically on both sides of the center. For example, at $\epsilon(= -\eta) = 1.0$, the minima are displaced around $x_0 = 0.3$, whereas at $\epsilon(= -\eta) = -1.0$, the minima are found to be at $x_0 = -0.3$. Also, the presence of disorder in the potential leads to a slightly larger depth of the potential well located at $x_0 = \pm 0.3$ compared to the other wells for the aforementioned interactions, which is clearly distinguishable by the red dotted line in the figure. These particular features highlight intriguing competition between the potential and nonlinearity towards the localization-delocalization behavior. Additionally, the effect of Rabi-coupling towards localization is clearly evident when studying the magnitude of V_{eff} in Fig. 4.17(b).

4.3.5 Dynamics of localized and delocalized states

So far, we have analyzed the effect of the SO and Rabi coupling along with the interaction inhomogeneity on the localization of the condensate and studied their role using the variational approach. In this section, we present the dynamics of those localized and delocalized states by perturbing the ground state through velocity or performing a quench on the strength of the secondary potential.

4.3.5.1 Velocity perturbed Dynamics

In this section, we present the dynamics that ensued in the condensate as a result of the finite equal and opposite velocity imparted to the condensate in the localized or delocalized state in the presence of the interaction inhomogeneities. After imparting the velocity, we analyze the condensate dynamics utilizing the real-time propagation scheme.

In Fig. 4.18, we show the temporal evolution of spin-up component condensate density for various interaction inhomogeneities. In panel (a), we observe the initial localized state obtained when the phase between spatial inhomogeneity and potential is zero ($\theta = 0$), with parameters $\epsilon = \eta = 0.2$, $k_L = 0.6$, and $\Omega = 1.0$. After applying a velocity perturbation at $t = 20$, we observe a slight change in the condensate. Only a small fraction generates ripples in space, while the maximum density remains almost unchanged compared to the ground state density. A similar behaviour is observed for the localized condensate when the phase shift is $\theta = \pi/2, \epsilon(= -\eta) = 1.0$ (see panel (c)). In panel (b), the delocalized condensate density demonstrates expansion in space over time after the velocity perturbation at $t = 20$ (after the red dashed line). In sum-

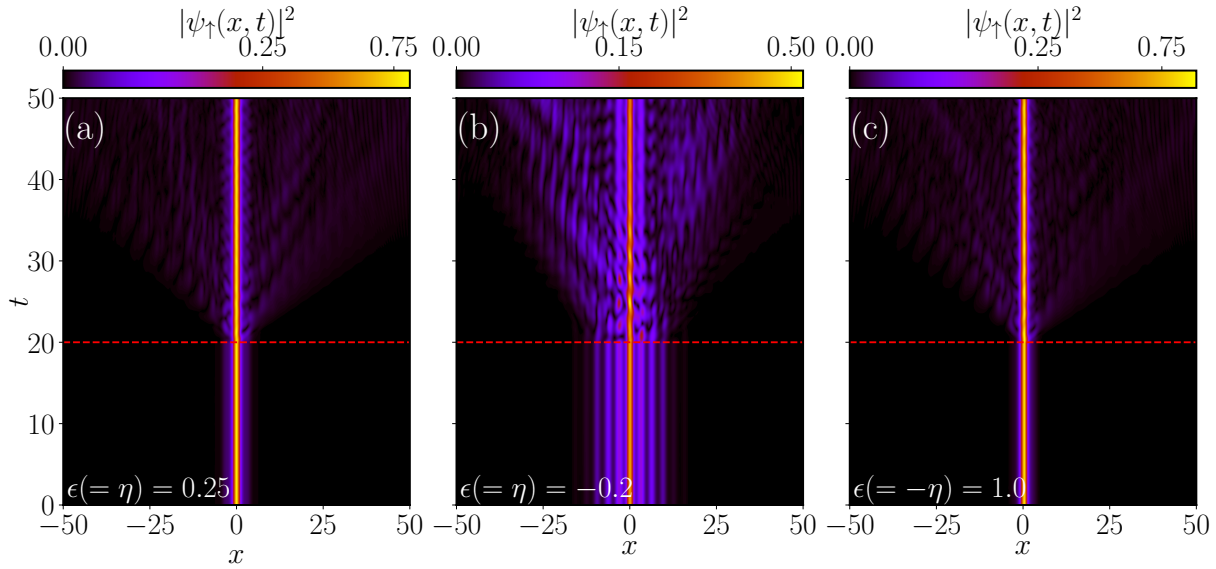

Figure 4.18: Pseudo color representation of the velocity-induced dynamics of the spin-up component density for localized (a) and delocalized (b) states of the case when the inhomogeneity has the same phase as the potential. (c) shows the localized state for the case when the inhomogeneous interaction and potential have $\pi/2$ phase difference. The other parameters are $k_L = 0.6$ and $\Omega = 1$. Both the localized states (a) and (c) do not show any change in shape and size upon perturbing with the velocity, while the delocalized state (b) shows a spread in shape with time.

mary, it can be said that localized condensates [see Fig. 4.18(a) and Fig. 4.18(c)] remain stable against small perturbations, while delocalized condensates [see Fig. 4.18(b)] exhibit instability under similar perturbations [132].

4.3.5.2 Quench induced dynamics

Apart from the analysis of the localized and delocalized phases depending upon the ground state density with various coupling and interactions, now in this section, we explore the dynamics of the different phases of the condensate upon quenching of trap potentials [225, 28, 226]. Firstly, we analyze the dynamics generated by applying the quench of the trap potential from the initial to different final strengths. In Fig. 4.19, we show the temporal average of the condensate width $\overline{w} = 1/T \int_0^T w(t)dt$, for quenching of the potential from initial ($V_2 = 0.1$) to lower trapping strength. In Fig. 4.19(a) we show the variation of mean width with $\epsilon(=\eta)$ as the dynamics are generated through two types of quenching: (i) by quenching the secondary lattice strength $V_2 = 0.1 \rightarrow 0.0$ (black solid line with square markers) and (ii) by quenching $V_2 = 0.1 \rightarrow 0.05$ (red dashed line with circular markers). We also show the $\overline{w}$ (green dotted line with triangular markers) corresponding to the ground state condensate. We find that for repulsive interaction $\epsilon(=\eta) > 0$, the $\overline{w}$ is of the same order compared to the $\overline{w}$ obtained

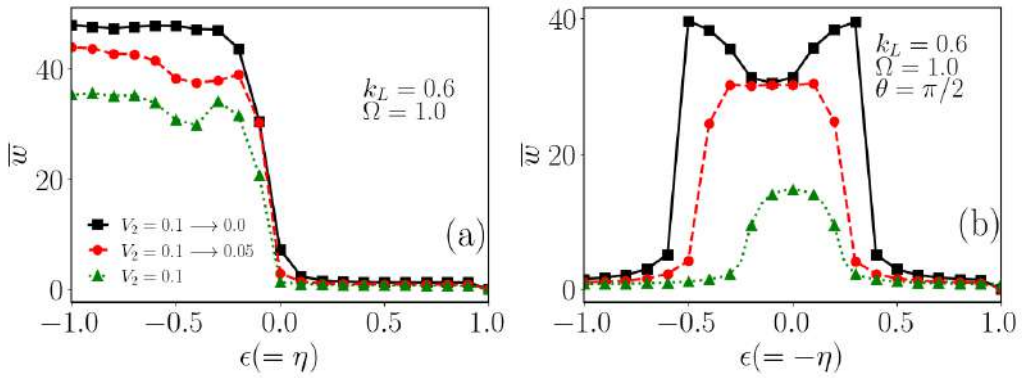

Figure 4.19: Time averaged mean-width ($\overline{w}$) of the condensate as a function of the inhomogeneity ($\epsilon = -\eta$) for different quenching of the secondary potential (V_2) from initial value 0.1 to the final value 0.0 (black rectangle) and 0.05 (red dots). The green triangle represents the case when $V_2 = 0.1$. The other parameters are $k_L = 0.6$, and $\Omega = 1.0$. For the case (a) when the inhomogeneity and potential have the same phase, and (b) when the phase between the potential and nonlinear inhomogeneity is $\pi/2$.

without quenching. This particular feature implies that the condensate stability in the localized region is primarily caused by the repulsive inhomogeneity present in the system [132].

On the other hand, with attractive interaction ($\epsilon(=\eta) < 0$), the $\overline{w}$ tends to increase towards a larger value to the order of $\overline{w} \sim \mathcal{O}(10^1)$. Moreover, in the case of periodic quenching (when final $V_2 = 0$), the mean width is higher compared to the case of quasiperiodic quenching (when $V_2 = 0.05$), which indicates that even a low but finite disorder is good enough to resist the expansion. Note that as we use the equal interspecies interaction, the density of the spin-up and spin-down components remains equal. Therefore, for the sake of brevity, we have only shown the dynamical evolution of the spin-up component. The other component just follows up on the spin-up component dynamics.

In Fig. 4.19(b), we present the mean condensate width with the variation of $\epsilon(=-\eta)$ in the presence of the phase shift $\theta = \pi/2$. Similar to $\theta = 0$ here also, we observe that in the localized region, $\overline{w}$ remains almost constant at the same order, $\mathcal{O}(10^{-1})$, irrespective of the strength of quenching of the trap. However in the delocalized region, the $\overline{w}$ follows similar behavior as observed for $\theta = 0$ (See Fig. 4.19(a)). In general, we find that the periodic quenching (final $V_2 = 0$) results in attaining the higher $\overline{w}$ compared to those for quasiperiodic quenching (final $V_2 = 0.05$). We also notice a slight shift of the delocalized regions towards the left side of $\epsilon(=-\eta) < 0$ for the delocalized regions compared to the case without quenching (dotted line with green triangles). This feature can be attributed to the comparatively weak localization of the condensate with phase shift $\pi/2$ compared to the localization without phase shift. We

also find the manifestation of the localization-delocalization transition with a change in inhomogeneity in the dynamics of the condensate captured through the variation of the mean condensate width in Fig. 4.19(b) in comparison to the results obtained using the ground state in Fig. 4.8(b).

4.4 Summary and Conclusion

In this Chapter, we have numerically investigated the effect of interaction inhomogeneity on the localization-delocalization transition of the SO coupled binary quasi-one dimensional BECs trapped in the quasiperiodic potentials. By assuming the form of the spatial modulation of the interaction inhomogeneity same as that of the quasiperiodic potential we have shown that the condensed undergoes a localization to delocalization transition as the inhomogeneous interaction strength varies from attractive to repulsive. However, when a phase difference of $\pi/2$ is introduced between the inhomogeneity and the lattice potential, we have shown a remarkable localization-delocalization-localization transition as a function of the inhomogeneity strength. Furthermore, we have also analyzed the effect of the SO and the Rabi coupling on the localization-delocalization transition for different strengths of the inhomogeneity. For weak inhomogeneity strength, the increase in the SO coupling strength leads to localization-delocalization similar to the one observed for non-interacting homogeneous SO coupled BECs [128].

Furthermore, we have utilized the variational approach to understand the competing nature of the quasiperiodic disorder due to the inhomogeneity and the potential responsible for the localization-delocalization-localization, which is revealed clearly in the oscillatory nature of the depth of the effective potential as a function of the inhomogeneity strength. We have also demonstrated the manifestation of the localization-delocalization in the quench dynamics of the condensate. Our present analysis provides an alternate disorder parameter other than the external potential to attain this behavior.

Chapter 5

Spin-dependent localization of spin-orbit and Rabi-coupled Bose-Einstein condensates in a random potential

In previous Chapter 4, we presented a comprehensive role of spin-orbit (SO) coupling and interaction on the localization-delocalization transition of the binary condensate confined in the quasiperiodic potential. In this Chapter we extend our analysis to SO coupled BECs trapped in the random disordered potential. The main focus of the Chapter is to develop a comprehensive understanding of the interplay between SO, disorder, and interactions on the localization-delocalization transitions in SO coupled binary BECs. Here we show that for weak random potential upon an increase in the SO coupling, a re-entrant transition takes place from a broad to narrow localized state and back at a higher SO coupling. The main focus of the Chapter is to show the appearance of spin-dependent localization as the interactions increase beyond threshold values for a sufficiently strong disorder. The Chapter is based on the work published in New Journal of Physics [227].

5.1 Introduction

Following the discussion of SO and Rabi coupling on spinor BEC in quasiperiodic potential in the last chapter, we now focus on their effects in presence of a random disordered potential. In this section, we begin by summarizing key experimental and theoretical developments on Anderson localization in random disordered systems and outline the literature gap that motivates the present work.

Similar to the advancements in AL under quasiperiodic disorder, the study of random disordered potentials gained momentum following the first experimental realization of AL in BECs with random speckle potential [21]. For example, Clément *et al.* [125, 87] reported the suppression of transport and disorder-induced trapping of quasi-1D and 3D interacting BECs. Following that, characterization of exponential and algebraic localization also theoretically studied in Ref. [23], which was later verified in the experiment [21].

In addition to the random speckle potential, several numerical studies have employed a simplified Gaussian random impurity model to effectively mimic disorder. A detailed discussion of this model is provided in section 1.2.4.3 of Chapter 1. This model is widely used in numerical simulations with mean-field GP equations. For example, Cheng and Adhikari [126] numerically explored the Anderson-like localization of a scaler BEC in such random disordered potential. They further reported the condensate fragmentation under strong repulsion. A key feature of random potentials is that the localized profile evolves from Gaussian to exponential with increasing disorder strength—a behavior not observed in quasiperiodic systems. This behvaiour is similar to the algebric and exponential localization regions found with random speckle potential [23]. This behavior is similar to the algebraic and exponential localization regimes identified in random speckle potentials [23]. With binary condensates, Xi et al.[127] reported the spatial phase separation due to the imbalance between intraspecies and interspecies interactions. The random disordered systems also exhibit complex dynamics, including spin precession and spin-component separation induced by spin-dependent velocities[146, 147, 228, 229]. The complexity of these localized states presents significant challenges in formulating a unified physical framework for their systematic understanding.

So far, most studies on localization in random potentials have focused on weakly interacting scaler or binary condensates. However, the combined effects of spin-orbit and Rabi coupling, interactions, and disorder remain largely unexplored. In this work, we perform a comprehensive study to analyze how SO coupling, self-interaction, and disorder affect various types of ground state localization in condensates, extending beyond the conventional Anderson localization framework. We also demonstrate that increasing inter-species interaction beyond a certain threshold leads to spin-dependent localization-delocalization effects, as the Manakov symmetry is lifted.

The Chapter is structured as follows. Section 5.2 introduces the model in terms of the Gross-Pitaevskii equations and defines physical observables and characteristics of the random potential. Next, section 5.3 explores the impact of SO and Rabi couplings

on localization in the non-interacting case. In Sec. 5.4, we concentrate on the spin-dependent localization of self-interacting BEC for two non-Manakov's realizations of nonlinearities. Finally, in Sec. 5.5 we conclude the chapter.

5.2 Mean-field model, observables, and disorder

In this Section, we formulate the main features of the model and discuss their relation to the disorder in one-dimensional systems.

5.2.1 Coupled Gross-Pitaevskii equations

We consider a pseudospin-1/2 quasi-1D condensate strongly confined along the transverse direction, which can be modelled using the coupled Gross-Pitaevskii equations (GPEs) as,

$$\mathrm{i}\frac{\partial\psi_\uparrow}{\partial t} = \left[-\frac{1}{2}\frac{\partial^2}{\partial x^2} + g_{\uparrow\uparrow}|\psi_\uparrow|^2 + g_{\uparrow\downarrow}|\psi_\downarrow|^2 + V(x)\right]\psi_\uparrow - \mathrm{i}k_L\frac{\partial\psi_\uparrow}{\partial x} + \Omega\psi_\downarrow, \tag{5.1a}$$

$$\mathrm{i}\frac{\partial\psi_\downarrow}{\partial t} = \left[-\frac{1}{2}\frac{\partial^2}{\partial x^2} + g_{\downarrow\downarrow}|\psi_\downarrow|^2 + g_{\downarrow\uparrow}|\psi_\uparrow|^2 + V(x)\right]\psi_\downarrow + \mathrm{i}k_L\frac{\partial\psi_\downarrow}{\partial x} + \Omega\psi_\uparrow, \tag{5.1b}$$

where $\psi_\uparrow$ and $\psi_\downarrow$ ($\psi_{\uparrow,\downarrow} \equiv \psi_{\uparrow,\downarrow}(x,t)$) represent the pseudo spin-up and spin-down components of the condensate wavefunction $\psi = \left(\psi_\uparrow, \psi_\downarrow\right)^{\mathrm{T}}$, respectively, where T stands for transposition. For stationary states $\psi_{\uparrow,\downarrow}(x,t) = \psi_{\uparrow,\downarrow}(x)\exp(-\mathrm{i}\mu t)$, where μ is the chemical potential common for both spin components. Here $g_{\uparrow\uparrow}$ and $g_{\downarrow\downarrow}$ are the intra-species nonlinearities for spin-up and spin-down components, respectively, and $g_{\uparrow\downarrow}$ represents the inter-species interaction. In what follows, we will study stationary states and omit explicit $x-$dependence for brevity when it will not cause confusion.

The GPEs (5.1a)-(5.1b) correspond to the SO coupling Hamiltonian in the form $-\mathrm{i}k_L\sigma_z\partial/\partial x$ and the Rabi coupling $\Omega\sigma_x$ with σ_i ($i = x, z$) being the corresponding Pauli matrices. The spin-orbit and Rabi coupling strengths are denoted as k_L and Ω, respectively, while the random potential is $V(x)$. We consider realizations of self-interaction with different inter- and intra-spin nonlinearities, thus, with lifted Manakov's symmetry [230]. The Manakov's symmetry realized at $g_{\uparrow\uparrow} = g_{\downarrow\downarrow} = g_{\uparrow\downarrow} = g_{\downarrow\uparrow}$ produces the BEC possessing the spin rotational invariance and considerably simplifies the analysis by gauging away the SO interaction in the absence of the Rabi coupling [231]. This symmetry can be lifted as a result of spin-dependent scattering length in interatomic collisions. As will show in this Chapter, this lifted symmetry plays a critical role in the

spin-dependent BEC localization.

The proposed model for the localization of quasi-1D spin-orbit coupled Bose-Einstein condensates in a random potential can be experimentally realized utilizing two hyperfine states of ^{87}Rb atom considering pseudo spin-up atomic state $|\uparrow\rangle \equiv |F = 1, m_F = 0\rangle$, and pseudo spin-down state $|\downarrow\rangle \equiv |F = 1, m_F = -1\rangle$ coupled using two Raman lasers with wavelength $\lambda = 804.1$ nm where the spin-orbit coupling k_L can be tuned by varying the angle between the laser beams [105]. The condensate is trapped under the strong transverse frequency $\omega_\perp \sim 10^3$ s^{-1} with the characteristic length scale $a_\perp \sim 1$ μm and the characteristic energy scale $\hbar\omega_\perp \sim 5$ nK. Variation of the angle between the beams permits to produce dimensionless spin-orbit coupling k_L and Rabi frequency Ω considered in the work in the interval from ~ 0.1 to ~ 5.

In the absence of external magnetic field the interatomic scattering lengths $a_{\uparrow\uparrow}, a_{\downarrow\downarrow}$, and $a_{\downarrow\uparrow}, a_{\uparrow\downarrow}$ are of the order of $100a_0$ where a_0 is the Bohr's radius, and can be tuned by appropriate experimental setup [73, 232–234]. For these interatomic scattering lengths and above given $a_\perp$, the resulting dimensionless interaction parameters $g_{\uparrow\uparrow}, g_{\downarrow\downarrow}$, and $g_{\uparrow\downarrow}, g_{\downarrow\uparrow}$ in the range used in our simulations can be achieved for the total number of atoms $\mathcal{N} < 10^4$. For larger $\mathcal{N}$, similar nonlinear interactions can be achieved at properly tuned smaller interatomic scattering lengths.

To obtain the dimensionless Eq. (5.1a)-(5.1b), we consider the transverse harmonic oscillator length $a_\perp = \sqrt{\hbar/(m\omega_\perp)}$ as a characteristic length scale with $\omega_\perp$ as the transverse harmonic trapping frequency, $\omega_\perp^{-1}$ as the timescale and $\hbar\omega_\perp$ as the characteristic energy scale. The interaction parameters can be defined in terms of $g_{\uparrow\uparrow,(\downarrow\downarrow)} = 2\mathcal{N}a_{\uparrow\uparrow,(\downarrow\downarrow)}/a_\perp$, and $g_{\uparrow\downarrow} = 2\mathcal{N}a_{\uparrow\downarrow}/a_\perp$, where, $a_{\uparrow\uparrow,(\downarrow\downarrow)}$ and $a_{\uparrow\downarrow}$ represent the intra- and inter-component scattering lengths, respectively, and $\mathcal{N}$ represents the total number of atoms in the condensate. The dimensionless spin-orbit k_L and Rabi Ω coupling are defined in the units of $a_\perp^{-1}$ and $2\omega_\perp$, respectively. The wavefunction is rescaled with $\sqrt{a_\perp}$ and follows the normalization condition $N_\uparrow + N_\downarrow = 1$, where

$$N_\uparrow = \int_{-\infty}^{\infty} |\psi_\uparrow|^2 dx, \qquad N_\downarrow = \int_{-\infty}^{\infty} |\psi_\downarrow|^2 dx. \tag{5.2}$$

In addition to the functions $\psi_\uparrow$ and $\psi_\downarrow$, dependent on the SO coupling and self-interaction, it is worth introducing a set of function $\phi_\alpha(x)$ (the index $\alpha = 0, 1, \ldots$, numerates the energy states and $\alpha = 0$ corresponds to the ground state in the absence of SO coupling and the self-interactions) describing the spinless states with the eigenenergies ϵ_α in the

potential $V(x)$. The corresponding eigenstates in the Rabi coupling have the form

$$\phi_{\bar{\alpha}}(x) = \frac{\phi_\alpha(x)}{\sqrt{2}}\,[1, \pm 1]^{\mathrm{T}}, \tag{5.3}$$

with the energies $\epsilon_{\bar{\alpha}} = \epsilon_\alpha + \lambda_{\bar{\alpha}}\Omega$, where $\bar{\alpha} = (\alpha|\lambda_{\bar{\alpha}})$ is a compound index with the second component $\lambda_{\bar{\alpha}} = \pm 1$ corresponding to the $\langle \sigma_x \rangle$ value.

5.2.2 Definition of observables

The localization at different spatial scales is characterized by the spin-projected width w_j, center of mass $\langle x_j \rangle$ and the IPR (inverse participation ratio) χ_j ($j = (\uparrow, \downarrow)$) defined as:

$$w_j^2 = \frac{1}{N_j}\int_{-\infty}^{\infty}(x - \langle x_j \rangle)^2 |\psi_j|^2 dx, \tag{5.4}$$

$$\langle x_j \rangle = \frac{1}{N_j}\int_{-\infty}^{\infty} x|\psi_j|^2 dx, \tag{5.5}$$

and

$$\chi_j = \frac{1}{N_j^2}\int_{-\infty}^{\infty} |\psi_j|^4 dx, \tag{5.6}$$

where N_j is defined by Eq. (5.2).

It is instructive for further analysis to present the local density $n_j(x) \equiv \left|\psi_j(x)\right|^2$ using the Fourier components $n_j(p)$ as:

$$n_j(x) = \int_{-\infty}^{\infty} n_j(p)\exp(\mathrm{i}px)\frac{dp}{\sqrt{2\pi}}, \tag{5.7}$$

resulting in,

$$\chi_j = \frac{1}{N_j^2}\int_{-\infty}^{\infty} n_j^2(p)dp. \tag{5.8}$$

Equation (5.8) (see also Ref. [235]) shows that increasing the contribution of the higher momenta to the probability can increase the IPR.

We consider spin-dependent observables

$$\langle \sigma_i \rangle = \int_{-\infty}^{\infty} \psi^{\dagger} \sigma_i \psi dx, \tag{5.9}$$

and characterize the purity of the system in the spin subspace as $P = \sum_i \langle \sigma_i \rangle^2$ [236]. Here $P = 1$ corresponds to a pure state with the spin on the Bloch sphere, while $P = 0$ is the fully mixed state with zero length of the spin vector.

We also utilize the "spin miscibility" parameter characterizing the joint distribution of densities of spin components defined as

$$\eta = 2 \int_{-\infty}^{\infty} |\psi_{\uparrow}||\psi_{\downarrow}| dx, \tag{5.10}$$

where $\eta = 1$ and $\eta = 0$ correspond to fully miscible and immiscible realizations, respectively. For real wavefunctions, we have $\eta = |\langle \sigma_x \rangle|$. Although the purity and spin miscibility are mutually related, they can demonstrate quite different dependence on the system parameters.

5.2.3 Characterization of disorder

To study the evolution of localization of the nonlinear SO coupled condensate in a random potential, we consider the Lifshitz form [237] of the random potential as:

$$V(x) = \frac{U_0}{\zeta \sqrt{\pi}} \sum_{s=1}^{\mathcal{N}_s} \exp\left(-\frac{(x - x_s)^2}{\zeta^2} \right), \tag{5.11}$$

where U_0 corresponds to the strength of a narrow spike of the width ζ at uncorrelated random positions x_s with $\mathcal{N}_s$ being the total number of spikes. The mean value $\langle V(x) \rangle$ is defined as:

$$\langle V(x) \rangle \equiv \frac{1}{2L} \int_{-L}^{L} V(x) dx = \bar{n} U_0, \tag{5.12}$$

with $\bar{n} = \mathcal{N}_s / 2L$ being the average concentration of the spikes and $2L$ being the length of the system. To characterize statistical properties of the random potentials in (5.11) common for all the disorder realizations, we introduce the correlation function $C(d) = \langle V(x) V(x+d) \rangle - \langle V(x) \rangle^2$ as a function of the distance d between the potential observation points. By assuming an uncorrelated distribution of the positions of the

spikes x_s, we obtain following Ref. [238]:

$$\begin{aligned} C(d) &= \langle V(x)V(x+d)\rangle - \langle V(x)\rangle^2 \\ &= \left(\langle V^2(x)\rangle - \langle V(x)\rangle^2\right)\exp\left(-d^2/2\zeta^2\right), \end{aligned} \tag{5.13}$$

where $\langle V^2(x)\rangle - \langle V(x)\rangle^2 = \bar{n}U_0^2/\sqrt{\sqrt{2}\pi\zeta}$.

While $\langle V(x)\rangle$ and $\langle C(d)\rangle$ present x_s- realization-independent statistical characteristics of the random potential (5.11), the random distribution of the spikes can show various realization-dependent patterns of local concentrations, which can localize the BEC beyond the Anderson localization physics. The Broad basin-like domains with $(\langle V(x)\rangle_b - \langle V(x)\rangle)^2 \ll \bar{n}U_0^2/\zeta$ (here $\langle V(x)\rangle_b$ stands for the potential averaged over the basin region) located between stronger peaks of $V(x)$ produce regions with the effective potential minima which can localize the condensate. Next,let us consider fluctuations with the local concentration of spikes $n < \bar{n}$ of the length l producing local potential $V_{\rm loc} < \langle V(x)\rangle$. For a complete void with $n = 0$, the probability of its realization is given by $\exp(-\bar{n}l)$ with the number of voids $\sim L/l \times \exp(-\bar{n}l)$. This void-like fluctuation becomes sufficient to localize the BEC if $l \gtrsim \pi/\sqrt{\langle V(x)\rangle}$. Since the probability of large basin-like regions or voids is small, for finite length systems, it can strongly depend on the x_s realization at all equal other parameters of the disorder. This combination of localization in the basin-like potentials and the voids is critical for the understanding of the spin-related effect in the ground state of the BEC in a random potential. Detailed analysis of localized states in random one-dimensional potentials has been done in Ref. [239].

The matter wave states in a random potential can be approximately separated into two groups. The first group is well-localized states in the regions of a relatively smaller concentration of the spikes. The ground and low-energy states of our interest belong to this group. The other group is Anderson localized states with the spatial dependence of the form $\phi_\alpha(x) \approx \cos(k_\alpha x + \varphi_\alpha)\xi_\alpha(x)$, where $\xi_\alpha(x)$ is an extended function at the energy-dependent localization length $\ell(k_\alpha)$ with $k_\alpha\ell(k_\alpha) \gtrsim 2\pi$, and φ_α is the corresponding phase. For the model of disorder presented by Eq. (5.11) for slow particles with $k_\alpha\zeta \ll 1$, we obtain the localization length as $\ell(k_\alpha) \sim k_\alpha^2/\bar{n}U_0^2$. As we will show, spin-orbit interaction couples these groups of states and further leads to a sufficient modification in the nature of the localized states.

In laboratory experiment, the random potential is produced by using scattered coherent Gaussian laser light from the rough surface of a glass diffuser. The resulting intensity pattern is due to constructive and destructive interference of light from dif-

ferent scattering regions, forming a high contrast randomized distribution of the light intensity. The necessary condition for a good random potential is that the produced profile must significantly extend the laser wavelength [87, 240]. With an optimal number of scatterers relative to the diffuser size, destructive interference can generate the "void" regions, while alternating interference patterns may generate the "basins". The resulting dimensionless potential parameter U_0 can be tuned in the range from ~ 0.05 to ~ 0.5 [87, 21].

5.3 Localization of non-interacting BEC

In this Section, we consider BEC without self-interactions, where the GPEs (Eqs. (5.1a)-(5.1b)) become a pair of two coupled linear partial differential equations. In the presence of randomness, the roles of the SO and Rabi couplings become highly nontrivial and can lead to modification of the position and shape of the condensate.

5.3.1 Details of calculation procedure

We explore the effect of SO and Rabi coupling by analyzing the condensate ground state obtained by solving the coupled linear GPEs (5.1) in the potential (5.11) using split-step Crank-Nicholson scheme [156, 224]. We consider the Gaussian wavefunction as the initial state with the imposition of antisymmetric condition given as $\psi_\uparrow(x) = -\psi_\downarrow(-x)$ on between two components. To obtain the localized ground state, we use the imaginary time propagation method aided with split-time Cranck-Nicholson scheme. In the simulation runs presented below, we have considered the spatial steps as $\Delta x = 0.025$, and time steps as $\Delta t = 10^{-4}$. To generate the random potential, we choose the number of spikes $\mathcal{N}_s = 512$ within the range $-51.2 < x < 51.2$ with $\bar{n} = 5$ and Gaussian width $\zeta = 0.1$.

5.3.2 Different localized ground state phases in the random potential

Before analyzing the effect of the SO and Rabi coupling on the BEC localization in detail, we first notice that in the absence of self-interaction, we have $\chi_\downarrow = \chi_\uparrow$, $w_\uparrow = w_\downarrow$, and $\langle x_\uparrow \rangle = \langle x_\downarrow \rangle$. Therefore, in this Section, we use common notations χ, w, and $\langle x \rangle$, respectively, for both components. To ensure that the analysis takes into account the realization-dependent properties, wherever relevant we present results for two distinct

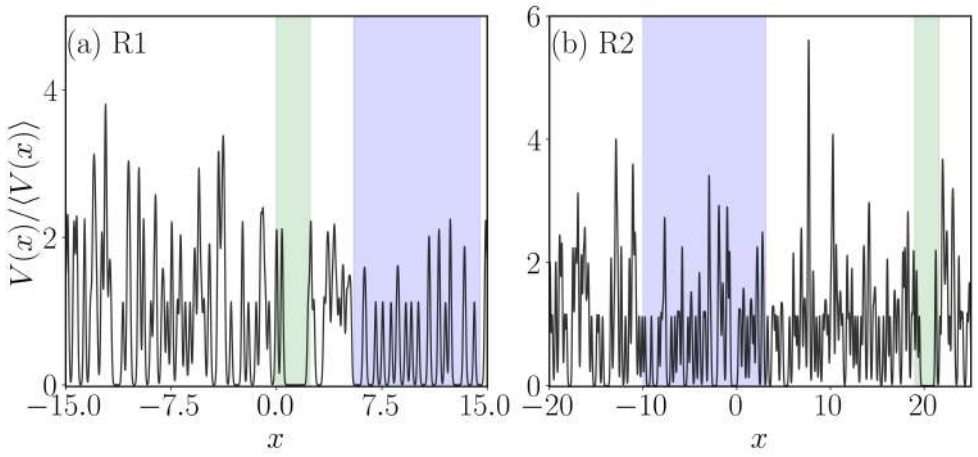

Figure 5.1: The ratio $V(x)/\langle V(x)\rangle$ for realizations (a) R1 and (b) R2, where $\langle V(x)\rangle = \bar{n}U_0$ with $\bar{n} = 5$ and $\zeta = 0.1$. The green and blue shaded regions are drawn respectively to guide the eyes in the void and basin-like regions of the random potential where condensate has a high tendency to get localized.

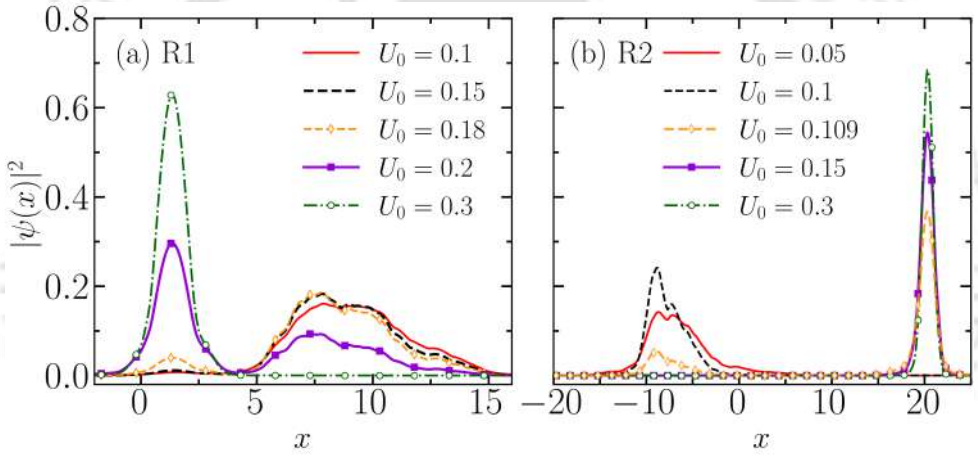

Figure 5.2: The total density profile for different U_0 at $k_L = \Omega = 0$ for (a) R1 and (b) R2. At small U_0 the BEC is localized in the basin-like regions of $V(x)$. With the increase in U_0 it moves to the $V(x)$ voids (cf. Fig. 5.1). Here the interactions are $g_{\uparrow\uparrow} = g_{\downarrow\downarrow} = g_{\uparrow\downarrow} = 0$.

random realizations labelled as R1 and R2 shown in Fig. 5.1 with the corresponding ground state densities $\phi_0^2(x)$ shown in Fig. 5.2.

Comparison of Figs. 5.1 and 5.2 shows that at a small U_0 the condensate is localized in broad basins of the potential $V(x)$. With the increase in U_0, a double peak structure including a peak localized in a void of $V(x)$ is being formed by the BEC tunneling between the basin and the void. At a sufficiently large U_0 the density gets completely confined in this void. Depending on the tunneling probability determined mainly by the basin-void separation, the transition occurs either gradually or sharply with the change in U_0, at a relatively large and a relatively small tunneling probability, respectively. These single peak distributions are confirmed by the analysis of the width and

the IPR presented in Fig. 5.3. Upon increasing U_0, when χ becomes greater than ≈ 0.6 and the probability density resembles the localization in a high rectangular potential well. Thus, in the case of R2, the localization towards the void takes place at lower U_0 compared to R1, but the overall effect of the potential is the same in both realizations. As a result, for the BEC well-localized in a void of the random potential of the width

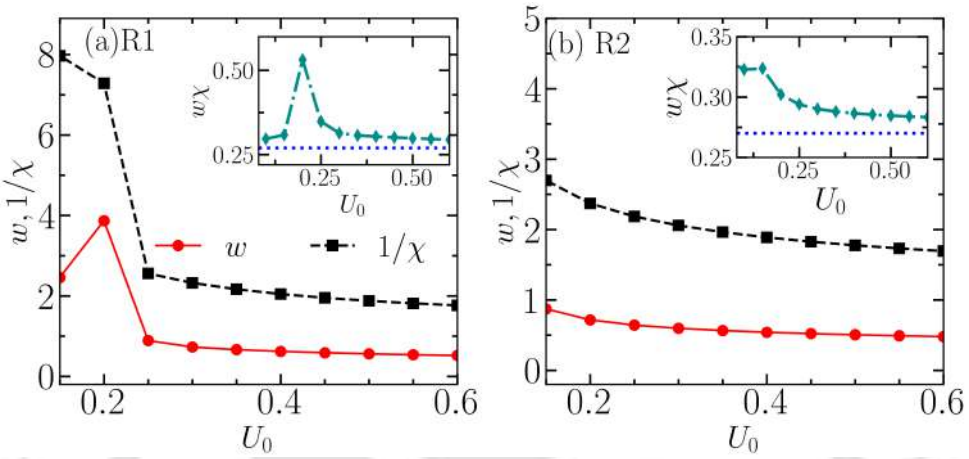

Figure 5.3: The BEC width w and participation ratio $1/\chi$ as a function of U_0 for realizations R1 (a) and R2 (b). Insets show the variation of $w\chi$ with U_0 that asymptotically approaches $w\chi \approx 0.27$ for high U_0, corresponding to well-defined localization in the voids of the random potential. All the other parameters are the same as in Fig. 5.2. The blue dotted line is drawn at exactly $w\chi = 0.27$.

l centered at $\langle x \rangle$, we can use at $\langle x \rangle - l/2 < x < \langle x \rangle + l/2$ with the corresponding approximation $\phi_0^2 = 2\cos^2(\pi(x - \langle x \rangle)/l)/l$, [see Eq. (5.3)] and obtain $\chi = 3/2l$ and $w = \sqrt{(\pi^2 - 6)}l/(2\sqrt{3}\pi)$. Thus, the product $w\chi \approx 0.27$, as shown in the insets of Fig. 5.3 for a relatively large U_0, while sufficiently larger values of $w\chi$ correspond to the double-peak localization at smaller U_0.

5.3.3 Effect of SO and Rabi coupling on the localization for non-interacting BEC

In order to explore the effect of SO and Rabi couplings, in Fig. 5.4, we compare the IPR χ as a function of U_0 at $k_L = 0.5$, $\Omega = 1.0$ with the IPR for $k_L = \Omega = 0.0$. Notably, in the presence of k_L and Ω (solid line) the IPR always remains slightly larger compared to the $k_L = \Omega = 0$ (dashed line) choice irrespective of the realizations. However, for small U_0, where χ is small [Fig. 5.3], the differences between the IPRs tend to be significantly larger in comparison to the localized state for higher disorder strength. Here we notice that in the absence of spin-orbit coupling, Rabi coupling does not influence the BEC localization and *vice versa*. In turn, Fig. 5.4 shows that the interplay of the SO and

Rabi couplings exerts a more pronounced influence on broad condensate states than on strongly localized ones, as can be analyzed below in this subsection.

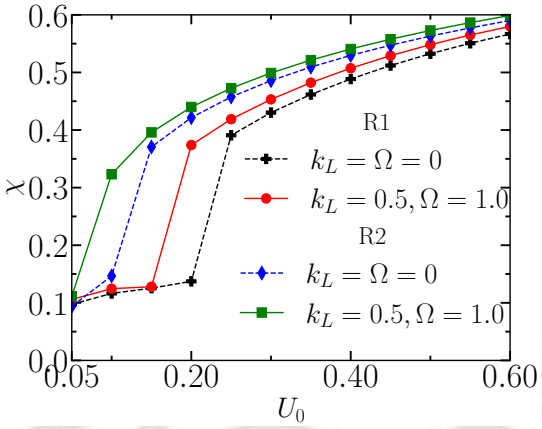

Figure 5.4: The IPR χ as a function of U_0 at $k_L = \Omega = 0$ (dashed lines) and $k_L = 0.5$, $\Omega = 1.0$ (solid lines) for realizations R1 and R2. The increase in χ indicates the localization with increasing U_0 for all cases. Notably, both realizations show slightly higher χ values in the presence of non-zero SO and Rabi coupling, highlighting the influence of spin-dependent couplings on localization.

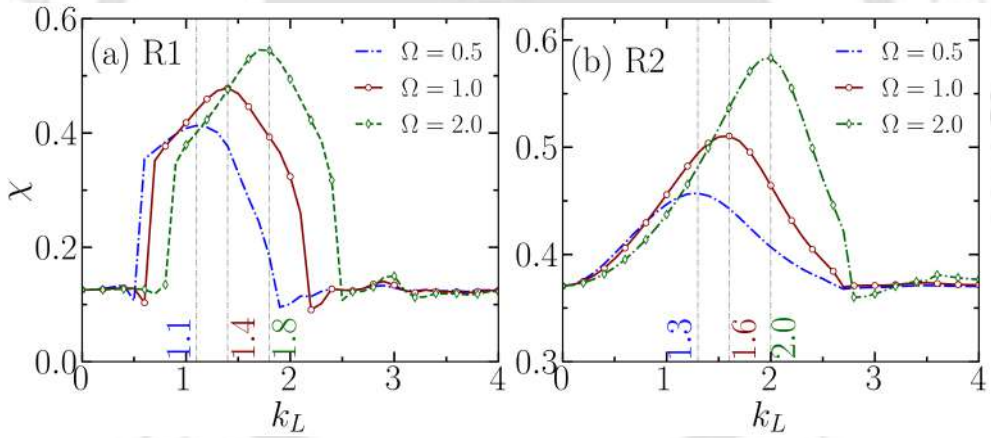

Figure 5.5: The IPR χ as a function of SO coupling parameter k_L for two realizations as (a) R1, and (b) R2. Here $\Omega = 0.5$ (blue dashed line), $\Omega = 1.0$ (red solid line), and $\Omega = 2.0$ (green dotted line). Upon increasing k_L, the IPR initially increases and reaches the maximum at intermediate k_L (shown by vertical dashed lines) resembling the localization, and then decreases to the χ value at $k_L = 0$. In both cases $U_0 = 0.15$.

In Fig. 5.5 we show the variation of χ as a function of k_L at different Ω for the above R1 and R2 realizations. In Fig. 5.5(a) we notice that the IPR remains almost k_L-independent with $\chi \approx 0.15$ for very low and high value of SO coupling $k_L < 0.5$, and $k_L > 2.5$, respectively with a steep increase and decrease at certain values of k_L. Upon increasing Rabi coupling Ω the amplitude of χ and the critical value of k_L at which the IPR attains maximum shifts to larger values. Similarly, Fig. 5.5(b) depicts

a similar dependence except that the critical k_L values differ from realization R1. In addition to that, in the panel (b) the initial value of $\chi \approx 0.38$ at $U_0 = 0.15$, corresponding to localization at $k_L = 0$ in the void (see Fig. 5.6(b)) in comparison to the broadly localized BEC [see Fig. 5.6(a)] for R1. For both the realizations χ attains maximum at $k_L^2 \approx 2\Omega$.

Figures 5.5 and 5.6 present the key results of this Section. The behavior of IPR as a function of k_L can qualitatively be understood as follows. For relatively weak SO coupling, one can use perturbation theory [241] with the basis of $\phi_{\bar{\alpha}}(x)$ by calculating modified energies and wavefunctions of the BEC states such that correction to the energy of the state $\bar{\alpha}$ is $\delta\epsilon_{\bar{\alpha}}$. It is important to mention that since the spectrum is dense, after these corrections the order of the index α does not correspond to the order of the energy levels anymore such that inequality $\epsilon_{\bar{\alpha}} + \delta\epsilon_{\bar{\alpha}} > \epsilon_{\bar{\kappa}} + \delta\epsilon_{\bar{\kappa}}$ can be satisfied at $\alpha < \kappa$ and $\lambda_{\bar{\alpha}} = \lambda_{\bar{\kappa}}$.

For the energy correction of the state $\bar{\alpha}$ we obtain by summation over $\bar{\nu}$ eigenstates in the random potential (cf. Eq.(5.3)):

$$\delta\epsilon_{\bar{\alpha}} = k_L^2 \sum_{\bar{\nu}\neq\bar{\alpha}} \frac{|K_{\nu,\alpha}|^2}{\epsilon_\alpha - \epsilon_\nu + \Omega(\lambda_{\bar{\alpha}} - \lambda_{\bar{\nu}})}, \tag{5.14}$$

where $\lambda_{\bar{\alpha}} \neq \lambda_{\bar{\nu}}$ and

$$K_{\nu,\alpha} = -\mathrm{i}\int_{-\infty}^{\infty} \phi_\nu(x)\phi'_\alpha(x)dx \tag{5.15}$$

is the corresponding matrix element of momentum with $\phi'_\alpha(x) = d\phi_\alpha(x)/dx$. Similarly, we obtain for wavefunction correction:

$$\delta\phi_{\bar{\alpha}} = k_L \sum_{\bar{\nu}\neq\bar{\alpha}} \frac{K_{\nu,\alpha}}{\epsilon_\alpha - \epsilon_\nu + \Omega(\lambda_{\bar{\alpha}} - \lambda_{\bar{\nu}})}\phi_{\bar{\nu}}. \tag{5.16}$$

For a state demonstrating Anderson localization with $\phi_\nu(x) \approx \cos(k_\nu x + \varphi_\nu)\xi_\nu(x)$ and a localized on the spatial scale l state $\phi_0 = \sqrt{2}\cos\left(\pi(x - \langle x\rangle)/l\right)/\sqrt{l}$, the momentum matrix element $K_{\nu,\alpha}$ can be presented as:

$$K_{\nu,\alpha} = -\pi\left(\frac{2}{l}\right)^{3/2} k_\nu \xi_\nu(\langle x\rangle)\frac{\sin(k_\nu l/2 + \varphi_\nu)\cos(k_\nu l/2)}{k_\nu^2 - (\pi/l)^2}. \tag{5.17}$$

As a result, the Fourier transform of the density acquires higher momentum components resulting (cf. Eq. (5.8) and Ref. [235]) in the increase in the IPR with the decrease

of the spatial scale of the wavefunction.

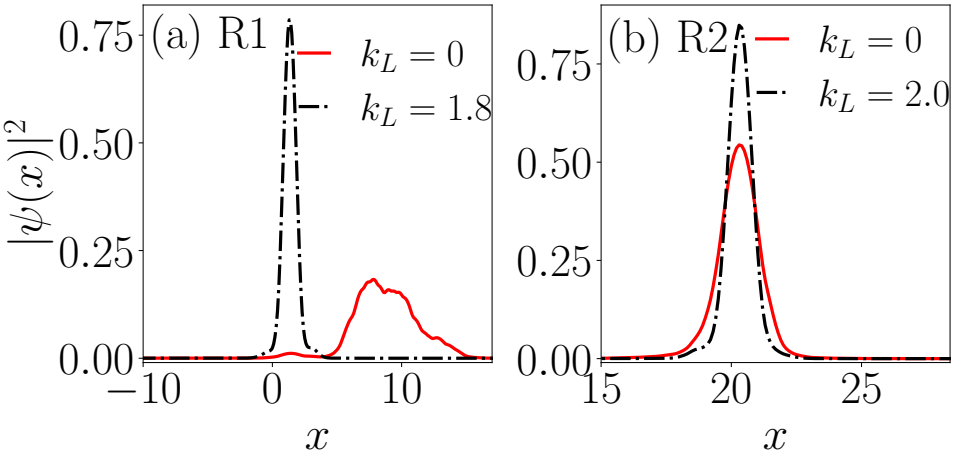

Figure 5.6: (a) Total density profile for $k_L = 0$ (red solid line), and $k_L = 1.8$ (black dashed line) which corresponds to the k_L at which IPR attains the maximum in Fig. 5.5(a) for realization R1. (b) Total density profile at $k_L = 0$ (red solid line), and $k_L = 2.0$ (black dashed line), the SO coupling associated to the maximum of the IPR in Fig. 5.5(b) for realization R2. The other parameters are $\Omega = 2$ and $U_0 = 0.15$ in both cases.

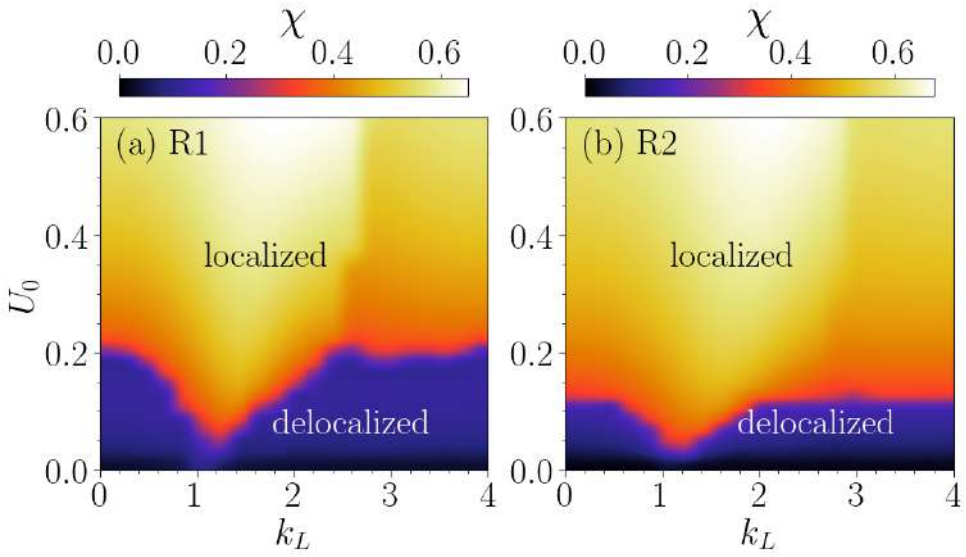

Figure 5.7: Pseudo-color representation of the IPR χ in the (k_L, U_0) plane keeping $\Omega = 1$ for realizations R1 (a) and R2 (b). The localized region is characterized by $\chi \gtrsim 0.3$, while $\chi < 0.3$ indicates the broadly localized condensate, marked as "delocalized" in this and the following Figures. Notably, for both the realizations, with weak disorder strength $U_0 \approx 0.15$, the condensate gets localized for $k_L \approx 1.25$, whereas at higher k_L values, it remains broadly localized in the basin. In the case of R2 (b), the transition from broadly to strongly localized state starts at lower $U_0 \geq 0.1$, compared to $U_0 \geq 0.2$ for realization R1 in (a).

The matrix element in Eq. (5.17) rapidly decreases with the increase in k_ν limiting the summation range over ν and with the increase in l demonstrating that the pertur-

bation corrections are smaller for broadly localized states. We notice one important observation, specific for the low-energy states in a random potential and, thus, dependent on its realization. The energy correction strongly depends on the shape of the wavefunction and, therefore, on the state number α. Therefore, if perturbed energy $\epsilon_{\bar{\alpha}} + \delta\epsilon_{\bar{\alpha}}$ of a state with $\alpha > 0$ becomes smaller than that of the state with $\alpha = 0$ and $\lambda_{\bar{0}} = -1$ (now $\epsilon_{\bar{0}} + \delta\epsilon_{\bar{0}}$), the former becomes the ground state. We can see this in Fig. 5.5, where χ for realization R1 abruptly changes at a certain value of k_L and a more localized state becomes the ground state. This is illustrated in the Figures 5.5 and 5.6. Figure 5.5(a) shows a relatively weak effect of SO coupling on the ground state up to a certain value of k_L due to its broad localization in a basin of $V(x)$. Then, at a certain value of k_L the ground state jumps to a narrow state [see Fig. 5.6(a)] in the $V(x)$ void nearby with this state remaining the ground state in a relatively broad range of k_L. On the contrary, in the realization R2 [see Fig. 5.5(b)] the initial ground state is relatively narrow, the position jump does not occur, and the modification of χ is smaller than that for the R1 realization. After the jump in the IPR for realization R1, both realizations behave with k_L in a similar fashion since the BEC is well localized in a void of $V(x)$.

In the strong SO coupling limit one can use linear combinations of degenerate at $\Omega = 0$ time-reversed states $\phi_0(x)\exp(-\mathrm{i}k_L x)[1,0]^{\mathrm{T}}$ and $\phi_0(x)\exp(\mathrm{i}k_L x)[0,1]^{\mathrm{T}}$ to describe the ground state wavefunction at nonzero Ω. These states have energies $\epsilon_0 - k_L^2/2$ and nonzero Ω produces a doublet of the eigenstates

$$\psi = \phi_0(x)[\exp(-\mathrm{i}(k_L x + \gamma)), \pm\exp(\mathrm{i}k_L x)]/\sqrt{2}, \tag{5.18}$$

with the ground state corresponding to $-\exp(\mathrm{i}k_L x)$ for the spin-down component, where γ is the corresponding phase shift. This doublet shows a weak Rabi splitting due to a small spin component

$$\langle\sigma_x\rangle = -\left|\int_{-\infty}^{\infty}\phi_0^2(x)\exp(2\mathrm{i}k_L x)dx\right|. \tag{5.19}$$

The corresponding χ parameters here are the same as those at $k_L = 0$, in agreement with Fig. 5.5. Due to a small overlap of the spin-up and spin-down components of the ground state spinor, the corresponding spin state is strongly mixed with $P \ll 1$ while the spin miscibility η is still equal to one since their absolute values remain unchanged. The clear-cut criteria of transition from weak to strong SO coupling for the system cannot be formulated since all involved energies are of the same order of mag-

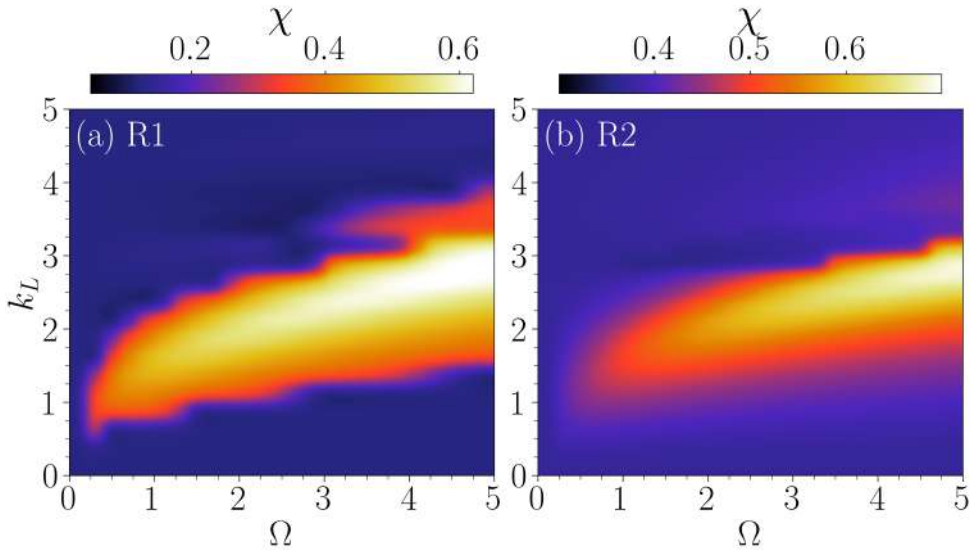

Figure 5.8: Pseudo-color representation of the IPR χ of the spin-up component in $\Omega - k_L$ plane showing the different localization regions for realizations R1 (a) and R2 (b). In panel (a), the broad localization region is characterized with $\chi \leq 0.15$, and the localized region ranges within the range $0.3 \lesssim \chi \lesssim 0.6$. Similarly, the transition boundary in panel (b) is characterized within $0.4 \lesssim \chi \lesssim 0.5$ and in the localized region $\chi \geq 0.5$.

nitude. A general criterion can be formulated as $k_L^2 \gtrsim \Omega$, similar to the transition from plane wave to stripe phases in disorder-free systems. This condition imposes the upper limit on the transition $k_L \sim \Omega^{1/2}$. Another criterion can be formulated as $k_L/\chi \gtrsim 1$, corresponding to a relatively weak spin splitting compared to 2Ω, (cf. Eq. (5.19)) and this condition is $\Omega-$independent. A complementary scenario is the violation of the lower-order perturbation theory producing relatively weak splitting of the states since the energy shift depends on the spin of the state. States are getting closer in the energy, and this gives a qualitative condition of the transition from weak to strong SO coupling. Since in the system we consider, χ and Ω are of the order of 1, all these conditions correspond to the transition at $k_L \sim 1$ also.

Furthermore, to get a comprehensive picture of the parameter-dependent localization scales, we perform an extensive simulation for different ranges of disorder strength U_0 and SO coupling k_L by keeping the Rabi coupling at $\Omega = 1.0$. In Fig. 5.7, we present the pseudo color plot of the IPR χ in the (k_L, U_0) plane for realizations R1 and R2. Here, we have used the criteria, $\chi \geq 0.35$ to characterize the condensate in a localized state. In case of R1 [Fig. 5.7(a)], the IPR remains $\chi \gtrsim 0.4$ and become almost independent of k_L after $U_0 \geq 0.2$, whereas for R2 [Fig. 5.7(b)], the threshold value of U_0 above which the χ is greater than 0.4, is around $U_0 \geq 0.1$. However, at $k_L \approx 1.25$ the IPR becomes $\chi \approx 0.4$ at a very low value of $U_0 \approx 0.05$ irrespective of realizations.

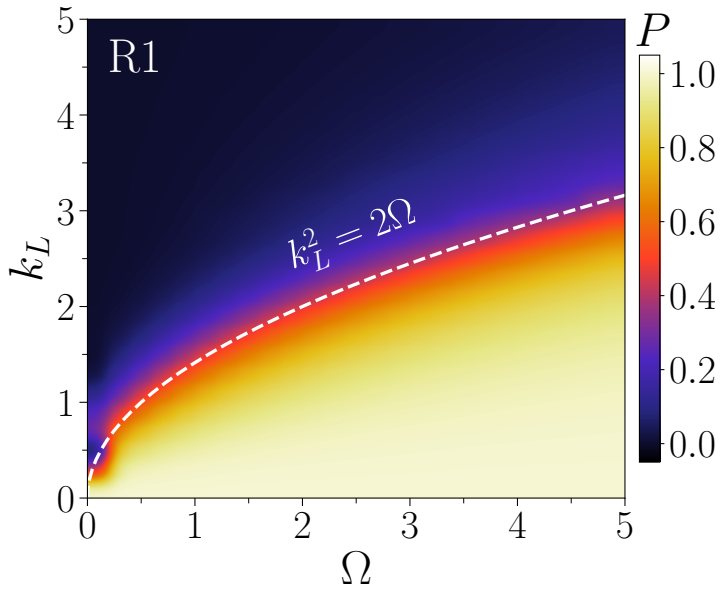

Figure 5.9: Pseudo-colormap representation of purity P in $\Omega - k_L$ plane at $U_0 = 0.15$, $g = 0$ for realization R1. The white dashed line, drawn at $k_L^2 = 2\Omega$ indicates the transition from a pure to a mixed state, as the purity P decreases towards 0. For R2 realization, this transition follows the same relationship.

Next, Fig. 5.8 illustrates the pseudo color representation of the IPR χ in (Ω, k_L) plane by keeping the disorder strength $U_0 = 0.15$. In the case of R1 in Fig. 5.8(a), the IPR remains at $\chi \lesssim 0.25$ for the broadly localized region at very low and high k_L values for a particular Ω. On the other hand, in the localized region, the IPR lies within $0.4 \lesssim \chi \lesssim 0.6$. Using the IPR variation it can be said that the condensate makes a transition from broad to narrow localized and once again it goes to a broadly localized state for higher values of $k_L \gtrsim 3.0$ for a fixed Ω. Similar features of the modification in the spatial scale of localization are also observed in Fig. 5.8(b) for realization R2, except the amplitude of χ is larger in comparison to R1 both for narrow- and broadly localized regions.

Further, we analyze the effect of k_L and Ω on the relation between localization and spin state by calculating the purity P of the condensate. In Fig. 5.9, we show the pseudo color map representation of the purity in (k_L, Ω) plane at $U_0 = 0.15$ for realization R1. The transition of purity towards zero, maintaining the relation $k_L^2 > 2\Omega$ (as marked by a yellow line) signifies the transition from the pure to the mixed phase of the condensate. Note that the condition for this transition is similar to the condition of transition of plane wave to stripe phase of the condensate in disorder-free systems.

So far, we have observed the transition between broad and narrow localized BEC caused by the interplay of the random potential and Rabi, and the SO couplings. To

understand the effect of the nonlinearities, in the next Section, we explore the pattern of localization in the presence of intra- and inter-species interactions.

5.4 Localization-delocalization in the presence of self-interaction without Manakov's symmetry

In this Section we investigate the effect of the self-interactions without Manakov's symmetry, that is with lifted spin rotational invariance, on the BEC localization. The absence of spin rotational invariance considerably extends the variety of realizations of the condensate localization, as will be shown in the following.

5.4.1 Qualitative analysis

The Gross-Pitaevskii equations (5.1) do not represent an integrable system [242] making approaches similar to the perturbation theory of the previous Section impossible. However, one can perform a semiquantitative analysis and compare it with the exact numerical results, as it will be done in what follows.

In general, the cross-spin repulsion $g_{\uparrow\downarrow}$ and the difference in the self-interaction ($g_{\uparrow\uparrow} \neq g_{\downarrow\downarrow}$) tend to form different populations ($N_\uparrow \neq N_\downarrow$) by competing with the Rabi coupling. To begin with understanding the joint effect of the spin-related couplings and self-interaction we assume that the BEC is near the threshold described by the trial wavefunction

$$\psi_{\rm tr} = \frac{\phi_{\rm g}(x)}{\sqrt{2}} \left[\sqrt{1+\varepsilon}\exp(i\theta), -\sqrt{1-\varepsilon}\exp(-i\theta)\right]^{\rm T}, \tag{5.20}$$

where $|\varepsilon| \ll 1$, and $\phi_{\rm g}(x)$ depend on the random potential, SO coupling, and self-interaction. The position-dependent phase θ corresponds to the effect of SO coupling.

We expand the total BEC energy in terms of $\varepsilon = N_\uparrow - N_\downarrow$ to the first relevant contributions as

$$\tilde{\epsilon}_{\rm tr}(\varepsilon) \quad - \quad \tilde{\epsilon}_{\rm tr}(0) = \frac{\chi}{4}\left(g_{\uparrow\uparrow} - g_{\downarrow\downarrow}\right)\varepsilon + \left[\frac{\chi}{8}\left(g_{\uparrow\uparrow} - g_{\downarrow\downarrow}\right) - \frac{\Omega}{2}\langle\sigma_x\rangle - \frac{\chi}{4}g_{\uparrow\downarrow}\right]\varepsilon^2, \tag{5.21}$$

where

$$\langle \sigma_x \rangle = -\int_{-\infty}^{\infty} \phi_g^2(x) \cos(2\theta)\, dx, \tag{5.22}$$

and the interaction-dependent χ is the same for both spin components. In Eq.(5.21)

$$\tilde{\epsilon}_{\rm tr}(0) = \tilde{\epsilon}_{\rm lin} + \frac{\chi}{8}\left(g_{\downarrow\downarrow} + g_{\uparrow\uparrow}\right) + \frac{\chi}{4} g_{\uparrow\downarrow}, \tag{5.23}$$

where $\tilde{\epsilon}_{\rm lin}$ is the contribution of the terms not including self-interactions explicitly.

One can draw several following conclusions from Eqs. (5.21), (5.22), and (5.23).

(i) At $k_L = 0$ and $g_{\downarrow\downarrow} = g_{\uparrow\uparrow} = 0$ to have the effect on the BEC, the repulsion $g_{\uparrow\downarrow}$ should exceed a certain threshold with $g_{\uparrow\downarrow}\chi > 2\Omega$. Thus, a competition between Ω and $g_{\uparrow\downarrow}\chi$, makes the effect of cross-spin repulsion relatively weaker for extended states with $\chi \ll 1$. At $g_{\downarrow\downarrow} = g_{\uparrow\uparrow}$ the energy depends on ε^2, making the ground state double degenerate while any $g_{\downarrow\downarrow} \neq g_{\uparrow\uparrow}$ lifts this degeneracy.

(ii) At $k_L = 0$ and nonzero $g_{\downarrow\downarrow} - g_{\uparrow\uparrow}$, the transition for spin inequality has no threshold since same spin repulsion yields a term linear in ε in the energy and the resulting $N_\uparrow - N_\downarrow$ depends on $g_{\downarrow\downarrow} - g_{\uparrow\uparrow}$..

(iii) Self-repulsion expands the BEC when the self-interaction energy becomes close to the ground state energy in the non-self-interacting system (e.g., Ref. [243]). Thus, nonlinearities decrease $\chi_\uparrow$ and $\chi_\downarrow$, making them different, as it depends on the self-interaction parameters and causing spin-dependent broadening. Different density profiles for spin-up and spin-down components contribute to all their spin-related properties.

(iv) Spin-orbit coupling in one-dimensional systems has a complex role in the presence of nonlinearities and disorder [242]. Firstly, it modifies the mean value of $\langle \sigma_x \rangle$ by adding phases to the wavefunction components. Secondly, it can increase the role of the self-interaction producing $z-$axis spin polarization since fully $z-$polarized spin states acquire the contribution of $-k_L^2/2$ to the total energy. Thus, one can expect its critical role in the presence of nonlinearities, as we will explore further below.

To investigate numerically the effect of spin-related interaction and the nonlinearities on the localization of the condensate, we explore below two scenarios. Firstly, we tune the inter-species repulsion $g_{\uparrow\downarrow}$, and secondly, vary the intra-species interaction $g_{\uparrow\uparrow(\downarrow\downarrow)}$. In both cases, we show that the inequality $g_{\uparrow\uparrow} \neq g_{\downarrow\downarrow}$ is critically important for the BEC properties.

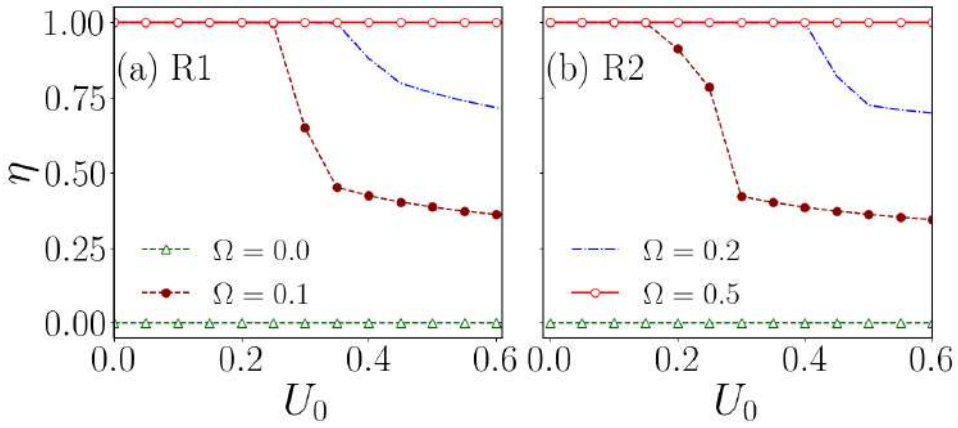

Figure 5.10: Variation of miscibility η with disorder strength U_0 for different Rabi-coupling Ω in case of realizations R1 (a), and R2 (b). For $\Omega \leq 0.2$, η decreases with the increment of U_0 beyond a threshold value of U_0. In the case of R2, the threshold value for $\eta \ll 1$ is lower than R1. Here, other parameters are $g_{\uparrow\uparrow} = 0.1$, $g_{\downarrow\downarrow} = 0.5 g_{\uparrow\uparrow}$, $g_{\uparrow\downarrow} = 1.0$, and SO coupling $k_L = 0$.

5.4.2 Effect of the Rabi coupling and disorder strength on the spin miscibility

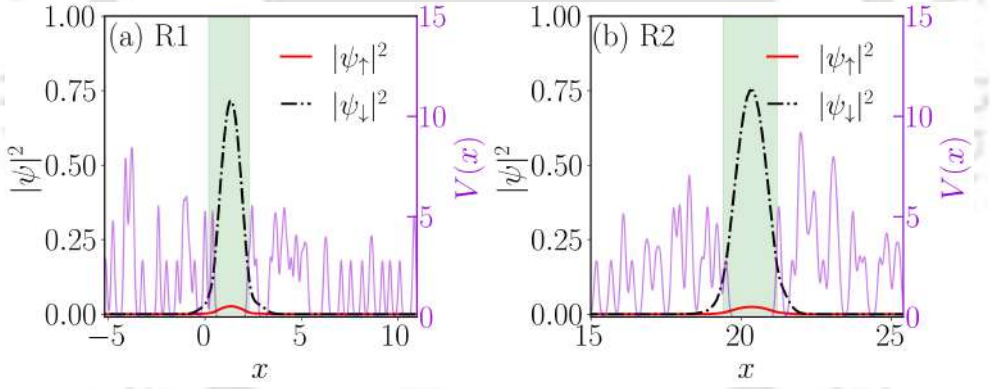

Figure 5.11: Condensate density at $\Omega = 0.1$, $U_0 = 0.5$. The interaction and SO coupling parameters are $g_{\uparrow\uparrow} = 0.1$, $g_{\downarrow\downarrow} = 0.05$, $g_{\uparrow\downarrow} = 1.0$, and $k_L = 0$. The random potential profile is shown with light violet lines along the right side axis. The shaded region is drawn to show the void of the potential.

After introducing at $k_L = 0$ a small imbalance between $g_{\uparrow\uparrow}$ and $g_{\downarrow\downarrow}$ to break the symmetry of the Hamiltonian, the competition between the inter-species interaction $g_{\uparrow\downarrow}$ and the Rabi coupling Ω significantly affects the spin miscibility η (see Eq. (5.21)). In addition to that, the random potential plays a critical role in this parameter.

To investigate the effect of the disorder, in Fig. 5.10 we show the η [see Eq. 6.9] as a function of U_0 for different Ω for the realizations R1 and R2. For both realizations, the miscibility $\eta \equiv 0$ for $\Omega = 0$ since here we have $\psi_\uparrow \equiv 0$. At $\Omega > 0$ and small U_0 one still obtains $\eta = 1$ since the product $g_{\uparrow\downarrow}\chi$ for extended states is small and cannot overcome

the effect of the Rabi splitting. After a certain threshold in U_0, corresponding to the condition $g_{\uparrow\downarrow}\chi > 2\Omega$, the spin miscibility decreases as expected from Eq. (5.21) and (5.22). This threshold value of U_0 increases with increasing Ω up to a certain range, beyond that Ω the condensate remains perfectly miscible for higher Rabi coupling. The threshold values U_0 in the case of R2 (Fig. 5.10 panel (b)) are lower compared to R1, which complements the analysis of Fig. 5.7. After reaching the spin population imbalance, the inter-species repulsion can spatially separate spin components leading to $\langle x_\uparrow \rangle \neq \langle x_\downarrow \rangle$. Following the decay, η achieves a plateau-like behavior with a small slope, where it remains approximately constant while the plateau amplitude decreases with the increase in Ω. Conclusively, the influence of the Rabi coupling towards spin mixing can effectively be reduced with the increase of the disorder strength as illustrated in Fig. 5.11. We notice that the redistribution of population from the spin-up $|\psi_\uparrow|^2$ to the spin-down $|\psi_\downarrow|^2$ takes place, in which both components still remain in the void of the potential due to a relatively weak inter-species repulsion. This phenomenon can be attributed to the *induced localization* as recently has been observed in [124].

A qualitative description of two features of this plateau-like behavior related to the fact that it is characterized by the $N_\uparrow \ll N_\downarrow \approx 1$ inequality is in the order here. First, $\psi_\downarrow \approx \phi_0$ in the given potential $V(x)$ such that the wavefunction can be presented as $\psi = [\sqrt{N_\uparrow}\psi_\uparrow, \sqrt{N_\downarrow}\phi_0]^{\mathrm{T}}$, where $\psi_\uparrow$ satisfies the GPE (5.1a) with $\psi_\downarrow \approx \phi_0$ (cf. Eq. (5.3)). Next, taking into account that $\chi_\downarrow \sim \chi_\uparrow \sim \chi$ we find that the spin miscibility in Eq. (6.9) shows $\eta \sim \sqrt{N_\uparrow} \gg N_\uparrow$. Minimization of the total energy with spin-dependent contributions yields $N_\uparrow \sim (\Omega/(g_{\uparrow\downarrow}\chi))^2$, and therefore $\eta \sim \Omega/(g_{\uparrow\downarrow}\chi) \gg N_\uparrow$.

5.4.3 Effect of finite inter-species interaction $g_{\uparrow\downarrow}$ on the localization

So far, our results revealed that the interplay of the disordered potential and the imbalance between intra-species interaction leads to the exchange of population from one component to another. Here we will show that nonlinearities can lead to stronger localization of one component at the expense of weaker localization of the other in the presence of a sufficiently strong disorder.

To understand the role of the inter-species interaction $g_{\uparrow\downarrow}$ we begin with the populations, followed by the variation of the IPR with $g_{\uparrow\downarrow}$ at the Rabi coupling $\Omega = 0.5$ for realization R1. Note that, the results for R2 exhibit similar qualitative features as those for R1. Therefore, in what follows we will only discuss the results pertaining to the R1 case. The populations $N_{\uparrow(\downarrow)}$ presented in Fig. 5.12 show that for the broadly localized condensate at $U_0 = 0.15, k_L = 0$, it remains the same across all the range of $g_{\uparrow\downarrow}$ where

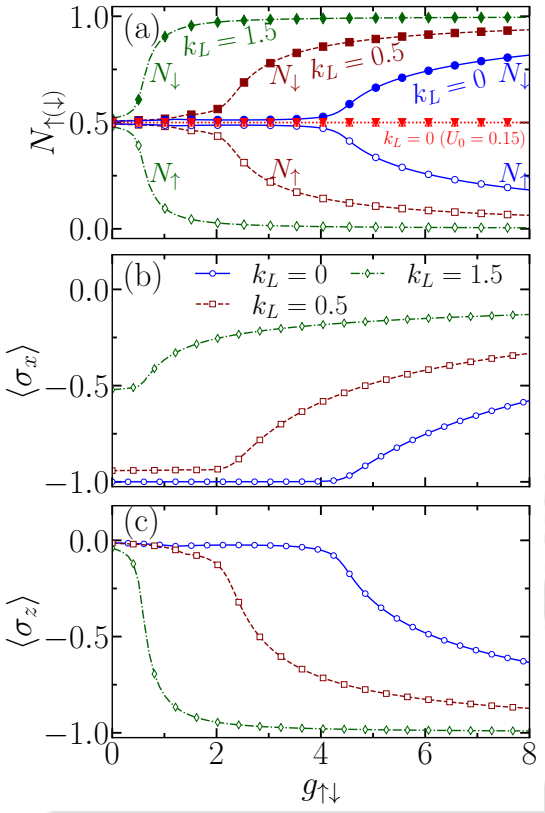

Figure 5.12: (a) Variation of populations with inter-species interaction $g_{\uparrow\downarrow}$ by keeping intra-species interactions at $g_{\uparrow\uparrow} = 0.1, g_{\downarrow\downarrow} = 0.5 g_{\uparrow\uparrow}$, and the coupling parameters are $k_L = 0$ (blue circle marked solid line), $k_L = 0.5$ (brown square marked dashed line), and $k_L = 1.5$ (green diamond marked dash-dotted line) at $\Omega = 0.5$. Since $g_{\uparrow\uparrow} > g_{\downarrow\downarrow}$, owing to repulsion, we obtain $N_\uparrow < N_\downarrow$. Here, we also show the populations for $U_0 = 0.15$, $k_L = 0$ (red triangles with dotted line) in order to compare it with $N_{\uparrow(\downarrow)}$ at $U_0 = 0.5$ (blue solid line). Variations of $\langle \sigma_x \rangle$ and $\langle \sigma_z \rangle$ as a function of inter-species interaction $g_{\uparrow\downarrow}$ for $k_L = 0$ (blue solid line), 0.5 (brown dashed line), and 1.5 (green dash-dotted line) at $U_0 = 0.5$ are shown in panels (b) and (c), respectively.

small χ leads to $g_{\uparrow\downarrow}\chi < 2\Omega$, rendering the components in the miscible state. In contrast, the narrow localized condensate at $U_0 = 0.5$ shows that the populations in both components remained approximately constant at $N_\uparrow \approx N_\downarrow \approx 0.5$ only up to $g_{\uparrow\downarrow} \leq 4.6$ and then shows an increase in $N_\downarrow$ and corresponding decrease in population in spin-up component $N_\uparrow$ in case of $k_L = 0$. Similarly, the inclusion of $k_L = 0.5$ (brown dashed line), 1.5 (green dash-dotted line) decrease the threshold value of interspecies interaction $g_{\uparrow\downarrow}$ for the separation of the condensate population. For $k_L = 0.5$, and $k_L = 1.5$ the populations in both component remain nearly constant at 0.5 upto $g_{\uparrow\downarrow} \leq 2.1$, and $g_{\uparrow\downarrow} \leq 0.5$, respectively.

Next, in Fig. 5.13(a), we show the variation of the IPR $\chi_{\uparrow(\downarrow)}$ with $g_{\uparrow\downarrow}$ at $U_0 = 0.15$ and $U_0 = 0.5$ by keeping the coupling parameters at $k_L = 0$ and $\Omega = 0.5$. For $U_0 = 0.15$, one can notice the decreasing behavior of $\chi_\uparrow = \chi_\downarrow$ indicates the consid-

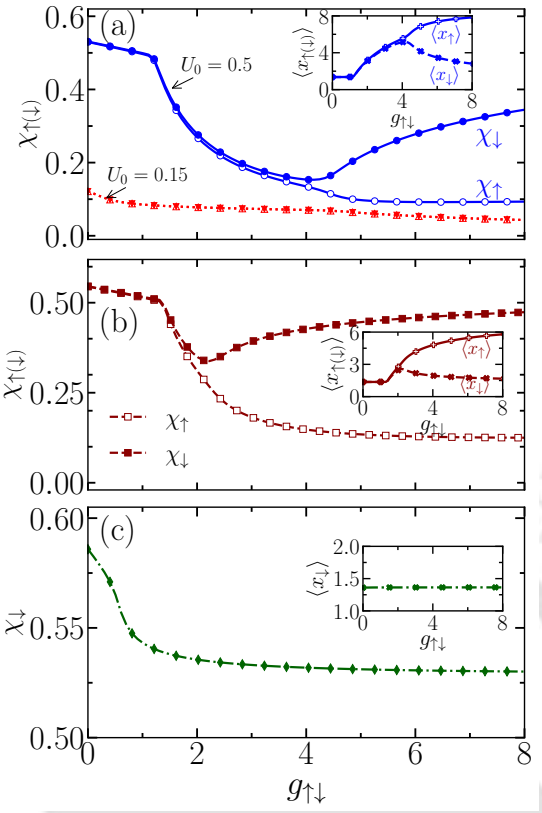

Figure 5.13: (a) Variation of the IPR $\chi_{\uparrow(\downarrow)}$ as a function of $g_{\uparrow\downarrow}$ at two different disorder strengths as : $U_0 = 0.15$, and $U_0 = 0.5$ at $k_L = 0$. IPR at (b) $k_L = 0.5, U_0 = 0.5$, and (c) $k_L = 1.5, U_0 = 0.5$. In figure (c), only $\chi_\downarrow$ has shown as the population in the spin-up component is zero. Here, the other parameters are $g_{\uparrow\uparrow} = 0.1, g_{\downarrow\downarrow} = 0.05$, and $\Omega = 0.5$. Inset figures show the center of mass of the spin-up and spin-down condensate which gets separated beyond the threshold value of $g_{\uparrow\downarrow}$. The results are shown for realization R1.

erable broadening of the condensate. Conversely, for $U_0 = 0.5$, initially, the IPR for both components remains the same and exhibits a decreasing trend until $g_{\uparrow\downarrow} \approx 4.6$. However, as $g_{\uparrow\downarrow}$ increases further, $\chi_\downarrow$ starts to increase due to the higher condensate density. The increase in $\chi_\downarrow$ is complemented by the decreasing behavior of $\chi_\uparrow$. This observation aligns well with the findings in Fig. 5.12.

Notice that a considerable separation of $\chi_\uparrow$ and $\chi_\downarrow$ for $U_0 = 0.5$ starts at $g_{\uparrow\downarrow}\chi$ close to $2\Omega = 1$, corresponding to the condition (i) formulated after Eq. (5.21). For the broadly localized state at $U_0 = 0.15$, this product is always considerably less than 1, and the separation does not occur. The difference in the behavior of $\chi_\uparrow$ and $\chi_\downarrow$ is attributed to strongly different populations $N_\uparrow$ and $N_\downarrow$ with $N_\uparrow \ll N_\downarrow$ and their spatial separation since in the GPEs we have cross-interaction terms $g_{\uparrow\downarrow}|\psi_\downarrow|^2\psi_\uparrow$ and $g_{\uparrow\downarrow}|\psi_\uparrow|^2\psi_\downarrow$ in Eq. (5.1a) and (5.1b), respectively. As a result, at a large $g_{\uparrow\downarrow}$, $\chi_\uparrow$ tends to almost constant while $\chi_\downarrow$ still decreases.

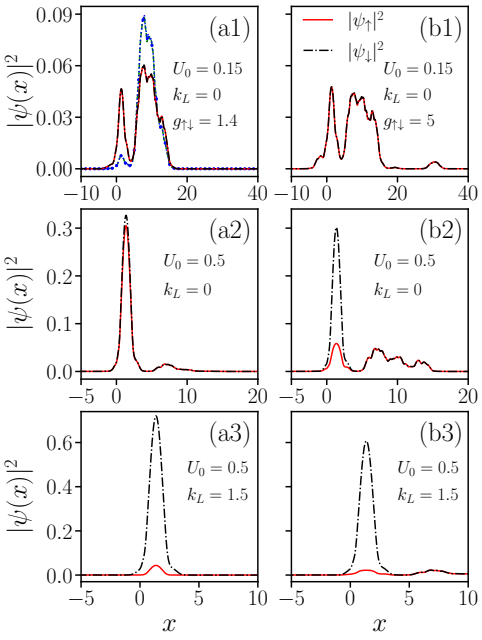

Figure 5.14: Condensate density of up (solid red line), and down (dash-dotted black line) components for different disorder and SO coupling strengths as $U_0 = 0.15, k_L = 0$ (a1, b1), $U_0 = 0.5, k_L = 0$ (a2, b2), and $U_0 = 0.5, k_L = 1.5$ (a3, b3) at inter-species interaction $g_{\uparrow\downarrow} = 1.4$ (left column), and $g_{\uparrow\downarrow} = 5.0$ (right column). The intra-species interactions are $g_{\uparrow\uparrow} = 0.1$, $g_{\downarrow\downarrow} = 0.05$, and $\Omega = 0.5$. In panel (a1) the density $|\psi_\uparrow|^2 = |\psi_\downarrow|^2$ (blue and green dashed lines) at $g_{\uparrow\downarrow} = 0$ is plotted for comparison.

Figures 5.12 and 5.13 show that the critical value of $g_{\uparrow\downarrow}$ causing spin polarization and the IPR difference decreases upon increasing the k_L. This behavior corresponds to Eq.(5.19), where at a strong SO coupling the role of the Rabi interaction rapidly decreases and the effect of cross-repulsion becomes dominant. Also, the $g_{\uparrow\downarrow}$ repulsion produces state with $\langle\sigma_z\rangle = N_\uparrow - N_\downarrow$. At a sufficiently strong $g_{\uparrow\downarrow}$ one obtains $N_\uparrow - N_\downarrow \approx -1$ and purity $P \approx 1.0$ in Fig. 5.12(c). For example, at $k_L = 0.5$ in Fig. 5.13(b), the $\chi_\downarrow$ starts increasing with respect to $\chi_\uparrow$ beyond $g_{\uparrow\downarrow} \approx 2.0$, which is perfectly complemented by the populations in Fig. 5.12. Furthermore, the IPR at $k_L = 1.5$ [see Fig. 5.13(c)] exhibits similar trend. Since with the increase in $g_{\uparrow\downarrow}$ one reaches $N_\uparrow \ll 1$, we present only $\chi_\downarrow$ in this case.

The role of k_L can be formulated in terms of the joint effect of self-interaction and SO coupling. At a given choice of the intra-spin nonlinearities, they produce a state with $\langle\sigma_z\rangle < 0$ resulting in $\langle\sigma_z\rangle \approx -1$ for a sufficiently large $g_{\downarrow\uparrow}$. This cooperates with the effect of SO coupling in producing states with $\langle\sigma_z\rangle \approx \pm 1$ with the corresponding energy contribution $-k_L^2/2$. Thus, a strong SO coupling leads to the formation of the $\langle\sigma_z\rangle \approx -1$ states at a smaller $g_{\downarrow\uparrow}$, corresponding to the presented Figures.

In Fig. 5.14, we show the spin-projected condensate density at $g_{\uparrow\downarrow} = 1.4$ (left col-

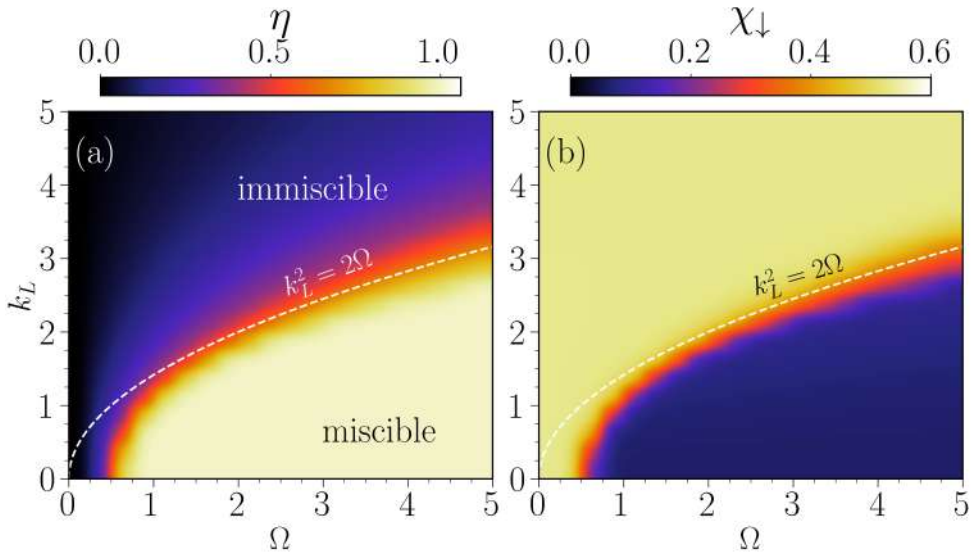

Figure 5.15: Pseudocolor representation of (a) spin miscibility η, and (c) IPR of spin-down $\chi_\downarrow$ in the (Ω, k_L) plane at $g_{\uparrow\uparrow} = 0.1, g_{\downarrow\downarrow} = 0.05, g_{\uparrow\downarrow} = 5.0$. The condensate undergoes a transition from miscible ($\eta \approx 1$) to immiscible ($\eta \ll 1$) region where two regions are separated by following the $k_L^2 = 2\Omega$ relation as marked by the green line. While transitioning from miscible to immiscible region, the $\chi_\downarrow$ increases beyond $k_L^2 > 2\Omega$. Here, the disorder strength is $U_0 = 0.5$ for R1.

umn), and $g_{\uparrow\downarrow} = 5.0$ (right column). At a weak disorder $U_0 = 0.15$ (a1, b1), broadly localized condensates remain perfectly miscible ($\eta \approx 1$) for any value of interactions. In contrast to that, for the narrow localized state at $U_0 = 0.5$, interaction leads to separate spin-up and spin-down components decreasing the spin miscibility. The induced localization of the spin-down component occurs by transferring the density mostly from the void at $\langle x \rangle \approx 1.3$. Lastly, the inclusion of the k_L enhance the transfer of density from one component to another into the void, as shown in the IPR in Fig. 5.13(b,c).

In general, the Figures 5.12-5.14 highlight the qualitative picture for the ground state localization in a random potential. The self-interaction energy due to the inter-spin repulsion can be minimized by diminishing the product $N_\uparrow N_\downarrow$ and the spatial overlap of $\psi_\uparrow$ and $\psi_\downarrow$. This repulsion leads to the localization of different spin species in different regions of $V(x)$ such as voids and basins corresponding to the common chemical potential of these components in Eqs. (5.1a) and (5.1b) at the stationary state. Thus, increasing inter-species interaction induces localization of one component displaced with respect to the other. With the increase in $g_{\downarrow\uparrow}$ at $g_{\uparrow\uparrow} > g_{\downarrow\downarrow}$ the BEC is accumulated in the spin-down state as $\chi_\downarrow$ and $\langle x_\downarrow \rangle$ gradually approach their values for the non self-interacting BEC. This picture works for initially sufficiently well-localized BEC in the void while the initially broadly localized state inside the basin with a small IPR remains inside the basin and broadens with the increasing inter-spin repulsion.

Spin-orbit coupling enhances the effect of the $g_{\uparrow\uparrow} - g_{\downarrow\downarrow}$ difference and leads to the separation of spin-up and spin-down components at a weaker $g_{\uparrow\downarrow}$ interaction.

To further understand the effect of SO and Rabi coupling on induced localization, we calculate the miscibility and IPR for an extensive range of k_L and Ω by keeping disorder strength $U_0 = 0.5$ and $g_{\uparrow\downarrow} = 5.0$. In Fig. 5.15, we present the miscibility and corresponding $\chi_{\uparrow(\downarrow)}$ in (Ω, k_L) plane. The miscibility in panel (a) highlights the decrease in η of localized condensate from the perfectly miscible state by following the $k_L^2 = 2\Omega$ relation for the non-zero value of Ω. In the immiscible region ($k_L^2 > 2\Omega$), increasing k_L predominantly causes the transfer of density from the spin-up to spin-down component, reducing the spin-up density to almost negligible value due to the condition $g_{\uparrow\uparrow} > g_{\downarrow\downarrow}$ [Fig. 5.14(a3,b3)]. As a result, $\chi_\uparrow$ in these immiscible regions becomes insignificant. However, the $\chi_\uparrow$, and $\chi_\downarrow$, shows that in the perfectly miscible region at $k_L^2 \ll 2\Omega$ the IPR remain $\chi_\uparrow \approx \chi_\downarrow \approx 0.08$, while in the immiscible region, the $\chi_\downarrow$ increases to 0.6 results in localizing the down-component with respect to spin-up component as shown in Fig. 5.15(b).

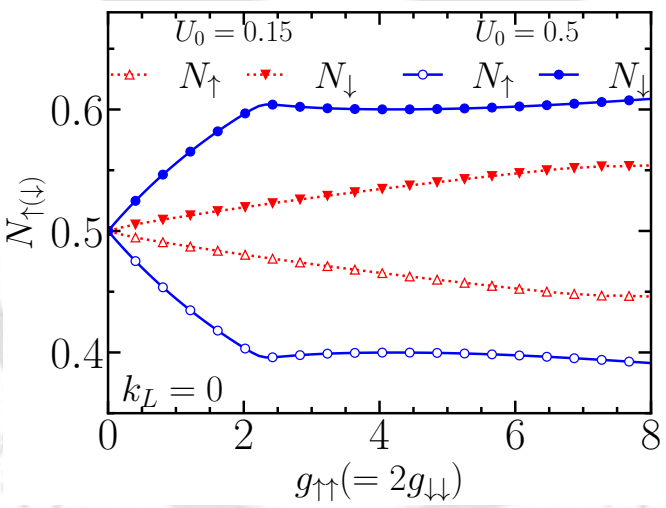

Figure 5.16: Populations of spin-up $N_\uparrow$ (open markers), and spin-down $N_\downarrow$ (filled markers) components as a function of intra-species interaction $g_{\uparrow\uparrow}(= 2g_{\downarrow\downarrow})$ at $k_L = 0$. The other parameters are $g_{\uparrow\downarrow} = 0$, and $\Omega = 0.5$.

5.4.4 Impact of unequal intra-species interaction with $g_{\uparrow\downarrow} = 0$ on localization

In the previous section, we explored the effect of inter-species interactions on the localized condensates by keeping the different small intra-species interactions constant.

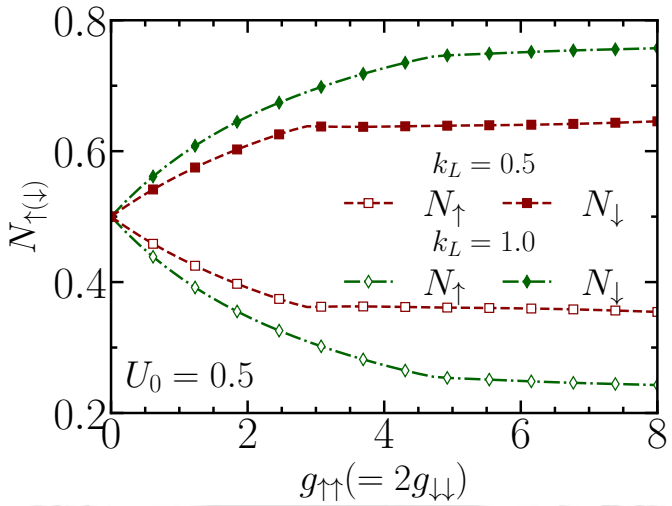

Figure 5.17: Populations of spin-up $N_\uparrow$ (open markers) and spin-down $N_\downarrow$ (filled markers) components as a function of intra-species interaction $g_{\uparrow\uparrow}(= 2g_{\downarrow\downarrow})$ at $k_L = 0.5$, and $k_L = 1.0$. Here, the other parameters are $g_{\uparrow\downarrow} = 0$, and $\Omega = 0.5, U_0 = 0.5$. Upon increasing k_L, leads to an increase in the rate of change of $N_{\uparrow(\downarrow)}$ with the variation of $g_{\uparrow\uparrow}$.

In this subsection, we investigate the effect of the intra-species interactions by keeping $g_{\uparrow\downarrow} = 0$.

To investigate their effect, in Fig. 5.16, we plot the populations of spin-up and spin-down components as a function of $g_{\uparrow\uparrow}$ while the ratio between interactions kept as $g_{\downarrow\downarrow}/g_{\uparrow\uparrow} = 0.5$. One can notice that with the increasing $g_{\uparrow\uparrow}$, the populations in Fig. 5.16 starts separating as $g_{\uparrow\uparrow} \neq 0$. The separation of $N_\uparrow$, and $N_\downarrow$ occurs for both narrow ($U_0 = 0.5$) or a broadly localized state ($U_0 = 0.15$). Notice that the splitting for $U_0 = 0.5$ is considerably stronger than that at $U_0 = 0.15$ since the value of χ at $U_0 = 0.5$ is considerably larger than that at $U_0 = 0.15$. At $k_L = 0$, by using condition $|\varepsilon| \ll 1$, that is $\chi(g_{\uparrow\uparrow} - g_{\downarrow\downarrow}) \ll \Omega$, we obtain from Eq. (5.21):

$$N_\uparrow - N_\downarrow = -\chi \frac{g_{\uparrow\uparrow} - g_{\downarrow\downarrow}}{4\Omega}, \tag{5.24}$$

where at a weak self-interaction one can take χ for the ϕ_0 function. This equation describes well the initial splitting in Fig. 5.16, valid up to $g_{\uparrow\uparrow} < 2$, in agreement with Fig. 5.19 demonstrating $\chi_\downarrow$ and $\chi_\uparrow$ as a function of $g_{\uparrow\uparrow}$.

In addition to that, the inclusion of $k_L = 0.5, 1.0$ [see Fig. 5.17] enhance the separation of $N_{\uparrow(\downarrow)}$ between the components. For very high $g_{\uparrow\uparrow}$ values, the populations for both components saturate at a constant value.

Next, Fig. 5.18 illustrates the spatial variation of the condensate density for spin-up and spin-down components at different intra-species interaction as (a1, b1) $g_{\uparrow\uparrow} =$

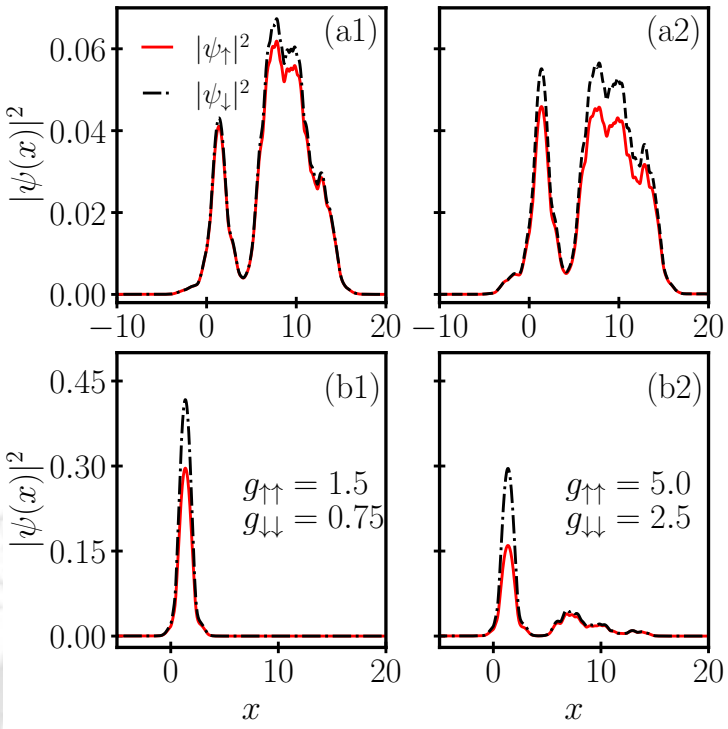

Figure 5.18: Ground state density profile of spin-up $|\psi_\uparrow|^2$ (red solid line), and spin-down $|\psi_\downarrow|^2$ (black dash-dotted line) for different inter-species interactions (a1, b1) $g_{\uparrow\uparrow} = 1.5, g_{\downarrow\downarrow} = 0.75$, and (a2, b2), $g_{\uparrow\uparrow} = 5.0, g_{\downarrow\downarrow} = 2.5$. Here, the disorder strength is kept at $U_0 = 0.15$ (in top panel), and $U_0 = 0.5$ (in bottom panel). The other parameters are $g_{\uparrow\downarrow} = 0$, and $k_L = 0, \Omega = 0.5$ for realization R1.

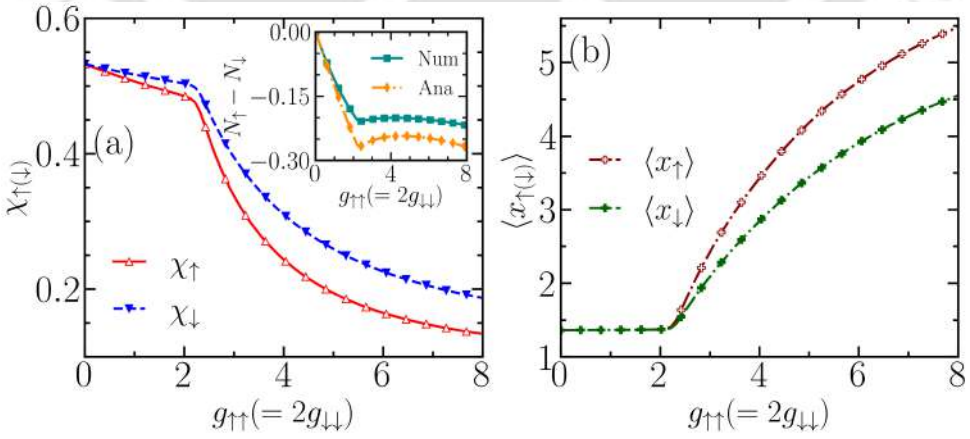

Figure 5.19: (a) Variation of the IPRs $\chi_{\uparrow(\downarrow)}$ as a function of the intra-species interaction $g_{\uparrow\uparrow}(= 2g_{\downarrow\downarrow})$ for disorder strength $U_0 = 0.5$. With the increase in $g_{\uparrow\uparrow}$, the IPR in both components decreases, resembling the broadening of the condensate irrespective of disorder strength U_0. Other parameters are the same as Fig. 5.16. (b) The center of mass position for the up (red line) and down component (dashed blue line) as a function of the intra-species interaction $g_{\uparrow\uparrow}$.

1.5, $g_{\downarrow\downarrow} = 0.75$, and (a2, b2) $g_{\uparrow\uparrow} = 5.0, g_{\downarrow\downarrow} = 2.5$ with disorder strength $U_0 = 0.15$ (upper panel), and $U_0 = 0.5$ (lower panel). Here, the separation of two components occurs even when the condensate is broadly localized at the basin. As the intra-species interaction $g_{\uparrow\uparrow}$ increases, the miscibility decreases, and both components of the condensate start to spread toward the basin, eventually leading to delocalization as characterized also with the IPRs and centers of mass $\langle x_{\uparrow(\downarrow)} \rangle$ in Fig. 5.19(a) and 5.19(b).

A comparison of Figs. 5.17-5.19 with Figs. 5.12-5.14 illustrates similarities and differences between the effects of intra- and inter-spin interactions. At nonzero $g_{\downarrow\downarrow}$ and $g_{\uparrow\uparrow}$ a sufficiently strong Rabi coupling forms a highly miscible state with $\eta \approx 1$ localized either in a void or in a basin of the random potential. The choice of the localization position can be understood from Eq. (5.23) by choosing the minimum of $\tilde{\epsilon}_{p|\mathrm{lin}} + \chi_p \left(g_{\downarrow\downarrow} + g_{\uparrow\uparrow}\right)/8$, where index p corresponds to the void or basin, respectively. In a simplified analysis, we can assume that $\tilde{\epsilon}_{v|\mathrm{lin}} \approx \pi^2/(2l^2)$, $\tilde{\epsilon}_{b|\mathrm{lin}} \approx \langle V(x) \rangle$ with $\chi_v \approx 3/(2l)$ and $\chi_b \ll \chi_v$, where l is the void width. Thus, the BEC is localized in the void if

$$\frac{\pi^2}{2l^2} + \frac{3}{16l}\left(g_{\downarrow\downarrow} + g_{\uparrow\uparrow}\right) \lesssim \langle V(x) \rangle, \tag{5.25}$$

and in the basin otherwise, in agreement with our numerical results.

Although, at $g_{\uparrow\downarrow} = 0$, there is no direct interaction between the spin components, their separation in a random potential occurs since at $g_{\uparrow\uparrow} > g_{\downarrow\downarrow}$ given parameters of the system we consider, the spin-up BEC fraction energetically prefers to localize in the basins leaving $N_\downarrow$ in the voids to keep their common chemical potential. The degree of this separation is controlled by the Rabi coupling making it prohibited at sufficiently large Ω. Thus, the possible separation of the spin components here is caused not by their repulsion but by preferable localization dependent on the spin-dependent self-interaction. At a sufficiently large $g_{\uparrow\uparrow} - g_{\downarrow\downarrow}$ one can obtain $N_\downarrow \gg N_\uparrow$. The self repulsion in each spin component decreases their IPRs $\chi_\downarrow$ and $\chi_\uparrow$, and the overlap of $|\psi_\downarrow|$ and $|\psi_\uparrow|$ increases. The effect of SO coupling, enhancing the spin disproportion, is similar for both types of self-interaction.

In Fig. 5.20 we plot the miscibility and IPR in (Ω, k_L) plane by keeping $g_{\uparrow\uparrow} = 5.0, g_{\downarrow\downarrow} = 2.5$, and Rabi coupling $\Omega = 0.5$. At a small k_L and a relatively small Ω one obtains disproportion of $N_\uparrow$ and $N_\downarrow$ with $\eta \ll 1$. With the increase in Ω, the role of the self-interaction with respect to the Rabi coupling decreases. Consequently, η approaches 1, as shown in panel (a). The increase in the self-repulsion decreases both $\chi_\downarrow$ and $\chi_\uparrow$, as presented in the (b) panel.

With the increase in k_L, panel (a) shows that the transition from miscibility to im-

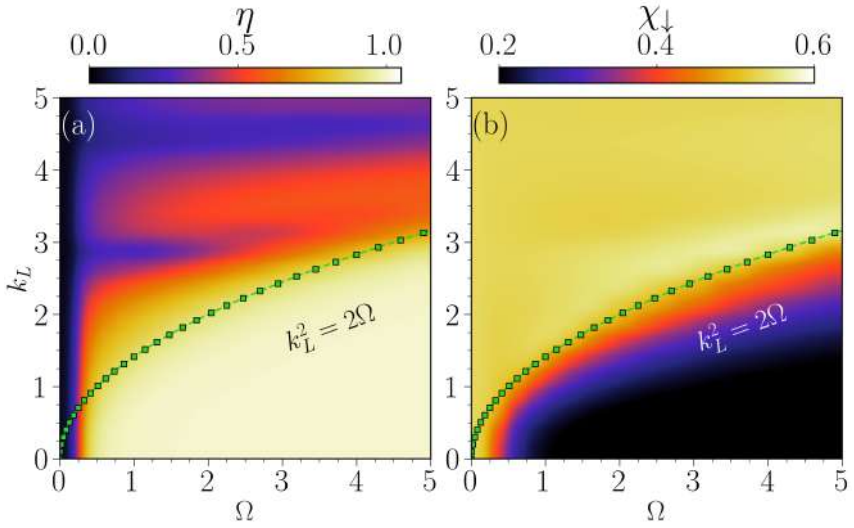

Figure 5.20: Pseudocolor representation of (a) spin-miscibility η, (b) IPR of spin-down $\chi_\downarrow$ components in (k_L, Ω) plane at intra-species interactions $g_{\uparrow\uparrow} = 5.0, g_{\downarrow\downarrow} = 0.5 g_{\uparrow\uparrow}$, and inter-species interaction $g_{\uparrow\downarrow} = 0.0$. Here, the $k_L^2 = 2\Omega$ line is drawn to show the transition from broadly localized condensate in the basin to narrowly localized condensate towards the void. Here, the IPR for down component follows $k_L^2 = 2\Omega$ relation.

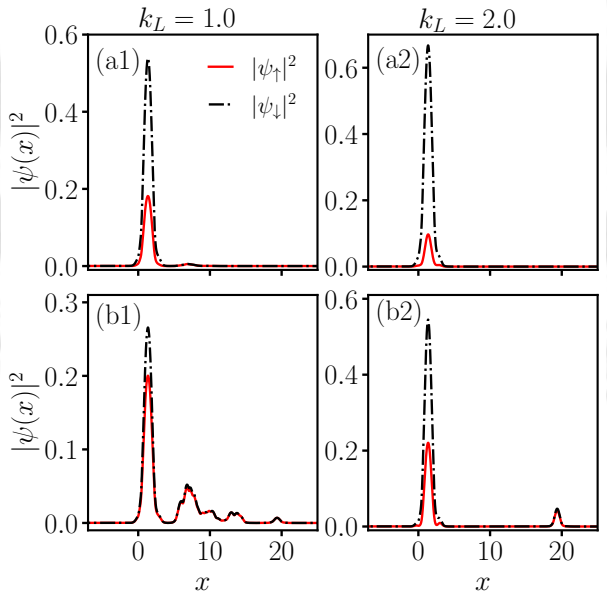

Figure 5.21: Ground state density profile of spin-up $|\psi_\uparrow|^2$ (red solid line), and spin-down $|\psi_\downarrow|^2$ (black dashed line) for different inter-species interactions (a1, b1) $k_L = 1.0$, and (a2, b2), $k_L = 2.0$. Here, the disorder strength is kept at $\Omega = 0.5$ (in the top panel), and $\Omega = 2.0$ (in the bottom panel). The other parameters are $g_{\uparrow\downarrow} = 0$, and $g_{\uparrow\uparrow} = 5.0$, $g_{\downarrow\downarrow} = 2.5$ and the disorder strength $U_0 = 0.5$ for realization R1.

miscibility requires $k_L \gtrsim \sqrt{2\Omega}$. This is due to the involvement of spin-projected probability density distributions dependent on the disorder and self-interactions. Here the same spin repulsion decreases the IPRs of both spin components and increases their overlap and the spin miscibility. This, to increase the separation and decrease the miscibility, one needs a stronger SO coupling with k_L^2 exceeding 2Ω by a value of the order of $g_{\downarrow\downarrow}\chi_v$. However, the modification of $\chi_\downarrow$ roughly follows this boundary where $|\psi_\downarrow|^2$ shows transition from delocalized to localized spin-down BEC component in $k_L^2 \gtrsim 2\Omega$ region. Since at these system parameters, the condensate population for a spin-up component in the immiscible region is very low, we present only the results of $\chi_\downarrow$.

For a better understanding of the effect of SO coupling, we present in Fig. 5.21 the spin-projected probability density distributions. This Figure shows that at a large k_L the BEC is almost fully polarized in the spin-down state with $N_\downarrow \approx 1$ localized in the void of the random potential. The reason for localization in the void rather than in the basin can be seen from the argument similar to Eq. (5.25) since $\pi^2/(2l^2) + 3g_{\downarrow\downarrow}/(4l) \lesssim \langle V(x)\rangle$.

5.5 Summary and Conclusion

We have investigated the effects of the interplay between disorder, self-interactions, Rabi, and spin-orbit coupling on the localization of a Bose-Einstein condensate located in a one-dimensional random potential. This potential produces two distinct types of the ground state localization: one in the void-like and the other one in the basin-like regions of the random potential. Both localization patterns are different from conventional Anderson localization attributed to the interference of matter waves scattered by different defects.

Our study considered both non-self-interacting condensates and condensates with two types of nonlinear interactions, which lift Manakov's symmetry. Initially, we examined how SO coupling affects the localization of a linear condensate without self-interactions. In the absence of these interactions SO coupling significantly modifies the shape and spatial scale of the localized condensate, influencing its spatial positioning. An interesting manifestation of this effect is that SO coupling can move localized states from the basin to the void regions.

By considering different types of self-interaction we observed that they have markedly distinct impacts on condensate behavior. These nonlinearities lead to pronounced spin-dependent effects related to the lifted Manakov's symmetry, resulting in the spa-

tial redistribution of spin population and separation of spin components between the voids and basins of the random potential. The combined effects of SO coupling and self-interactions amplify the impact of nonlinearities, produce highly spin-polarized condensate, and lead to the localization of one spin component of the condensate at the expense of the other. In contrast to the formation of the stripe phase at a sufficiently SO coupling in the absence of disorder, here it causes localization of the condensate. This behavior has been identified by analyzing the probability density distributions, spin expectation values, spin miscibility, and purity.

Chapter 6

Rabi-induced localization and resonant delocalization of a binary condensate in a spin-asymmetric quasiperiodic potential

In the previous Chapters (Chapters 3, 4, 5), we investigated the role of spin-orbit (SO) and Rabi couplings in dictating the localization-delocalization transitions in binary condensates trapped under quasiperiodic and random disorder potential. Based upon the analysis we developed a notion that while SO coupling promotes a spatial decoupling of spin components, the Rabi interaction fosters their coupling. However, the presence of both couplings makes the system quite complicated. To simplify the analysis in this Chapter we have considered the asymmetric spin-dependent potentials, where one spin component experiences a trapping potential while the other does not. Here, we rigorously show that the Rabi coupling induces localization between the components as it is raised above the threshold value. The induced localization depends on the external potential. While the localization is *mutually induced* by both components for the quasiperiodic confinement, for a harmonic trap it is induced in the potential-free component by the interaction of free component. The Chapter begins with a brief literature review on spin-asymmetric potentials, Rabi coupling in binary systems, and the motivation for this study, followed by a detailed analysis of numerical results based on mean-field Gross-Pitaevskii simulations.

6.1 Introduction

Following the first experimental realization of localization of the condensate in the random [21] and quasiperiodic [20] potentials, the field has witnessed a great number of theoretical and experimental works. Various analytical [244, 23] and numerical [22, 126, 132, 245, 155] approaches based on the mean-field Gross-Pitaevskii (GP) equation have been used to investigate the complex interplay between disorder and interactions on the localization.

Subsequently, with the realization of SO coupled BECs [105] spin-dependent localization have been explored in quasiperiodic [24, 128, 200] and random potentials [127, 130, 227]. These systems also exhibit very intriguing nonlinear dynamics due to the spin-dependent velocities [146, 147, 246]. Additionally, it has been reported that the interplay between the interspecies and intraspecies interactions—especially for broken Manakov's symmetry [121] can produce spatially asymmetric localization of the condensate [227].

Trombettoni et al.[247] developed a theoretical framework showing that Rabi coupling enables population exchange in deep optical lattices. The coupling also mediates the transformation of dark solitons into vector dark solitons[248], and affects miscibility in both non-dipolar [249, 250] and dipolar condensates [251, 252], where it is also crucial for immiscibility–miscibility transitions [251] Furthermore, Rabi coupling supports the formation of complex excitations such as vector rogue waves [253], stabilizes soliton-like states under time-dependent modulation in quasi-2D geometries [254], and inhibits vortex formation in rotating spinor BECs [255]. The impact of Rabi coupling on localization has also been studied using simplified theoretical models involving spin-asymmetric potentials —where one spin component is trapped while the other remains free. For instance, Santos and Cardoso [124] explored the role of Rabi-like linear coupling towards localization in a such spin-asymmetric system, where they reported the induce localization in the free component as the coupling increases.

The application of linear Rabi coupling goes beyond static cases. In experiments, time modulation of Rabi coupling is widely utilized to tune SO coupling in real time. Several studies have suggested controlling SO coupling through rapid modulation of laser intensities [154, 134]. In a similar vein, time-modulated Rabi frequencies have been used to realize different quantum phases [256], artificial gauge fields [257], matter-wave control [258], and to probe Landau-Zener tunneling [259, 260]. Under rapid modulation, Deconinck et al.[261] derived analytical solutions for linearly coupled Gross-Pitaevskii equations using a unitary transformation that absorbs the time-dependent

Rabi frequency under Manakov symmetry. Building on this, Nistazakis et al.[153] numerically implemented Rabi switch to transfer nonlinear structures between components, with reduced efficiency observed when the symmetry is broken. More recently, Abdullaev et al. [135] investigated parametric resonances and Josephson-like oscillations in SO-coupled BECs under time-modulated Raman coupling.

While the SO coupling promotes a spatial decoupling of spin components, the Rabi interaction fosters their coupling. A comprehensive understanding of localization in SO and Rabi coupled BECs remains challenging due to the complex interplay between disorder, interactions, and spin-related couplings [227], especially if SO and Rabi coupling do not commute. To address this complexity, various simplified models have been proposed in recent years. Those often involve asymmetric spin-dependent potentials, where one spin component experiences a trapping potential while the other does not. In such setups, the trapped component exhibits localization, which in turn induces localization in the untrapped one either through density-density interaction or through the Rabi coupling. In this context, Wang *et al.* [203] investigated induced localization in an SO-coupled BEC confined in a double-well potential. They demonstrated that an imbalance between intra- and inter-species interactions can drive a transition from a spin-balanced phase to a spin-localized phase. Similarly, Santos and Cardoso [124] explored the localization in binary BEC where one component is trapped in a quasiperiodic potential and coupled to the free component via linear Rabi coupling and reported the related induced localization.

While the model by Santos and Cardoso [124] offers a basic understanding of induced localization and interaction effects in spin-asymmetric potentials, a comprehensive investigation of Rabi coupling in such settings remains largely unexplored. Motivated by this, and by prior studies on time-driven Rabi dynamics in binary condensates, here, we present a detailed study of Rabi-induced localization—both in static and dynamically driven scenarios with spin-asymmetric potential.

The Chapter is organized as follows. Section 6.2 introduces the mean-field model based on the binary Gross-Pitaevskii equations and defines key observables. In Section 6.3, we present numerical results highlighting the role of linear Rabi coupling in the ground state, including critical localization behavior and the pronounced effects of even weak nonlinearities. We also provide an analytical comparison between quasiperiodic and harmonic traps. Section 6.4 explores the impact of time-periodic Rabi coupling on localized condensates, for both linear systems and those with broken Manakov symmetry. Finally, in Section 6.5, we summarize this Chapter.

6.2 Mean-field model and observables

In this Section we discuss the mean-field dynamical model used in the present work and define the relevant observables used to characterize the induced localizations.

6.2.1 Coupled Gross-Pitaevskii equations

We consider a pseudospin-1/2 quasi-one-dimensional condensate trapped strongly in the transverse direction, modeled by the coupled Gross-Pitaevskii equations [124, 224, 227]:

$$\mathrm{i}\frac{\partial\psi_\uparrow}{\partial t} = \left[-\frac{1}{2}\frac{\partial^2}{\partial x^2} + g_{\uparrow\uparrow}|\psi_\uparrow|^2 + g_{\uparrow\downarrow}|\psi_\downarrow|^2 + V_\uparrow(x)\right]\psi_\uparrow + \Omega_0\psi_\downarrow, \tag{6.1a}$$

$$\mathrm{i}\frac{\partial\psi_\downarrow}{\partial t} = \left[-\frac{1}{2}\frac{\partial^2}{\partial x^2} + g_{\downarrow\downarrow}|\psi_\downarrow|^2 + g_{\downarrow\uparrow}|\psi_\uparrow|^2 + V_\downarrow(x)\right]\psi_\downarrow + \Omega_0\psi_\uparrow, \tag{6.1b}$$

where $\psi_\uparrow$ and $\psi_\downarrow$ ($\psi_{\uparrow,\downarrow} \equiv \psi_{\uparrow,\downarrow}(x,t)$) represent the pseudo spin-up and spin-down components of the condensate wavefunction $\psi = \left(\psi_\uparrow, \psi_\downarrow\right)^{\mathrm{T}}$, respectively, where T stands for transposition. For stationary states $\psi_{\uparrow,\downarrow}(x,t) = \psi_{\uparrow,\downarrow}(x)\exp(-\mathrm{i}\mu t)$, where μ is the chemical potential. Here, $g_{\uparrow\uparrow}$ and $g_{\downarrow\downarrow}$ are the intra-species interaction strengths, $g_{\uparrow\downarrow}$, and $g_{\downarrow\uparrow}$ are inter-species interactions, and Ω_0 is the Rabi coupling strength. From now on for brevity, we will remove the (x,t) notations in $\psi_{\uparrow(\downarrow)}$ when it does not cause confusion.

The GPEs (6.1a)-(6.1b) correspond to the binary BEC Hamiltonian with the linear Rabi coupling $\Omega_0\sigma_x$ with σ_x being the corresponding Pauli matrix. The trapping potential is $V_j(x)$ with $j = \{\uparrow,\downarrow\}$. Here we consider the condensate interacting with the trapping potential only in the spin-up component [124], such as:

$$V_\uparrow(x) = V(x), \qquad V_\downarrow(x) = 0. \tag{6.2}$$

In order to analyze the induced localization from one spin-component on the other we consider $V(x)$ as a quasiperiodic potential of the form,

$$V(x) = V_1\sin^2(k_1x) + V_2\sin^2(k_2x), \tag{6.3}$$

where V_1 and V_2 are the primary and secondary optical lattice amplitudes, respectively. This potential has minima at points $x = x_i \geq 0$ and $x = -x_i < 0$ ($i = 0, 1\ldots, x_0 = 0$,

and $x_{i+1} > x_i$) where

$$V'(x) = V_1 k_1 \sin(2k_1 x_i) + V_2 k_2 \sin(2k_2 x_i) = 0, \tag{6.4}$$

$$V''(x) = 2\left(V_1 k_1^2 \cos(2k_1 x_i) + V_2 k_2^2 \cos(2k_2 x_i)\right) > 0,$$

characterized by corresponding local oscillator frequencies $\omega_i = \sqrt{V''(x)}$ at $x = x_i$.

In experiments, the pseudospin-1/2 Rabi-coupled BEC can be realized by using two hyperfine states of ^{87}Rb atoms as pseudo spin-up $|\uparrow\rangle \equiv |F = 1, m_F = 0\rangle$ and spin-down $|\downarrow\rangle \equiv |F = 1, m_F = -1\rangle$ which are coupled by a pair of Raman lasers with wavelength 804.1 nm. Recoil momentum $k_L = \sin(\theta/2)k_p$, where k_p is the photon wavevector, and the recoil energy $E_L = \hbar^2 k_L^2/2m$ provide relevant scales for tuning the SO and Rabi couplings [105, 134]. In quasi-1D, the condensate is strongly confined in transverse direction with $\omega_\perp \sim 10^3\ \mathrm{s}^{-1}$ with corresponding $a_\perp \sim 1\ \mu$m and $\hbar\omega_\perp \sim 5$ nK. The inter and intra-spin scattering lengths being typically of the order of 5 nm can be further controlled by using Feshbach resonances.

Here we propose a feasible experimental scheme to realize spin-dependent potentials in pseudospin-1/2 condensates. To generate such potentials, Bragg diffraction can be employed to selectively "tune out" specific wavelengths of optical lattices [262]. The experiment begins by creating a BEC trapped under a superimposed optical lattice potential $U_1(x)$ and $U_2(x)$. Initially, atoms are condensed in one of the hyperfine states, and a short laser pulse is applied, causing Bragg diffraction into higher momentum states. Subsequently, the lattice wavelengths are finely tuned so that atoms in the spin-up component experience only U_1, while those in spin-down interact solely with U_2. This approach has previously been used to realize binary BECs in spin-dependent twisted-bilayer lattices [262]. For our model, once the condensate is loaded into spin-dependent lattices, one of the lattice potential is slowly ramped down to avoid excitations, allowing that component to become free from trapping while the other is confined with the optical lattice. Finally, an external magnetic field that couples the components acts as the linear Rabi coupling for the GP model.

To obtain the dimensionless Eq. (6.1a)-(6.1b), we consider the transverse harmonic oscillator length $a_\perp = \sqrt{\hbar/(m\omega_\perp)}$ as a characteristic length scale with $\omega_\perp$ as the transverse harmonic trapping frequency, $\omega_\perp^{-1}$ as the timescale and $\hbar\omega_\perp$ as the characteristic energy scale. The interaction parameters can be defined in terms of $g_{\uparrow\uparrow,(\downarrow\downarrow)} = 2\mathcal{N}a_{\uparrow\uparrow,(\downarrow\downarrow)}/a_\perp$, and $g_{\uparrow\downarrow} = 2\mathcal{N}a_{\uparrow\downarrow}/a_\perp$, where, $a_{\uparrow\uparrow,(\downarrow\downarrow)}$ and $a_{\uparrow\downarrow}$ represent the intra- and inter-component scattering lengths, respectively, and $\mathcal{N}$ represents the total number of

atoms in the condensate. The dimensionless Rabi coupling Ω_0 is defined in the units of $2\omega_\perp$ with the wavefunction being rescaled with $\sqrt{a_\perp}$.

6.2.2 Definition of spin-dependent observables

To characterize the localization and delocalization at different spatial scales we start with the occupation numbers N_j, where

$$N_j = \int_{-\infty}^{\infty} |\psi_j|^2 dx, \tag{6.5}$$

with $N_\uparrow + N_\downarrow = 1$. The width w_j is given by

$$w_j^2 = \frac{1}{N_j} \int_{-\infty}^{\infty} (x - \langle x_j \rangle)^2 |\psi_j|^2 dx, \tag{6.6}$$

where the center of mass position $\langle x_j \rangle$:

$$\langle x_j \rangle = \frac{1}{N_j} \int_{-\infty}^{\infty} x |\psi_j|^2 dx. \tag{6.7}$$

The shape is characterized by the inverse participation ratio (IPR) χ_j :

$$\chi_j = \frac{1}{N_j^2} \int_{-\infty}^{\infty} |\psi_j|^4 dx. \tag{6.8}$$

We also utilize the "spin miscibility" parameter characterizing the joint distribution of densities of spin components defined as

$$\eta = 2 \int_{-\infty}^{\infty} |\psi_\uparrow||\psi_\downarrow| dx, \tag{6.9}$$

with $\eta = 1$ ($\eta = 0$) corresponding to fully miscible (immiscible) realizations. For real wavefunctions $\eta = |\langle \sigma_x \rangle|$.

After obtaining the initial ground state $\psi_j(x, 0)$, we use the time-varying Rabi frequency to study the dynamics of the condensate. For this purpose we calculate the time correlation function corresponding to different states which is defined in terms of the absolute value of the overlap function as,

$$c_j(t) = \Big| \int_{-\infty}^{\infty} \psi_j(x, t) \psi_j(x, 0) dx \Big|, \tag{6.10}$$

where $c_j(0) = N_j(0)$. As we will see below, the criteria of induced delocalization can be obtained by considering evolution of $c_j(t)$ for given spin state [164].

6.3 Ground state of induced localization

To understand the role of Rabi coupling in inducing localization and shaping the ground-state structure of a binary condensate, we present a detailed analysis of the ground-state profiles of the spin components when they are linearly coupled via the Rabi frequency. We begin by examining the non-interacting case and investigate how Rabi coupling influences localization in the spin-down component induced by the spin-up component, and vice versa. The results of mean-field simulations are complemented by an eigenmode analysis, which allows us to determine the threshold Rabi frequency beyond which induced localization emerges in the spin components. We then extend this analysis to include interactions, exploring how Rabi coupling affects induced localization in the interacting binary condensate.

6.3.1 Calculation procedure

We begin our analysis by presenting the numerical results obtained by solving the pair of coupled GPEs (Eqs. (6.1a)-(6.1b)) in which the spin-up component is trapped with a bichromatic lattice potential (6.3) and the trapless spin-down component interacts with spin-up component by linear Rabi coupling. For all of our calculations, the primary and secondary lattice strengths are considered as $V_1 = 1$ and $V_2 = 0.5$, respectively, with wavenumbers $k_1 = 0.35$ and $k_2/k_1 = (\sqrt{5}-1)/2$, corresponding to the inverse golden ratio.

To obtain the ground state we begin with the imaginary time propagation (ITP) considering the coupled GPEs (5.1) with the potential (6.3) using time-splitting Fourier spectral method [263]. However, since the spin-down component is not subjected to the external potential, obtaining the ground state using the ITP becomes particularly challenging for low Rabi coupling strengths ($\Omega_0 < 0.2$). To address this, we also solve the linearized GPEs as an eigenvalue problem to compute the full spectrum of eigenvalues and corresponding eigenstates without any self-interactions. This matrix method involves constructing a $(2N \times 2N)$ matrix that represents the coupled linear GPEs, where N is the number of grid points for the spatial domain being discretized at $x = [-L, L]$ with $L = N\Delta x/2$. We use the same spatial step size $\Delta x = 0.025$ and grid size $N = 8192$ as in the ITP to ensure consistency. Once the matrix is constructed,

it is diagonalized using the ARPACK package in Python. A key advantage of this matrix-based method is that it treats the problem as stationary, making it well-suited for exploring regimes with weak Rabi coupling. This allows us to probe the low Ω_0 region more effectively than with the ITP approach.

Thus, to obtain the ground state for non-interacting part of the problem we use both the ITP and matrix method to solve the coupled GPEs, while, at nonzero self-interaction, we resort to the ITP only, by choosing the initial state as an antisymmetric Gaussian wavefunction: $\psi_\uparrow(x) = -\psi_\downarrow(x)$. The imaginary and real-time propagation is utilized with time step $\Delta t = 10^{-4}$ to study the ground state and dynamics of the condensate.

6.3.2 Ground state of non-interacting BEC: Rabi-induced localization

As the spin-up component interacts with the quasiperiodic potential, the other one is expected to be correlated with it due to the Rabi coupling acting since minimization of the Rabi energy requires similarity of these densities (see section 6.3.4 for details). To quantitatively investigate the localization induced by the Rabi coupling, in Fig. 6.1, we present the condensate density profile $|\psi_{\uparrow(\downarrow)}|^2$ for different values of Ω_0. At very small $\Omega_0 = 0.08$, both components are broadly distributed over the $[-L, L]$ range, showing different patterns. While $|\psi_\uparrow|^2$ is located mainly in the vicinities of the minima x_i (see Eq. (6.4)), $|\psi_\downarrow|^2$ shows a more continuous distribution with peaks near x_i minima [see Fig. 6.1(a)]. The distinct peaks of $|\psi_\downarrow(x_i)|^2$ demonstrate the effect of Rabi-coupling to couple the components even at very low values of Ω_0. Conversely, for larger values of Ω_0, both components are localized near the minima at $x = 0$ [see figure 6.1(b,c)]. With the further increase of Ω_0, $|\psi_\downarrow|^2$ closely follows the $|\psi_\uparrow|^2$. In this context, it is instructive to compare the insets in Fig. 6.1(b) and Fig. 6.1(c, d). The inset in Fig. (c) depicts that for a moderate Rabi coupling, the BEC shows two distinct types of localization: the exponential one for the spin-down and the Gaussian one for the spin-up states, respectively. For a strong Rabi coupling, where $\Omega_0 \sim \lambda$, both components show the Gaussian-like localization. This is in agreement with the findings of Santos and Cardoso in Ref. [124].

The effect of the Rabi coupling can be further understood by analyzing the population $N_{\uparrow(\downarrow)}$ (Fig. 6.2(a)), width $w_{\uparrow(\downarrow)}$ (Fig. 6.2(b)), and IPR $\chi_{\uparrow(\downarrow)}$ (Fig. 6.2(c)), and chemical potential μ (Fig. 6.2(d)) of the condensate. This behavior can be compared with induced localization for the harmonic oscillator potential with the frequency ω_0 (see Eq. (6.4)

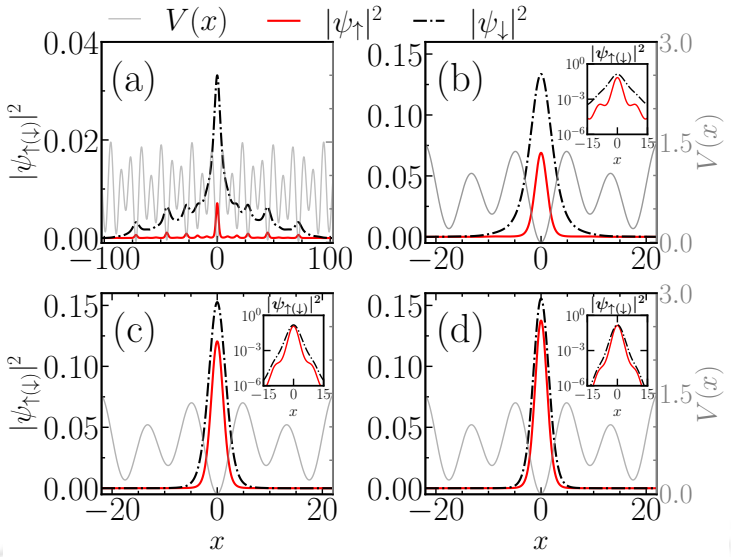

Figure 6.1: The BEC density $|\psi_{\uparrow(\downarrow)}|^2$ for different values of Rabi coupling Ω_0: (a) $\Omega_0 = 0.08$, (b) $\Omega_0 = 0.2$, (c) $\Omega_0 = 0.4$, and (d) $\Omega_0 = 0.6$. Increasing Ω_0 equalizes the spin-up and spin-down profiles. In the insets of (b)-(d), the density is plotted on a semilogarithmic scale to highlight the exponential and Gaussian behavior of the localized condensate, as it depends on Ω_0. Here, all the interactions $g = g_{\uparrow\uparrow} = g_{\downarrow\downarrow} = 0$.

and section 6.3.4).

Figure 6.2(a) shows that for weak Rabi coupling $\Omega_0 \lesssim 0.2$ the trapped condensate population $N_\uparrow \ll 1$, while $N_\downarrow$ is close to 1 because at small Ω_0 one has $|\psi_\uparrow|^2 \ll |\psi_\downarrow|^2$, corresponding to the fact that minimizing the BEC energy requires a large occupation of the broad spin down state. Increasing the Rabi coupling Ω_0 tends to equalize the population of both components. On the other hand, condensate width is very large for $\Omega_0 < 0.1$, beyond that the decreasing width $w_{\uparrow(\downarrow)}$ reveals that the increase in Ω_0 leads to mutual localization of the spin-related components eventually following each other [see Fig. 6.2(b)]. Interestingly, for the harmonic potential [see section 6.3.4], this localization process is different because of the strong confinement of the spin-up component in the harmonic potential. Comparing width $w_{\uparrow(\downarrow)}$ and IPR $\chi_{\uparrow(\downarrow)}$ in Figs. 6.2(b,c) clearly shows that $\chi_\downarrow$ increases with Ω_0, demonstrating again the Rabi-induced localization, complemented by inset semilogscale profiles in Fig. 6.1. In that context, the linearly decreasing chemical potential $\mu \approx -\Omega_0$ [Fig. 6.2(d)] at $\Omega_0 \geq 0.5$ defines the formation of bound state of similar spin-up and spin-down components due to a strong coupling.

In Fig. 6.3 we show different energies as a function of Ω_0 keeping the other parameters the same as in Fig. 6.2. These energies are defined as follows. The potential energy

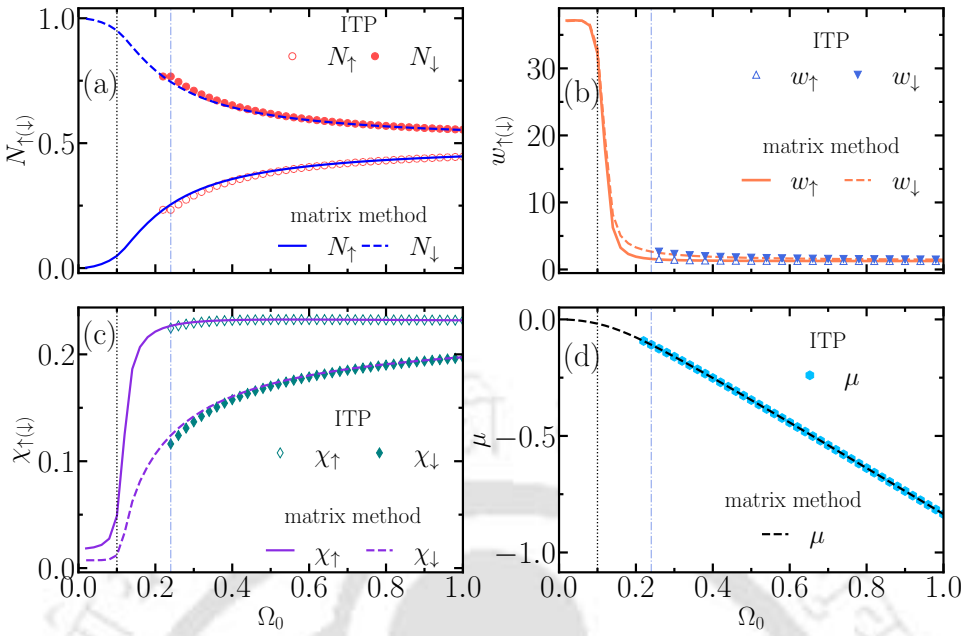

Figure 6.2: (a) Variation of population $N_{\uparrow(\downarrow)}$, (b) width $w_{\uparrow(\downarrow)}$, (c) IPR $\chi_{\uparrow(\downarrow)}$ and (d) chemical potential μ as a function of Ω_0 at $V_2/V_1 = 0.5, V_1 = 1.0, g = 0$. Here, the solid and dashed lines represent the entities obtained with the matrix method. The quantities obtained by the ITP method are shown by markers. Increase in Ω_0 results in transfer of probability from $\downarrow$ to $\uparrow$ component. The increasing IPR indicates that the spin-down and spin-up components are tending to localize with the same profile due to the Rabi coupling, while spin-up is localized by the $V_\uparrow(x)$ potential also.

corresponding to Eq. (6.2) becomes

$$E_{\text{pot}} = \int_{-\infty}^{\infty} V_\uparrow(x)|\psi_\uparrow|^2 dx, \tag{6.11}$$

the kinetic energy

$$E_k = \frac{1}{2}\int_{-\infty}^{\infty} |\psi'_\uparrow|^2 dx + \frac{1}{2}\int_{-\infty}^{\infty} |\psi'_\downarrow|^2 dx, \tag{6.12}$$

and the Rabi coupling energy

$$E_\Omega = \Omega_0 \int_{-\infty}^{\infty} (\psi^*_\downarrow \psi_\uparrow + \psi^*_\uparrow \psi_\downarrow) dx. \tag{6.13}$$

For small Ω_0 the potential energy exceeds the kinetic term. As Ω_0 increases, these energies become close ($E_k \approx E_{\text{pot}}$) since the dominance of the Rabi coupling E_Ω, which decreases approximately linearly with Ω_0, requires that $\psi_\uparrow \approx -\psi_\downarrow$ (see Sec. 6.3.4 for details).

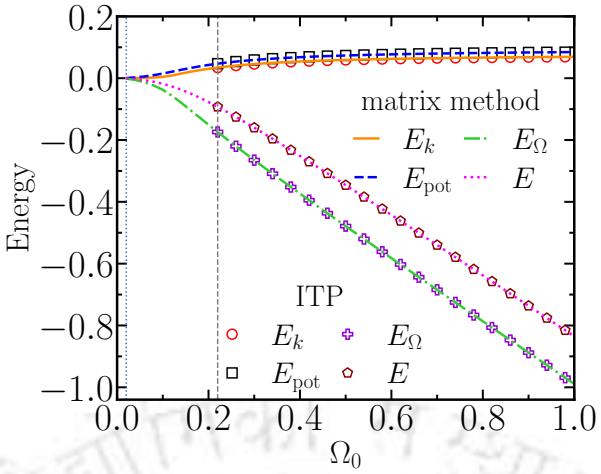

Figure 6.3: Variation of different energies as a function of Rabi coupling Ω_0 at $V_2/V_1 = 0.5$, $V_1 = 1.0$, $g = 0$. As Ω_0 increases, the ratio of potential $E_{\rm pot}$ and kinetic E_k energy approaches 1 while the large negative E_Ω minimizes the total energy $E = E_{\rm pot} + E_k + E_\Omega$.

6.3.3 Ground state of self-interacting condensate

In this subsection we explore the effect of the self-interaction described by a single parameter g on the ground state of the condensate, where $g = g_{\uparrow\uparrow} = g_{\downarrow\downarrow}$ and $g_{\uparrow\downarrow} = g_{\downarrow\uparrow} = 0$. The resulting self-interaction energy is given by:

$$E_{\rm int} = \frac{g}{2} \sum_{j=\uparrow,\downarrow} \int_{-\infty}^{\infty} |\psi_j|^4 dx = \frac{g}{2} \sum_{j=\uparrow,\downarrow} N_j^2 \chi_j. \tag{6.14}$$

In Fig. 6.4, we show the condensate density for different g by keeping Rabi coupling at $\Omega_0 = 0.3$. At $g = 0$, the condensate is perfectly localized near $x = 0$ as seen in Fig. 6.1(b). The repulsive intra-species interactions result in expanding the condensate from the central minimum and eventually leads to its fragmentation at various positions. For example, in Fig. 6.4(a) $g = 0.1$, the BEC localized at $x = 0$ fragments with two additional peaks situated at $x \sim \pm 80$, where another minimum of $V(x)$ is located. With the further increase in g, the condensate breaks into more fragments as in Fig. 6.4(c-d) fragmentation occurs with five peaks situated around $x \sim \pm 70, \pm 80$, and $x = 0$.

This strong effect of self-interaction is the specific feature of the quasiperiodic potential having a variety of minima with small $V(x_i)$ and close ω_i. Thus, a relatively weak self-repulsion can effectively redistribute the condensate density between these minima with similar energies. This effect of self-repulsion is enhanced by the fact that spread of spin-down component is not influenced by the quasiperiodic potential. At

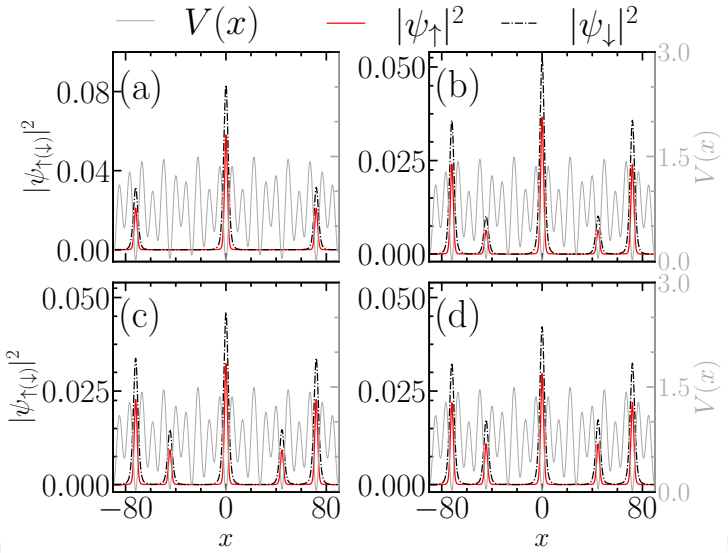

Figure 6.4: The condensate density $|\psi_{\uparrow(\downarrow)}|^2$ is shown for different self-interaction strengths: (a) $g = 0.1$, (b) $g = 0.3$, (c) $g = 0.4$, and (d) $g = 0.5$. Increasing the repulsive interaction causes the condensate to break into multiple fragments, forming several peaks at potential minima located at $x \neq 0$. The other parameters are kept as follows: $V_1 = 1.0$, $V_2 = 0.5$, $k_1 = 0.35$, $k_2/k_1 = (\sqrt{5}-1)/2$, and $\Omega_0 = 0.3$.

a moderate or strong Ω_0, where $|\psi_\downarrow| \approx |\psi_\uparrow|$, the critical self-interaction $g_{\rm cr}$ that begins the occupation of the wing $x_i \neq 0$ minima, can be estimated as $g_{\rm cr}\chi_0/2 \approx E_i - E_0$, where $\chi_0 = \sqrt{\omega_0/2\pi}$ is the IPR of the state localized near $x = 0$ and E_i is the closest to $E_0 \approx \omega_0$ energy. Thus, even a relatively small $g \sim 0.1$ can cause density redistribution between the distant minima seen as the BEC fragmentation.

6.3.4 Analytical approaches and scaling analysis

Here we consider analytical approaches to the induced by the Rabi coupling localization for several realizations of interest. As in the main text, we assume self interaction $g_{\uparrow\uparrow} = g_{\downarrow\downarrow} = g$ with no cross-spin coupling and present the GPEs as:

$$\mu\psi_\uparrow = \left[-\frac{1}{2}\frac{d^2}{dx^2} + g|\psi_\uparrow|^2 + V_\uparrow(x)\right]\psi_\uparrow + \Omega_0\psi_\downarrow, \tag{6.15a}$$

$$\mu\psi_\downarrow = \left[-\frac{1}{2}\frac{d^2}{dx^2} + g|\psi_\downarrow|^2\right]\psi_\downarrow + \Omega_0\psi_\uparrow. \tag{6.15b}$$

Below we consider a harmonic trap $V_\uparrow(x) = \lambda^2 x^2/2 - V_0$, where V_0 is a uniform shift, which can influence the total wavefunction while acting on one spin component only. We present the wave function in the form with $\psi_\uparrow = \sqrt{N_\uparrow}\phi_\uparrow(x)$, $\psi_\downarrow = \sqrt{N_\downarrow}\phi_\downarrow(x)$, where functions $\phi_\uparrow(x)$ and $\phi_\uparrow(x)$ are normalized to 1. Next, we consider how the

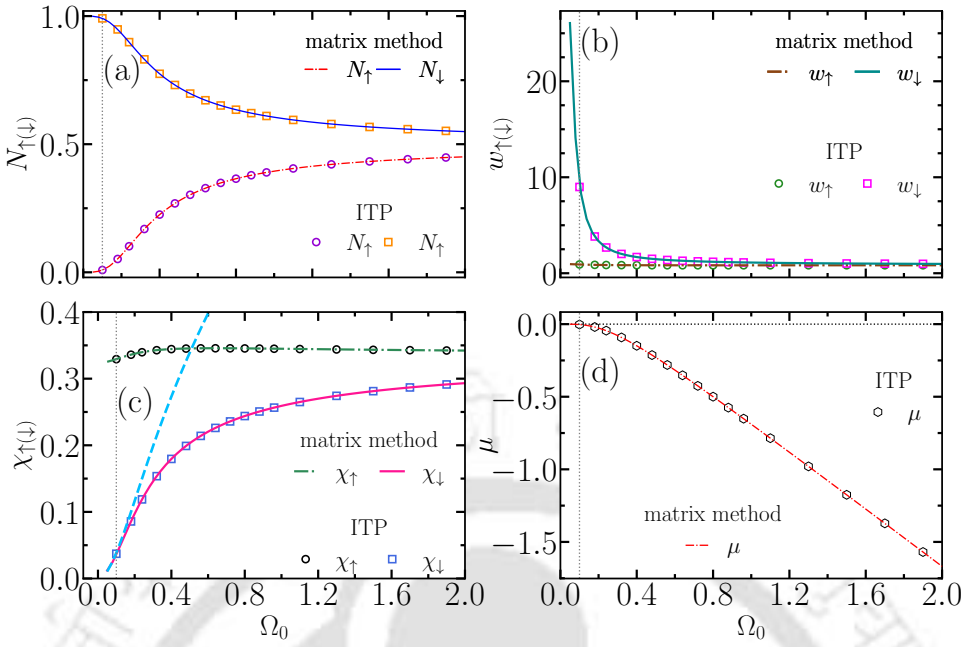

Figure 6.5: (a) Variation of population as a function of Rabi coupling Ω_0 for $V = V_\uparrow(x) = x^2/2$. (b) Width $w_{\uparrow(\downarrow)}$, (c) IPR $\chi_{\uparrow(\downarrow)}$, and (d) the chemical potential as a function of Ω_0 at $g = 0$. The increasing IPR indicates that the condensate of spin-down component tends to localize due to the interaction with spin-up one. In panel (c), the dashed cyan line is drawn to show the comparison with $\chi_\downarrow = \sqrt{|\mu|/2}$ corresponding to $\psi_\downarrow$ in Eq. (6.16).

spin-projected states behave in the case of strong $\Omega_0 > \lambda$ and weak $\Omega_0 \ll \lambda$ Rabi couplings. General results presented in Fig. 6.5 will be discussed below in terms of strong and weak couplings and briefly connected to the results for the quasiperiodic potential in Fig. 6.2.

6.3.4.1 Strong Rabi coupling

We begin with the very strong Rabi coupling $\Omega_0 \gg \lambda$, where one expects $\langle\sigma_x\rangle = -1$ with $N_\uparrow = N_\downarrow = 1/2$ and $\phi_\downarrow(x) = -\phi_\uparrow(x)$. We introduce the ansatz $\phi^{[\mathrm{lim}]}(x) = \phi_\downarrow(x) = -\phi_\uparrow(x) = \exp\left(-x^2/2a^2\right)/\sqrt{a}\pi^{1/4}$ and minimize the total energy with respect to a to obtain the ground state. The spin-diagonal kinetic energy (see Eq. (6.12)) for the spin-down state described by $\phi^{[\mathrm{lim}]}(x)$ is $1/8a^2$ and the total (sum of the kinetic and potential energies given by Eq. (6.11)) for spin-up state is $1/4a^2 + \lambda^2 a^2/8$. By minimizing their sum we obtain $a_0 = 2^{1/4}/\sqrt{\lambda}$ and, as a result, Eqs. (6.11) and (6.12) yield for this state $E_k = E_{\mathrm{pot}} = \lambda/4\sqrt{2}$.

Closely to this limit, we obtain corrections with respect to the small $\lambda/\Omega_0 \ll 1$, where $N_\downarrow \neq N_\uparrow$ with spin-up $\phi_\uparrow(x) = \exp\left(-x^2/2a_\uparrow^2\right)/\sqrt{a_\uparrow}\pi^{1/4}$ and spin-down as

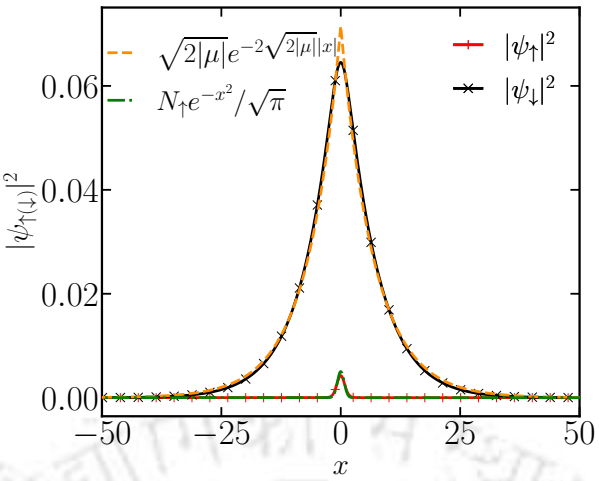

Figure 6.6: The condensate density profile at $\Omega_0 = 0.1$ with the harmonic trap configuration as: $V_\uparrow(x) = (\lambda x)^2/2, V_\downarrow(x) = 0$. The numerical density profiles $|\psi_{\uparrow(\downarrow)}|^2$ are compared with analytical expressions for harmonic oscillator ($|\psi_\uparrow|^2$) and exponential localization ($|\psi_\downarrow|^2$).

$\phi_\downarrow(x) = \exp\left(-x^2/2a_\downarrow^2\right)/\sqrt{a_\downarrow}\pi^{1/4}$ with $a_\uparrow = a_0$. Thus, we obtain $N_\downarrow - N_\uparrow = \sqrt{2}\lambda/8\Omega_0$ and $(a_\downarrow - a_0)/a_0 = \lambda/2\sqrt{2}\Omega_0$, demonstrating that the corrections are linear in the small λ/Ω_0 ratio. This asymptotic behavior matches well Fig. 6.2 with $\omega_0 \approx 0.54$ (see Eq. (6.4)) taken as the λ.

Next, we briefly discuss the effect of self-repulsion g on the state corresponding to $\phi^{[\mathrm{lim}]}(x)$ (see Eq. (6.14)). According to this equation, here the total spin-diagonal contribution to the energy acquires the term $E_{\mathrm{int}} = g\chi^{[\mathrm{lim}]}/4$, where $\chi^{[\mathrm{lim}]} = 1/\sqrt{2\pi}a_0$ is the corresponding IPR. Minimization of total energy yields an increase in the width $\delta a = g/16\sqrt{\pi}\lambda$ with a relatively small effect of the nonlinearity. It increases the width of the state and, therefore, increases the spin-diagonal energy difference, decreasing the effect of a strong Rabi coupling on the state disproportion.

6.3.4.2 Weak Rabi coupling

Here we consider a weak Rabi coupling $\lambda/\Omega_0 \ll 1$ with nonzero V_0. We begin with assuming the spin-down wavefunction in the form

$$\psi_\downarrow = -2^{1/4}|\mu|^{1/4}\exp\left(-\sqrt{2|\mu|}|x|\right) \tag{6.16}$$

normalized to $N_\downarrow = 1$ with the accuracy of $N_\uparrow \ll 1$ and the corresponding $\chi_\downarrow = \sqrt{|\mu|/2}$. Then, the $\Omega_0\psi_\uparrow$ with $\psi_\uparrow = \sqrt{N_\uparrow}\phi_0(x)$, where $\phi_0(x) = \lambda^{1/4}\exp\left(-x^2\lambda/2\right)/\pi^{1/4}$ is the ground state wavefunction in the $\lambda^2x^2/2$ potential is considered as the source of

a weak perturbation potential localizing $\psi_\downarrow$ on the spatial scale $1/\sqrt{|\mu|} \gg 1/\sqrt{\lambda}$, with an example shown in Fig. 6.6. Thus, we can write Eq. (6.15b) in the form:

$$\mu\psi_\downarrow = -\frac{1}{2}\frac{d^2}{dx^2}\psi_\downarrow + \frac{\Omega\sqrt{N_\uparrow}}{2^{1/4}|\mu|^{1/4}}\phi_0(x)\psi_\downarrow \tag{6.17}$$

and obtain for a weak narrow potential [264]

$$\mu = -\frac{1}{2\sqrt{2}}\frac{\Omega_0^2 N_\uparrow}{|\mu|^{1/2}}\left(\int_{-\infty}^{\infty}\phi_0(x)dx\right)^2, \tag{6.18}$$

resulting in the relation between μ and $N_\uparrow$:

$$\mu = -\left(\sqrt{\frac{\pi}{2}}\frac{\Omega_0^2}{\lambda^{1/2}}N_\uparrow\right)^{2/3}. \tag{6.19}$$

Next, to obtain second relation between μ and $N_\uparrow$, we use at $\sqrt{|\mu|}|x| \ll 1$, Eq. (6.15a) with Eq. (6.16) in the form:

$$\mu\sqrt{N_\uparrow}\phi_0(x) = \left(\frac{\lambda}{2} + V_0\right)\sqrt{N_\uparrow}\phi_0(x) - 2^{1/4}\Omega_0|\mu|^{1/4}. \tag{6.20}$$

Multiplying both sides of Eq. (6.20) by $\phi_0(x)$ and integrating we obtain by neglecting the left-hand side of this equation:

$$N_\uparrow = 32\pi\frac{\Omega_0^4}{(\lambda+2V_0)\lambda^3}; \qquad \mu = -8\pi\frac{\Omega_0^4}{(\lambda+2V_0)^{2/3}\lambda^{7/3}}. \tag{6.21}$$

Notice that at $V_0 = 0$ we obtain a simple relation: $\mu = -\Omega_0 N_\downarrow/4$ in agreement with numerical calculations. The difference between spin-dependent localizations can be seen with the products $w_\uparrow\chi_\uparrow = 0.300 \approx 1/2\sqrt{\pi}$, as expected for the harmonic oscillator and $w_\downarrow\chi_\downarrow = 0.343 \approx 1/2\sqrt{2}$, corresponding to the exponential localization.

With the knowledge of the induced localization for harmonic oscillator, we can understand the behavior of the condensate in the quasiperiodic potential. At large and moderate Ω_0 it is very similar to the behavior in the harmonic oscillator potential with the frequency ω_0. With the decrease in Ω_0 the spin-down component spreads as $\chi_\downarrow^{-1} \sim 1/\sqrt{|\mu|} \sim \omega_0^{3/2}/\Omega_0^2$ and at $\Omega_0^{[cr]}$ corresponding to $\chi_\downarrow x_1 \lesssim 1$ extends to the wing minima causing the extension of the spin-up component following by a fast increase in the width of both. Thus, from Eq. (6.4) we can see that at the rescaling of

the quasiperiodic potential as $\left(\tilde{V}_1, \tilde{V}_2\right) = \nu\left(V_1, V_2\right)$ and $\left(\tilde{k}_1, \tilde{k}_2\right) = \kappa\left(k_1, k_2\right)$, the critical $\tilde{\Omega}_0^{[\mathrm{cr}]}$ rescales as $\nu^{-3/8}\kappa^{-1/4}$. At a very small Ω_0 the width follows that for free particle localized in a one-dimensional box.

Now we discuss the role of the self-interaction in different spin components. Following Eq. (6.14), for this purpose we compare the quantities $N_\uparrow^2\chi_\uparrow \sim \Omega_0^8\lambda^{-15/2}$ and $\chi_\downarrow \sim \sqrt{|\mu|} \sim \Omega_0^2\lambda^{-3/2}$. Thus, in weak Rabi fields, self interaction is much stronger in the spin-down component than in the spin up one since the spin up one has a low occupation probability. Thus, while the spin-up component interacts with the external potential, the spin-down component holds the self-interaction. A more detailed comparison of $g\chi_\downarrow$ and $|\mu|$ shows that self-interactions play an essential destructive role in the induced localization at $g \sim \sqrt{|\mu|} \sim 4\sqrt{\pi}\Omega_0^2\lambda^{-3/2}$.

After analyzing the role of Rabi coupling in the induced localization of the non-interacting and interacting binary condensate now we proceed to explore the dynamics of the localized states.

6.4 Dynamics of induced localized condensates

In this Section, we proceed to study the BEC dynamics caused by periodical driving with the time modulated Rabi frequency as:

$$\Omega(t) = \begin{cases} \Omega_0, & t < 0 \\ \Omega_0 + \Omega_1 \sin(\omega_{\mathrm{osc}} t), & t > 0 \end{cases} \tag{6.22}$$

where at $t < 0$ the condensate is in the ground state. For capturing the dynamics we use different entities such as the density, miscibility (6.9), and correlation function (6.10). To make the time modulation a (possibly strong) perturbation, we always maintain $\Omega_1 = \Omega_0/2$ condition and the oscillation frequency ω_{osc} is varied within the interval from 0.1 to 1.0.

6.4.1 Effect of the oscillating Rabi frequency on the linear condensate

To begin our analysis for the linear condensate, in Fig. 6.7, we show the evolution of the density $|\psi_{\uparrow(\downarrow)}|^2$ in the (t, x) plane for oscillation frequencies ranging between $\omega_{\mathrm{osc}} = [0.1 - 1.0]$ while keeping $\Omega_0 = 0.4$, and $\Omega_1 = 0.2$ such that $\Omega(t)$ oscillates between a relatively weak (0.2) and a relatively strong (0.6) values (cf. Fig. 6.1). For

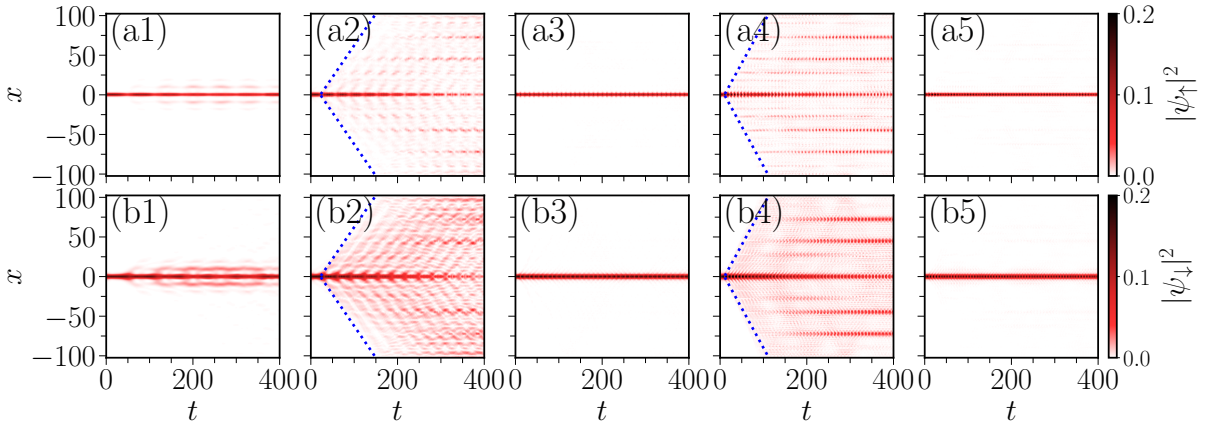

Figure 6.7: Pseudo-colormap representation of the condensate densities $|\psi_\uparrow|^2$ (upper panel) and $|\psi_\downarrow|^2$ (lower panel) in the (t, x) plane for different frequencies $\omega_{\rm osc}$: (a1, b1) $\omega_{\rm osc} = 0.1$, (a2, b2) $\omega_{\rm osc} = 0.2$, (a3, b3) $\omega_{\rm osc} = 0.4$, (a4, b4) $\omega_{\rm osc} = 0.8$, and (a5, b5) $\omega_{\rm osc} = 1.0$. For $\omega_{\rm osc} = 0.2$ (a2, b2) and $\omega_{\rm osc} = 0.8$ (a4, b4), the density expands. However, the expansion dynamics for $\omega_{\rm osc} = 0.8$ differ from those at $\omega_{\rm osc} = 0.2$. Specifically, at $\omega_{\rm osc} = 0.8$, the density $|\psi_{\uparrow(\downarrow)}|^2$ eventually settles at different potential minima (a4, b4), whereas for $\omega_{\rm osc} = 0.2$ (a2, b2), it expands with a nearly uniform velocity. For other $\omega_{\rm osc}$, the condensate remained localized around $x = 0$. The other parameters are $\Omega_0 = 0.4$, $\Omega_1 = 0.2$, and $g = 0$.

$\omega_{\rm osc} = 0.1$ in (a1, b1), the density mainly remains localized near $x = 0$, although, due to the potential-free spin-down component, it exhibits oscillations within two nearest minima $\pm x_1$. This behavior demonstrates that the BEC acquires a relatively small energy, leading to confined oscillations within a *double (triple) well*.

Next, the density propagation at $\omega_{\rm osc} = 0.2$ [in (a2,b2)] exhibits driven expansion all over the space, indicating delocalization of the condensate. However, the effect is more pronounced for $|\psi_\downarrow|^2$ (in b2) than for $|\psi_\uparrow|^2$ (in a2) due to the confinement of the latter. The spin-down component is emitted from the central minimum as separate jets with the velocity of the order of $\sqrt{\omega_0}$, corresponding to the spread a Gaussian wavepacket with the initial energy $\sim \omega_0$ (see Eq. (6.4)). The decreasing of $|\psi_\downarrow|^2$ in the vicinity of the $x = 0$ minimum pulls the $|\psi_\uparrow|^2$ out of this region and leads to its time-dependence and delocalization. Simultaneously, increasing in $\Omega(t)$ to $\approx \Omega_0 + \Omega_1$ periodically pumps the probability from $\uparrow$ to $\downarrow$ component while lowering in $\Omega(t)$ to $\approx \Omega_0 - \Omega_1$ in the same period causes emission of spin-down jets.

Similarly, for $\omega_{\rm osc} = 0.8$ [see (a4, b4)], the condensate initially expands up to $t \lesssim 200$ and starts breaking symmetrically into multiple fragments at different $x \neq 0$ minima of $V(x)$. This feature is more clearly visible with different time snapshots of total density $|\psi|^2$ shown in Fig. 6.8. Comparison of Figs. 6.8(a) and 6.8(b) illustrates that at $\omega_{\rm osc} = 0.8$ (in (b)) the density symmetrically breaks into multiple fragments beyond $t > 200$ at $V(x)$ minima around $x \sim \pm 50, \pm 80$ and remains *frozen* there. In contrast, the

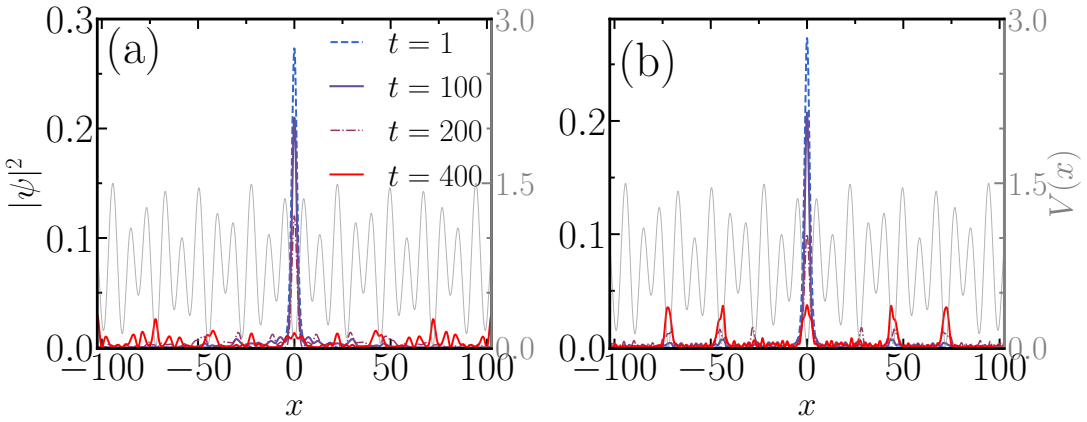

Figure 6.8: The total density profile $|\psi|^2 = |\psi_\uparrow|^2 + |\psi_\downarrow|^2$ is shown at different time snapshots $t = (1, 100, 200, 400)$ for (a) $\omega_{\rm osc} = 0.2$ and (b) $\omega_{\rm osc} = 0.8$. For $\omega_{\rm osc} = 0.8$, the density fragments into four distinct minima of the potential located at non-zero positions $x \neq 0$ at large time snap ($t = 400$), whereas for $\omega_{\rm osc} = 0.2$, the condensate expands uniformly with time.

density at $\omega_{\rm osc} = 0.2$ (in 6.8(a)) expands with uniform velocity being distributed uniformly all over the space, which we define as *tree-* like expansion resulting in delocalization. A possible explanation for the two distinct types of delocalization phenomena is as follows: for lower oscillation frequencies such as $\omega_{\rm osc} = 0.2$, the timescale over which the condensate density expands is comparable to the semi-adiabatic timescale associated with the modulation frequency of $\Omega(t)$. This leads to a relatively modest expansion of the condensate. In contrast, at $\omega_{\rm osc} = 0.8$, the rapid variation of $\Omega(t)$ causes the condensate expansion timescale to become shorter relative to the modulation timescale of $\Omega(t)$, resulting in the condensate becoming effectively frozen at different minima. However, for other frequencies such as $\omega_{\rm osc} = 0.4$ (a3, b3) and 1.0 (a5, b5), the condensate remains localized near $x = 0$. At this juncture, it is worth noting that Nakamura *et al.* [265] reported the resonant driven levitation of binary condensates subjected to two distinct harmonic traps separated by different height and trap centers. They further demonstrated that this vertical transition is analogous to the Franck-Condon effect observed in molecular physics.

Characterizing the localization and delocalization is a challenging task because of one of the components is potential-free and Rabi coupling $\Omega_0 = 0.4$ is not strong enough. Therefore, the evolution of the density pattern cannot give much insight. In that context, we use other set of observables: miscibility $\eta(t)$ (Eq. (6.9)) and correlation functions $c_j(t)$ (Eq. (6.10)) to characterize these processes [30, 139, 164].

Given the unequal populations of the spin components, we analyze miscibility $\eta(t)$ to characterize differences in driven localization or delocalization. Figure 6.9 repre-

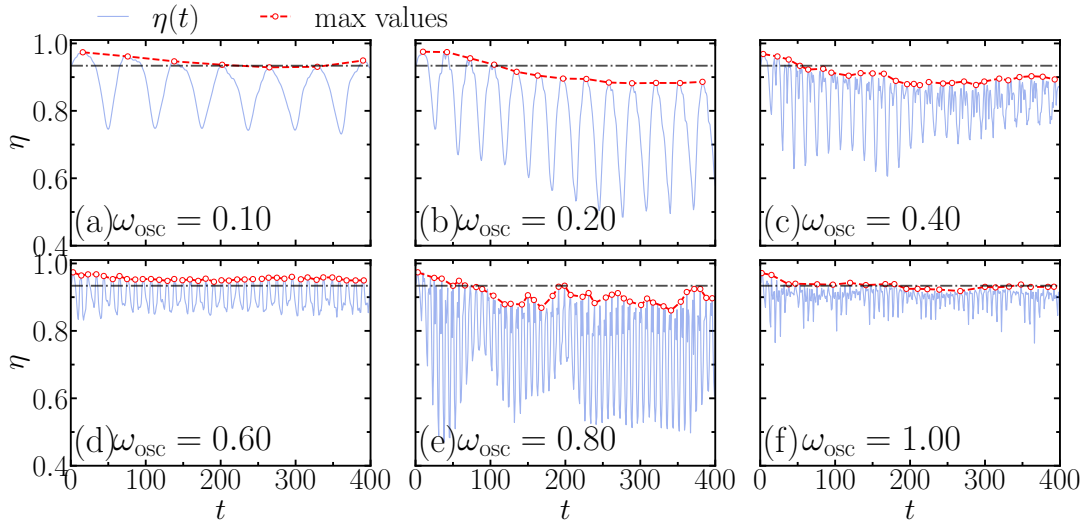

Figure 6.9: Time dependence of miscibility η for different oscillation frequencies of the Rabi field ω_{osc}: (a) $\omega_{osc} = 0.1$, (b) $\omega_{osc} = 0.2$, (c) $\omega_{osc} = 0.4$, (d) $\omega_{osc} = 0.6$, (e) $\omega_{osc} = 0.8$, and (f) $\omega_{osc} = 1.0$. The black dash-dotted line indicates the initial miscibility $\eta(0) = 0.934$, obtained from the ground state before the time-dependent Rabi field is switched on ($\Omega_1 = 0$). The function $\eta(t)$ represents the miscibility after turning on the Rabi field ($\Omega_1 \neq 0$). A red circle-marked dashed line highlights the maximum values of $\eta(t)$. Comparing $\eta(0)$ with the red-circled maxima shows that the miscibility gradually decreases over time for $\omega_{osc} = 0.2$, 0.6, and 0.8, indicating expansion of the condensate.

sents the miscibility $\eta(t)$ for the same oscillation frequencies as in Fig. 6.7. The maximum of $\eta(t)$ is highlighted with a red circle-marked dashed line in each panel from (a)-(f), and the black dash-dotted line is drawn at $\eta = 0.934$ to indicate the extent of miscibility. In addition it should be noted that the expansion of the condensate gets manifested in the decreasing trend of $\eta(t)$ from initial value $\eta(0) = 0.934$ which is depicted through the red markers in figures (b), (c), and (e) for $\omega_{osc} = 0.2, 0.4$, and 0.8, respectively. For other cases, the miscibility remains nearly constant and also follows approximately $\eta(t) \gtrsim 0.934$. Therefore, the transition from localization to delocalization can be characterized through the decreasing miscibility $\eta(t) < \eta(0)$.

Furthermore, we compute the spin-projected correlation functions $c_\uparrow(t)$ and $c_\downarrow(t)$ (see Fig.6.10) for the same set of ω_{osc} as in Fig.6.9. Notably, $c_\uparrow(t)$ (purple solid line) and $c_\downarrow(t)$ (orange dash-dotted line) consistently maintain a close to π phase difference for all the cases. For comparison, we also include the stationary correlation functions, represented by a sky-blue dashed line for $c_\uparrow(0)$ and a green dotted line for $c_\downarrow(0)$, to contrast with the dynamically modulated at $\omega_{osc} \neq 0$.

The decrease in $c_j(t)$ with time demonstrates the condensate escape from the ground state. Note that $c_j(t)$ are close to $c_j(0)$ for $\omega_{osc} = 0.1, 0.6, 1.0$ as shown in panels (a), (d), and (f), respectively. Thus, with the course of time, the spin components remain close

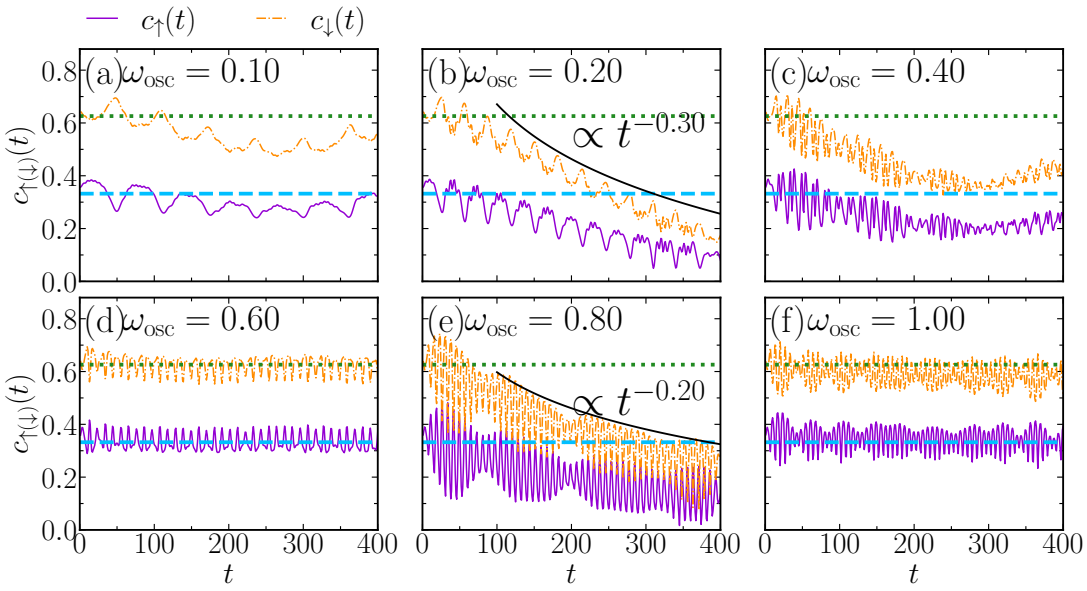

Figure 6.10: Temporal variation of the correlation function $c_{\uparrow(\downarrow)}(t)$ is shown for different oscillation frequencies ω_{osc}: (a) $\omega_{osc} = 0.1$, (b) $\omega_{osc} = 0.2$, (c) $\omega_{osc} = 0.4$, (d) $\omega_{osc} = 0.6$, (e) $\omega_{osc} = 0.8$, and (f) $\omega_{osc} = 1.0$. The spatiotemporal expansion of the condensate can be characterized by a power-law behavior of the form $t^{-\alpha}$ for $\omega_{osc} = 0.2$ and $\omega_{osc} = 0.8$, where $c_{\uparrow(\downarrow)}(t)$ exhibits a decreasing trend over time. The values of the exponent α are found to be 0.3 for $\omega_{osc} = 0.2$, and 0.2 for $\omega_{osc} = 0.8$. The dashed line (skyblue color), and dotted line (green color) is drawn to compare with the static case $\Omega_1 = 0$. The other parameters are same as Fig. 6.7

to the initial state in the vicinity of $x = 0$, as mentioned earlier in Fig. 6.7. Conversely, for $\omega_{osc} = 0.2$ [in figure (b)] and $\omega_{osc} = 0.8$ [in figure (e)], the $c_j(t)$ decrease by following power laws with approximate exponents $t^{-0.5}$ and $t^{-0.3}$, respectively. Also, at $\omega_{osc} = 0.4$ [in (c)], the $c_j(t)$ show a feeble decrement with time. The escape of the condensate can be characterized through the power-like decrease of the time-correlation functions. Also note that, the decrease in $c_\uparrow(t)$ is less in compare to $c_\downarrow(t)$ from their respective initial $c_j(0)$ values, because of the trapping potential in spin-up component try to prevent the decrease in $c_\uparrow(t)$.

So far, our analysis reveals several effects of periodic Rabi frequency towards delocalization of the condensate in the absence self-interactions. Following this, in the next subsection we explore the effect of $\Omega(t)$ at self-interactions $g > 0$.

6.4.2 Resonant frequency for delocalization

Here we discuss estimation of the resonant frequency for non-interacting BECs using the matrix method. The solution of coupled GPEs (6.15a-6.15b) computes eigenvalues associated with the ground and excited states of the Hamiltonian, where the lowest

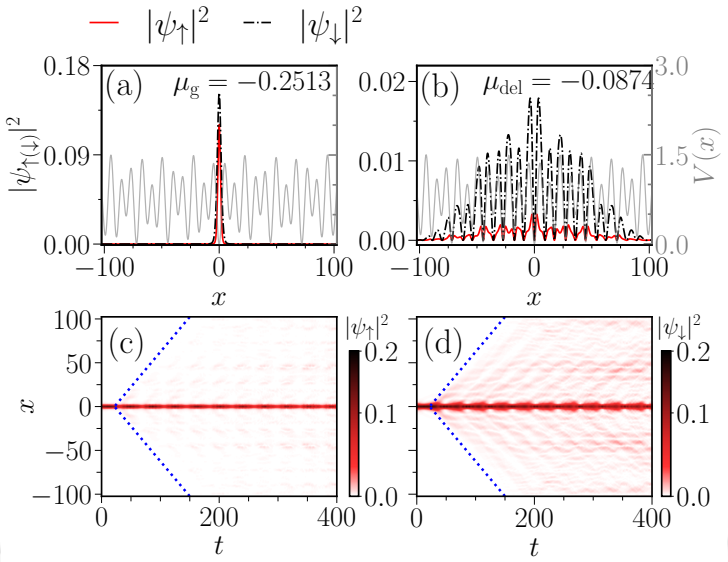

Figure 6.11: (upper panel) The condensate density $|\psi_{\uparrow(\downarrow)}|^2$ associated with the ground state (a) and the excited state (b) of the coupled GPEs. (lower panel) Pseudo-colormap representation of the condensate densities (c) $|\psi_\uparrow|^2$ and (d) $|\psi_\downarrow|^2$ at $\Omega_0 = 0.4, \Omega_1 = 0.2, \omega_{osc} = 0.1639$. Here, the oscillation frequency $\omega_{osc} = 0.1639$ is obtained by taking the energy difference between the ground (a) and excited states (b) of the system as $\omega_{osc} \approx |\mu_g - \mu_{ex}| \approx 0.1639$. Other parameters are $V_2/V_1 = 0.5, V_1 = 1.0, g = 0$.

eigenvalue corresponds to the ground state [see Fig. 6.2(d)]. Here we utilize the difference between the ground-state and excited-state eigenvalues to obtain the approximate resonant frequency that drives the condensate delocalization.

We begin by solving the coupled GPE with quasiperiodic trap subjected to spin-up component by keeping $\Omega_0 = 0.4$. Subsequently, first fifty eigenvalues are obtained, in which the 0^{th} eigenvalue $\mu_g \equiv \mu^{[0]} = -0.2513$ represents the ground state chemical potential [see Fig. 6.11(a)]. Following that, we examine excited states eigenvalues ($\mu^1_{ex}, \mu^2_{ex}, \mu^3_{ex} \ldots \mu^{50}_{ex}$) and wavefunction in order to find the appropriate delocalized condensate. We found that for low-energy eigenstates, both components are localized symmetrically on either side of $x = 0$, occupying different minima of the potential. For higher excited states, where $|\mu|$ is close to 0, the eigenstates are extended all over the space, overcoming the effect of the potential. We have chosen those eigenstates as the delocalized states. For example, in Fig. 6.11(b), we present the condensate density with eigenvalue $\mu_{del} = \mu^{23}_{ex} = -0.0874$, where the density efficiently tunnels through the quasiperiodic trap. Therefore, the energy difference between the μ_g and μ_{del} can be defined as the energy required to efficiently tunnel the condensate from the central minimum. Therefore, the approximate resonant frequency turns out to be $\omega_{osc} \approx |\mu_g - \mu_{del}| \approx 0.1639$ for $\Omega_0 = 0.4$.

Next, in Fig. 6.11(c) and 6.11(d), we show the evolution of condensate density $|\psi_\uparrow|^2$,

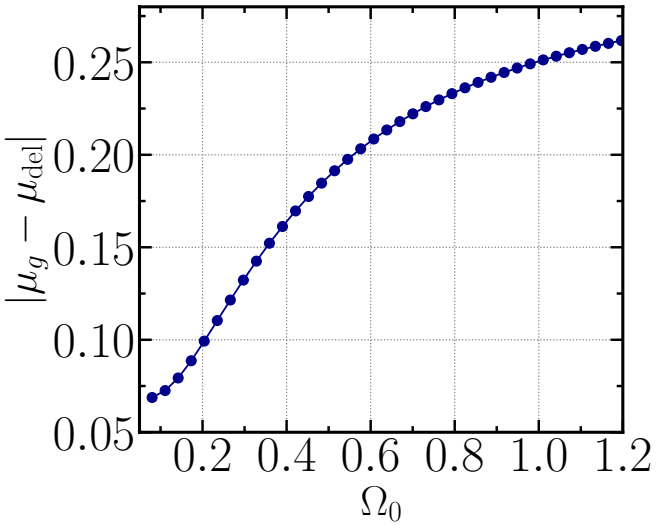

Figure 6.12: Variation of the resonant frequency $\omega_{\rm osc}$ obtained by calculating the difference as $|\mu_g - \mu_{\rm ex}|$ with Rabi coupling Ω_0 by keeping $V_2/V_1 = 0.5$, $V_1 = 1.0$, and $g = 0$. The resonant frequency initially increases almost linearly with Ω_0 and then saturates at higher values of Ω_0.

and $|\psi_\downarrow|^2$, respectively by keeping $\Omega_0 = 0.4, \Omega_1 = 0.2$, and oscillation frequency at $\omega_{\rm osc} = 0.1639$. Under this periodic driving, the condensate exhibits uniform expansion, albeit with a lower intensity compared to the case of $\omega_{\rm osc} = 0.2$ shown in Fig. 6.7(a2,b2). This suggests that $\omega_{\rm osc} \sim 0.1639$ resonantly drives the delocalization. It is important to note that, although the resonant frequency is estimated here by taking $\Omega_0 = 0.4$, the Ω_1 term in $\Omega(t)$ make the dynamics nonlinear and, thus, effectively modifies the resonant frequency for delocalization.

In Fig. 6.12, we illustrate the variation of the resonant frequency as a function of Ω_0. For low values of Ω_0, the resonant frequency increases almost linearly with Ω_0, followed by a saturation trend at larger values, where in the ground state the components behave as Gaussian localized states strongly localized in harmonic confinement with $N_\uparrow \approx\sim N_\downarrow$. Under such conditions, the potential-free spin-down component closely follows the spin-up component. Although the matrix method gives only an approximate value of the resonant frequency, it provides valuable insights into the Rabi-driven delocalization of a condensate.

After discussing the frequency driven dynamics for non-interacting condesates, in the following, we examine the similar driven dynamics for interacting case.

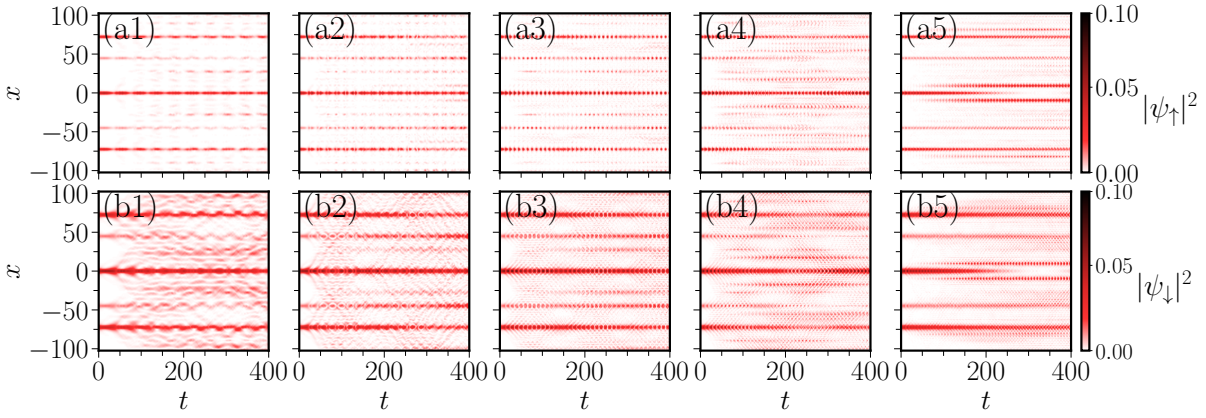

Figure 6.13: Evolution of the density $|\psi_\uparrow|^2$ (upper panel) and $|\psi_\downarrow|^2$ (lower panel) with the self interaction $g = 0.3$ for different ω_{osc} as: (a1, b1) $\omega_{\text{osc}} = 0.15$, (a2, b2) $\omega_{\text{osc}} = 0.30$, (a3, b3) $\omega_{\text{osc}} = 0.6$, (a4, b4) $\omega_{\text{osc}} = 0.75$, and (a5, b5) $\omega_{\text{osc}} = 0.9$. For different ω_{osc} different types of features are visible: at $\omega_{\text{osc}} = 0.15, 0.3$, each fragmented condensate starts expanding, but at $\omega_{\text{osc}} = 0.6$, fragmented parts do not show much expansion. In contrast, for other $\omega_{\text{osc}} = 0.75, 0.9$, more fragments are generated with time. The other parameters are $\Omega_0 = 0.3, \Omega_1 = 0.15$.

6.4.3 Dynamics of induced localization in presence of interaction

As we have discussed earlier in subsection 6.3.3 that the self-interactions lead to fragmentation of the condensate across different potential minima and the number of fragments increases with the strength of the self-interaction. Our aim here is to analyze the dynamics of those fragmented condensates under the influence of the periodic Rabi frequency.

To begin with, in Fig. 6.13 we present the evolution of the densities $|\psi_{\uparrow(\downarrow)}|^2$ for different ω_{osc}, while keeping $g = 0.3$, $\Omega_0 = 0.3$, and $\Omega_1 = 0.15$. Initially at $t = 0$, five distinct fragments are located around $x = 0, \pm 25, \pm 75$ [see Fig.6.4(b)]. At $\omega_{\text{osc}} = 0.15$ (a1, b1), the condensate density expands uniformly from each of these fragments. At $\omega_{\text{osc}} = 0.3$ (a2, b2), the expansion becomes less pronounced compared to the previous case. In contrast, for $\omega_{\text{osc}} = 0.6$, the fragmented densities remain localized at their respective positions, exhibiting no significant expansion over time. However, for higher frequencies such as $\omega_{\text{osc}} = 0.75$ and 0.9, the condensate symmetrically breaks into more fragments as time progresses. Since interactions inherently induce the BEC fragmentation, the exact identification of dynamically localized and delocalized behavior becomes even more challenging than in the non-interacting case. To quantify different regimes, in Fig. 6.14 we show the miscibility $\eta(t)$ for different ω_{osc}. Unlike the non-interacting case, here the decrease in $\eta(t)$ from $\eta(0)$ does not provide significant information into the condensate expansion. Nevertheless, the amplitude of $\eta(t)$ provides a qualitative explanation of the phenomena. For instance, in Fig.6.14(a), the

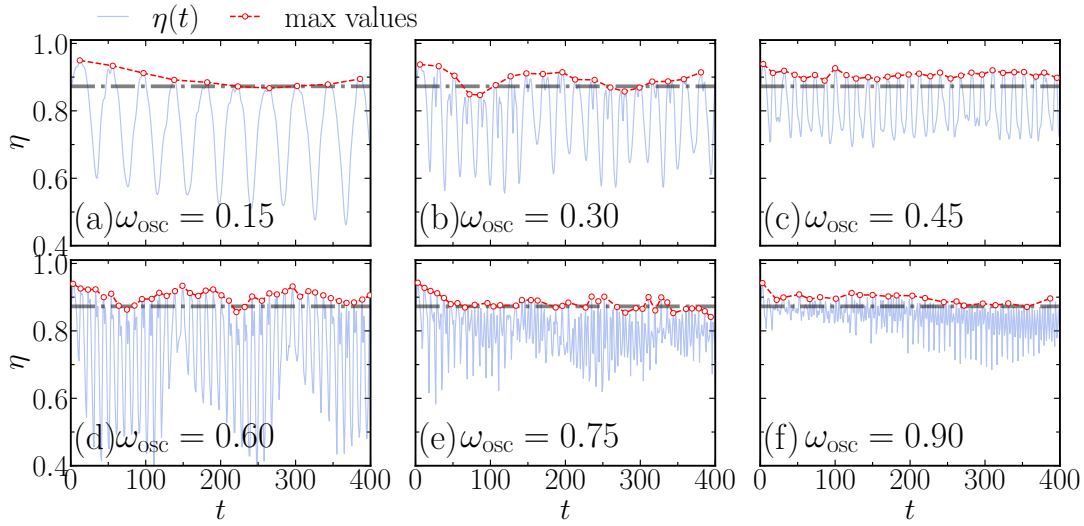

Figure 6.14: Evolution of miscibility $\eta(t)$ for $g = 0.3$ and different oscillation frequencies as (a) $\omega_{osc} = 0.1$, (b) $\omega_{osc} = 0.2$, (c) $\omega_{osc} = 0.4$, (d) $\omega_{osc} = 0.6$, (e) $\omega_{osc} = 0.8$, and (f) $\omega_{osc} = 1.0$.. The black dash-dotted line indicates the initial miscibility $\eta(0) = 0.873$, obtained from the ground state before the time-dependent Rabi field is switched on ($\Omega_1 = 0$).The red circle dots show the evolution of the maximum values of $\eta(t)$.

amplitude of $\eta(t)$ lies in the range $0.5 \lesssim \eta(t) \lesssim 0.9$. Similarly, for $\omega_{osc} = 0.3$ and 0.6 [Figs. 6.14(b, d)], $\eta(t)$ oscillates between $0.6 \lesssim \eta(t) \lesssim 0.9$ and $0.4 \lesssim \eta \lesssim 0.9$, respectively. On the other hand, for higher frequencies, $\eta(t)$ remain within a narrow interval, i.e. $0.7 \lesssim \eta \lesssim 0.9$. However, the large amplitude variation of $\eta(t)$ demonstrates the expansion from the condensate's initial positions, whereas, the small amplitude variation signifies no as such expansion of the condensate from their respective positions.

Furthermore, we examine the correlation function $c_j(t)$ in Fig. 6.15 for the same set of ω_{osc} as shown in Fig. 6.14. The values of $c_j(t)$ at $\omega_{osc} = 0$ are indicated by a blue dashed line at $c_\uparrow \approx 0.3$ and a green dotted line at $c_\downarrow \approx 0.7$ in each panel. Notably, at $\omega_{osc} = 0.15$ (panel (a)), the power-law decay of $c_j(t)$ reflects the expansion of the density from its initial distribution. The observed power-law behavior follows an exponent of $t^{-0.11}$. Similarly, for $\omega_{osc} = 0.3$ (panel (b)), although $c_j(t)$ decreases, the absence of a power-law trend indicates the suppression of condensate expansion as we have seen in the non-interacting case (Fig. 6.10). Similarly, at $\omega_{osc} = 0.45, 0.6$ (panels (c,d)), the decrement of $c_j(t)$ is further suppressed. On the other hand, for $\omega_{osc} = 0.75, 0.9$, the relatively larger power-law decay rate demonstrates the expansion and possibly further fragmentation of the condensate.

As a result, we observe that the overall influence of the periodic Rabi frequency on

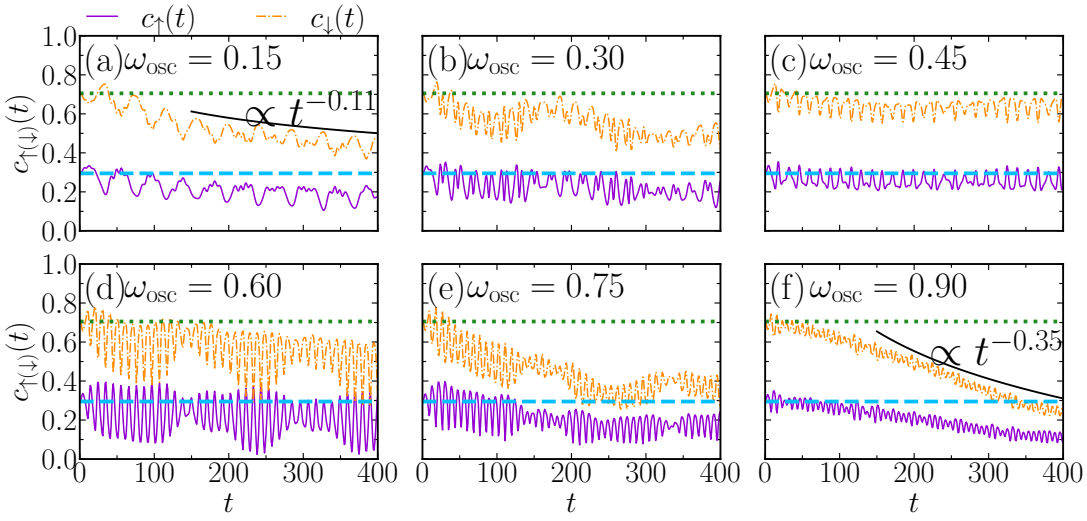

Figure 6.15: Time evolution of the correlation function $c_{\uparrow(\downarrow)}(t)$ is shown at $g = 0.3, \Omega_0 = 0.3, \Omega_1 = 0.15$ for different oscillation frequencies $\omega_{\rm osc}$: (a) $\omega_{\rm osc} = 0.15$, (b) $\omega_{\rm osc} = 0.3$, (c) $\omega_{\rm osc} = 0.45$, (d) $\omega_{\rm osc} = 0.6$, (e) $\omega_{\rm osc} = 0.75$, and (f) $\omega_{\rm osc} = 0.9$. Here, the dashed line (skyblue color), and dotted line (green color) is drawn to compare with the static case $\omega_{\rm osc} = 0$. The expansion of the condensate can be characterized by highlighting the power-law decrement from $c_j(0)$.

the condensate is qualitatively similar to that in the non-interacting case. However, the interference of spin jets from different $\pm x_i$ minima makes the *tree-like* expansion pattern in the non-interacting case similar to a much richer *parquet-like* pattern in the presence of interactions.

6.5 Summary and Conclusion

We have systematically investigated the localization and driven dynamics of a Rabi-coupled Bose-Einstein condensate subjected to a quasiperiodic potential in one spin component while the other one is potential-free. Using the mean-field Gross-Pitaevskii equation, we have explored how the Rabi coupling, the potential, and nonlinear interactions jointly influence the ground state and the spatiotemporal characteristics of the condensate dynamics. For the linear condensates the results obtained by the imaginary time evolution align well with those obtained from the eigenmode analysis, highlighting the robustness of the induced localization mechanism.

In the absence of nonlinear interactions, we observe that the induced localization, where each component influences localization on the other, occurs when Rabi coupling exceeds a threshold value. With the introduction of self-interactions, both components exhibit localized and fragmented structures of the condensate.

After obtaining the ground state, we have studied the dynamics of the condensate under a periodically modulated Rabi frequency. When the driving frequency resonates with the intrinsic excitation modes of the localized system, we observe dynamically induced delocalization in both components accompanied by population redistribution. At higher harmonics of the resonant frequency, the condensate transitions into fragmented states, indicating mode-selective excitation. To quantitatively characterize these dynamical states, we have analyzed the evolution of miscibility and the temporal correlation functions of the spin components. Notably, similar features of drive-induced delocalization persist in the presence of interactions.

Chapter 7

Conclusions and future scope

7.1 Main conclusions of the thesis

In this thesis, we have explored various localization-delocalization phases through analytical and numerical studies of weakly-interacting quasi-1D condensates. In our studies, two types of disordered potentials were considered: quasiperiodic and random. We began by characterizing localization behavior via the non-equilibrium dynamics of the condensate. In subsequent chapters, the focus shifted to ground-state properties, examining the roles of spin-orbit (SO) coupling, Rabi coupling, and different mean-field interactions under both quasiperiodic and random disorder. Finally, we extended our analysis to study both the ground state and dynamics of a spin-imbalanced binary condensate, where the imbalance arises from a spin-asymmetric potential. The detailed conclusions of these studies are presented below.

In **Chapter 3**, we investigated the ground state and associated dynamics of quasi-1D scalar BECs confined in both bichromatic optical lattices and random disordered potentials. Our results show that increasing the repulsive interaction strength leads to a transition from localized to delocalized ground states in both types of potentials. To ensure the out-of-equilibrium dynamics, we performed an interaction quenching —instantaneous switching off nonlinearity to zero from the value at which the ground state was prepared, and analyzed the condensate dynamics. This out-of-equilibrium dynamics was characterized using observables such as the time correlator function, power spectral density, and the maximal Lyapunov exponent. For weak interaction quenches (localized regime), the time correlator exhibits regular dynamics, either periodic or quasiperiodic. In contrast, strong interaction quenches (in delocalized phases), lead to chaotic dynamics, as reflected by an irregular correlator, a broadband power

spectrum, and a positive Lyapunov exponent. We also identified a quasiperiodic route to chaos in both bichromatic and random potentials. In the case of random disorder, the transition of the time correlator from regular to chaotic effectively distinguishes between localized and delocalized regions of the condensate. Furthermore, we found that the critical nonlinearity required to trigger chaotic dynamics decreases with decreasing disorder strength, a trend that parallels the ground-state localization–delocalization transition driven by increasing interaction strength. Through this comprehensive study, we demonstrated how the interplay between interaction, disorder, and quench dynamics can serve as a powerful technique for characterizing localized and delocalized phases of a BEC via its dynamical behavior.

In **Chapter 4**, we have considered spin-orbit (SO) coupled binary condensate to explore the role of interaction inhomogeneity in localization-delocalization transition trapped in weak quasiperiodic potential. Considering the interaction inhomogeneity similar to the external quasiperiodic trap, we observed that the condensate undergoes localization to delocalization phase transition as the interaction strength is tuned from attractive to repulsive value. The scenario changes significantly when a phase difference of $\pi/2$ is introduced in between the inhomogeneity and trapping potential. In that case, the resulting competition between inhomogeneity and quasiperiodic potential results in localization-delocalization-localization transition as a function of interaction strength. Furthermore, we analyzed the influence of SO and Rabi coupling on the localization behavior, highlighting their roles in shaping the phase transition. To gain more insight on these phases, we employed the Gaussian variational approach to effectively explain these localization-delocalization transitions. Finally, the stability of both localized and delocalized states was examined through velocity perturbation and trap quenching dynamics of the condensate.

In **Chapter 5**, we extended our analysis of the localization–delocalization phase transition to SO coupled condensates trapped in a random disordered potential. This analysis focused on the combined effects of disorder, self-interactions, Rabi, and SO coupling, examined through various observables such as density distributions, spin expectation values, spin miscibility, and the purity of the condensate. The random potential supports two qualitatively distinct types of ground-state localization: one in void-like regions and another in basin-like regions of the potential landscape. Notably, both localization patterns differ from conventional Anderson localization. We have explored both non-interacting and interacting regimes, including systems with two types of nonlinear interactions that break Manakov's symmetry. Initially, we analyzed the role of SO coupling, which significantly alters the spatial profile and localization

characteristics of the condensate. A interesting manifestation is that SO coupling can shift the localized condensate from basin-like to void-like regions, thereby changing its spatial positioning. Unlike the formation of stripe phases observed at large SO coupling in regular trapped systems, in the presence of disorder, it causes localization of the condensate. The introduction of nonlinear interactions further lead to pronounced effects on spin-dependent localization, particularly due to the broken Manakov symmetry. This often involves spin population redistribution and spatial separation of spin components between the voids and basins of the random potential. The interplay between SO coupling and nonlinear interactions amplifies these effects, leading to strong spin polarization and localization of one spin component at the cost of delocalizing other.

In **Chapter 6**, we explored the localization and driven dynamics of a Rabi-coupled binary BEC confined in a spin-asymmetric quasiperiodic potential, where only one component experiences the external trap while the other remains free. We began by solving the coupled Gross-Pitaevskii equations using imaginary time propagation to examine how Rabi coupling induces localization between the components. This Rabi-induced localization was characterized through several physical observables, including population imbalance, condensate width, inverse participation ratio, and various energy contributions. In the non-interacting regime, these findings were further supported by eigenmode analysis, which confirmed the robustness of the localization mechanism. Upon introducing interactions, the condensate exhibited fragmentation across multiple potential minima, highlighting the nonlinear effects. Following the ground-state analysis, we investigated the condensate dynamics under a periodically modulated Rabi frequency. When the driving frequency matched the system's intrinsic excitation modes, we observed dynamically induced delocalization in both components. At higher harmonics of the resonant frequency, the dynamics leads to frozen states at different potential minima. To characterize different dynamical phases, we have analyzed the spin miscibility and time correlation functions of the condensate. Notably, similar features of resonant induced delocalization persist even in presence of interactions.

7.2 Scope for future work

The works presented in this thesis open up several promising avenues for future research within the domain of ultracold atomic BECs, particularly in the context of localization phenomena and condensate control. An immediate extension of the current

work would be to explore the localization–delocalization transitions of condensates with quasi-particle excitations subjected to quasiperiodic or random potentials, using the Gross-Pitaevskii (GP) formalism. Such an approach would parallel the theoretical treatment in Ref.[23], which offers a foundational basis for understanding the interplay between disorder and interactions in the quasiparticle regime. On the similar line, a recent study[155] has revealed Anderson localization of elementary excitations by incorporating quantum and thermal corrections, thereby opening the door for studying finite-temperature effects and quantum fluctuations of disordered condensates. Another compelling direction would be to investigate the low-lying excitation modes of both localized and delocalized condensates to assess their dynamical and energetic stability.

Following the systematic exploration of homogeneous and inhomogeneous interaction profiles in this thesis, it would be particularly interesting to examine the influence of long-range dipolar interactions on localization behavior. The addition of spin-orbit (SO) and Rabi couplings to such dipolar systems could lead to novel localization regimes arising from the competition between long-range anisotropic interactions and synthetic spin-dependent couplings.

Furthermore, the role of Rabi coupling in inducing localization under spin-asymmetric quasiperiodic potentials, as demonstrated here, invites a natural extension to the case of random disordered potentials. Investigating whether similar localization–delocalization dynamics persist in fully disordered systems could provide a deeper understanding of the universality and limitations of Rabi-induced localization mechanisms.

In higher dimensional systems like in quasi-2D, an interesting future direction would be the study of spinor condensates subjected to spin-dependent moiré superlattices, as recently proposed in Ref. [262]. Such structured potentials, with tunable spatial periodicity and spin dependence, are experimentally realizable and provide a highly controllable platform to study localization and other novel phases in ultracold atoms.

Overall, these potential extensions can give insights to Anderson localization experiments, making them highly relevant for ongoing and future explorations in the field of disordered ultracold atomic systems.

Bibliography

[1] A. Aspect and M. Inguscio, "Anderson localization of ultracold atoms," *Physics Today*, vol. 62, no. 8, pp. 30–35, 2009.

[2] P. W. Anderson, "Absence of Diffusion in Certain Random Lattices," *Phys. Rev.*, vol. 109, pp. 1492–1505, Mar 1958.

[3] N. Mott and W. T. and, "The theory of impurity conduction," *Advances in Physics*, vol. 10, no. 38, pp. 107–163, 1961.

[4] M. Cutler and N. F. Mott, "Observation of Anderson localization in an electron gas," *Phys. Rev.*, vol. 181, pp. 1336–1340, May 1969.

[5] M. E. Gertsenshtein and V. B. Vasil'ev, "Waveguides with random inhomogeneities and brownian motion in the lobachevsky plane," *Theory of Probability & Its Applications*, vol. 4, no. 4, pp. 391–398, 1959.

[6] R. Abou-Chacra, D. J. Thouless, and P. W. Anderson, "A selfconsistent theory of localization," *Journal of Physics C: Solid State Physics*, vol. 6, p. 1734, may 1973.

[7] E. Abrahams, P. W. Anderson, D. C. Licciardello, and T. V. Ramakrishnan, "Scaling theory of localization: Absence of quantum diffusion in two dimensions," *Phys. Rev. Lett.*, vol. 42, pp. 673–676, Mar 1979.

[8] P. A. Lee and T. V. Ramakrishnan, "Disordered electronic systems," *Rev. Mod. Phys.*, vol. 57, pp. 287–337, Apr 1985.

[9] F. Evers and A. D. Mirlin, "Anderson transitions," *Rev. Mod. Phys.*, vol. 80, pp. 1355–1417, Oct 2008.

[10] D. S. Wiersma, P. Bartolini, A. Lagendijk, and R. Righini, "Localization of light in a disordered medium," *Nature*, vol. 390, pp. 671–673, Dec 1997.

[11] F. Scheffold, R. Lenke, R. Tweer, and G. Maret, "Localization or classical diffusion of light?," *Nature*, vol. 398, pp. 206–207, Mar 1999.

[12] T. Schwartz, G. Bartal, S. Fishman, and M. Segev, "Transport and Anderson localization in disordered two-dimensional photonic lattices," *Nature*, vol. 446, pp. 52–55, Mar 2007.

[13] C. M. Aegerter, M. Störzer, S. Fiebig, W. Bührer, and G. Maret, "Observation of Anderson localization of light in three dimensions," *J. Opt. Soc. Am. A*, vol. 24, pp. A23–A27, Oct 2007.

[14] J. Topolancik, B. Ilic, and F. Vollmer, "Experimental observation of strong photon localization in disordered photonic crystal waveguides," *Phys. Rev. Lett.*, vol. 99, p. 253901, Dec 2007.

[15] R. Dalichaouch, J. P. Armstrong, S. Schultz, P. M. Platzman, and S. L. McCall, "Microwave localization by two-dimensional random scattering," *Nature*, vol. 354, pp. 53–55, Nov 1991.

[16] C. Dembowski, H.-D. Gräf, R. Hofferbert, H. Rehfeld, A. Richter, and T. Weiland, "Anderson localization in a string of microwave cavities," *Phys. Rev. E*, vol. 60, pp. 3942–3948, Oct 1999.

[17] A. A. Chabanov, M. Stoytchev, and A. Z. Genack, "Statistical signatures of photon localization," *Nature*, vol. 404, pp. 850–853, Apr 2000.

[18] P. Pradhan and S. Sridhar, "Correlations due to localization in quantum eigenfunctions of disordered microwave cavities," *Phys. Rev. Lett.*, vol. 85, pp. 2360–2363, Sep 2000.

[19] R. Weaver, "Anderson localization of ultrasound," *Wave Motion*, vol. 12, no. 2, pp. 129–142, 1990.

[20] G. Roati, C. D'Errico, L. Fallani, M. Fattori, C. Fort, M. Zaccanti, G. Modugno, M. Modugno, and M. Inguscio, "Anderson localization of a non-interacting Bose–Einstein condensate," *Nature*, vol. 453, pp. 895–898, Jun 2008.

[21] J. Billy, V. Josse, Z. Zuo, A. Bernard, B. Hambrecht, P. Lugan, D. Clément, L. Sanchez-Palencia, P. Bouyer, and A. Aspect, "Direct observation of Anderson localization of matter waves in a controlled disorder," *Nature*, vol. 453, pp. 891–894, Jun 2008.

[22] S. K. Adhikari and L. Salasnich, "Localization of a Bose-Einstein condensate in a bichromatic optical lattice," *Phys. Rev. A*, vol. 80, p. 023606, Aug 2009.

[23] L. Sanchez-Palencia, D. Clément, P. Lugan, P. Bouyer, G. V. Shlyapnikov, and A. Aspect, "Anderson localization of expanding Bose-Einstein condensates in random potentials," *Phys. Rev. Lett.*, vol. 98, p. 210401, May 2007.

[24] Y. Cheng, G. Tang, and S. K. Adhikari, "Localization of a spin-orbit-coupled Bose-Einstein condensate in a bichromatic optical lattice," *Phys. Rev. A*, vol. 89, p. 063602, Jun 2014.

[25] G. Kopidakis, S. Komineas, S. Flach, and S. Aubry, "Absence of wave packet diffusion in disordered nonlinear systems," *Phys. Rev. Lett.*, vol. 100, p. 084103, Feb 2008.

[26] S. Gangwar, R. Ravisankar, P. Muruganandam, and P. K. Mishra, "Dynamics of quantum solitons in lee-huang-yang spin-orbit-coupled Bose-Einstein condensates," *Phys. Rev. A*, vol. 106, p. 063315, Dec 2022.

[27] N. Cherroret, T. Scoquart, and D. Delande, "Coherent multiple scattering of out-of-equilibrium interacting bose gases," *Annals of Physics*, vol. 435, p. 168543, 2021. Special Issue on Localisation 2020.

[28] R. Ravisankar, H. Fabrelli, A. Gammal, P. Muruganandam, and P. K. Mishra, "Effect of rashba spin-orbit and rabi couplings on the excitation spectrum of binary Bose-Einstein condensates," *Phys. Rev. A*, vol. 104, p. 053315, Nov 2021.

[29] R. Du, J.-C. Xing, B. Xiong, J.-H. Zheng, and T. Yang, "Quench dynamics of Bose-Einstein condensates in boxlike traps," *Chin. Phys. Lett.*, vol. 39, p. 070304, 2022.

[30] I. Březinová, L. A. Collins, K. Ludwig, B. I. Schneider, and J. Burgdörfer, "Wave chaos in the nonequilibrium dynamics of the Gross-Pitaevskii equation," *Phys. Rev. A*, vol. 83, p. 043611, Apr 2011.

[31] G. Bergmann, "Weak localization in thin films: a time-of-flight experiment with conduction electrons," *Physics Reports*, vol. 107, no. 1, pp. 1–58, 1984.

[32] Y. Kuga and A. Ishimaru, "Retroreflectance from a dense distribution of spherical particles," *Journal of the Optical Society of America A*, vol. 1, no. 8, pp. 831–835, 1984.

[33] P.-E. Wolf and G. Maret, "Weak localization and coherent backscattering of photons in disordered media," *Physical review letters*, vol. 55, no. 24, p. 2696, 1985.

[34] F. Jendrzejewski, K. Müller, J. Richard, A. Date, T. Plisson, P. Bouyer, A. Aspect, and V. Josse, "Coherent backscattering of ultracold atoms," *Physical Review Letters*, vol. 109, no. 19, p. 195302, 2012.

[35] C. D'Errico, *Anderson Localization of a Weakly Interacting Bose-Einstein Condensate*. PhD thesis, University of Florence, Florence, Italy, 2008.

[36] A. Lagendijk, B. v. Tiggelen, and D. S. Wiersma, "Fifty years of Anderson localization," *Phys. Today*, vol. 62, no. 8, pp. 24–29, 2009.

[37] A. A. Gogolin, V. MelNikov, and E. I. Rashba, "Conductivity in a disordered one-dimensional system induced by electron-phonon interaction," *Soviet Journal of Experimental and Theoretical Physics*, vol. 42, p. 168, July 1975.

[38] A. A. Gogolin, "Electron density distribution for localized states in a one-dimensional disordered system," *Soviet Journal of Experimental and Theoretical Physics*, vol. 44, p. 1003, Nov. 1976.

[39] S. John, "Electromagnetic absorption in a disordered medium near a photon mobility edge," *Phys. Rev. Lett.*, vol. 53, pp. 2169–2172, Nov 1984.

[40] E. Akkermans, P. E. Wolf, and R. Maynard, "Coherent backscattering of light by disordered media: Analysis of the peak line shape," *Phys. Rev. Lett.*, vol. 56, pp. 1471–1474, Apr 1986.

[41] M. P. V. Albada and A. Lagendijk, "Observation of weak localization of light in a random medium," *Phys. Rev. Lett.*, vol. 55, pp. 2692–2695, Dec 1985.

[42] P.-E. Wolf and G. Maret, "Weak localization and coherent backscattering of photons in disordered media," *Phys. Rev. Lett.*, vol. 55, pp. 2696–2699, Dec 1985.

[43] M. V. Berry and S. Klein, "Transparent mirrors: rays, waves and localization," *European Journal of Physics*, vol. 18, p. 222, may 1997.

[44] M. Störzer, P. Gross, C. M. Aegerter, and G. Maret, "Observation of the critical regime near Anderson localization of light," *Phys. Rev. Lett.*, vol. 96, p. 063904, Feb 2006.

[45] Y. Lahini, A. Avidan, F. Pozzi, M. Sorel, R. Morandotti, D. N. Christodoulides, and Y. Silberberg, "Anderson localization and nonlinearity in one-dimensional disordered photonic lattices," *Phys. Rev. Lett.*, vol. 100, p. 013906, Jan 2008.

[46] Bose, "Plancks gesetz und lichtquantenhypothese," *Zeitschrift für Physik*, vol. 26, no. 1, pp. 178–181, 1924.

[47] A. Einstein, "Quantum theory of the monatomic ideal gas," *Sitzber. Kgl. Preuss. Akad. Wiss.*, p. 261, 1924.

[48] A. Einstein, "Quantum theory of the monatomic ideal gas. part ii," *Sitzber. Kgl. Preuss. Akad. Wiss.*, p. 3, 1925.

[49] P. Kapitza, "Viscosity of liquid helium below the λ-point," *Nature*, vol. 141, no. 3558, pp. 74–74, 1938.

[50] J. F. Allen and A. D. Misener, "Flow of liquid helium ii," *Nature*, vol. 141, pp. 75–75, Jan 1938.

[51] F. London, "On the Bose-Einstein condensation," *Phys. Rev.*, vol. 54, pp. 947–954, Dec 1938.

[52] L. Landau, "Theory of the superfluidity of helium ii," *Phys. Rev.*, vol. 60, p. 356, 1941.

[53] O. Penrose, "Cxxxvi. on the quantum mechanics of helium ii," *The London, Edinburgh, and Dublin Philosophical Magazine and Journal of Science*, vol. 42, no. 335, pp. 1373–1377, 1951.

[54] O. Penrose and L. Onsager, "Bose-Einstein condensation and liquid helium," *Phys. Rev.*, vol. 104, no. 3, p. 576, 1956.

[55] R. Pathria and P. D. Beale, "Statistical mechanics," in *Statistical Mechanics (Third Edition)* (R. Pathria and P. D. Beale, eds.), pp. 583–635, Boston: Academic Press, third edition ed., 2011.

[56] M. H. Anderson, J. R. Ensher, M. R. Matthews, C. E. Wieman, and E. A. Cornell, "Observation of Bose-Einstein condensation in a dilute atomic vapor," *Science*, vol. 269, no. 5221, pp. 198–201, 1995.

[57] K. B. Davis, M. O. Mewes, M. R. Andrews, N. J. van Druten, D. S. Durfee, D. M. Kurn, and W. Ketterle, "Bose-Einstein condensation in a gas of sodium atoms," *Phys. Rev. Lett.*, vol. 75, pp. 3969–3973, Nov 1995.

[58] C. C. Bradley, C. A. Sackett, J. J. Tollett, and R. G. Hulet, "Evidence of Bose-Einstein condensation in an atomic gas with attractive interactions," *Phys. Rev. Lett.*, vol. 75, pp. 1687–1690, Aug 1995.

[59] D. G. Fried, T. C. Killian, L. Willmann, D. Landhuis, S. C. Moss, D. Kleppner, and T. J. Greytak, "Bose-Einstein condensation of atomic hydrogen," *Phys. Rev. Lett.*, vol. 81, pp. 3811–3814, Nov 1998.

[60] K. W. Madison, F. Chevy, W. Wohlleben, and J. Dalibard, "Vortex formation in a stirred Bose-Einstein condensate," *Phys. Rev. Lett.*, vol. 84, pp. 806–809, Jan 2000.

[61] J. R. Abo-Shaeer, C. Raman, J. M. Vogels, and W. Ketterle, "Observation of vortex lattices in Bose-Einstein condensates," *Science*, vol. 292, no. 5516, pp. 476–479, 2001.

[62] M. Tsubota, "Quantum turbulence," *Journal of the Physical Society of Japan*, vol. 77, no. 11, pp. 111006–111006, 2008.

[63] I. Bloch, J. Dalibard, and W. Zwerger, "Many-body physics with ultracold gases," *Rev. Mod. Phys.*, vol. 80, pp. 885–964, Jul 2008.

[64] A. S. Bradley and B. P. Anderson, "Energy spectra of vortex distributions in two-dimensional quantum turbulence," *Phys. Rev. X*, vol. 2, p. 041001, Oct 2012.

[65] L. Chomaz, S. Baier, D. Petter, M. Mark, F. Wächtler, L. Santos, and F. Ferlaino, "Quantum-fluctuation-driven crossover from a dilute Bose-Einstein condensate to a macrodroplet in a dipolar quantum fluid," *Phys. Rev. X*, vol. 6, no. 4, p. 041039, 2016.

[66] G. Modugno, "Anderson localization in Bose-Einstein condensates," *Rep. Prog. Phys.*, vol. 73, no. 10, p. 102401, 2010.

[67] D. Petrov and G. Astrakharchik, "Ultradilute low-dimensional liquids," *Phys. Rev. Lett.*, vol. 117, no. 10, p. 100401, 2016.

[68] C. Cabrera, L. Tanzi, J. Sanz, B. Naylor, P. Thomas, P. Cheiney, and L. Tarruell, "Quantum liquid droplets in a mixture of Bose-Einstein condensates," *Science*, vol. 359, no. 6373, pp. 301–304, 2018.

[69] H. Feshbach, "Unified theory of nuclear reactions," *Annals of Physics*, vol. 5, no. 4, pp. 357–390, 1958.

[70] H. Feshbach, "A unified theory of nuclear reactions. ii," *Annals of Physics*, vol. 19, no. 2, pp. 287–313, 1962.

[71] U. Fano, "Sullo spettro di assorbimento dei gas nobili presso il limite dello spettro d'arco," *Il Nuovo Cimento*, vol. 12, pp. 154–161, Mar. 1935.

[72] S. Inouye, M. Andrews, J. Stenger, H.-J. Miesner, D. M. Stamper-Kurn, and W. Ketterle, "Observation of feshbach resonances in a Bose–Einstein condensate," *Nature*, vol. 392, no. 6672, pp. 151–154, 1998.

[73] S. L. Cornish, N. R. Claussen, J. L. Roberts, E. A. Cornell, and C. E. Wieman, "Stable ^{85}Rb Bose-Einstein condensates with widely tunable interactions," *Phys. Rev. Lett.*, vol. 85, pp. 1795–1798, Aug 2000.

[74] C. Chin, V. Vuletić, A. J. Kerman, and S. Chu, "High resolution feshbach spectroscopy of cesium," *Phys. Rev. Lett.*, vol. 85, pp. 2717–2720, Sep 2000.

[75] M. Theis, *Tuning the Scattering Length with an Optically Induced Feshbach Resonance*. Diploma thesis, University of Innsbruck, Innsbruck, Austria, 2005.

[76] P. O. Fedichev, Y. Kagan, G. V. Shlyapnikov, and J. T. M. Walraven, "Influence of nearly resonant light on the scattering length in low-temperature atomic gases," *Phys. Rev. Lett.*, vol. 77, pp. 2913–2916, Sep 1996.

[77] J. L. Bohn and P. S. Julienne, "Prospects for influencing scattering lengths with far-off-resonant light," *Phys. Rev. A*, vol. 56, pp. 1486–1491, Aug 1997.

[78] F. K. Fatemi, K. M. Jones, and P. D. Lett, "Observation of optically induced feshbach resonances in collisions of cold atoms," *Phys. Rev. Lett.*, vol. 85, pp. 4462–4465, Nov 2000.

[79] M. Theis, G. Thalhammer, K. Winkler, M. Hellwig, G. Ruff, R. Grimm, and J. H. Denschlag, "Tuning the scattering length with an optically induced feshbach resonance," *Phys. Rev. Lett.*, vol. 93, p. 123001, Sep 2004.

[80] R. Ciuryło, E. Tiesinga, and P. S. Julienne, "Optical tuning of the scattering length of cold alkaline-earth-metal atoms," *Phys. Rev. A*, vol. 71, p. 030701, Mar 2005.

[81] R. Ciuryło, E. Tiesinga, and P. S. Julienne, "Stationary phase approximation for the strength of optical Feshbach resonances," *Phys. Rev. A*, vol. 74, p. 022710, Aug 2006.

[82] C. N. Cohen-Tannoudji, "Nobel lecture: Manipulating atoms with photons," *Rev. Mod. Phys.*, vol. 70, pp. 707–719, Jul 1998.

[83] R. Grimm, M. Weidemüller, and Y. B. Ovchinnikov, "Optical dipole traps for neutral atoms," vol. 42 of *Advances In Atomic, Molecular, and Optical Physics*, pp. 95–170, Academic Press, 2000.

[84] L. Sanchez-Palencia and M. Lewenstein, "Disordered quantum gases under control," *Nature Phys.*, vol. 6, pp. 87–95, Feb 2010.

[85] U. Gavish and Y. Castin, "Matter-wave localization in disordered cold atom lattices," *Phys. Rev. Lett.*, vol. 95, p. 020401, Jul 2005.

[86] B. Paredes, F. Verstraete, and J. I. Cirac, "Exploiting quantum parallelism to simulate quantum random many-body systems," *Phys. Rev. Lett.*, vol. 95, p. 140501, Sep 2005.

[87] D. Clément, A. F. Varòn, J. A. Retter, L. Sanchez-Palencia, A. Aspect, and P. Bouyer, "Experimental study of the transport of coherent interacting matter-waves in a 1D random potential induced by laser speckle," *New Journal of Physics*, vol. 8, no. 8, p. 165, 2006.

[88] S. S. Kondov, W. R. McGehee, J. J. Zirbel, and B. DeMarco, "Three-dimensional Anderson localization of ultracold matter," *Science*, vol. 334, no. 6052, pp. 66–68, 2011.

[89] F. Jendrzejewski, A. Bernard, K. Müller, P. Cheinet, V. Josse, M. Piraud, L. Pezzé, L. Sanchez-Palencia, A. Aspect, and P. Bouyer, "Three-dimensional localization of ultracold atoms in an optical disordered potential," *Nature Physics*, vol. 8, no. 5, pp. 398–403, 2012.

[90] S. Aubry and G. André, "Analyticity breaking and Anderson localization in incommensurate lattices," *Ann. Israel Phys. Soc*, vol. 3, no. 133, p. 18.

[91] D. H. White, T. A. Haase, D. J. Brown, M. D. Hoogerland, M. S. Najafabadi, J. L. Helm, C. Gies, D. Schumayer, and D. A. W. Hutchinson, "Observation of two-dimensional Anderson localisation of ultracold atoms," *Nat. Commun.*, vol. 11, p. 4942, Oct 2020.

[92] G. Semeghini, M. Landini, P. Castilho, S. Roy, G. Spagnolli, A. Trenkwalder, M. Fattori, M. Inguscio, and G. Modugno, "Measurement of the mobility edge for 3d Anderson localization," *Nature Physics*, vol. 11, no. 7, pp. 554–559, 2015.

[93] A. L. Fetter and J. D. Walecka, *Quantum theory of many-particle systems*. International series in pure and applied physics, San Francisco, Calif. ;: McGraw-Hill, 1971.

[94] N. P. Proukakis and K. Burnett, "Theory of bose–einstein condensation for trapped atoms," *Philosophical Transactions of the Royal Society of London. Series A: Mathematical, Physical and Engineering Sciences*, vol. 355, p. 2235–2245, Dec. 1997.

[95] C. J. Pethick and H. Smith, *Bose–Einstein Condensation in Dilute Gases*. Cambridge University Press, 2001.

[96] L. Pitaevskii and S. Stringari, *Bose-Einstein Condensation*. International Series of Monographs on Physics, Clarendon Press, 2003.

[97] J. Weiner, V. S. Bagnato, S. Zilio, and P. S. Julienne, "Experiments and theory in cold and ultracold collisions," *Rev. Mod. Phys.*, vol. 71, pp. 1–85, Jan 1999.

[98] W. Bao, P. A. Markowich, and H. Wang, "Ground, Symmetric and Central Vortex States in Rotating Bose-Einstein Condensates," *Communications in Mathematical Sciences*, vol. 3, no. 1, pp. 57 – 88, 2005.

[99] W. Bao, Q. Du, and Y. Zhang, "Dynamics of rotating bose–einstein condensates and its efficient and accurate numerical computation," *SIAM Journal on Applied Mathematics*, vol. 66, no. 3, pp. 758–786, 2006.

[100] Y. Zhang and W. Bao, "Dynamics of the center of mass in rotating bose–einstein condensates," *Applied Numerical Mathematics*, vol. 57, no. 5, pp. 697–709, 2007. Special Issue for the International Conference on Scientific Computing.

[101] B. Jackson, J. F. McCann, and C. S. Adams, "Vortex formation in dilute inhomogeneous Bose-Einstein condensates," *Phys. Rev. Lett.*, vol. 80, pp. 3903–3906, May 1998.

[102] P. Leboeuf and N. Pavloff, "Bose-Einstein beams: Coherent propagation through a guide," *Phys. Rev. A*, vol. 64, p. 033602, Aug 2001.

[103] V. Dunjko, V. Lorent, and M. Olshanii, "Bosons in cigar-shaped traps: Thomas-fermi regime, tonks-girardeau regime, and in between," *Phys. Rev. Lett.*, vol. 86, pp. 5413–5416, Jun 2001.

[104] W. Bao and W. Tang, "Ground-state solution of bose–einstein condensate by directly minimizing the energy functional," *Journal of Computational Physics*, vol. 187, no. 1, pp. 230–254, 2003.

[105] Y.-J. Lin, K. Jiménez-García, and I. B. Spielman, "Spin–orbit-coupled bose–einstein condensates," *Nature*, vol. 471, pp. 83–86, Mar 2011.

[106] Y. A. Bychkov and E. I. Rashba, "Oscillatory effects and the magnetic susceptibility of carriers in inversion layers," *Journal of Physics C: Solid State Physics*, vol. 17, p. 6039, nov 1984.

[107] G. Dresselhaus, "Spin-orbit coupling effects in zinc blende structures," *Phys. Rev.*, vol. 100, pp. 580–586, Oct 1955.

[108] P. Wang, Z.-Q. Yu, Z. Fu, J. Miao, L. Huang, S. Chai, H. Zhai, and J. Zhang, "Spin-orbit coupled degenerate fermi gases," *Phys. Rev. Lett.*, vol. 109, p. 095301, Aug 2012.

[109] T.-L. Ho, "Spinor Bose condensates in optical traps," *Phys. Rev. Lett.*, vol. 81, pp. 742–745, Jul 1998.

[110] L. Tao and E. Y. Tsymbal, "Persistent spin texture enforced by symmetry," *Nature communications*, vol. 9, no. 1, p. 2763, 2018.

[111] Y. K. Kato, R. C. Myers, A. C. Gossard, and D. D. Awschalom, "Observation of the spin hall effect in semiconductors," *Science*, vol. 306, no. 5703, pp. 1910–1913, 2004.

[112] I. Žutić, J. Fabian, and S. Das Sarma, "Spintronics: Fundamentals and applications," *Rev. Mod. Phys.*, vol. 76, pp. 323–410, Apr 2004.

[113] M. Z. Hasan and C. L. Kane, "Colloquium: Topological insulators," *Rev. Mod. Phys.*, vol. 82, pp. 3045–3067, Nov 2010.

[114] X.-L. Qi and S.-C. Zhang, "Topological insulators and superconductors," *Rev. Mod. Phys.*, vol. 83, pp. 1057–1110, Oct 2011.

[115] M. Johanning, A. F. Varón, and C. Wunderlich, "Quantum simulations with cold trapped ions," *Journal of Physics B: Atomic, Molecular and Optical Physics*, vol. 42, p. 154009, jul 2009.

[116] I. Bloch, J. Dalibard, and S. Nascimbène, "Quantum simulations with ultracold quantum gases," *Nature Physics*, vol. 8, no. 4, pp. 267–276, 2012.

[117] G. Ricard, F. Novkoski, and E. Falcon, "Effects of nonlinearity on Anderson localization of surface gravity waves," *Nature Communications*, vol. 15, no. 1, p. 5726, 2024.

[118] P. Lugan, D. Clément, P. Bouyer, A. Aspect, and L. Sanchez-Palencia, "Anderson localization of bogolyubov quasiparticles in interacting bose-einstein condensates," *Phys. Rev. Lett.*, vol. 99, p. 180402, Nov 2007.

[119] B. Shapiro, "Expansion of a Bose-Einstein condensate in the presence of disorder," *Phys. Rev. Lett.*, vol. 99, p. 060602, Aug 2007.

[120] Y. Cheng and S. K. Adhikari, "Symmetry breaking in a localized interacting binary Bose-Einstein condensate in a bichromatic optical lattice," *Phys. Rev. A*, vol. 81, p. 023620, Feb 2010.

[121] Y. Cheng and S. K. Adhikari, "Spatially-antisymmetric localization of matter wave in a bichromatic optical lattice," *Laser Physics Letters*, vol. 7, no. 11, p. 824, 2010.

[122] D.-N. S. Kui-Tian Xi, Jinbin Li, "Localization of a two-component bose–einstein condensate in a two-dimensional bichromatic optical lattice," *Physica B: Condensed Matter*, vol. 436, pp. 149–156, 2014.

[123] S. K. Adhikari, "Localization of a Bose-Einstein condensate vortex in a bichromatic optical lattice," *Phys. Rev. A*, vol. 81, p. 043636, Apr 2010.

[124] M. C. P. dos Santos and W. B. Cardoso, "Anderson localization induced by interaction in linearly coupled binary Bose-Einstein condensates," *Phys. Rev. E*, vol. 103, p. 052210, May 2021.

[125] D. Clément, A. F. Varón, M. Hugbart, J. A. Retter, P. Bouyer, L. Sanchez-Palencia, D. M. Gangardt, G. V. Shlyapnikov, and A. Aspect, "Suppression of transport of an interacting elongated Bose-Einstein condensate in a random potential," *Phys. Rev. Lett.*, vol. 95, p. 170409, Oct 2005.

[126] Y. Cheng and S. K. Adhikari, "Matter-wave localization in a random potential," *Phys. Rev. A*, vol. 82, p. 013631, Jul 2010.

[127] K.-T. Xi, J. Li, and D.-N. Shi, "Localization of a two-component bose-einstein condensate in a one-dimensional random potential," *Physica B: Condensed Matter*, vol. 459, pp. 6–11, 2015.

[128] C. Li, F. Ye, Y. V. Kartashov, V. V. Konotop, and X. Chen, "Localization-delocalization transition in spin-orbit-coupled Bose-Einstein condensate," *Scientific Reports*, vol. 6, p. 31700, Aug 2016.

[129] Z. Oztas, "Spin orbit coupled Bose einstein condensate in a two dimensional bichromatic optical lattice," *Physics Letters A*, vol. 383, no. 6, pp. 504–508, 2019.

[130] H. Zhang, S. Liu, and Y. Zhang, "Anderson localization of a spin–orbit coupled Bose-Einstein condensate in disorder potential," *Chin. Phys. B*, vol. 31, p. 070305, jun 2022.

[131] P. Muruganandam, R. K. Kumar, and S. K. Adhikari, "Localization of a dipolar bose–einstein condensate in a bichromatic optical lattice," *Journal of Physics B: Atomic, Molecular and Optical Physics*, vol. 43, p. 205305, oct 2010.

[132] Y. Cheng and S. K. Adhikari, "Localization of collisionally inhomogeneous condensates in a bichromatic optical lattice," *Phys. Rev. A*, vol. 83, p. 023620, Feb 2011.

[133] J. B. Sudharsan, R. Radha, and P. Muruganandam, "Collisionally inhomogeneous bose–einstein condensates with binary and three-body interactions in a bichromatic optical lattice," *Journal of Physics B: Atomic, Molecular and Optical Physics*, vol. 46, p. 155302, jul 2013.

[134] K. Jiménez-García, L. J. LeBlanc, R. A. Williams, M. C. Beeler, C. Qu, M. Gong, C. Zhang, and I. B. Spielman, "Tunable spin-orbit coupling via strong driving in ultracold-atom systems," *Phys. Rev. Lett.*, vol. 114, p. 125301, Mar 2015.

[135] F. K. Abdullaev, M. Brtka, A. Gammal, and L. Tomio, "Solitons and josephson-type oscillations in Bose-Einstein condensates with spin-orbit coupling and time-varying raman frequency," *Phys. Rev. A*, vol. 97, p. 053611, May 2018.

[136] J. E. Lye, L. Fallani, M. Modugno, D. S. Wiersma, C. Fort, and M. Inguscio, "Bose-Einstein condensate in a random potential," *Phys. Rev. Lett.*, vol. 95, p. 070401, Aug 2005.

[137] C. Fort, L. Fallani, V. Guarrera, J. E. Lye, M. Modugno, D. S. Wiersma, and M. Inguscio, "Effect of optical disorder and single defects on the expansion of a Bose-Einstein condensate in a one-dimensional waveguide," *Phys. Rev. Lett.*, vol. 95, p. 170410, Oct 2005.

[138] M. Modugno, "Collective dynamics and expansion of a Bose-Einstein condensate in a random potential," *Phys. Rev. A*, vol. 73, p. 013606, Jan 2006.

[139] E. V. Doggen and J. J. Kinnunen, "Quench-induced delocalization," *New J. Phys.*, vol. 16, no. 11, p. 113051, 2014.

[140] B. Damski, J. Zakrzewski, L. Santos, P. Zoller, and M. Lewenstein, "Atomic Bose and Anderson glasses in optical lattices," *Phys. Rev. Lett.*, vol. 91, p. 080403, Aug 2003.

[141] P. Muruganandam and S. K. Adhikari, "Chaotic oscillation in an attractive Bose-Einstein condensate under an impulsive force," *Phys. Rev. A*, vol. 65, p. 043608, Mar 2002.

[142] P. Verma, A. Bhattacherjee, and M. Mohan, "Chaos in bec trapped in tilted optical superlattice potential with attractive interaction," *Journal of Physics: Conference Series*, vol. 350, p. 012003, mar 2012.

[143] E. Tosyali, F. Aydogmus, and A. Yilmaz, "Regular and chaotic solutions in bec for tilted bichromatical optical lattice," *International Journal of Modern Physics B*, vol. 32, no. 23, p. 1850254, 2018.

[144] Z. Oztas and O. Nabiollahi, "Anderson localization and quenched induced dynamics of spin orbit coupled Bose–Einstein condensate in a random potential," *Phys. Scr.*, vol. 99, no. 6, p. 065913, 2024.

[145] F. Li and W. Li, "Chaotic and regular spatial structures of bose–einstein condensates with a spatially modulated atom-atom interaction and without an external trapping potential*," *Communications in Theoretical Physics*, vol. 77, p. 095701, may 2025.

[146] S. Mardonov, M. Modugno, and E. Y. Sherman, "Dynamics of spin-orbit coupled Bose-Einstein condensates in a random potential," *Phys. Rev. Lett.*, vol. 115, p. 180402, Oct 2015.

[147] S. Mardonov, V. V. Konotop, B. A. Malomed, M. Modugno, and E. Y. Sherman, "Spin-orbit-coupled soliton in a random potential," *Phys. Rev. A*, vol. 98, p. 023604, Aug 2018.

[148] S. Mardonov, M. Modugno, E. Y. Sherman, and B. A. Malomed, "Rabi-coupling-driven motion of a soliton in a Bose-Einstein condensate," *Phys. Rev. A*, vol. 99, p. 013611, Jan 2019.

[149] E. Doron and S. Fishman, "Anderson localization for a two-dimensional rotor," *Phys. Rev. Lett.*, vol. 60, pp. 867–870, Mar 1988.

[150] I. Manai, J.-F. m. c. Clément, R. Chicireanu, C. Hainaut, J. C. Garreau, P. Szriftgiser, and D. Delande, "Experimental observation of two-dimensional Anderson localization with the atomic kicked rotor," *Phys. Rev. Lett.*, vol. 115, p. 240603, Dec 2015.

[151] S. S. Maurya, J. B. Kannan, K. Patel, P. Dutta, K. Biswas, J. Mangaonkar, M. S. Santhanam, and U. D. Rapol, "Interplay between quantum diffusion and localization in the atom-optics kicked rotor," *Phys. Rev. E*, vol. 106, p. 034207, Sep 2022.

[152] S. S. Maurya, J. B. Kannan, K. Patel, P. Dutta, K. Biswas, M. S. Santhanam, and U. D. Rapol, "Asymmetric dynamical localization and precision measurement of the micromotion of a Bose-Einstein condensate," *Phys. Rev. A*, vol. 110, p. 053307, Nov 2024.

[153] H. E. Nistazakis, Z. Rapti, D. J. Frantzeskakis, P. G. Kevrekidis, P. Sodano, and A. Trombettoni, "Rabi switch of condensate wave functions in a multicomponent bose gas," *Phys. Rev. A*, vol. 78, p. 023635, Aug 2008.

[154] Y. Zhang, G. Chen, and C. Zhang, "Tunable spin-orbit coupling and quantum phase transition in a trapped Bose-Einstein condensate," *Scientific Reports*, vol. 3, no. 1, p. 1937, 2013.

[155] M. Zohra and A. Boudjemâa, "Anderson localization of elementary excitations in disordered binary Bose mixtures: Effects of the Lee-Huang-Yang quantum and thermal corrections," *Phys. Rev. A*, vol. 110, p. 053305, Nov 2024.

[156] P. Muruganandam and S. K. Adhikari, "Fortran programs for the time-dependent Gross-Pitaevskii equation in a fully anisotropic trap," *Comput. Phys. Commun.*, vol. 180, no. 10, pp. 1888–1912, 2009.

[157] S. Koonin, *Computational Physics: Fortran Version*. Taylor & Francis Limited (Sales), 2019.

[158] "Issue information," *Numerical Methods for Partial Differential Equations*, vol. 41, no. 3, p. e23111, 2025.

[159] R. Dautray, M. Artola, J. Amson, M. Cessenat, and J. Lions, *Mathematical Analysis and Numerical Methods for Science and Technology: Volume 3 Spectral Theory and Applications*. Mathematical Analysis and Numerical Methods for Science and Technology, Springer Berlin Heidelberg, 1999.

[160] B. Weizhu and C. Yongyong, "Mathematical models and numerical methods for spinor Bose-Einstein condensates.," *Communications in Computational Physics*, vol. 24, no. 4, pp. 899–965, 2018.

[161] P. Banger, P. Kaur, and S. Gautam, "Semi-implicit finite-difference methods to study the spin-orbit- and coherently-coupled spinor bose–einstein condensates," *International Journal of Modern Physics C*, vol. 33, no. 04, p. 2250046, 2022.

[162] K. S. Gangwar, *Structure and Dynamics of the Spin Orbit Coupled Ultra Dilute Quantum Droplets*. Ph.d. thesis, Indian Institute of Technology Guwahati, 2025. Advisor: Mishra, Pankaj Kumar.

[163] W. H. Press, B. P. Flannery, S. A. Teukolsky, and W. T. Vetterling, *Numerical Recipes in FORTRAN 77: The Art of Scientific Computing*. Cambridge University Press, 2 ed., Sept. 1992.

[164] S. K. Sarkar, T. Mishra, P. Muruganandam, and P. K. Mishra, "Quench-induced chaotic dynamics of Anderson-localized interacting Bose-Einstein condensates in one dimension," *Phys. Rev. A*, vol. 107, p. 053320, May 2023.

[165] G. Roati, M. Zaccanti, C. D'Errico, J. Catani, M. Modugno, A. Simoni, M. Inguscio, and G. Modugno, "^{39}K Bose-Einstein condensate with tunable interactions," *Phys. Rev. Lett.*, vol. 99, p. 010403, Jul 2007.

[166] P. Muruganandam, R. K. Kumar, and S. K. Adhikari, "Localization of a dipolar bose–einstein condensate in a bichromatic optical lattice," *J. Phys. B: At. Mol. Opt. Phys.*, vol. 43, no. 20, p. 205305, 2010.

[167] Y. Cheng and S. Adhikari, "Spatially-antisymmetric localization of matter wave in a bichromatic optical lattice," *Laser Phys. Lett.*, vol. 7, pp. 824–830, aug 2010.

[168] Y. Cheng and S. K. Adhikari, "Localization of a bose-fermi mixture in a bichromatic optical lattice," *Phys. Rev. A*, vol. 84, p. 023632, Aug 2011.

[169] Y. Cheng and S. K. Adhikari, "Matter-wave localization in a weakly perturbed optical lattice," *Phys. Rev. A*, vol. 84, p. 053634, Nov 2011.

[170] Y. Cheng, G. Tang, and S. K. Adhikari, "Localization of a spin-orbit-coupled Bose-Einstein condensate in a bichromatic optical lattice," *Phys. Rev. A*, vol. 89, p. 063602, Jun 2014.

[171] D. M. Abrams, R. Mirollo, S. H. Strogatz, and D. A. Wiley, "Solvable model for chimera states of coupled oscillators," *Phys. Rev. Lett.*, vol. 101, p. 084103, Aug 2008.

[172] B. Deissler, M. Zaccanti, G. Roati, C. D'Errico, M. Fattori, M. Modugno, G. Modugno, and M. Inguscio, "Delocalization of a disordered bosonic system by repulsive interactions," *Nature Phys.*, vol. 6, no. 5, pp. 354–358, 2010.

[173] W. Cardoso, A. Avelar, and D. Bazeia, "Anderson localization of matter waves in chaotic potentials," *Nonlinear Anal. Real World Appl.*, vol. 13, no. 2, pp. 755–763, 2012.

[174] K.-T. Xi, J. Li, and D.-N. Shi, "Localization of a two-component bose–einstein condensate in a one-dimensional random potential," *Physica B*, vol. 459, pp. 6–11, 2015.

[175] E. Lucioni, B. Deissler, L. Tanzi, G. Roati, M. Zaccanti, M. Modugno, M. Larcher, F. Dalfovo, M. Inguscio, and G. Modugno, "Observation of subdiffusion in a disordered interacting system," *Phys. Rev. Lett.*, vol. 106, p. 230403, Jun 2011.

[176] A. S. Pikovsky and D. L. Shepelyansky, "Destruction of Anderson localization by a weak nonlinearity," *Phys. Rev. Lett.*, vol. 100, p. 094101, Mar 2008.

[177] N. Cherroret, B. Vermersch, J. C. Garreau, and D. Delande, "How nonlinear interactions challenge the three-dimensional Anderson transition," *Phys. Rev. Lett.*, vol. 112, p. 170603, May 2014.

[178] L. Sanchez-Palencia, D. Clément, P. Lugan, P. Bouyer, and A. Aspect, "Disorder-induced trapping versus Anderson localization in bose–einstein condensates expanding in disordered potentials," *New J. Phys.*, vol. 10, p. 045019, apr 2008.

[179] Y. Shin, M. Saba, T. A. Pasquini, W. Ketterle, D. E. Pritchard, and A. E. Leanhardt, "Atom interferometry with Bose-Einstein condensates in a double-well potential," *Phys. Rev. Lett.*, vol. 92, p. 050405, Feb 2004.

[180] M. Saba, T. Pasquini, C. Sanner, Y. Shin, W. Ketterle, and D. Pritchard, "Light scattering to determine the relative phase of two Bose-Einstein condensates," *Science*, vol. 307, no. 5717, pp. 1945–1948, 2005.

[181] Y. Shin, G.-B. Jo, M. Saba, T. A. Pasquini, W. Ketterle, and D. E. Pritchard, "Optical weak link between two spatially separated Bose-Einstein condensates," *Phys. Rev. Lett.*, vol. 95, p. 170402, Oct 2005.

[182] C. Chin, R. Grimm, P. Julienne, and E. Tiesinga, "Feshbach resonances in ultracold gases," *Rev. Mod. Phys.*, vol. 82, pp. 1225–1286, Apr 2010.

[183] H. Ott, J. Fortágh, S. Kraft, A. Günther, D. Komma, and C. Zimmermann, "Nonlinear dynamics of a Bose-Einstein condensate in a magnetic waveguide," *Phys. Rev. Lett.*, vol. 91, p. 040402, Jul 2003.

[184] K. D. Rao and M. Swamy, *Spectral Analysis of Signals*, pp. 721–751. Singapore: Springer Singapore, 2018.

[185] S. Dalui, B. R. Majhi, and P. Mishra, "Induction of chaotic fluctuations in particle dynamics in a uniformly accelerated frame," *Int. J. Mod. Phys. A*, vol. 35, no. 18, p. 2050081, 2020.

[186] I. Vlachos and D. Kugiumtzis, *State Space Reconstruction from Multiple Time Series*, pp. 378–387. World Scientific, 2009.

[187] M. B. Kennel, R. Brown, and H. D. I. Abarbanel, "Determining embedding dimension for phase-space reconstruction using a geometrical construction," *Phys. Rev. A*, vol. 45, pp. 3403–3411, Mar 1992.

[188] S. Wallot and D. Mønster, "Calculation of average mutual information (ami) and false-nearest neighbors (fnn) for the estimation of embedding parameters of multidimensional time series in matlab," *Front. Psychol.*, vol. 9, p. 1679, 2018.

[189] A. Wolf, J. B. Swift, H. L. Swinney, and J. A. Vastano, "Determining lyapunov exponents from a time series," *Physica D*, vol. 16, no. 3, pp. 285–317, 1985.

[190] A. M. Fraser and H. L. Swinney, "Independent coordinates for strange attractors from mutual information," *Phys. Rev. A*, vol. 33, pp. 1134–1140, Feb 1986.

[191] H. Kantz and T. Schreiber, *Nonlinear time series analysis*, vol. 7. Cambridge university press, 2004.

[192] L. E. Young-S., P. Muruganandam, S. K. Adhikari, V. Lončar, D. Vudragović, and A. Balaž, "Openmp gnu and intel fortran programs for solving the time-dependent gross–pitaevskii equation," *Comput. Phys. Commun.*, vol. 220, pp. 503–506, 2017.

[193] D. E. Sigeti, "Exponential decay of power spectra at high frequency and positive lyapunov exponents," *Physica D: Nonlinear Phenomena*, vol. 82, no. 1-2, pp. 136–153, 1995.

[194] U. Frisch and R. Morf, "Intermittency in nonlinear dynamics and singularities at complex times," *Phys. Rev. A*, vol. 23, pp. 2673–2705, May 1981.

[195] I. M. Lifshits, M. L. I'lya, S. A. Gredeskul, L. A. Pastur, *et al.*, *Introduction to the theory of disordered systems*. Wiley-VCH, 1988.

[196] M. P. A. Fisher, P. B. Weichman, G. Grinstein, and D. S. Fisher, "Boson localization and the superfluid-insulator transition," *Phys. Rev. B*, vol. 40, pp. 546–570, Jul 1989.

[197] R. T. Scalettar, G. G. Batrouni, and G. T. Zimanyi, "Localization in interacting, disordered, bose systems," *Phys. Rev. Lett.*, vol. 66, pp. 3144–3147, Jun 1991.

[198] F. Stellin, M. Filoche, and F. Dias, "Localization landscape for interacting bose gases in one-dimensional speckle potentials," *arXiv preprint arXiv:2208.09976*, 2022.

[199] P. Lugan, D. Clément, P. Bouyer, A. Aspect, M. Lewenstein, and L. Sanchez-Palencia, "Ultracold bose gases in 1d disorder: From lifshits glass to Bose-Einstein condensate," *Phys. Rev. Lett.*, vol. 98, p. 170403, Apr 2007.

[200] S. K. Sarkar, R. Ravisankar, T. Mishra, P. Muruganandam, and P. Mishra, "Signature of localization–delocalization in collisional inhomogeneous spin-orbit coupled condensates," *Journal of Physics B: Atomic, Molecular and Optical Physics*, vol. 58, p. 065001, mar 2025.

[201] D. S. Hall, M. R. Matthews, J. R. Ensher, C. E. Wieman, and E. A. Cornell, "Dynamics of component separation in a binary mixture of Bose-Einstein condensates," *Phys. Rev. Lett.*, vol. 81, pp. 1539–1542, Aug 1998.

[202] E. A. Ostrovskaya and Y. S. Kivshar, "Localization of two-component Bose-Einstein condensates in optical lattices," *Phys. Rev. Lett.*, vol. 92, p. 180405, May 2004.

[203] W.-Y. Wang, F.-Q. Dou, and W.-S. Duan, "Interaction induced localization of a spin–orbit-coupled Bose-Einstein condensate in a double-well potential," *The European Physical Journal D*, vol. 73, pp. 1–6, 2019.

[204] D. A. Zezyulin and V. V. Konotop, "Localization of ultracold atoms in zeeman lattices with incommensurate spin-orbit coupling," *Phys. Rev. A*, vol. 105, p. 063323, Jun 2022.

[205] S. Roy, T. Mishra, B. Tanatar, and S. Basu, "Reentrant localization transition in a quasiperiodic chain," *Phys. Rev. Lett.*, vol. 126, p. 106803, Mar 2021.

[206] S.-L. Zhu, D.-W. Zhang, and Z. D. Wang, "Delocalization of relativistic dirac particles in disordered one-dimensional systems and its implementation with cold atoms," *Phys. Rev. Lett.*, vol. 102, p. 210403, May 2009.

[207] S. Roy and S. Basu, "Interplay of off-diagonal random disorder and quasiperiodic potential in a one-dimensional Aubry-André model," *Europhys. Lett.*, vol. 128, no. 4, p. 47005, 2020.

[208] C. Wu, J. Fan, G. Chen, and S. Jia, "Non-hermiticity-induced reentrant localization in a quasiperiodic lattice," *New J. Phys.*, vol. 23, no. 12, p. 123048, 2021.

[209] R. Qi, J. Cao, and X.-P. Jiang, "Multiple localization transitions and novel quantum phases induced by a staggered on-site potential," *Phys. Rev. B*, vol. 107, p. 224201, Jun 2023.

[210] X.-P. Jiang, Y. Qiao, and J.-P. Cao, "Mobility edges and reentrant localization in one-dimensional dimerized non-Hermitian quasiperiodic lattice," *Chinese Phys. B*, vol. 30, no. 9, p. 097202, 2021.

[211] S. Vaidya, C. Jörg, K. Linn, M. Goh, and M. C. Rechtsman, "Reentrant delocalization transition in one-dimensional photonic quasicrystals," *Phys. Rev. Res.*, vol. 5, p. 033170, Sep 2023.

[212] Z.-S. Xu, J. Gao, A. Iovan, I. M. Khaymovich, V. Zwiller, and A. W. Elshaari, "Observation of reentrant metal-insulator transition in a random-dimer disordered ssh lattice," 2023.

[213] L. Zhou, H. Pu, and W. Zhang, "Anderson localization of cold atomic gases with effective spin-orbit interaction in a quasiperiodic optical lattice," *Phys. Rev. A*, vol. 87, p. 023625, Feb 2013.

[214] S. Ray, M. Pandey, A. Ghosh, and S. Sinha, "Localization of weakly interacting bose gas in quasiperiodic potential," *New Journal of Physics*, vol. 18, p. 013013, dec 2015.

[215] S. Ray, B. Mukherjee, S. Sinha, and K. Sengupta, "Bosons with incommensurate potential and spin-orbit coupling," *Phys. Rev. A*, vol. 96, p. 023607, Aug 2017.

[216] H. Sakaguchi and B. A. Malomed, "Matter-wave solitons in nonlinear optical lattices," *Phys. Rev. E*, vol. 72, p. 046610, Oct 2005.

[217] F. Abdullaev, A. Abdumalikov, and R. Galimzyanov, "Gap solitons in bose–einstein condensates in linear and nonlinear optical lattices," *Physics Letters A*, vol. 367, no. 1, pp. 149–155, 2007.

[218] Y. Li, L. P. Pitaevskii, and S. Stringari, "Quantum tricriticality and phase transitions in spin-orbit coupled Bose-Einstein condensates," *Phys. Rev. Lett.*, vol. 108, p. 225301, May 2012.

[219] V. Achilleos, D. J. Frantzeskakis, P. G. Kevrekidis, and D. E. Pelinovsky, "Matter-wave bright solitons in spin-orbit coupled Bose-Einstein condensates," *Phys. Rev. Lett.*, vol. 110, p. 264101, Jun 2013.

[220] P. Vinayagam, R. Radha, S. Bhuvaneswari, R. Ravisankar, and P. Muruganandam, "Bright soliton dynamics in spin orbit-rabi coupled Bose-Einstein condensates," *Communications in Nonlinear Science and Numerical Simulation*, vol. 50, pp. 68–76, 2017.

[221] A. Di Carli, G. Henderson, S. Flannigan, C. D. Colquhoun, M. Mitchell, G.-L. Oppo, A. J. Daley, S. Kuhr, and E. Haller, "Collisionally inhomogeneous Bose-Einstein condensates with a linear interaction gradient," *Phys. Rev. Lett.*, vol. 125, p. 183602, Oct 2020.

[222] Y. Cheng, "Effective potential of two coupled binary matter wave bright solitons with spatially modulated nonlinearity," *Journal of Physics B: Atomic, Molecular and Optical Physics*, vol. 42, p. 205005, oct 2009.

[223] L. E. Young-S, D. Vudragović, P. Muruganandam, S. K. Adhikari, and A. Balaž, "Openmp fortran and c programs for solving the time-dependent Gross-Pitaevskii equation in an anisotropic trap," *Computer Physics Communications*, vol. 204, pp. 209–213, 2016.

[224] R. Ravisankar, D. Vudragović, P. Muruganandam, A. Balaž, and S. K. Adhikari, "Spin-1 spin–orbit- and Rabi-coupled Bose–Einstein condensate solver," *Comput. Phys. Commun.*, vol. 259, p. 107657, 2021.

[225] R. Ravisankar, T. Sriraman, L. Salasnich, and P. Muruganandam, "Quenching dynamics of the bright solitons and other localized states in spin–orbit coupled Bose–Einstein condensates," *J. Phys. B*, vol. 53, no. 19, p. 195301, 2020.

[226] S. Gangwar, R. Ravisankar, S. I. Mistakidis, P. Muruganandam, and P. K. Mishra, "Spectrum and quench-induced dynamics of spin-orbit-coupled quantum droplets," *Phys. Rev. A*, vol. 109, p. 013321, Jan 2024.

[227] S. K. Sarkar, S. Mardonov, E. Ya Sherman, P. Muruganandam, and P. K. Mishra, "Spin-dependent localization of spin–orbit and Rabi-coupled Bose-Einstein condensates in a random potential," *New Journal of Physics*, vol. 27, p. 023018, feb 2025.

[228] Y. Zhai and Y. Zhang, "Patterning by dynamically unstable spin–orbit-coupled Bose–Einstein condensates," *Chaos, Solitons & Fractals*, vol. 174, p. 113835, 2023.

[229] Y. Xu, Y. Chen, and X. Chen, "Fast transport and splitting of spin-orbit-coupled spin-1 Bose-Einstein condensates," *Phys. Rev. A*, vol. 109, p. 063310, Jun 2024.

[230] S. V. Manakov, "On the theory of two-dimensional stationary self-focusing of electromagnetic waves," *Sov. Phys. JETP*, vol. 65, p. 248, 1974.

[231] I. V. Tokatly and E. Y. Sherman, "Gauge theory approach for diffusive and precessional spin dynamics in a two-dimensional electron gas," *Ann. Phys.*, vol. 325, p. 1104, 2010.

[232] A. Marte, T. Volz, J. Schuster, S. Dürr, G. Rempe, E. G. M. van Kempen, and B. J. Verhaar, "Feshbach resonances in Rubidium 87: Precision measurement and analysis," *Phys. Rev. Lett.*, vol. 89, p. 283202, Dec 2002.

[233] M. Erhard, H. Schmaljohann, J. Kronjäger, K. Bongs, and K. Sengstock, "Measurement of a mixed-spin-channel Feshbach resonance in ^{87}Rb," *Phys. Rev. A*, vol. 69, p. 032705, Mar 2004.

[234] M. Egorov, B. Opanchuk, P. Drummond, B. V. Hall, P. Hannaford, and A. I. Sidorov, "Measurement of *s*-wave scattering lengths in a two-component Bose-Einstein condensate," *Phys. Rev. A*, vol. 87, p. 053614, May 2013.

[235] M. Modugno, E. Y. Sherman, and V. V. Konotop, "Macroscopic random Paschen-Back effect in ultracold atomic gases," *Phys. Rev. A*, vol. 95, p. 063620, Jun 2017.

[236] K. Blum, *Density Matrix Theory and Applications*. Springer, NY, Heidelberg, 2012.

[237] I. M. Lifshits, S. A. Gredeskul, and L. A. Pastur, *Introduction to the theory of disordered systems*. Wiley-VCH, 1988.

[238] B. I. Shklovskii and A. L. Efros, *Electronic Properties of Doped Semiconductors*. Springer, 1984.

[239] M. Y. Azbel, "Eigenstates and properties of random systems in one dimension at zero temperature," *Phys. Rev. B*, vol. 28, pp. 4106–4125, Oct 1983.

[240] M. Pasek, G. Orso, and D. Delande, "Anderson localization of ultracold atoms: Where is the mobility edge?," *Phys. Rev. Lett.*, vol. 118, p. 170403, Apr 2017.

[241] L. S. Levitov and E. I. Rashba, "Dynamical spin-electric coupling in a quantum dot," *Phys. Rev. B*, vol. 67, p. 115324, Mar 2003.

[242] Y. V. Kartashov, V. V. Konotop, M. Modugno, and E. Y. Sherman, "Solitons in inhomogeneous gauge potentials: Integrable and nonintegrable dynamics," *Phys. Rev. Lett.*, vol. 122, p. 064101, Feb 2019.

[243] J. Li, E. Y. Sherman, and A. Ruschhaupt, "Quantum control of classical motion: piston dynamics in a Rabi-coupled Bose-Einstein condensate," *New J. of Phys.*, vol. 26, p. 053031, 2024.

[244] L. Sanchez-Palencia, "Smoothing effect and delocalization of interacting Bose-Einstein condensates in random potentials," *Phys. Rev. A*, vol. 74, p. 053625, Nov 2006.

[245] L. W. Cheuk, A. T. Sommer, Z. Hadzibabic, T. Yefsah, W. S. Bakr, and M. W. Zwierlein, "Spin-injection spectroscopy of a spin-orbit coupled fermi gas," *Phys. Rev. Lett.*, vol. 109, p. 095302, Aug 2012.

[246] Z. Gui, Z. Zhang, J. Su, H. Lyu, and Y. Zhang, "Spin-orbit-coupling-induced phase separation in trapped Bose gases," *Phys. Rev. A*, vol. 108, p. 043311, Oct 2023.

[247] A. Trombettoni, H. Nistazakis, Z. Rapti, D. Frantzeskakis, and P. Kevrekidis, "Soliton dynamics in linearly coupled discrete nonlinear schrödinger equations," *Mathematics and Computers in Simulation*, vol. 80, no. 4, pp. 814–824, 2009. Nonlinear Waves: Computation and Theory VIII.

[248] C.-F. Liu, M. Lu, and W.-Q. Liu, "Dynamics of vector dark soliton induced by the rabi coupling in one-dimensional trapped bose–einstein condensates," *Physics Letters A*, vol. 376, no. 3, pp. 188–196, 2012.

[249] I. M. Merhasin, B. A. Malomed, and R. Driben, "Transition to miscibility in a binary bose–einstein condensate induced by linear coupling," *Journal of Physics B: Atomic, Molecular and Optical Physics*, vol. 38, p. 877, mar 2005.

[250] I. M. Merhasin, B. A. Malomed, and R. Driben, "Miscibility transition in a binary bose-einstein condensate induced by linear interconversion," *Physica Scripta*, vol. 2005, p. 18, jan 2005.

[251] G. Gligorić, A. Maluckov, M. Stepić, L. c. v. Hadžievski, and B. A. Malomed, "Transition to miscibility in linearly coupled binary dipolar bose-einstein condensates," *Phys. Rev. A*, vol. 82, p. 033624, Sep 2010.

[252] E. Chiquillo, "Quasi-one-dimensional spin-orbit- and rabi-coupled bright dipolar bose-einstein-condensate solitons," *Phys. Rev. A*, vol. 97, p. 013614, Jan 2018.

[253] T. Kanna, A. Annamalar Sheela, and R. Babu Mareeswaran, "Spatially modulated two- and three-component rabi-coupled gross–pitaevskii systems," *Journal of Physics A: Mathematical and Theoretical*, vol. 52, p. 375201, aug 2019.

[254] H. Susanto, P. Kevrekidis, B. Malomed, and F. Abdullaev, "Effects of time-periodic linear coupling on two-component bose–einstein condensates in two dimensions," *Physics Letters A*, vol. 372, no. 10, pp. 1631–1638, 2008.

[255] J.-C. Zhao, C.-D. Li, Y.-Q. Li, and J.-G. Wang, "Rabi-coupled binary bose-einstein condensates with spatially modulated nonlinear spin-orbit coupling," *International Journal of Theoretical Physics*, vol. 60, pp. 3609–3617, Sep 2021.

[256] J. Struck, C. Ölschläger, R. L. Targat, P. Soltan-Panahi, A. Eckardt, M. Lewenstein, P. Windpassinger, and K. Sengstock, "Quantum simulation of frustrated classical magnetism in triangular optical lattices," *Science*, vol. 333, no. 6045, pp. 996–999, 2011.

[257] F. Meinert, M. J. Mark, K. Lauber, A. J. Daley, and H.-C. Nägerl, "Floquet engineering of correlated tunneling in the Bose-Hubbard model with ultracold atoms," *Phys. Rev. Lett.*, vol. 116, p. 205301, May 2016.

[258] F. K. Abdullaev, P. G. Kevrekidis, and M. Salerno, "Compactons in nonlinear Schrödinger lattices with strong nonlinearity management," *Phys. Rev. Lett.*, vol. 105, p. 113901, Sep 2010.

[259] A. J. Olson, S.-J. Wang, R. J. Niffenegger, C.-H. Li, C. H. Greene, and Y. P. Chen, "Tunable Landau-Zener transitions in a spin-orbit-coupled Bose-Einstein condensate," *Phys. Rev. A*, vol. 90, p. 013616, Jul 2014.

[260] J. M. Gomez Llorente and J. Plata, "Modulation of spin–orbit coupled Bose–Einstein condensates: analytical characterization of acceleration-induced transitions between energy bands," *Journal of Physics B: Atomic, Molecular and Optical Physics*, vol. 57, p. 235301, nov 2024.

[261] B. Deconinck, P. G. Kevrekidis, H. E. Nistazakis, and D. J. Frantzeskakis, "Linearly coupled Bose-Einstein condensates: From Rabi oscillations and quasiperiodic solutions to oscillating domain walls and spiral waves," *Phys. Rev. A*, vol. 70, p. 063605, Dec 2004.

[262] Z. Meng, L. Wang, W. Han, F. Liu, K. Wen, C. Gao, P. Wang, C. Chin, and J. Zhang, "Atomic Bose–Einstein condensate in twisted-bilayer optical lattices," *Nature*, vol. 615, pp. 231–236, Mar 2023.

[263] S. S. Rawat, S. K. Jha, M. K. Verma, and P. K. Mishra, "quTARANG: A High-performance computing Python package to study turbulence using the Gross-Pitaevskii equation," *Computer Physics Communication*, vol. 315, p. 109725, 2025.

[264] L. D. Landau and E. M. Lifshits, *Quantum Mechanics - Nonrelitavistic Theory*. Elsevier, 2013.

[265] K. Nakamura, A. Kohi, H. Yamasaki, V. M. Pérez-García, and V. V. Konotop, "Levitation of spinor bose-einstein condensates: Macroscopic manifestation of the franck-condon effect," *Europhysics Letters*, vol. 80, p. 50005, oct 2007.